Measurement of Human Lens Stiffness for Modelling Presbyopia Treatments

Geoffrey S. Wilde

Brasenose College

University of Oxford

A thesis submitted for the degree of

Doctor of Philosophy

Hilary Term, 2011

Abstract

Measurement of Human Lens Stiffness for Modelling Presbyopia Treatments
Geoffrey S. Wilde
Brasenose College, University of Oxford
A thesis submitted for the degree of Doctor of Philosophy
Hilary Term, 2011

Computational models of human accommodation hold the promise of an improved understanding of the mechanism and of the development of presbyopia. A detailed and reliable model could greatly assist the design of treatments to restore accommodation to presbyopic eyes. However, a large quantity of data is required for such an endeavour. Currently, the details of the age-related increase in the stiffness of the lens is a major source of uncertainty as the published data differ markedly depending on the form of testing employed.

A new version of the spinning lens test is presented, based on the method originated by Fisher, R. F. (1971) 'The elastic constants of the human lens', *Journal of Physiology*, 212(1):147–180. This test assesses the stiffness of the lens substance by photographically measuring the deformations induced by rotation of the lens about its axis of symmetry. The principal changes introduced in the present version are the removal of the capsule from the lens prior to testing, the synchronization of the photography with the orientation of the lens, and the use of a hyperelastic finite-element model of the test coupled with a numerical optimization procedure to quantify the heterogeneous stiffness of the lens. These alterations, together with further improvements, provide a substantially more accurate means of measuring the stiffness of the lens 'substance'.

Measurements made with the new test on a series of human lenses are reported. Good-quality tests were obtained for 29 lenses aged from 12 to 58 years. The older lenses were found to be much stiffer than younger lenses. In younger lenses the cortex of the lens is found to be stiffer than the nucleus, but the nucleus stiffens more rapidly, surpassing the cortex by about 44 years. These results differ substantially from those of the original spinning test.

The stiffness values calculated for the lens substance are used in a series of hyperelastic finite-element models of the accommodation mechanism. Models corresponding to subjects aged 29 and 45 years follow clinical measurements of the decline in accommodation amplitude between these ages. Adjusting the material parameters values indicates that it is the increase in stiffness which is largely responsible for the modelled fall in accommodation amplitude. The 45-year model is adapted to represent the effect of laser lentotomy, a proposed presbyopia treatment. Among the lentotomy options trialled, the best result is a modest 0.4 D increase in the modelled accommodation amplitude.

Acknowledgments

The cast of characters are credited in order of appearance in the plot.
Stuart Judge, the instigator
Harvey Burd, the supervisor
Florence, the leading lady
Wellcome Trust and the Laser Zentrum Hannover, the funders
John Richards and Ashley Brown, the makers
Valerie Smith and colleagues at the Bristol Eye Bank
The people of room 11, past and present

Contents

1

Introduction

1.1 Physiological background

The human crystalline lens is one component of the optics of the eye. In conjunction with the cornea, it focuses incoming light on the retina. In young subjects the lens can change shape and thereby increase the optical power of the eye, bringing near objects into focus; this process is called accommodation. The capacity of the lens to change shape diminishes gradually with age and is usually negligible by an age of 50 years. This loss of accommodation is known as presbyopia. The predominant causes of presbyopia remains a matter of some contention.

There is currently considerable interest in establishing treatments to restore accommodation to presbyopic subjects. A more quantitative description of the mechanics involved in accommodation and a firm understanding of the development of presbyopia would be of considerable benefit for guiding the development of such treatments.

1.1.1 The crystalline lens

The location of the crystalline lens within the eye is illustrated in figure 1.1. The crystalline lens lies on the optical axis, immediately behind the iris. Its shape is roughly that of an oblate spheroid with a diameter of 9–10 mm and a thickness (along the optical axis of the eye) of 4–5 mm in an adult. The constituents of the lens are illustrated in figure 1.2. The exterior

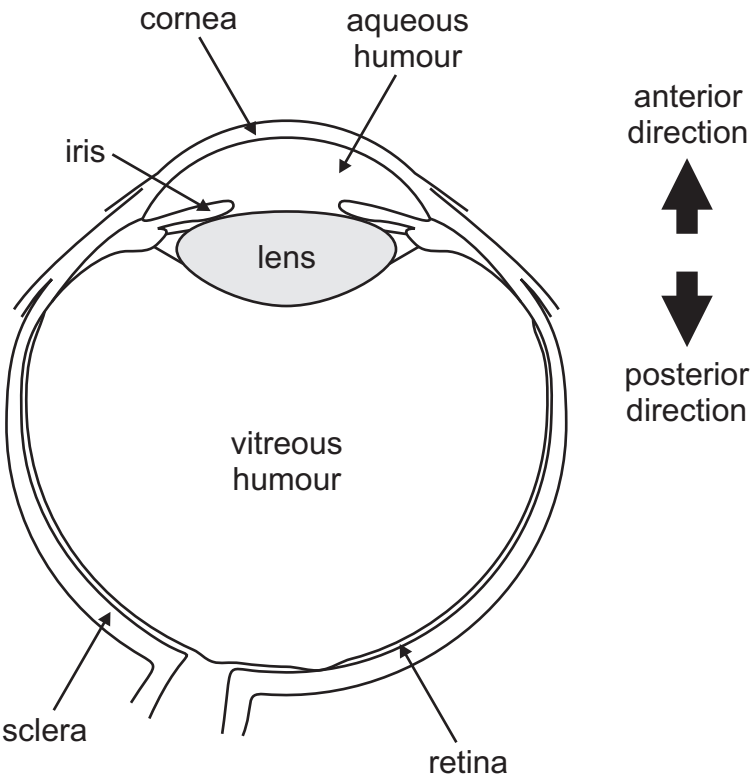

Figure 1.1 – *The principal structures of the eye globe.*

of the lens is covered by the capsule, an extracellular membrane of around 10 μm thickness (though this varies with position and age, Fisher and Pettet, 1972; Barraquer et al., 2006). The substance of the lens within the capsule is composed of specialized cells known as lens fibres due to their long thin form. These are arranged in orderly concentric shells, with each cell running from the vicinity of the anterior pole of the lens (closest to the cornea) to the vicinity of the posterior pole (closest to the retina). Most cells do not reach the poles but meet other cells of the same shell in a pattern of lines known as sutures. These patterns become more complex towards the outside of the lens.

New shells of cells are added to the outside of the lens substance throughout life. The new fibre cells are produced by the differentiation of peripheral members of a layer of cuboid epithelial cells which lies inside the anterior surface of the lens capsule. The epithelial cells are also responsible for the production and maintenance of the lens capsule. Once new fibre cells have grown to form a complete shell, they lose their cellular nuclei and become largely inert. Due to the pattern of shell growth, the age of the lens tissue increases gradually from the outside to the core. The oldest, central portion of the lens is known as the nucleus and

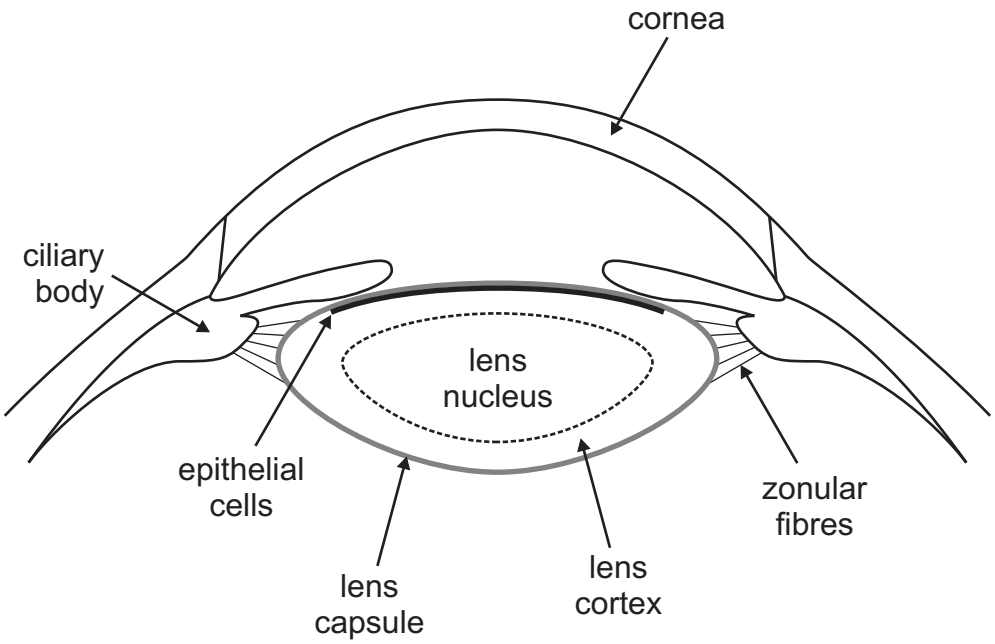

Figure 1.2 – *The components of the lens and the surrounding structures.*

the remainder the cortex. A demarcation between the two regions is visible using *in vivo* slit-lamp photography (Brown, 1973; Dubbelman et al., 2003). This may correspond to a barrier to diffusion, identified at a similar position within the lens (Sweeney and Truscott, 1998; Moffat and Pope, 2002).

The lens is held in place by the zonular fibres which run radially from the encircling ciliary body to attachment points in the peripheral zone of the lens capsule. The ciliary body is a ring of muscle and other tissue contiguous with the iris and in contact with the sclera (the outer layer of the globe of the eye). The anterior of the lens is bathed in the aqueous humour of the anterior chamber of the eye, while the posterior is surrounded by the more gelatinous vitreous humour which fills the region between the lens and the retina.

The lens achieves a high degree of transparency due to the orderly arrangement of the fibre cells, and their relative homogeneity. It contributes to the optics of the eye due to its high refractive index compared to the surrounding aqueous and vitreous humours. This is achieved by a high concentration of proteins within the lens fibre cells (about 35 % of wet weight according to Heys et al., 2004). The refractive index is not constant throughout the lens, but increases gradually from about 1.37 at the surface to about 1.42 at the centre, reflecting the variation in the protein concentration within the lens (Jones et al., 2005).

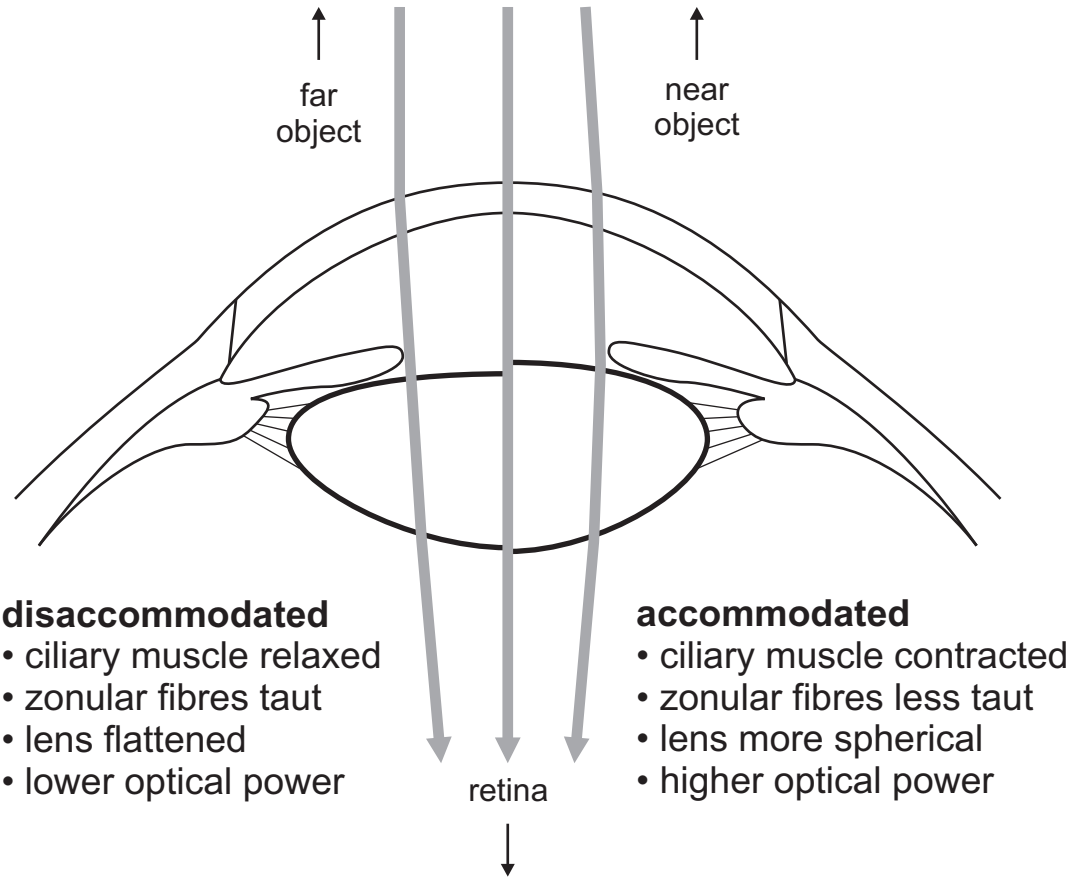

Figure 1.3 – *The disaccommodated and accommodated states of the anterior segment. The left half of the diagram shows the disaccommodated configuration, in which light from a far object is focused on the retina. The right half of the diagram shows the accommodated configuration, in which light from a near object is focused on the retina.*

1.1.2 The process of accommodation

The lens is the component which provides adjustable optical power to young eyes. This is achieved by a shape change in the lens induced by the contraction of the ciliary muscle. When the ciliary muscle is relaxed it has a relatively large radius which induces tension in the zonular fibres and stretches the lens radially outward. This flattens the lens and reduces its optical power, bringing distant objects into focus on the retina. When the ciliary muscle contracts it moves radially inward which reduces the tension in the zonular fibres and allows the lens to return to a more spherical form. The increased curvature increases its optical power, bringing closer objects into focus on the retina. The process which induces this second configuration is termed accommodation, and the eye and the lens are described as accommodated when viewing near objects. The reverse process is disaccommodation and the eye and the lens are disaccommodated (or unaccommodated) when viewing distant ob-

jects. These two states are illustrated in figure 1.3. The gradient refractive index of the lens substance means that the increase in power of the lens from disaccommodated to accommodated does not depend only on the increase in the curvature of the surfaces of the lens, it also depends on the changes in curvature of the contours of constant refractive index within the lens (Garner and Smith, 1997), though this effect is difficult to measure directly. In addition to the changes in lens shape the anterior surface of the lens tends to move forward with accommodation, while the posterior surface effectively remains stationary. These movements are sufficiently small that they contribute little to the change in power of the eye.

The above description of the accommodation is essentially that proposed by von Helmholtz (1855). Alternative mechanisms have been suggested. For example Coleman (1970) adds a crucial role for the pressure of vitreous humour on the posterior surface of the lens in determining its accommodated and disaccommodated shapes. Meanwhile Schachar (1992) argues that the increased curvature of the accommodated lens is achieved by an increase in the zonular tension at the lens equator rather than the decrease which is suggested under the Helmholtz mechanism. However, the bulk of the evidence favours the Helmholtz mechanism so the alternatives will not be addressed in detail. For example Fisher (1982) rebuts the Coleman mechanism and Wilson (1997) provides evidence against the Schachar mechanism.

1.1.3 Presbyopia and changes in the lens with age

The capacity of humans to accommodate diminishes with age, and is generally absent by 50 years. The condition of being unable to accommodate is known as presbyopia. The progression of presbyopia can be measured by determining the the amplitude of accommodation, that is the difference between the optical power of the eye when fully accommodated and when fully disaccommodated, conventionally measured in diopters ($\mathrm{D} \equiv \mathrm{m}^{-1}$). This has been found to decline in an essentially linear fashion from youth until the eye is fully presbyopic, as displayed in figure 1.4.

The loss of amplitude is due to a reduction in the optical power of the lens when maximally accommodated, so the closest point which can be brought into focus (the near point) recedes with age. This only becomes noticeable when the near point approaches the small-

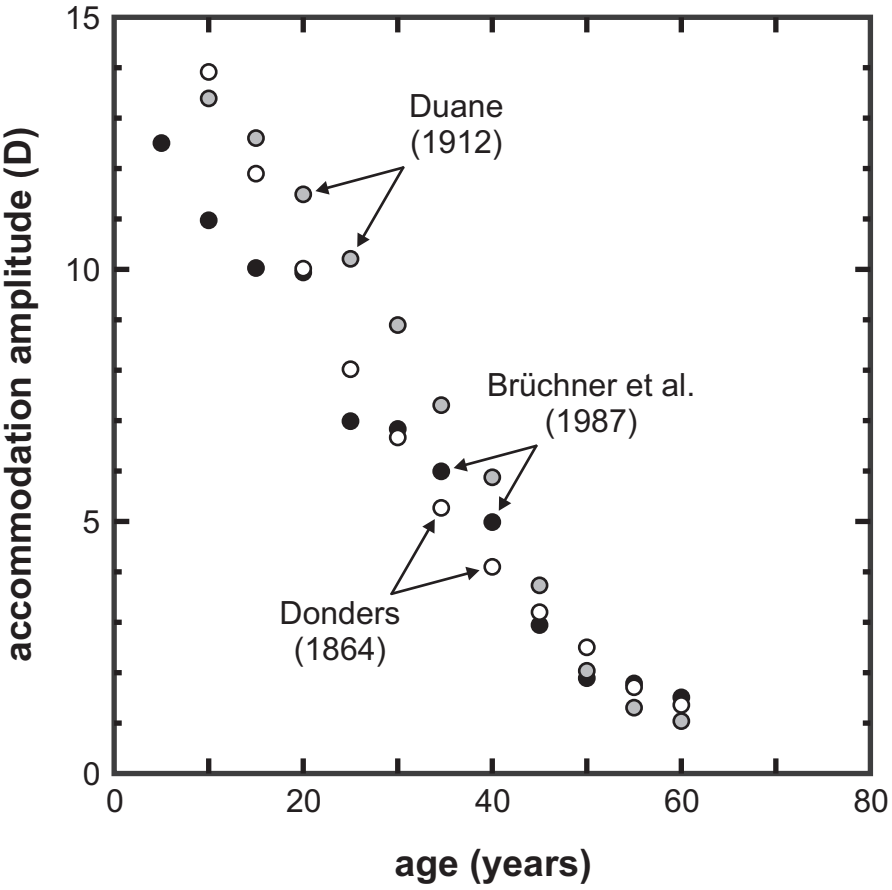

Figure 1.4 – *The subjective amplitude of accommodation measured for individuals of different ages in three studies (Donders, 1864; Duane, 1912; Brückner et al., 1987), averaged over 5-year intervals. (Adapted from figure 1 in Weale, 1990).*

est working distance used by a person (for example 4 D of accommodation is required to be able to focus on a book at 250 mm as well as on distant objects). Even when fully presbyopic the depth of field provided by the pupil allows clear vision over a moderate range of distances, depending on the lighting conditions. The depth of field causes differences between subjective and objective measurements of accommodation. Subjective measurements of accommodation rely on the subject reporting whether a given visual target can be brought into focus, while objective measurements directly determine the optical power of the eye when given different accommodation stimuli. A large depth of field increases the range over which subjective focus is achieved, while the objective optical power remains at a single point within that range. The residual subjective accommodation measured in subjects older than about 50 years (as seen in figure 1.4) is ascribed to depth of focus, and is not found when accommodation is measured objectively (Hamasaki et al., 1956).

The lens and surrounding tissues undergo a number of changes with age which could plausibly contribute to the development of presbyopia. The most obvious potential cause is the substantial stiffening of the lens substance with age which directly diminishes the degree to which the lens will alter shape in response to a given change in zonular tension (Fisher, 1971; Glasser and Campbell, 1998; 1999). However, the magnitude of the increase in stiffness remains uncertain as differing test methods yield quite different results (compare for example Fisher, 1971 and Heys et al., 2004).

Geometric changes in the lens, zonular fibres and ciliary body are also potential contributors to the development of presbyopia. Fisher (1973) suggested that the decline in accommodation amplitude is due to the increasing stiffness of the lens substance in combination with the decreasing stiffness of the capsule and the flattening of the lens. A decrease in the transmission of traction from the zonular fibres to the lens substance due to the increasing thickness of the lens was proposed as a cause by Koretz and Handelman (1986), while Strenk et al. (2005) implicated a forward and inward movement of the ciliary body with age, resulting in less tension in the zonular fibres.

Decreasing contractility of the ciliary muscle with age would also diminish accommodation, but a number of studies have concluded that it remains capable of movement after all accommodation is lost (for example Pardue and Sivak 2000).

1.1.4 Restoration of accommodation

The limitations imposed by presbyopia can be overcome in a number of ways. The usual method at present is the use of reading or multifocal glasses, which provide the required change in optical power without a change in the eye itself. It is also possible to treat the eye in order to create a multifocal effect, or to induce monovision in which one eye is rendered suitable for far vision and the other for near vision (see for example Leyland and Zinicola, 2003; Dexl et al., 2011). True restoration of accommodation, however, means allowing the optical power of the aged eye to adjust in response to the neurological accommodation signal in a manner comparable to the youthful eye. No currently available treatment provides significant restoration of objectively measured accommodation. However, a number of treatments

have been proposed which do aim to restore accommodation (a recent review is provided by Glasser, 2008).

One proposal, scleral expansion surgery is inspired by the questionable Schachar mechanism of accommodation (see section 1.1.2). The sclera is modified in order to increase the diameter of the ciliary muscle. This is intended to correct the decline in zonular tension that is thought to be responsible for presbyopia under the Schachar mechanism. A number of studies have found that the treatment does not restore accommodation (for example Mathews, 1999; Malecaze et al., 2001).

The remaining proposals (which are generally assume a more conventional view of the accommodation mechanism) can be grouped into three classes: implantation of accommodating intraocular lenses (accommodating IOLs), lens refilling, and laser lentotomy.

The implantation of accommodating intraocular lenses represents a further development of the current treatment of cataract. Typical cataract surgery involves the removal of the clouded lens substance and its replacement by a thin artificial intraocular lens of fixed optical power (a non-accommodating IOL). The IOL is usually placed within the remaining capsule. Some existing IOLs are intended to provide some accommodation by translating axially towards the cornea in response to ciliary muscle contraction and thereby altering the optical power of the eye (for example the Crystalens from Bausch and Lomb and the 1CU lens from Human Optics). However, the axial movement that these lenses achieve *in vivo* is found to be small and unreliable. Objective measurements suggest that the IOLs do not generally provide useful accommodation (Menapace et al., 2007). More complex designs intended to provide substantial accommodation with the relatively small movements provided by the ciliary muscle are currently being pursued (for example Hermans et al., 2008b).

A frequent complication for accommodating IOLs is the alteration in behaviour of the lens epithelial cells following the removal of the lens substance (Wormstone et al., 2009). The cells tend to proliferate over the whole capsule causing substantial light scatter when they colonize the posterior capsule (posterior capsule opacification). This is also a problem for non-accommodating IOLs, but can be treated by removing the problematic portion of capsule. Accommodating IOLs face a greater difficulty because removal of additional

capsule material after implantation is likely to adversely affect the mechanical coupling between the ciliary muscle and the device. Accommodating IOLs generally face a greater risk of posterior capsule opacification as their mechanical requirements limit the capacity to adopt features from non-accommodating IOLs which have been found to reduce the risk of epithelial cell proliferation.

Lens refilling also involves the replacement of the native lens substance. Rather than inserting a preformed device, a material such as a polymer is used to completely fill the emptied capsule (see for example Parel et al., 1986). The refilled lens is intended to be geometrically and mechanically similar to a youthful lens, and to deform correspondingly in response to ciliary muscle contraction. One of the challenges faced by lens refilling is the need to obtain the desired optical properties with the limited control available from the refilling process (Koopmans et al., 2006). This and the problem of polymer leakage can be overcome by introducing an intraocular lens at the anterior surface of the refilled lens (Nishi et al., 2008), though this reduces the mechanical equivalence to the youthful lens. Lens refilling also faces the problem of posterior capsule opacification (Nishi and Nishi, 1998).

While accommodating IOLs and lens refilling are generally envisaged as possible improvements on existing cataract treatment, if either become a reliable method for restoring accommodation they could be applied to clear lenses purely to treat presbyopia.

The laser lentotomy method leaves the native lens substance in place, in contrast to the use of accommodating IOLs and lens refilling. A pulsing femtosecond laser is used to treat the lens noninvasively to increase its compliance. The laser causes ablation of the lens substance in a small ($\sim 10\,\mu$m diameter) region at its focus. The repeated application of the laser is used to create a pattern of ablated tissue designed to enhance the amplitude of accommodation (see for example Schumacher et al., 2009). The ablated regions cause increased light scatter within the lens, so to maintain visual clarity they must not encroach on the optically active region surrounding the axis of the lens.

The three potential treatments for presbyopia described above all rely on the untreated portion of the accommodation apparatus to transmit appropriate forces to the optically active part to achieve the intended change in shape and optical power. Ensuring that the modified

system will operate correctly requires an solid understanding of the mechanics of the native system in addition to the changes caused by the treatment. Computational modelling of the accommodation system can play an important role in developing this understanding and informing the design of presbyopia treatments.

1.2 Objectives

The understanding of the mechanics of the accommodation system and of the development of presbyopia can be improved through computational modelling. This is currently impeded by the limited information on the material properties of the constituent tissues. The stiffness of the lens substance has been measured to increase with age, and this is generally believed to play a substantial role in the development of presbyopia. There is, however, no consensus on those stiffness values or the rate at which they increase, as different tests produce markedly different values.

This dissertation has two principal aims related to the mechanics of the human crystalline lens:

1. To further the understanding of the stiffness of the lens substance and how it changes with age. This is achieved through:
    i. the development of procedures to test the stiffness of the lens substance
    ii. the collection of new stiffness data from lenses over a range of ages relevant to the development of presbyopia.
2. To demonstrate the application of the new stiffness data in computational modelling of the accommodation mechanism. This encompasses:
    i. the use of the new stiffness data in new models of the native accommodation mechanism to examine the role of the lens substance in the development of presbyopia
    ii. the modification of one of the new models of the native accommodation mechanism to investigate the use of laser lentotomy as a treatment for presbyopia.

2

Literature: Stiffness of the lens tissues

Information on the stiffness of the tissues involved in accommodation is important for understanding the details of the mechanism in young subjects and of the development of presbyopia in older subjects. Computational modelling of the accommodation mechanism depends on good-quality information on the constituent tissues. The focus of the current work is the mechanics of the lens substance, but the capsule and zonular fibres are also relevant when modelling the accommodation mechanism.

Tissues of animals other than primates are of only limited utility for understanding human accommodation due to substantial differences between the lenses (Augusteyn, 2007) and variation in capacity to accommodate (Ott, 2006). There is also evidence that causes of presbyopia differ between humans and the common primate models used in research (Strenk et al., 2005). On this basis, only tests on human specimens are reviewed below.

2.1 Stiffness of the lens substance

The source of the elasticity of the lens substance has not been established. It is a soft and fragile tissue with a complex microstructure, so designing and interpreting tests to obtain stiffness data relevant to *in vivo* accommodation poses some difficulty. A number of test

methods have been used, leading to a wide range of values. The methods and their results are discussed below.

2.1.1 A summary of test procedures

A number of approaches have been used to test the stiffness of the lens substance. The method of testing a lens which most closely corresponds to its *in vivo* behavior is to extract the whole accommodation system as a unit and apply radial tractions to deform it in a manner similar to disaccommodation (Ziebarth et al., 2008). However, isolating the contribution of the lens substance from that of the capsule is difficult in these circumstances and has not been reported. An alternative is to remove the ciliary body and zonular fibres then deform the isolated lens in a similar manner by different means: either by compressing it axially (Itoi et al., 1965; Glasser and Campbell, 1999), or spinning it about its axis to induce radial forces (Fisher, 1971). A more invasive approach is to conduct small-scale indentation tests on a sectioned lens (Heys et al., 2004; 2007; Weeber et al., 2007) or on an isolated nucleus (Czygan and Hartung, 1996). When applied to sectioned lenses this method has the advantage of providing detailed information on the heterogeneity of lens stiffness, but the disadvantage that the cells of the lens substance are disrupted in the process. Standard dynamic mechanical analysis has also been applied to the lens substance (Weeber et al., 2005), providing data on the viscous as well as elastic properties of the lens. This requires the specimen to be cut into several pieces to conform to the apparatus and this may have a substantial influence on the results. A method which allows local measurements without sectioning the lens is the bubble-acoustic test (Hollman et al., 2007), in which a small bubble is created in an isolated but intact lens and then probed with ultrasound.

Of the above tests, those of Fisher (1971), Heys et al. (2004), Heys et al. (2007), Weeber et al. (2007) and Hollman et al. (2007) provide stiffness measurements for ages relevant to the development of presbyopia and in a form that can be transferred to other contexts, such as computational modelling, so these tests are examined in detail below. The compression test of Glasser and Campbell (1999) is also considered as it provides an additional comparison to the spinning test of (Fisher, 1971), which would otherwise be the only test examined which

induced deformation in the whole lens at once.

2.1.2 The spinning test of Fisher (1971)

To conduct the spinning lens test a specimen is rotated about its axis of symmetry at a fixed speed, inducing deformations which can be related to the apparent centrifugal forces experienced. The deformations can be measured using photography which provides information on the form as well as the magnitude of deformation, allowing some assessment of lens heterogeneity to be made.

The spinning lens test was devised by Fisher (1971), who advocated it in preference to axial compression of the lens because the lens fibre cells appeared far less disturbed after spinning than after compression. The test was applied to 40 lenses aged from 4 months to 67 years, making use of the change in both the thickness and diameter when spun to calculate a stiffness value for the nucleus and the cortex of each lens. The outcome indicated that both the nucleus and the cortex stiffened about 8-fold over the age-range tested, with the change in the cortex largely occurring up to 35 years and the change in the nucleus largely after 35 years. The method used by Fisher (1971) to calculate stiffness values was examined by Burd et al. (2006) who concluded that the approximations made in the analysis had a substantial effect on the values obtained from the test and that the presence of the capsule was not adequately addressed, as it was ignored based on the result of a test reported for a single lens. The test is discussed in more detail in chapter 4 together with a set of improvements which motivate the development of a new version of the test in the current work.

The spinning lens test has subsequently been applied, either to estimate the force involved in other forms of loading (Fisher, 1973; 1977), or to assess the change in deformability caused by laser treatment of isolated lenses (Schumacher et al., 2009). However, values of material stiffness were not reported in these cases.

2.1.3 The compression test of Glasser and Campbell (1999)

Measuring the load required to compress a lens axially by some specific amount is perhaps the most straightforward way to obtain stiffness information. As with the spinning test this method has the advantages of keeping the lens intact and deforming it in a manner broadly similar *to in vivo* disaccommodation. Taking account of the lens shape and the contact between the lens and the compressor is potentially complex, making it difficult to convert the spring stiffness that is measured into data which can be transferred to other contexts. It is also not suited to obtaining information on the heterogeneity of the mechanical response of the lens.

Compression tests were conducted by Glasser and Campbell (1999) on 19 lenses aged 5 to 96. The relative peak force required to compress the lenses by 375 μm was reported. This showed a roughly exponential increase with age, with the oldest lenses requiring about 30 times more force than the youngest (see figure 2.1).

This stiffness measurement applies to the lens as a whole, rather than the lens material, as it does not take into account the growth and change in shape of the lens with age; such changes, however, are small compared to the rate of stiffening measured. It is not clear if the reported results correspond to intact or decapsulated lenses (both tests were conducted but only one reported), or whether the removal of the capsule made a notable difference in the results. Perhaps a more important caveat: the relative force traces provided for a 41 and 96 year old lens (figure 12 a in Glasser and Campbell, 1999) indicate that the force at full compression is outside the linear range of the response so may not be comparable to stiffness measurements at smaller strains.

2.1.4 The indentation tests of Heys et al. (2004) and Heys et al. (2007)

Indentation tests were performed by Heys et al. (2004) to determine the variation in lens stiffness both with age between different lenses and with position within the lenses. These data were used for comparison with corresponding measurements of water content. Eighteen lenses aged from 14 to 76 years were tested. Each lens was sectioned through the equator

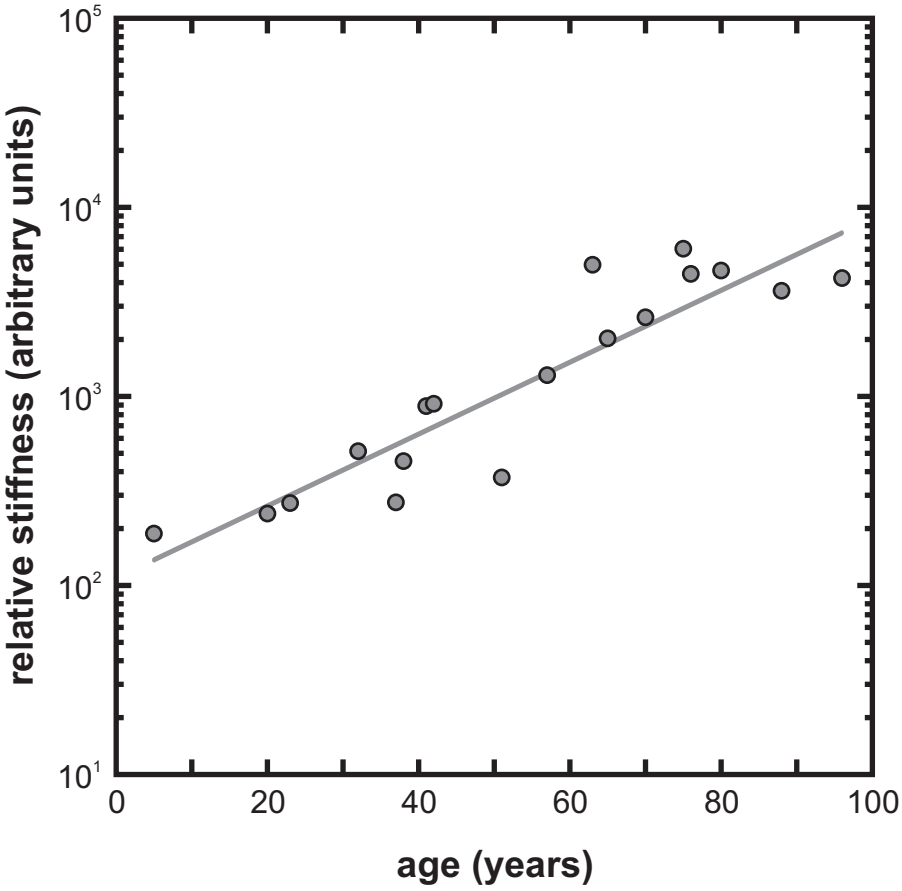

Figure 2.1 – *The relative lens stiffness values reported in Glasser and Campbell (1999), replotted for comparison with figures 2.3 and 2.4. (Adapted from figure 12 c in Glasser and Campbell, 1999).*

then a central core of diameter 8.5 mm was extracted with a trephine. The sample remained within a metal ring from the trephine while a series of indentation tests were performed across the sectioned surface. In each test a cylindrical probe of diameter 0.4 mm was pressed into the sample by a linearly increasing force. Shear modulus values were calculated from the force-displacement measurements using the relation

$$F = \frac{4GRd}{1-\nu} \tag{2.1}$$

where F is the total load, G is the shear modulus of the specimen, R is the radius of the probe, d is the depth of indentation, and $\nu = \frac{1}{2}$ is the Poisson's ratio of the specimen. This corresponds to an ideal small-strain indentation of a semi-infinite, incompressible, isotropic, elastic solid.

The stiffness at the centre of the lenses was found to increase 450-fold over the age-range tested, with a more modest 20-fold increase towards the outside of the sample. A

representative 64-year lens was reported to have a roughly linear increase in stiffness from about 2.5 kPa at the outermost measurement point to about 18 kPa at the centre of the sample. The outermost measurement points were 3.5 mm from the centre of the lens, so no testing was conducted on purely cortical material.

The indentation process was force-controlled, with the force applied increasing to 3 mN over 3 minutes. It is not clear how the soft young lenses were measured as equation 2.1 implies that the maximum force applied would have indented far deeper than the thickness of the specimen. If the test were halted at the reported typical indentation depth of 750 μm this would correspond to a duration of about 3 seconds for a specimen of 40 Pa, the value reported as typical for the nucleus of a 20-year lens. Even an indentation depth of 750 μm must be considered large, since the specimens would be about 2.5 mm deep at most. The use of equation 2.1 when testing close to the metal ring housing the sample means that these outer measurements must be viewed with considerable caution

The lenses reported in Heys et al. (2004) were frozen at −80 °C before being thawed for the test, which may have affected the stiffness measurement. A second series of indentation tests was performed on about 40 fresh human lenses aged from 0 to 88 years and the shear modulus values measured at the centre of the lenses were plotted in Heys et al. (2007). Among the youngest comparable lenses the fresh ones were about 5 or 6 times stiffer than their frozen counterparts, while the oldest comparable lenses were of similar stiffness whether fresh or frozen, and overall the fresh lens data displayed less scatter. The text of Heys et al. (2007) states that the change in stiffness between 20 and 60 years remained similar to the 450-fold increase reported for the frozen case, though the plotted data suggest the corresponding increase for the fresh lenses is at most 80-fold. The data from the fresh lenses appears preferable to that from the frozen lenses, but they have been reported in considerably less detail.

2.1.5 The oscillatory indentation test of Weeber et al. (2007)

Weeber et al. (2007) also applied an indentation test to measure the stiffness variation across sectioned lenses, though the conduct of the test differed in a number of respects from that

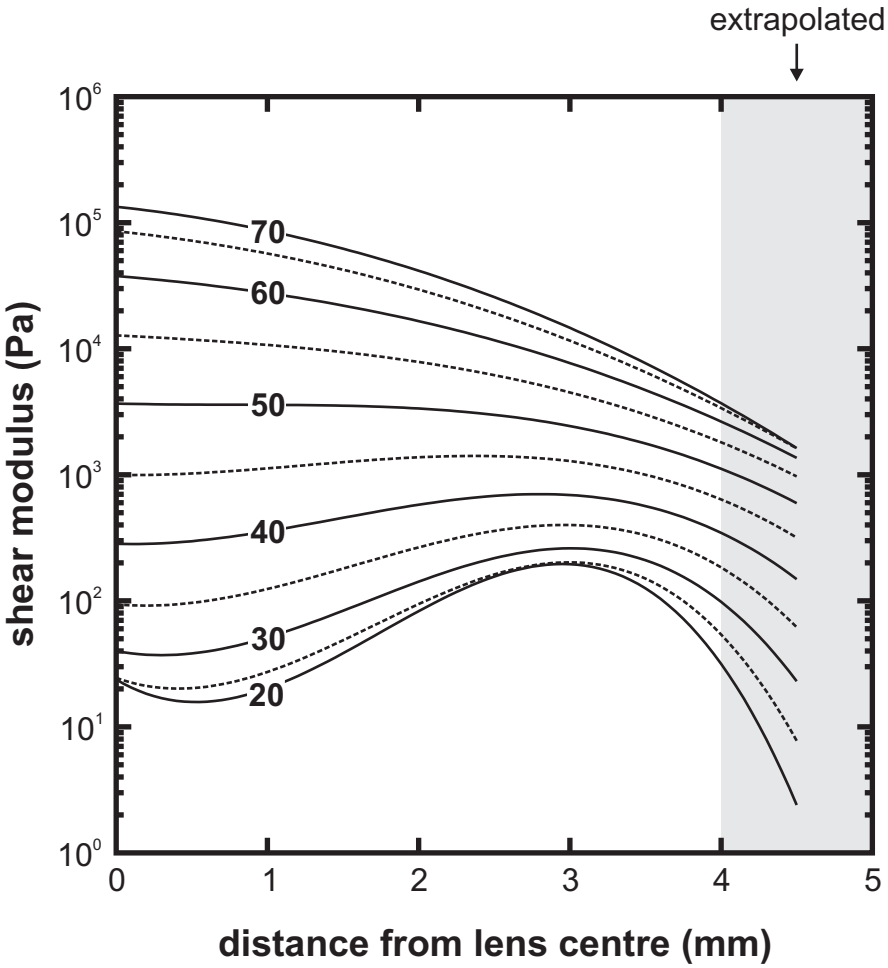

Figure 2.2 – *The shear modulus of the lens as a function of age and position, as calculated by Weeber et al. 2007. The measurements extend to 4 mm from the lens centre, so the region beyond this point is indicated as an extrapolation. (Adapted from figure 7 of Weeber et al. 2007).*

of Heys et al. (2004). At each test point in the equatorially sectioned lenses the probe was inserted 500 μm then oscillated at a range of frequencies and amplitudes (up to 50 μm) to obtain the dynamic response, with care being taken to limit the amplitude to the linear range of the material. The shear modulus values obtained were then modified to take account of the general shape of the lens and the effect of the implied gradient in stiffness at the test point.

Ten lenses aged from 19 to 78 years were tested. The centre of the oldest lens was found to be 10,000 times stiffer than the youngest lens, while the periphery, at 4 mm from the centre, was reported to be 100 times stiffer. The younger lenses, (up to a lens aged 49 years), exhibited a softer centre than periphery, while the reverse was true for the older lenses.

The principle summary of the shear modulus measurements from Weeber et al. (2007) is

Table 2.1 – *The values of the coefficients, c_{mn}, of equation 2.2 which best reproduce the curves of figure 7 of Weeber et al. (2007).*

		m			
		0	1	2	3
n	0	4.2459×10^{0}	-2.9055×10^{-1}	8.5584×10^{-3}	-6.0400×10^{-5}
	1	-3.0406×10^{0}	1.7185×10^{-1}	-3.1631×10^{-3}	1.8601×10^{-5}
	2	2.0923×10^{0}	-8.5154×10^{-2}	1.1379×10^{-3}	-5.1499×10^{-6}
	3	-3.8277×10^{-1}	1.4995×10^{-2}	-1.9391×10^{-4}	8.2153×10^{-7}

figure 7, replotted here as figure 2.2. The equation describing the stiffness profiles shown in figure 2.2 are not reported by Weeber et al. (2007), but are well matched by fitting the plotted curves with a function of the form

$$\log_{10}(\mu) = \sum_{m=0}^{3}\sum_{n=0}^{3} c_{mn}A^m r^n \quad , \tag{2.2}$$

where A is the age of the lens in years, r is the radial position in millimetres, and μ is the shear modulus in pascals. The coefficients, c_{mn}, which were found to best reproduce the published figure are given in table 2.1.

2.1.6 The bubble-acoustic test of Hollman et al. (2007)

The bubble-acoustic test reported by Hollman et al. (2007) allows the local mechanical properties of lenses to be probed without the need to section the lens. In principle it could be performed *in vivo*.

To conduct each bubble-acoustic test a small bubble (30–100 μm diameter; Erpelding et al., 2007) was induced at a target location within the lens using a laser pulse. An ultrasound probe was used to simultaneously apply an acoustic radiation force to the bubble and to track its resultant displacement. The size of the bubble was also assessed by measuring the back-scattered ultrasound. Tests were conducted on 5 lenses aged 40 or 41 years and 9 lenses aged between 63 and 70 years. Bubbles were created at points from 0 to 4 mm from the lens centre with a spacing of 1 mm. The measurements of bubble displacement (adjusted for bubble size) displayed very large variations even for measurements at the same position in lenses of similar ages. This meant that the two age groups were not statistically distinguish-

able. Nevertheless, the median Young's modulus measured at each location for each group were reported. The middle-aged lenses were mostly homogeneous with a Young's modulus of about 1.0 kPa, except at the centre where the value was 5.6 kPa (from just three measurements). The Young's modulus of the old lenses declined steadily from about 10.5 kPa at the centre to about 1.4 kPa at 4 mm from the centre.

The reason for the large variation in measurements was reported to be unclear, since tests on porcine lenses were more consistent. If this issue is resolved, the bubble-acoustic test should prove very useful. It has the potential, for example, to explore local anisotropy within the lens. The scale of the test is approaching the typical lengths of the cellular microstructure of the lens, so it may be necessary to assess how the behaviour at the test scale relates to the bulk behaviour of the lens before applying bubble-acoustic measurements to models of accommodation.

2.1.7 A comparison of stiffness measurements

Comparisons between the results of the different types of test are not straightforward as they provide stiffness values for different locations within the lens. The spinning lens test of Fisher (1971) provides data which approximately correspond to the nucleus and cortex of the lens whereas the indentation tests of Heys et al. (2004), Weeber et al. (2007) and Heys et al. (2007) and the bubble-base acoustic test of Hollman et al. (2007) each give essentially local measurements at a number of points restricted to the equatorial plane of the lens. The compression test of Glasser and Campbell (1999) provided a single relative stiffness value for the whole lens, so only the rate at which stiffness increases with age can be compared to the other tests.

The period most relevant to understanding the development of presbyopia is approximately from 20 years to 50 years. The shape of the lens develops in a consistent way from about 20 years and the development of presbyopia is complete by 50 years. A large increase in the stiffness of the lens substance over this span would suggest greater importance of this aspect in the development of presbyopia than a smaller increase. This change can be summarized by a stiffening index, $\hat{E}$, which for a given measurement of lens stiffness is equal to the

Table 2.2 – *The relative increase in stiffness between 20 and 50 years calculated from the age-stiffness relations obtained in the various tests. The values for the increase in stiffness from Glasser and Campbell (1999) are calculated from the reported best-fitting exponential (3.7) and cubic (4.9). The value for Weeber et al. (2005) is calculated from the slope reported for J' in figure 5 in that paper. The value for Heys et al. (2007) was calculated using the best-fitting exponential for stiffness values obtained from figure 1 in that paper.*

	nucleus **or** 0.5 mm	**cortex** **or** 3.5 mm	**whole lens**
Fisher (1971)	2.5	1.4	
Glasser and Campbell (1999)			3.7 or 4.9
Heys et al. (2004)	63	7.9	
Weeber et al. (2005)			6.9
Heys et al. (2007)	10		
Weeber et al. (2007)	229	14.1	

ratio of the typical value at 50 years to the typical value at 20 years. The stiffening indices for the various tests are given in table 2.2. There is a large variation between the tests, but the stiffening indices derived from Fisher (1971) are conspicuously low.

Representative stiffness values for the inner and outer regions of the lens are presented in figure 2.3 and figure 2.4 respectively. It is clear from these figures, and a comparison with figure 2.1, that the spinning lens test of Fisher (1971) produces values which differ considerably from the more recent tests, especially the indentation tests.

The spinning and indentation tests do agree that the outer region of young lenses is stiffer than the inner region, and that the inner region becomes stiffer with age, eventually reaching or surpassing the outer stiffness. The age at which the lens has approximately uniform stiffness differs between the tests, with Fisher (1971) indicating it occurs well after the lens is presbyopic, at about 70 years, while Heys et al. (2004) and Weeber et al. (2007) indicate ages of about 35 and 45 years respectively, prior to full presbyopia. The lenses tested by Hollman et al. (2007) which were aged 40 to 41 years also display uniform stiffness if the central measurement is discounted. The timing of the transition from a stiffer outside to a stiffer inside of the lens is likely to be important in understanding the development of presbyopia (Weeber and van der Heijde, 2007), especially in light of the gradient refractive index of the lens which means that internal deformations of the lens during accommodation affect its optical power in addition to the surface deformations. Slit lamp photography of lenses *in vivo*,

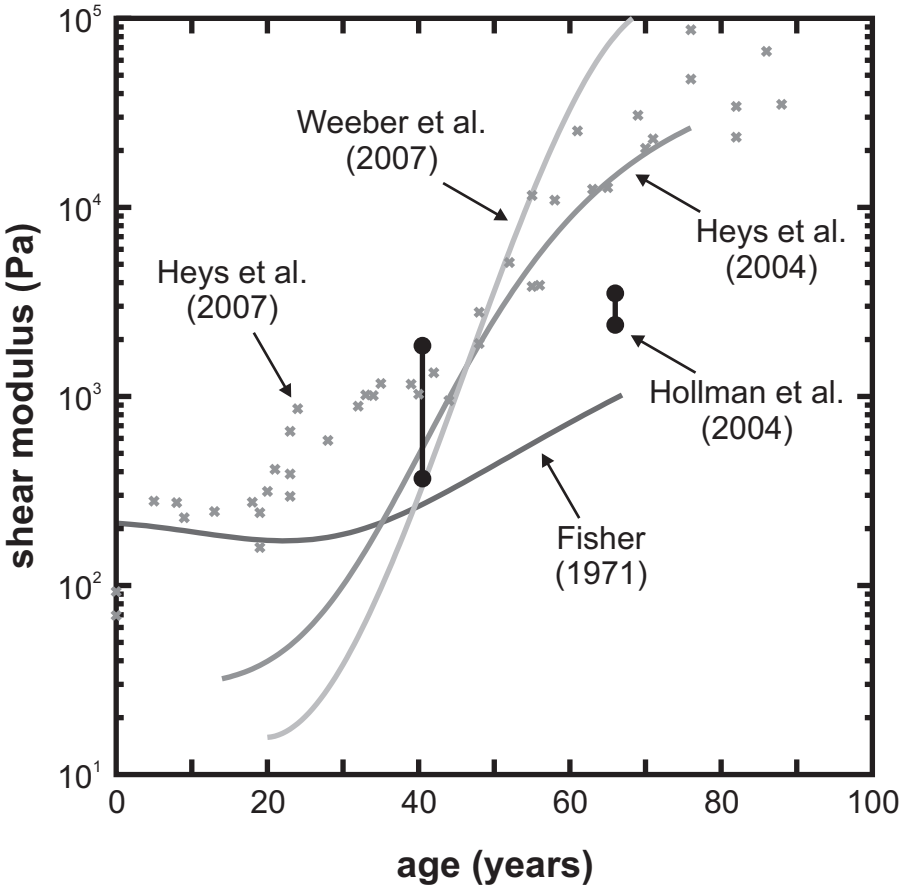

Figure 2.3 – *A comparison of age-stiffness relations of the inner region of the lens. The data from Fisher (1971) are for the nucleus. The data from Heys et al. (2004) and (2007) and Weeber et al. (2007)are for a point 0.5 mm from the axis of the lens. The data from Hollman et al. (2007) are for the centre and a point 1.0 mm from the centre of the lens.*

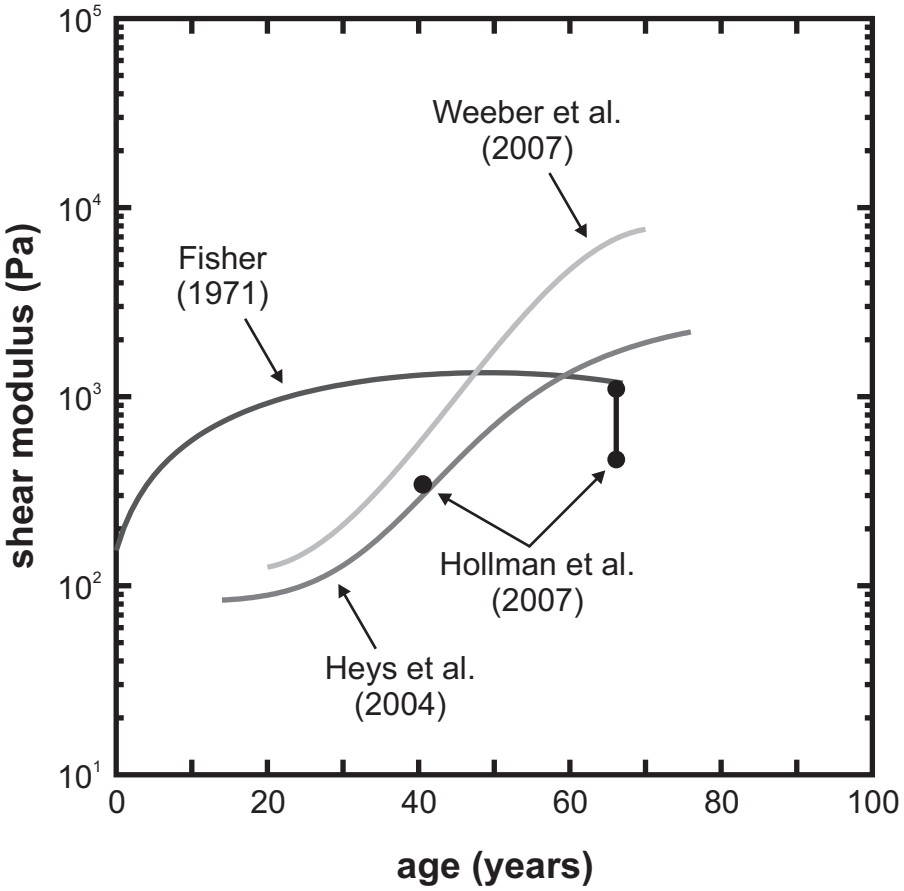

Figure 2.4 – *A comparison of age-stiffness relations for the outer region of the lens. The data from Fisher (1971) is for the cortex. The data from Heys et al. (2004) and Weeber et al. (2007) are for a point 3.5 mm from the axis of the lens. The data from Hollman et al. (2007) are for points 3.0 mm and 4.0 mm from the centre of the lens.*

in which internal features of the lens can be identified, indicate that the nucleus experiences greater axial strains than the cortex during accommodation, supporting the notion that the cortex is stiffer than the nucleus in lenses still able to accommodate (Patnaik, 1967; Brown, 1973; Dubbelman et al., 2003; Hermans et al., 2007).

The stiffness values, the rate of stiffness increase and the age at which the lens becomes uniform all differ between the various tests, with the results of (Fisher, 1971) distinctly different from the rest. It is not apparent which of the numerous differences between the methods employed in the tests have a significant effect on the results. The different preparation of the lenses (fresh or frozen, intact or sectioned) may play a role, though Hollman et al. (2007) used fresh intact lenses and also found the nucleus of old lenses to be much stiffer than Fisher (1971).

The spinning test is influenced by the stiffness of the cortex at the poles of the lens which the indentation tests do not examine; however, the compression test of Glasser and Campbell (1999) is also affected by the polar cortex yet shows a greater rate of stiffness increase. It is also possible that a more complex material model for the lens substance, such as anisotropic behaviour, would reconcile the measurements, but there is no indication of what form such a model would take.

The spinning lens test has a number of attractive features, but it seems likely that a number of limitations in the conduct and analysis of the test reported by Fisher (1971) gave it a muted response to the stiffness of the lens substance and hence an unrealistically low increase in stiffness.

2.2 Stiffness of the capsule

The capsule is a form of basement membrane produced and maintained by the epithelial cells which lie on the anterior surface of the lens substance. From a mechanical perspective the primary constituent of the capsule is a mesh of type IV collagen fibrils.

Several tests have been conducted to measure the stiffness of the human lens capsule. Two general methods have been adopted: biaxial inflation tests applied to some or all of the

anterior capsule (Fisher, 1969; Danielsen, 2004; Pedrigi et al., 2007) and uniaxial extension tests applied to excised rings of the anterior and posterior capsule (Krag et al., 1997; Krag and Andreassen, 2003a;b). The capsule is capable of sustaining large strains, up to 100 % linear strains for very young specimens (Krag et al., 1997). During accommodation, however, average area strains of about 5 % are typical (Hermans et al., 2009), so it is the stiffness measurements acquired at low strains which are of interest for understanding the usual *in vivo* behaviour of the capsule.

2.2.1 Biaxial testing

Fisher (1969) devised a test in which a disc of anterior capsule material is clamped around its edge, submerged in fluid, and caused to deform by increasing the pressure on the lower surface. The relationship between the pressure and the volume enclosed by the capsule material allows the stiffness of the capsule to be estimated using the assumptions that it maintains the form of a spherical cap and deforms in an eqi-biaxial manner. The Young's modulus was found to decline from about 6 MPa in childhood, to 3 MPa by 60 years, and to 1.5 MPa in extreme old age. The Poisson's ratio of the capsule material was determined separately by measuring how its thickness changed as the capsule distended. This yielded a value of 0.47, indicating the deformation of the capsule approximately conserved volume.

A similar test and analysis was used by Danielsen (2004) as part of a comparison of the properties of the anterior lens capsule to Descemet's membrane (a layer of the cornea). All the human capsule specimens examined were aged over 56 years with mean age of 80 years. These yielded an average stiffness consistent with the corresponding measurements of Fisher (1969) at a linear strain of 10 %, though a value for Young's modulus was not calculated.

An alternative method of inflation was adopted by Pedrigi et al. (2007) to examine the regional stiffness properties of capsules from normal and diabetic donors. In this approach the capsule is left in place around the lens substance and a needle inserted through the capsule to supply fluid at a pressure. The deformation of the capsule is measured by using two video cameras to track a number of markers placed on its surface. The movement of sets of markers are used to deduce the local stiffness using an inverse finite element method. The capsule

material is described by a Fung-type constitutive model with four parameters. Six normal lenses aged between 29 and 81 years (mean 67 years) were tested, and used to determine a single set of parameter values for the constitutive model. Burd (2009) showed that the biaxial behaviour of a Fung-type material with these parameter values is broadly consistent with the measurements of Fisher (1969) for a linear strain of 10 % or lower.

2.2.2 Uniaxial testing

A number of uniaxial stretching tests on the accommodation apparatus were reported by van Alphen and Graebel (1991). In each test the ciliary body, zonular fibres, and lens were removed from the eye as a unit. Two clamps (10 mm wide) were applied to opposite sides of the ciliary body in order to stretch the accommodation apparatus uniaxially. The applied load was recorded and photographs were used to measure the extensions experienced by each component of the specimen. Variations of the test in which different parts were cut or removed were used to separate the influence of the various tissues. This form of uniaxial stretching leads to complex loading and deformation of the specimen so only relatively rough calculations of the properties of the tissues were possible. The Young's modulus of the capsule at 10 % strain was calculated from 71 tests on samples aged from 0 to about 70 years. The typical values were about 0.7 MPa near birth and between 1.0 and 2.1 MPa among older samples, with a tendency to increased stiffness with age. The calculation of the stiffness of the capsule took no account of the presence of the lens substance nor the variation in the shape of the capsule along the axis of the test, so the results are broad approximations only.

A more refined method for determining the uniaxial response of samples from human lens capsules was presented by Krag et al. (1997). A ring of capsule material was cut from each specimen using a metal stencil and an excimer laser. The width and thickness of the ring was measured microscopically. It was then placed over two pins, one connected to a force transducer and the other to a motorized micropositioner and its load-elongation behaviour was recorded as the pins were moved apart. This test was developed primarily to investigate the mechanical properties of the capsule relevant during cataract surgery, in which a central disc of the capsule is surgically removed and the remaining material is subjected to large

strains. The secant Young's modulus calculated at 10 % strain was reported for 67 specimens from the anterior portion of the capsule and 25 specimens from the posterior capsule by Krag and Andreassen (2003a). The typical Young's modulus of the anterior capsule was reported to rise from 0.4 MPa at birth to 1.45 MPa by 35 years and then remain constant. The values for the posterior capsule appear consistent with this relation, though with considerable variation between samples.

2.2.3 Comparison of the measurements

Only the tests of Fisher (1969) and Krag and Andreassen (2003a) produce reliable results for a substantial number of lenses over a wide range of ages. Both tests indicate that the capsule is much stiffer than the lens substance. There is, however, a large difference in the stiffness values obtained from the two tests in specimens up to 60 years and the values exhibit opposite trends with age. Krag and Andreassen (2003a) suggested that the difference may arise because the value from the inflation test corresponded to larger strains; however, Burd (2009) calculated that the difference in strain was moderate and that the discrepancy remained after this was taken into account.

Burd (2009) proposed a new constitutive model for the lens capsule which includes an explicit representation of the collagen microstructure. This model of the collagen mesh behaves in a stiffer manner in response to biaxial traction than a homogeneous material with an equivalent uniaxial response. Thus this form of constitutive model provides a possible explanation for the differences seen between the tests of Fisher (1969) and Krag and Andreassen (2003a).

2.3 Stiffness of the zonular fibres

The major constituent of the zonular fibres is fibrillin, though its elasticity may be influenced by the reported presence of elastin or glycosaminoglycans (Bourge et al., 2007). Measurements of the stiffness of the zonular fibres are apparently limited to two sets of tests.

Fisher (1986) reported the Young's modulus of the zonular fibres calculated from the combined results of two tests applied to 12 specimens aged from 16 to 50 years. In the first test the ciliary body, zonular fibres, and lens were removed from the eye as a unit and stretched radially in a manner similar to *in vivo* disaccommodation. The changes in geometry of the tissues were measured photographically. In the second test the ciliary body and zonular fibres were removed from the lens, which was then subjected to a spinning test (as described in Fisher, 1971). The spinning test was used to estimate the radial load applied in the first test, under the assumption that the same magnitude of load will result in the same change in the thickness of the lens, despite the differences in the distribution of the load. This assumption is probably inaccurate as the deformation of the capsule is likely to be quite different in the two cases. The material of the zonular fibres was determined to have a Young's modulus of 350 kPa, which was found not to vary with age.

The uniaxial stretching tests of van Alphen and Graebel (1991) discussed in section 2.2.2 were also used to assess the stiffness of the zonular fibres for 54 specimens aged from 0 to about 70 years. The relation between the load applied to the clamps and the resulting extension of the zonular fibres was used to calculate their Young's modulus. A typical value of 1.5 MPa was calculated, though the individual measurements showed very large variations (the standard deviations reported for individual measurements were of the same order as the measurements themselves).

In many circumstances the total radial spring constant of all the zonular fibres considered as a single entity is a more natural value to consider than the Young's modulus of the tissue. Indeed, both Fisher (1986) and van Alphen and Graebel (1991) calculated Young's modulus from a spring-constant value by making assumptions about the number and cross-sectional area of zonular fibres. By examining these assumptions the total radial spring constant implied by the experiments can be deduced. The calculations of Fisher (1986) imply a total cross-sectional area of about 0.12 mm^2 for the zonular fibres (if the unextended length of the zonular fibres is assumed to be about 2.5 mm) and a radial spring constant of about 43 mN. The calculations of van Alphen and Graebel (1991) imply a total cross-sectional area of about 0.24 mm^2 for the zonular fibres (if each clamp is assumed to engage about one sixth of

the zonular fibres) and a radial spring constant of 360 mN.

The two methods adopted for measuring the stiffness of the zonular fibres both involve considerable uncertainties and lead to markedly different values for the Young's modulus. The values for the total radial spring constant display an even larger discrepancy. Fortunately, in many cases when modelling of the accommodation mechanism it is possible to make use of *in vivo* measurements (such as those of Strenk et al., 1999) to choose an appropriate value for the stiffness of the zonular fibres or the forces they exert on the lens (Burd et al., 2002; Hermans et al., 2008a).

3

Literature: Models of accommodation

A range of mathematical models have been developed to examine a various aspects of the accommodation process, most notably the development of presbyopia (for example Wyatt, 1993; van de Sompel et al., 2010). Such models allow the calculation of quantities not readily available through *in vivo* observations or *in vitro* experiments, such as the additional force exerted by the zonular fibres during the process of disaccommodation, or the internal deformations of the lens. They can also examine situations not present in nature to examine, for example, the importance of a particular feature to accommodation, or to assess a possible treatment of presbyopia. The accuracy of such models inevitably depends on the validity of the assumptions made and the quality of the data used in their construction.

3.1 Modelling methods

Several methods have been used to describe the mechanics of the accommodation apparatus. Due to the variety of aspects of accommodation under investigation, models range from a simple collection of springs and dash-pots characterizing the dynamics of the constituents (for example Beers, 1996) to extensive finite-element models which include a detailed geometry and constitutive models to represent the lens and other structures (for example Burd

et al., 2002). Only those models which include the geometric aspects necessary to represent the optics of the system are considered further.

3.1.1 Single component models

Three models (O'Neill and Doyle, 1968; Schachar et al., 1993; Chien et al., 2006) have examined just the capsule in an explicit manner, treating it as an axisymmetric membrane or shell. The influence of the lens substance and the zonular fibres were imposed as a pressure and a membrane traction respectively. O'Neill and Doyle (1968) only examined the anterior portion of the capsule, while Schachar et al. (1993) and Chien et al. (2006) considered the full capsule and required the enclosed volume to remain constant, effectively treating the lens substance as an incompressible fluid. Schachar et al. (1993) used a linear-elastic formulation leading to unrealistic deformations of the capsule, as demonstrated by Burd et al. (1999).

Koretz and Handelman (1986), by contrast, examined only the anterior portion of the lens substance. Its deformation was dictated by *in vivo* measurements of lens curvature and an assumption that spherical surfaces deformed to spherical surfaces. The lens substance was assumed to be homogeneous but anisotropic on the basis of preliminary calculations of stiffness reported by Fisher (1971). Reilly and Ravi (2010) adopted an even simpler series of models in which the whole lens was assumed to deform from one shape to a similar shape during accommodation (for example, from one ellipse to another ellipse) with the only other constraint being an assumption of incompressibility. While such restrictions on the form of the deformation can dramatically simplify calculations they entail substantial and opaque assumptions regarding the behaviour of the lens substance, and so drawing substantial conclusions from such models is problematic.

3.1.2 Finite-element models

A model which includes a realistic geometry for the lens and represents the capsule and the lens substance as distinct solid constituents is necessarily complex. The finite element method has proved a useful tool for producing complex mechanical models in a range of fields, and has become the mainstay for modelling the mechanics of accommodation. It

does, however, require many data (and substantial assumptions where data are unavailable) to construct a reasonable representation of the accommodation apparatus.

A preliminary finite-element model of the lens was developed by Burd et al. (1999), adopting a large-strain formulation to properly describe the mechanics of the capsule. The lens contents were treated as an incompressible fluid for comparison with Schachar et al. (1993). Three more complex finite-element models corresponding to ages 11, 29, and 45 years were reported by Burd et al. (2002), incorporating geometric and material data from a range of publications, in particular using Brown (1973) and Strenk et al. (1999) for lens shape, Fisher (1971) for the stiffness of the nucleus and cortex, and Krag et al. (1997) for the stiffness of the capsule. The accommodated configuration was assumed to be stress free; it was characterized by fifth-order polynomials joined by a circular arc at the lens equator, the same general form used by Schachar et al. (1993).

These models of Burd et al. (1999) have been adopted and adapted in a number of subsequent publications. For example, Martin et al. (2005) added a pressure from the vitreous, while Stachs et al. (2006) modified the geometry of the zonular fibres to reflect ultrasound measurements. The stiffness values used in the model were examined by van de Sompel et al. (2010).

Hermans et al. (2008a), building on the work of Hermans et al. (2006), constructed alternative geometries for lenses of the same ages as Burd et al. (2002). The outline of each lens was described by four conic sections with parameters chosen using data from Strenk et al. (1999), Dubbelman and van der Heijde (2001), and Dubbelman et al. (2005). The nuclei were based on data from Koretz et al. (2001), Koretz et al. (2002) and Hermans et al. (2007). Three alternative models were presented for each age, using the differing stiffness values reported by Fisher (1971), Heys et al. (2004), and Weeber et al. (2007). The zonular fibres were not included in this model, instead tractions were applied directly to the capsule at the points where the zonular fibres would attach.

A model of the accommodation mechanism incorporating residual stresses in the capsule and lens substance was presented by Weeber (2002). In this model, the unstressed state of the capsule was chosen to correspond to the fully-accommodated state of the lens, while the

unstressed state of the lens substance was chosen to correspond to the disaccommodated state of the lens. This was achieved by starting with an unstressed model in the accommodated state, simulating disaccommodation, then eliminating the stresses in the lens substance.

Weeber and van der Heijde (2007) presented a model in which the lens substance was divided into 10 concentric shells with stiffness values from Weeber et al. (2007), rather than the common division of nucleus and cortex. The outline of the lens was described by two conic sections joined by an arc at the lens equator. The parameters used the data from Strenk et al. (1999) and Dubbelman et al. (2005), and were chosen to correspond to the average over a wide age range (16 to 51 years).

Ripken et al. (2006) adapted the 29-year model of Burd et al. (2002) to represent a specific laser lentotomy procedure. The model of the treated lens incorporated thin layers (5 μm) of very soft material corresponding to the regions subjected to ablation. Cuts that would break the axisymmetry of the lens were not considered.

The typical model was extended to include the whole vitreous and a modified arrangement of zonular fibres by Ljubimova et al. (2008). The vitreous was modelled as an incompressible solid which resisted the posterior pull of the zonular fibres on the lens. This novel arrangement performed poorly when compared to *in vivo* measurements of the shape of the lens when disaccommodated.

3.2 Modelling results

3.2.1 Accommodation and presbyopia

The models for ages 11, 29 and 45 years described by Burd et al. (2002) were developed to assess whether the existing data on the accommodation apparatus could produce a model capable of reproducing the the behaviour of the accommodation mechanism and the progress of presbyopia. The 29-year and 45-year models agreed well with the clinical measurements of Duane (1922), while the 11-year model had less than half the expected amplitude of accommodation. It was concluded that the older lenses may capture the causes of presbyopia, but that additional data was required to ensure the models were appropriate.

Martin et al. (2005) adapted the two older models from Burd et al. (2002) by introducing a pressure on the posterior surface of the lens to represent the effect of the vitreous suggested by Coleman and Fish (2001). It was determined that the pressure reduced the amplitude of accommodation to unrealistically low levels, suggesting that the Coleman mechanism does not contribute to accommodation. This conclusion is not supported, however, because in the presence of the posterior pressure the fully-accommodated geometry of the lens models differed from the *in vivo* state (so it could be the difference in geometry rather than the presence of the pressure which is responsible for the low amplitude of accommodation).

A study reported by van de Sompel et al. (2010) also adapted the two older models of Burd et al. (2002) in order to explore a wider range of values for the mechanical and geometric parameters. A comparison between the role of geometry and stiffness in the decline of accommodation amplitude suggested geometry was the dominant cause. Those models with a very soft cortex displayed a small initial increase in optical power in response to radial stretching, as seen in some other models (Chien et al., 2006; Abolmaali et al., 2007). A gradient refractive index was considered when calculating the optics of the lens; however, when the model was subjected to disaccommodation the form of the index profile was dictated by the equatorial radius and the axial thickness of the lens rather than the deformation of the lens substance, so it provides little insight.

Weeber and van der Heijde (2007) compared the amplitude of accommodation for models incorporating the age-dependent stiffness gradient measured by Weeber et al. (2007) to the amplitude for similar models using age-dependent homogeneous stiffness values from Fisher (1971) and Weeber et al. (2005). The gradient-stiffness models indicated a significantly greater decline in accommodation amplitude between the ages of 20 and 60 years than the homogeneous models, and followed the clinical data more closely. The influence of the stiffness gradient on the internal deformations of the lens was investigated by Weeber and van der Heijde (2008), again using the data of Weeber et al. (2007). For the 20-year model the greatest axial strain was found to be at the centre of the soft nucleus, in qualitative agreement with Scheimpflug photography (for example Dubbelman et al., 2003). The total thickness change and the proportion of this change occurring in the cortex were greater in

the model than the *in vivo* measurements. The 40-year model behaved in a similar way to the 20-year case when subjected to the same equatorial stretch, while the stiff nucleus of the 60-year model experienced a smaller axial strain than the cortex. These different internal deformations may be of importance to the optics of the lens, due to the gradient that also exists in the refractive index.

The model of a lens subjected to laser lentotomy, developed by Ripken et al. (2006), was compared to an untreated lens to assess the effect of the treatment. The amplitude of accommodation was found to increase by a modest 0.18 D when the lentotomy cuts were included, though the change in the axial thickness of the lens was more substantial. The optical calculations are in doubt as the power of the lens is unrealistically low even in the undeformed fully-accommodated state.

3.2.2 Sensitivity studies

Modelling can also be used to investigate which aspects of the *in vivo* accommodation apparatus have a substantial influence on its behaviour. Weeber (2002) examined the effect of residual stresses in the lens, and found that they had only a small influence on its optical performance despite a more pronounced effect on the overall shape adopted by the lens. Similarly, Stachs et al. (2006) found that a more complex arrangement of zonular fibres had little impact on the modelled behaviour of the lens on the optical axis, but resulted in a 22 % smaller displacement of the lens equator in response to the simulated movement of the ciliary body. While the optical behavior of the lens is central to understanding the accommodation mechanism, achieving better accuracy throughout a model is useful for comparison with other *in vivo* measurements. Thus broader measures of the influence of such aspects of the model are preferable.

3.2.3 Zonular fibre traction

The simple shell model of O'Neill and Doyle (1968) was used to estimate the membrane traction required to deform the anterior capsule from an accommodated to a disaccommodated form. A value of 12.3 Nm^{-1} was obtained, corresponding to a total force of 348 mN for

a capsule of radius 4.5 mm. This is considerably higher than more recent calculations due to the high stiffness adopted for the capsule which was derived from tests on feline specimens.

Burd et al. (2002) reported the force required to stretch the modelled accommodation apparatus by the amount prescribed for full disaccommodation. The values ranged from about 60 mN for the 11-year model to about 100 mN for the 45-year model.

The models of Hermans et al. (2008a) were used to determine the net force applied by the ciliary body during disaccommodation by iteratively adjusting the applied tractions until the expected disaccommodated lens geometry was achieved. The results ranged from 32 mN to 70 mN depending on the age and stiffness data used form the model. These values were used to inform the design of an accommodating IOL that would operate with a net force of about 10 mN (Hermans et al., 2008b).

3.3 The state of modelling

The bulk of recent models have used the finite element method. The accommodation apparatus is treated in a broadly similar manner in most such models. Axisymmetry is generally assumed, and models consist of the lens substance (often divided into a distinct nucleus and cortex), the capsule, and usually the zonular fibres. The ciliary body is generally not represented explicitly, but the effect of its outward movement during disaccommodation is represented by prescribing the displacement of the of the outer ends of the zonular fibres. Some refinements have been considered, such as residual stresses or the addition of the vitreous, but considering the large uncertainties which currently exist in the appropriate values for basic mechanical properties of the lens substance and capsule, such further steps can only be exploratory. Without improvements in the data available for models, they can only provide limited insight into the accommodation mechanism.

4

Assessment of the spinning lens test

The spinning lens test is a useful means of determining the stiffness of the lens substance as it provides loading which is broadly comparable to *in vivo* accommodation and does not require the disruption of the structure of the lens fibre cells. However, the methods applied in the original spinning lens test of Fisher (1971) have a number of clear limitations which introduce substantial random and systematic errors. Some of these limitations are investigated by Burd et al. (2006), jointly written by the author.

The current work seeks to improve the spinning lens test by reducing the major sources of error and uncertainty that have been identified in the original test. This involves changes to both the experimental arrangements and to the analysis used to determine the stiffness from the raw results.

4.1 Details of the test of Fisher (1971)

The original spinning lens test of Fisher (1971) subjected human lenses to rotation about their axis while resting on a ring shaped support. Lenses were obtained within 24 hours of the death of the donor. The lens was extracted by cutting the zonular fibres with micro-scissors. Photographs were taken of the lens, both stationary and spinning, using a flashgun for illumination. These photographs were taken at random orientations unless the lens was stationary, in which case the lens was rotated 15° between each photograph. A range of

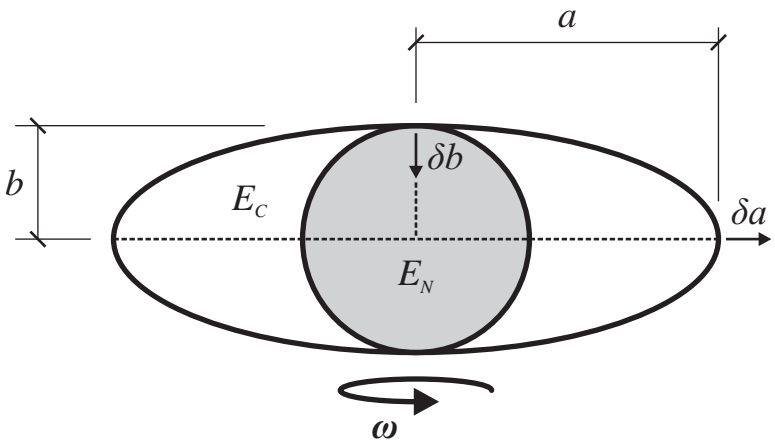

Figure 4.1 – *A cross-section of the idealized lens geometry used in the calculation of stiffness values by Fisher (1971). The symbols are described in the text.*

rotational speeds were applied, from 250 rpm to over 1000 rpm with increments of 250 rpm. Between each test the lens was returned to warmed saline. Measurements of the equatorial diameter and anterior axial thickness (the height of the anterior pole above the plane of the equator) were obtained from the photographs.

The mean equatorial radius, a, and anterior axial thickness, b, were calculated from the seven photographs of the lens when stationary. The changes in these dimensions were determined at each spinning speed to produce smoothed load-displacement plots. The unsigned displacements of the equator and anterior pole at a spinning speed of 1000 rpm were read from these curves to give the values δa and δb. The displacement values were each used to make an estimate the Young's modulus of the lens using a simplified homogeneous model of the spinning lens. As these two values disagreed in a systematic manner a similar, two-material model was developed, illustrated in figure 4.1.

In this model the lens was treated as a spheroid with semi-axes a and b. The nucleus of the lens was assumed to be a sphere of radius b at the centre of the lens possessing a different stiffness from the surrounding cortex. Both components were represented as incompressible, isotropic, and homogeneous materials. Vertical and shear stresses were taken to be negligible during spinning and an approximation was used for the force transmitted from the cortex to the nucleus. This model was used to calculate the stiffness of the nucleus and the cortex from the intermediate values calculated using the homogeneous model of the lens. Equivalently

they can be determined directly from the displacements:

$$E_N = \frac{49}{72}\rho\omega^2 ab^2 \frac{\delta a}{\delta b^2} \tag{4.1}$$

$$E_C = \frac{1}{24}\rho\omega^2 \left(3a\frac{a^2+7b^2}{\delta a} - 49\frac{b}{\delta b}\right) \quad , \tag{4.2}$$

where E_N and E_C are the Young's modulus of the nucleus and cortex respectively, ρ is the density of the lens (separately measured but not reported by Fisher, 1971), and ω is the angular velocity of the lens. The individual values obtained for E_N and E_C were not presented, but were instead summarized by polynomials describing the relationship between age and stiffness.

4.2 Limitations of the original spinning lens test

4.2.1 Influence of the capsule

The stiffness measurements reported by Fisher (1971) appear to come from tests conducted on lenses with intact capsules. The analysis of the tests, however, does not take account of the presence of the capsule. The justification provided is that removal of the capsule has only a small effect on the induced displacements: after removing the capsule there was reported to be no change in the equatorial displacement and a 20 % decrease in the magnitude of the polar displacement. This observation, however, refers to a single 21-year lens so it is not clear that it is either reliable or consistent across the range of ages tested.

If the capsule does restrict the deformation of the lens substance then the stiffness of the substance will affect the magnitude of the restriction. Softer lens substance will experience more restriction than stiffer lens substance, so the presence of the capsule will diminish the range of stiffness values obtained from a set of lenses.

4.2.2 Accuracy of measurements

The methods used to photograph the lens and take measurements from those photographs lead to relatively large errors in the calculated stiffness values. The standard deviation of the dimensions a and b calculated from different sets of photographs of the same stationary lens

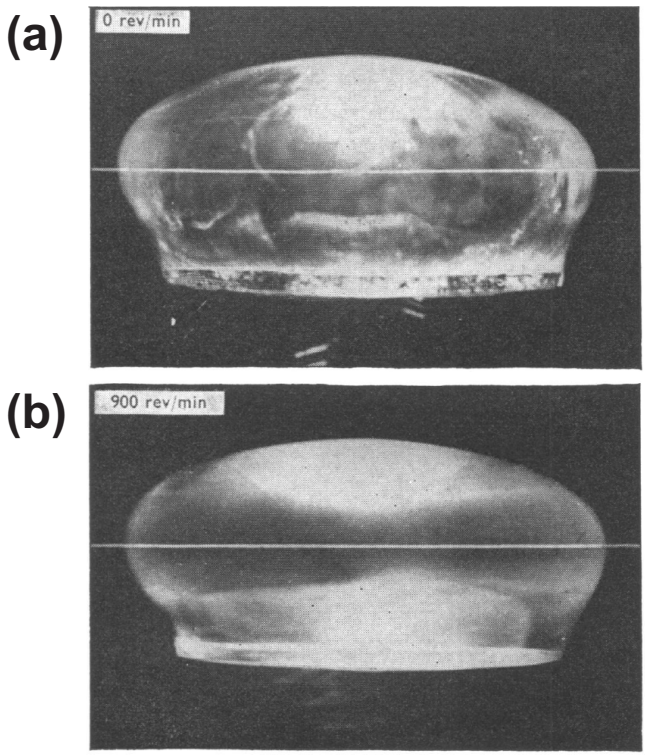

Figure 4.2 – *Two photographs of the same lens from Fisher (1971). The lens is stationary in photograph (a) in which the local details of the lens are visible. The lens is rotating at* 900 rpm *in photograph (b) and the surface details have become blurred by the motion.*

was reported to be 14 μm. Since lenses are not exactly axisymmetric, and cannot be perfectly aligned on the rotor, the difference in dimensions of the lens for different orientations is likely to be a substantial contributor to this variation. If a similar standard deviation applies to the measurements from the spinning lens then the standard deviation in the displacements, δa and δb, would be about 20 μm which is about 10 % of the typical values for young lenses and 30 % for a 60-year lens.

The calculation of the stiffness of the nucleus and the cortex using equations 4.1 and 4.2 magnifies the effect of measurement errors. For typical values of the parameters the relative error of E_N and of E_C is about twice the magnitude of the relative error in δa and δb if the latter are assumed to be independent of each other. This means that with the measurement variation given for a 60-year lens, the interval encompassing one standard deviation in each stiffness value covers roughly a four-fold range.

The measurements taken from photographs of the lens when spinning introduce an additional uncertainty as it is clear from the photographs reproduced by Fisher (1971) that the

lenses rotated substantially during the exposure period, leading to motion blur (see figure 4.2). The edges of the lens captured in the blurred photographs are the outermost points the lens occupied during the exposure period so any misalignment of the lens would lead to exaggerated measurements of the lens equator, and hence of δa. The anterior pole was reported to be without blurring when viewed through a microscope so is unlikely to be affected.

4.2.3 Approximate analytical model

The model used by Fisher (1971) to describe the spinning test is necessarily highly simplified to allow the analytical derivation of equations 4.1 and 4.2. The geometry of the lens is approximate and that of the nucleus differs substantially from reality. Vertical and shear forces are neglected and the potential restraint of the ring on which the lens sits is ignored. Finally, the approximation of the mechanical link between the nucleus and the cortex was chosen on the assumption that the nucleus was no stiffer than the cortex and it becomes increasingly unrealistic the further a given lens is from satisfying this condition.

Each of these approximations may lead to a considerable error in the calculation of the stiffness values. The neglect of the vertical and shear forces is examined as an example. An exact solution exists for the rotation of a homogeneous linear-elastic spheroid , equivalent to the homogeneous case of the model of Fisher (1971) with the inclusion of vertical and shear forces. Burd et al. (2006) give equations for the displacements obtained from this solution:

$$\delta a = \frac{\rho\omega^2 a^3}{2E}\left(\frac{4k^4+9k^2+12}{23k^4+24k^2+48}\right) \tag{4.3}$$

$$\delta b = \frac{\rho\omega^2 a^2 b}{E}\left(\frac{7k^4+10k^2+8}{23k^4+24k^2+48}\right) \quad , \tag{4.4}$$

where E is the Young's modulus and $k = \frac{a}{b}$ is the aspect ratio of the spheroid. If displacements are calculated using this model for values $a = 4.5$ and $b = 2$ (typical for a lens), and then used in equations 4.1 and 4.2, the resulting stiffness values are $E_N = 0.73E$ and $E_C = 1.54E$. So just the neglect of vertical and shear forces in the model of Fisher (1971) leads to a factor-of-two error in this estimate of the ratio of E_C to E_N.

4.3 Improvements in the current work

The implementation of the spinning lens test used in the current work seeks to address the limitations raised in section 4.1 and make further improvements. The problems relating to the capsule and photography are addressed by modifying the experimental procedure, while the remaining issues are countered by introducing a numerical model of the test for calculating the stiffness parameters of the lens, in preference to the approximate analytical model used by Fisher (1971).

4.3.1 Removal of the capsule

The most direct way to address the uncertain effect of the capsule during the spinning test is to remove it before testing. This creates some difficulties during the experiment since additional care is required to avoid damage to the lens substance both during and following the removal of the capsule. However, the elimination of the capsule means that no assumptions on its influence need to be introduced into the analysis of the stiffness of the lens substance. This is the approach adopted in the current series of spinning lens tests. The method used to remove the capsule and the subsequent testing are described in section 6.4.3. Additional spinning tests conducted on the intact lens prior to the removal of the capsule permit an assessment of the influence of the capsule during the test (see section 8.1.3). These tests may be used in future work to examine the properties of the capsule, making use of the stiffness values obtained for the lens substance of the same specimen in the decapsulated tests.

4.3.2 Photography and illumination

The errors introduced by the random lens orientation in photographs and the possible systematic errors caused by motion blur can both be avoided using an improved illumination scheme. The obvious solution to the former problem is to ensure that the lens is photographed at the same set of orientations when stationary and when spinning. By comparing photographs of the lens at the same orientation the deformation of the lens can be assessed without the differences in the overall form of the lens at different orientations causing scatter

in the results. This is implemented in the current spinning lens test by the timing system described in section 6.3. Motion blur is also essentially removed by using an appropriately brief flash duration when taking the photograph, made possible by bringing the flashgun close to the lens.

4.3.3 Modelling the test numerically

The analysis of the test reported by Fisher (1971) made a number of substantial simplifying assumptions to provide an analytical solution. Calculating the stiffness data from the photographs using a numerical method involving fewer approximations would improve the accuracy of the test. In the current spinning lens test, the finite element method is used to model the test, and an iterative optimization procedure is employed to obtain stiffness data from this model. The formulation used in the finite-element model is described in chapter 5, while the methods employed to construct models of spinning lens tests and optimization procedure are described in chapter 7.

The finite element method allows an essentially arbitrary geometry. This means that the specific form of each lens can be modelled, making use of measurements over the full lens outline rather than just the equatorial radius and anterior polar thickness. The deformation of the full outline can then be used to compare the model to the experiment. In addition to greater accuracy, this potentially provides greater sensitivity to the inhomogeneity of the lens than two displacement measurements would give. The automated processing used to obtain the lens outline is presented in section 7.2, and the method of comparing the deformed state of the experimental and modelled outlines is given in section 7.6.1.

The form of stiffness inhomogeneity within the lens can also be chosen freely in a finite-element model, though the choice requires additional information not available from the spinning test itself. It is possible to include a discrete nucleus with a more realistic shape, or to impose some form of continuously varying stiffness, as suggested by the indentation tests of Heys et al. (2004) and Weeber et al. (2007). Both of these options are considered in the current analysis, with details given in section 7.5.

A finite-element model of the spinning test naturally includes the effect of shear and ver-

tical stresses that develop within the lens during spinning, in contrast to the analytical model used by Fisher (1971). It also makes it practical to incorporate the effect of the lens support. The question of exactly how the support and the lens interact during spinning remains uncertain, so the two extremes (the lens fully fixed at the support and the lens free to slide over the support) are examined in the present analysis. Their respective implementations are described in section 7.4, while a comparison of the results is presented in section 8.2.2.

4.3.4 Other changes

Some additional changes have been made to the experimental procedure. Rather than placing the lens in warm saline after each test, the tests are conducted at room temperature and the lens is enclosed in a humid box throughout spinning to reduce drying. This avoids repeated repositioning the lens, which is certainly to be preferred once the capsule has been removed. The number of speeds at which the lenses are tested has been reduced as the lowest speeds generally do not induce enough deformation of the lens to be useful. One difference which is not advantageous is that currently testing can generally only commence two or more days after the death of the donor.

5

A framework for modelling lens mechanics

The analysis adopted for the new version of the spinning lens tests and the application of the resultant data to the *in vivo* accommodation system both require a computational model of the mechanical behaviour of the lens. An axisymmetric hyperelastic finite-element formulation has been identified as an appropriate approach. A summary of the mathematical approach and the numerical procedures adopted in the current work is given below, including the constitutive models used to describe the lens substance, the capsule and the zonular fibres. The selection of the parameters required to characterize a particular material is detailed as it arises in subsequent chapters.

5.1 Background

The computational models of the spinning lens test and the *in vivo* accommodation mechanism used in the current work owe their form to the use of the finite-element program OXFEM_HYPERELASTIC. This program was written by Dr Burd to provide numerical solutions for the large-strain elasticity problems typically encountered when modelling the mechanics of the eye and particularly the lens. In general, the options already provided in OXFEM_HYPERELASTIC have dictated the form adopted for the models, but where these

were considered to be inadequate for the current work the author has made additions to the program.

5.2 Kinematics

5.2.1 Large strain kinematics

The young lens deforms substantially during *in vivo* accommodation and disaccommodation. For example, Strenk et al. (1999), using magnetic-resonance imaging, found that on average for the subjects aged between 20 and 30 years the lens in a disaccommodated state had an equatorial diameter 7 % greater and an axial thickness 10 % less than when accommodating at 8 D (approximately the maximal accommodation effort at that age). The spinning lens test can also induce comparable changes in young lenses. The data plotted in Fisher (1971) and tabulated in Burd et al. (2006) indicate that for the lenses aged between 20 and 30 years, spinning at 1000 rpm produced an increase in the equatorial diameter of 2 % and a decrease in axial thickness of 8 % compared to the stationary state. A linear formulation, in which strains are assumed to be infinitesimal, is inadequate when analysing deformations of this magnitude. This is particularly true for models which include membranes such as the lens capsule, as these generally require a change in shape to achieve equilibrium. The current lens model is based upon the Lagrangian finite-deformation framework presented in Bonet and Wood (1997) and Holzapfel (2000). In addition to representing large strains rigorously this formulation allows the adoption of constitutive models that have been developed in other areas of soft tissue mechanics.

In brief, if a continuous body is deformed from an initial material configuration Ω_0 to a subsequent spatial configuration Ω, then there is a motion function $\chi : \Omega_0 \rightarrow \Omega$ which maps material points $\mathbf{X} \in \Omega_0$ to their subsequent spatial location $\mathbf{x} \in \Omega$. From this the deformation gradient tensor, $\mathbf{F}$, can by calculated as

$$\mathbf{F} = \frac{\partial \mathbf{x}}{\partial \mathbf{X}} \quad . \tag{5.1}$$

The deformation-gradient tensor provides the fundamental description of the deformation of

the body in the vicinity of a given point. In addition to information on the state of strain, the deformation-gradient tensor also contains information on the local rotation of the material. $\mathbf{F}$ can be decomposed into a rotational component, $\mathbf{Q}$, and a symmetric pure stretch component, $\mathbf{U}$; that is $\mathbf{F} = \mathbf{QU}$. The right Cauchy-Green strain tensor, $\mathbf{C} = \mathbf{F}^{\mathrm{T}}\mathbf{F} = \mathbf{U}^2$, is a measure of strain which is independent of the rotational component of $\mathbf{F}$ and can be readily calculated. Since the response of a material to a particular state of strain should not depend on how it has rotated, the right Cauchy-Green strain tensor is commonly used as the independent variable when defining such a response.

When considering an incompressible material, or a nearly-incompressible material such as the lens substance, it is convenient to consider the volumetric strain and the isochoric (volume-conserving) strain separately. The volumetric strain is equal to the determinant of the deformation-gradient tensor: $J = \det(\mathbf{F})$, while the isochoric component is $\hat{\mathbf{F}} = J^{-\frac{1}{3}}\mathbf{F}$. The isochoric component of the right Cauchy-Green strain tensor is $\hat{\mathbf{C}} = J^{-\frac{2}{3}}\mathbf{C}$.

5.2.2 Axisymmetry

The lens is approximately axisymmetric in form and is subjected to axisymmetric deformations both *in vivo* during accommodation and in the spinning lens test. This means the lens can be conveniently described by cylindrical coordinates (R, Z, Θ) in which the Z-axis is aligned with the axis of symmetry of the lens. In this coordinate system the geometry and loads, and consequently the resulting strains and stresses, do not vary with Θ (provided there is no symmetry-breaking behaviour such as buckling). This reduces the description of the lens geometry to two dimensions and greatly decreases the scale of the computations required to solve the problem numerically. Strains and stresses in the circumferential direction (aligned with the unit vector $\hat{\boldsymbol{\Theta}}$) still arise and must be included in the model.

5.3 Constitutive models

Three distinct components of the accommodation apparatus are modelled in the current work: the lens substance, the capsule, and the zonular fibres. The lens substance is mod-

elled during the analysis of the spinning lens test described in chapter 7, while all three components are used in the models of the accommodation system specified in chapter 9. The selection of parameters for the various materials are discussed in those chapters. Sections 5.3.1 to 5.3.4 discuss the most appropriate assumptions to make regarding the behaviour of the various tissues in order to obtain useful models of the system given the limits of the current state of knowledge.

5.3.1 Hyperelasticity

The large-strain formulation adopted encourages the use of hyperelastic constitutive models of the tissues of the accommodation apparatus. A purely elastic material is one in which the stresses at a given point depend only on the current state of strain at that point. If in addition the work done by the stresses in reaching that state of strain also depends only the current state of strain then the material is said to be hyperelastic. This allows the material to be characterized by a scalar-valued function, Ψ, which maps the strain state to the corresponding strain energy density (calculated with respect to the material configuration Ω_0). Derivatives of the strain energy function allow the stress and stiffness tensors to be calculated for any state of strain. This leads to a relatively compact means of specifying material behaviours.

5.3.2 The lens substance

Previous measurements of lens stiffness have generally treated the lens substance as a nearly-incompressible, isotropic, linear-elastic continuum. For example, Fisher (1971) and Heys et al. (2004) both assume this form of constitutive model when interpreting their experimental results. The stiffness measurements of Weeber et al. (2005) and Weeber et al. (2007) additionally incorporate viscoelasticity. Most existing models of the accommodation mechanism (such as Burd et al., 2002, Stachs et al., 2006, and Weeber and van der Heijde, 2007) similarly consider the lens substance to be a nearly-incompressible, isotropic, linear-elastic continuum. An exception is the model of Chien et al. (2006) which treats it as an incompressible fluid continuum.

The large strain formulation used in the current modelling of the lens requires a hyper-

elastic constitutive model for the lens substance. The nearly-incompressible neo-Hookean constitutive model described in Bonet and Wood (1997) is adopted as this provides a simple isotropic material which can be characterized by two parameters, μ and κ, which are equivalent at small strains to the shear and bulk modulus of linear elasticity respectively. This permits a correspondence with previous measurements and models. The strain energy function for this constitutive model is

$$\Psi = \frac{\mu}{2}\left(\mathrm{tr}\left(\hat{\mathbf{C}}\right) - 3\right) + \frac{\kappa}{2}(J-1)^2 \quad , \tag{5.2}$$

where $\hat{\mathbf{C}}$ is the isochoric component of the right Cauchy-Green strain tensor and J is the volumetric strain. For a nearly-incompressible substance $\mu \ll \kappa$. This constitutive model represents essentially the simplest suitable model of the lens substance.

The assumption that the lens substance is nearly incompressible is reasonable in view of its high water content (over 60 % by weight according to Fisher and Pettet, 1973). It is also supported by the observation that neither the nucleus nor the whole lens change volume during accommodation (Hermans et al., 2007; 2009). These observations do not rule out the possibility that the lens substance behaves in a poroelastic manner, with the water component able to flow relative to the solid component. Equally, though, there is no evidence that the mechanical behaviour of the lens depends on such flows and nor is there data to inform such a constitutive model. An assumption that the lens substance is locally nearly incompressible is therefore regarded as the most appropriate means of matching the observed large-scale incompressibility.

The consistent orientation of the lens fibre cells mean the lens substance is not structurally isotropic. If the cell membranes or related structures contribute significantly to the elasticity of the lens then the elastic response in the direction aligned with the cells would be expected to differ from that in the transverse directions (which might also need to be distinguished from each other due to the anisotropic shape of cell cross-sections). However, it is not currently known what constituents gives rise to the elasticity of the lens substance, and no measurements of local elastic anisotropy within the lens exist. This leaves elastic isotropy as the default assumption for the lens substance.

The viscoelastic nature of the lens will influence its dynamic response. However, when

the lens is subjected to a sustained effort to accommodate *in vivo* and when its rate of rotation is held constant for several seconds in the spinning lens test it is assumed that the response of the lens will be dominated by its asymptotic elasticity. Thus it is appropriate to model these situations using the considerably simpler option of a purely elastic material.

5.3.3 The lens capsule

The capsule is thin compared to the overall dimensions of the lens (the polar thickness of the isolated lens is over 200 times the anterior capsule thickness; Rosen et al., 2006; Barraquer et al., 2006). As such it can be modelled as a membrane described geometrically as a zero-thickness surface, but with the appropriate thickness value incorporated into the constitutive model. The mechanics of the capsule are therefore characterized by a function specifying the strain energy per unit undeformed area rather than volume.

The capsule displays a markedly non-linear response at stretch ratios over about 1.15 in uniaxial tension (Krag and Andreassen, 2003a). However, during accommodation the capsule strain is relatively small; for example Hermans et al. (2009) indicate that for young subjects the surface area of the lens when disaccommodated was on average 5 % greater than when accommodated. The constitutive model for an elastic membrane given in equation 5 of Burd (2009) is used to represent the capsule, as this can broadly reproduce the behaviour of the more complex structural model proposed in the same publication. The strain-energy area-density function is

$$\Psi_{2\mathrm{D}} = \frac{t_0 E}{2\left(1-\nu_{2D}^2\right)}\left((\lambda_1-1)^2+(\lambda_2-1)^2+2\nu_{2D}\,(\lambda_1-1)\,(\lambda_2-1)\right) \quad , \qquad (5.3)$$

where t_0 is the membrane thickness in the reference configuration, E is the Young's modulus, ν_{2D} is the in-plane Poisson's ratio, and λ_1 and λ_2 are the in-plane principal stretches of the membrane, equal to the eigenvalues of the deformation gradient tensor $\mathbf{F}$. The values of E and ν_{2D} are selected to reconcile the stiffness values reported for the capsule when tested uniaxially by Krag and Andreassen (2003a) and biaxially by Fisher (1969) (see section 9.1.2). The strain energy function is defined in terms of the principle stretches because in an axisymmetric membrane they necessarily lie in the meridional and circumferential directions, making their calculation straightforward. For large uniaxial stretch ratios ($\lambda \sim 1+\frac{1}{\nu_{2D}}$) the

constitutive model becomes unphysical as the transverse stretch ratio falls to zero, but this is not relevant for the stretch ratios that are encountered when modelling *in vivo* accommodation.

When subjected to compressive stresses a thin membrane will generally buckle, and therefore exhibit greatly reduced stiffness. Buckling in the circumferential direction cannot be represented explicitly in an axisymmetric model as the position of the buckled membrane would have to vary circumferentially. Instead the constitutive model is adjusted to reproduce the reduction in stiffness while maintaining symmetry. For a membrane that is free to buckle in either direction the strain energy function becomes

$$\Psi_{2D} = \begin{cases} \frac{t_0 E}{2\left(1-\nu_{2D}^2\right)}\left(\left(\lambda_1-1\right)^2+\left(\lambda_2-1\right)^2+2\nu_{2D}\left(\lambda_1-1\right)\left(\lambda_2-1\right)\right) & \lambda_1 \geq 1-\nu_{2D}(\lambda_2-1),\ \lambda_2 \geq 1-\nu_{2D}(\lambda_1-1) \\ \frac{t_0 E}{2}\left(\lambda_1-1\right)^2 & \lambda_1 \geq 1,\ \lambda_2 < 1-\nu_{2D}(\lambda_1-1) \\ \frac{t_0 E}{2}\left(\lambda_2-1\right)^2 & \lambda_1 < 1-\nu_{2D}(\lambda_2-1),\ \lambda_2 \geq 1 \\ 0 & \lambda_1, \lambda_2 < 1 \end{cases} \tag{5.4}$$

This function has continuous derivatives, but discontinuous second derivatives at the transitions between unbuckled and buckled states, leading to sudden changes in stiffness, a feature which can be problematic during simulation.

OXFEM_HYPERELASTIC includes an option to specify which buckling states are permissible for each membrane material included in a model. It also allows buckling to be prescribed for cases where the membrane is already buckled in the reference geometry. These features were implemented by the author for use with the lens capsule.

5.3.4 The zonular fibres

The zonular fibres are generally included in models of *in vivo* accommodation, as they transmit the movement of the ciliary body to the lens capsule. As thin radial fibres they are best modelled as bars. In an axisymmetric model the individual fibres are essentially combined into a continuous ring. Unlike a membrane, however, no circumferential stresses exist in the bars and the total cross-sectional area remains constant along the length of the bar element,

rather than increasing with radius. The mechanics of the zonular fibres are therefore characterized by a function specifying the strain energy per unit undeformed length rather than volume.

A neo-Hookean constitutive model is adopted for the zonular fibres. The stretch ratios in the directions orthogonal to the fibre are prescribed by an assumption of incompressibility, leaving just the stretch ratio parallel to the fibre, λ, as a variable in the strain energy line-density function. This takes the form

$$\Psi_{1D} = \frac{A_0 \mu}{2}\left(\lambda^2 + \frac{2}{\lambda} - 3\right) \quad , \tag{5.5}$$

where A_0 is the total cross-sectional area of the fibres in the reference configuration and μ is the shear modulus of the fibre material.

5.4 Finite-element formulation

5.4.1 Solution procedure

OXFEM_HYPERELASTIC is used to calculate an approximate solution to the elastic response of the lens to a given set of loading conditions. The problem of finding the displacement field which corresponds to an equilibrium point of the model is described by the weak formulation, which in axisymmetry can be written as

$$2\pi\left(\int_A \delta\Psi(\mathbf{u})\,R\,dA - \int_a \mathbf{b}\cdot\delta\mathbf{u}\,r\,da\right) = 0 \quad , \tag{5.6}$$

where A is the undeformed axisymmetric cross-section, a is the deformed axisymmetric cross-section, δ is the variational operator, Ψ is the strain energy density function, $\mathbf{u}$ is the displacement field, $\mathbf{b}$ is the body-force field, R is the radial coordinate in the undeformed configuration, and r is the radial coordinate in the deformed configuration.

The problem is discretized using the standard finite-element approach, in which the displacement field is approximated by piece-wise polynomial components specified over a predefined mesh of elements. Integration over each element is approximated using Gaussian quadrature. The problem is then linearized in order to apply the Newton-Raphson method

to find the correct discretized displacement field (to a specified tolerance for the maximum remaining out-of-balance force). Each iteration in the Newton-Raphson procedure requires the calculation of a tangent stiffness matrix which must be inverted to calculate the updated displacement field. In OXFEM_HYPERELASTIC the matrix inversion is performed using a direct frontal solver. The frontal solver avoids assembling the entire sparse matrix, but instead obtains the contribution of each element in turn, eliminating any completed row from the matrix before proceeding.

In general it is preferable to apply the loading conditions in a sequence of steps so that the initial point in the Newton-Raphson procedure is not too far from equilibrium. The standard option in OXFEM_HYPERELASTIC, '`Newton1`', uses a specified number of equal sized steps. The author added a second option, '`Newton2`', in which the step size is adjusted automatically depending on the number of iterations and the maximum out-of-balance force that the previous step produced. Thus if the convergence of the previous application of the Newton-Raphson procedure was slow, the following step will be decreased in size and *vice versa*. The adjustable step size is particularly useful when using OXFEM_SEARCHER (see section 7.6) where the same solution procedure is used to calculate the response for a range of material properties, which generally can be solved most efficiently with different step sizes. If the Newton-Raphson procedure fails to converge for some step then the `Newton2` option also makes a second attempt at increasing the loading using a smaller step size.

OXFEM_HYPERELASTIC has an optional line-search procedure based on the algorithm of Chrisfield (1991). The line-search seeks a scaling, η, to apply to the nodal displacements, $\delta\mathbf{u}$, calculated by the Newton-Raphson procedure after the first iteration of each step. A scaling is sought which decreases the component of the nodal forces acting in the direction of $\delta\mathbf{u}$. Actual nodal displacements of $\eta\,\delta\mathbf{u}$ are then imposed for the current iteration. In general the line search algorithm sets $\eta = 1$ (thereby having no effect) unless significant non-linearity is affecting the performance of the Newton-Raphson procedure. When there is such non-linearity, the line-search procedure helps avoid inaccurate linear extrapolation. The author made a minor modification to the line-search algorithm used in OXFEM_HYPERELASTIC, adjusting the the interpolation-extrapolation procedure that selects candidate values of η so

that more information from the previous candidate values is utilized.

5.4.2 Element selection

Axisymmetric finite-element models of incompressible and nearly-incompressible solids requires care in the selection of the element used (Sloan and Randolph, 1982). Using more elements in a given model generally allows for a more accurate solution as the discretized displacement field can more accurately reflect the undiscretized form. For low-order elements, however, the additional degrees of freedom provided by increasing the number of elements are overwhelmed by the additional constraints imposed by incompressibility, leading to an unreliable model. Fifteen-noded triangular elements (giving fourth-order displacements and third-order strains) are the lowest-order elements acceptable for an axisymmetric model of an incompressible substance when using full integration according to Sloan and Randolph (1982). These are adopted as the basic element used to describe the lens substance. A 13-point Gaussian quadrature rule with a degree of precision of 7 is used to perform the integration over these elements (Cowper, 1973).

Five-noded membrane elements are used to model the lens capsule as these match the order of the elements of the lens substance. A 5-point Gaussian quadrature rule with a degree of precision of 9 is used to perform the integration over these elements. The zonular fibres are modelled as 2-noded bar elements

6

The spinning lens test: Experiment

The new version of the spinning lens test developed by the author is based on the method reported by Fisher (1971), but incorporates the improvements discussed in section 4.3. During early testing it was assumed that the lens would quickly deteriorate after removal from its storage medium and especially after removal of the capsule. Hence, the procedures adopted emphasize rapid testing over other concerns.

6.1 Background

The development of a new lens spinning test was initiated at Oxford University by Dr Burd and Dr Judge, with the aim of addressing some of experimental and analytical limitations of the original lens spinning test of Fisher (1971). Several undergraduate projects contributed to the development of the test. Hirunyachote (2003) designed and commissioned the rotor, frame, and speed control. Spinning tests were conducted on porcine lenses using that version of the rig by Sorkin (2005). The contributions by the author to the experimental apparatus are redesigning the lens support and containment box, writing the program LENSCAM to allow the camera to be controlled from a laptop PC, and designing and programming the system which controls the flashgun.

In preparation for performing tests on human lenses approval was sought from the Berkshire Research Ethics Committee by Dr Burd and Dr Judge on the 15th of September 2006.

Following a meeting of the ethics committee on the 10th of October 2006 a favourable opinion was granted on the 21st of February 2007. A safety statement for the experimental procedures was prepared. The most recent version of this statement is included in appendix A.

6.2 The spinning rig

The spinning rig (figure 6.1) consists of a vertical rotor which can be spun at an adjustable speed, the lens support at the top of the rotor on which the test specimen sits and a box enclosing the support and specimen. The rig was inherited from previous project (Hirunyachote, 2003). The rotor and speed control have not been changed, while the lens support and box have been redesigned in the current work.

6.2.1 The rotor and speed control

The rotor shaft is aligned vertically, supported on two sets of bearings in a machined Dural metal frame. It is driven by a direct current electric motor (Maxon A-Max 22 mm diameter) connected at the base through a plastic sleeve to reduce vibration. Power is provided by a variable voltage supply (TTi EL301), allowing the rotational speed to be adjusted manually.

Two brass flywheels mounted on the rotor shaft provide the inertia needed to achieve a steady speed. The lower flywheel ('speed flywheel' in figure 4.1) is also used to measure the speed. It is painted alternately with 12 black and 12 white stripes and monitored by an optical reflection sensor fixed to the frame (Honeywell HOA0708; omitted from figure 6.1 for clarity). When the flywheel rotates, the sensor produces a corresponding periodic signal. This is fed into a digital counter which displays its frequency, allowing the voltage applied to the motor to be manually adjusted until the desired speed is achieved. The value on the display is 12 times the revolutions per second or one fifth of the revolutions per minute, so has a precision of 5 rpm. The process of adjusting the voltage to obtain the desired speed reading can sometimes take over a minute as the delayed response of both the rotor and the counter to their respective inputs makes fine adjustment slow. Higher speeds generally require more time for adjustment than lower speeds. Once a target speed has been achieved it is generally

stable; there is occasionally, however, a gradual drift in the speed reading of up to 20 rpm without further changes to the supplied voltage. When drift occurs after photographing has commenced the voltage setting is not altered to avoid the danger of manual over-correction.

The position of the rotor is monitored by two further optical sensors. The upper flywheel ('reset flywheel' in figure 6.1) is painted half black and half white, and monitored by a second reflection sensor (Honeywell HOA0708; omitted from figure 6.1). A thin disc with eight evenly spaced slots cut into its rim ('orientation disc' in figure 6.1) is attached to the rotor and monitored by a transmission sensor housed within the frame (Honeywell HOA2001). The signals from these two sensors are used in the timing system described in section 6.3.2.

6.2.2 The lens support and containment box

During a test the specimen sits atop the rotor, resting on an interchangeable support (figure 6.2) and enclosed in a Perspex box (figure 6.3). The lens support can be removed from the rotor shaft for cleaning or in case of damage. A socket milled into the rotor shaft accepts a pin projecting from the base of the support, which is then locked in place with two horizontal grub bolts. Adjusting the grub bolts so that the support is well aligned with the rotor axis is a time-consuming task, so the support is rarely removed from the rotor.

The standard support used for human lenses consists of a thin plastic ring glued to a castellated brass cylinder, both of 6.5 mm outer diameter (figure 6.2). The ring is fashioned from Delrin plastic rather than metal to lower the risk of damaging the lens while it is being positioned. The selected diameter allows a well positioned lens to spin at over 2000 rpm without being thrown off, while also allowing the equatorial region of the lens to deform freely while spinning. The four castellations of the brass segment allow a good view of the lower portion of the specimen at eight rotor orientations: four where there is a clear view through the central region and four where there are two smaller regions of clear viewing on each side. It is at these eight, evenly spaced 'window orientations' that photographs are taken. Additional orientations could be usefully photographed, especially if the support were blackened, but this has the cost of increasing the time to conduct the test, so only the eight most useful orientations have been used.

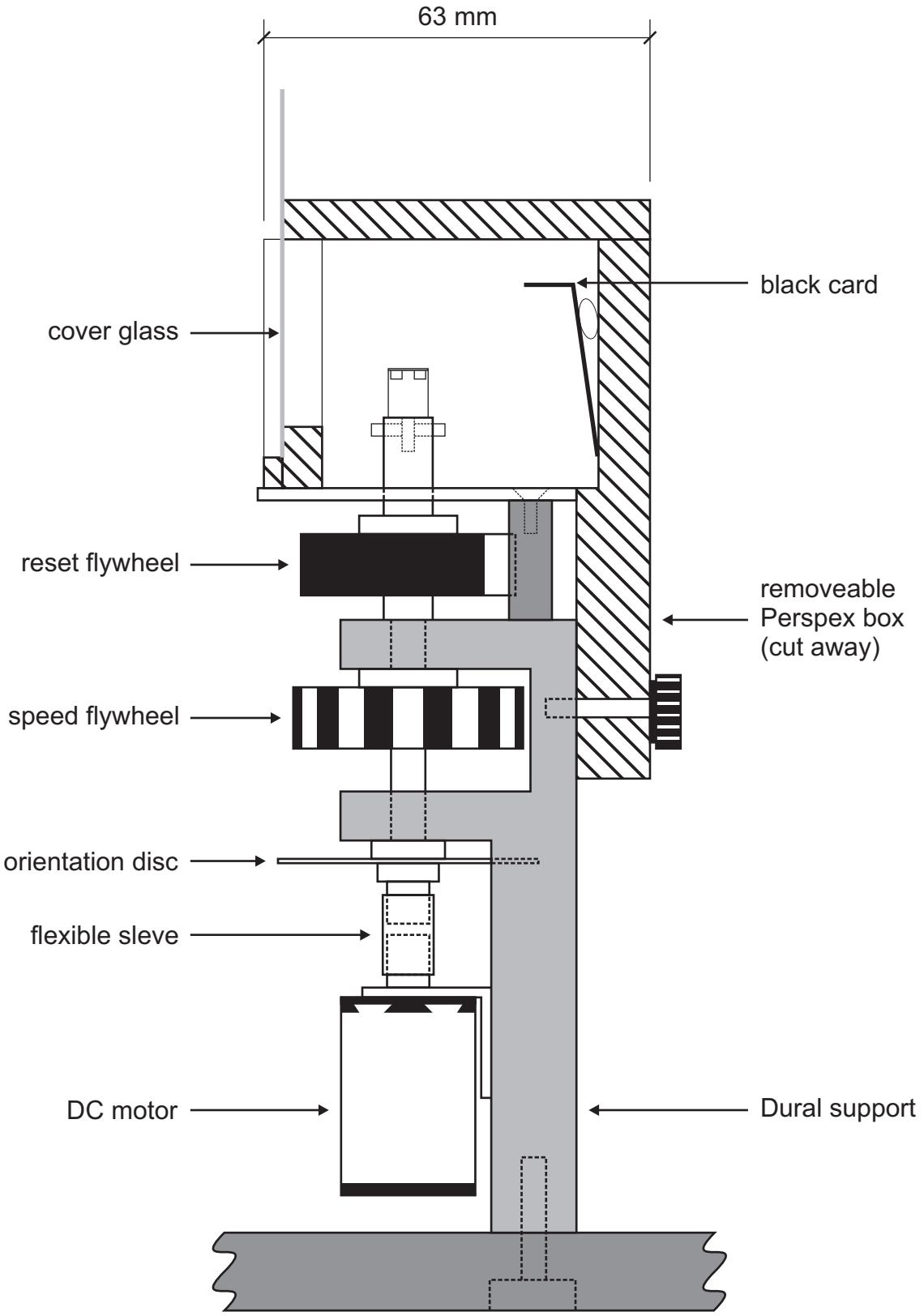

Figure 6.1 – *Side view of the spinning lens rig drawn to scale. Optical sensors omitted for clarity. (Adapted from Burd et al., 2011).*

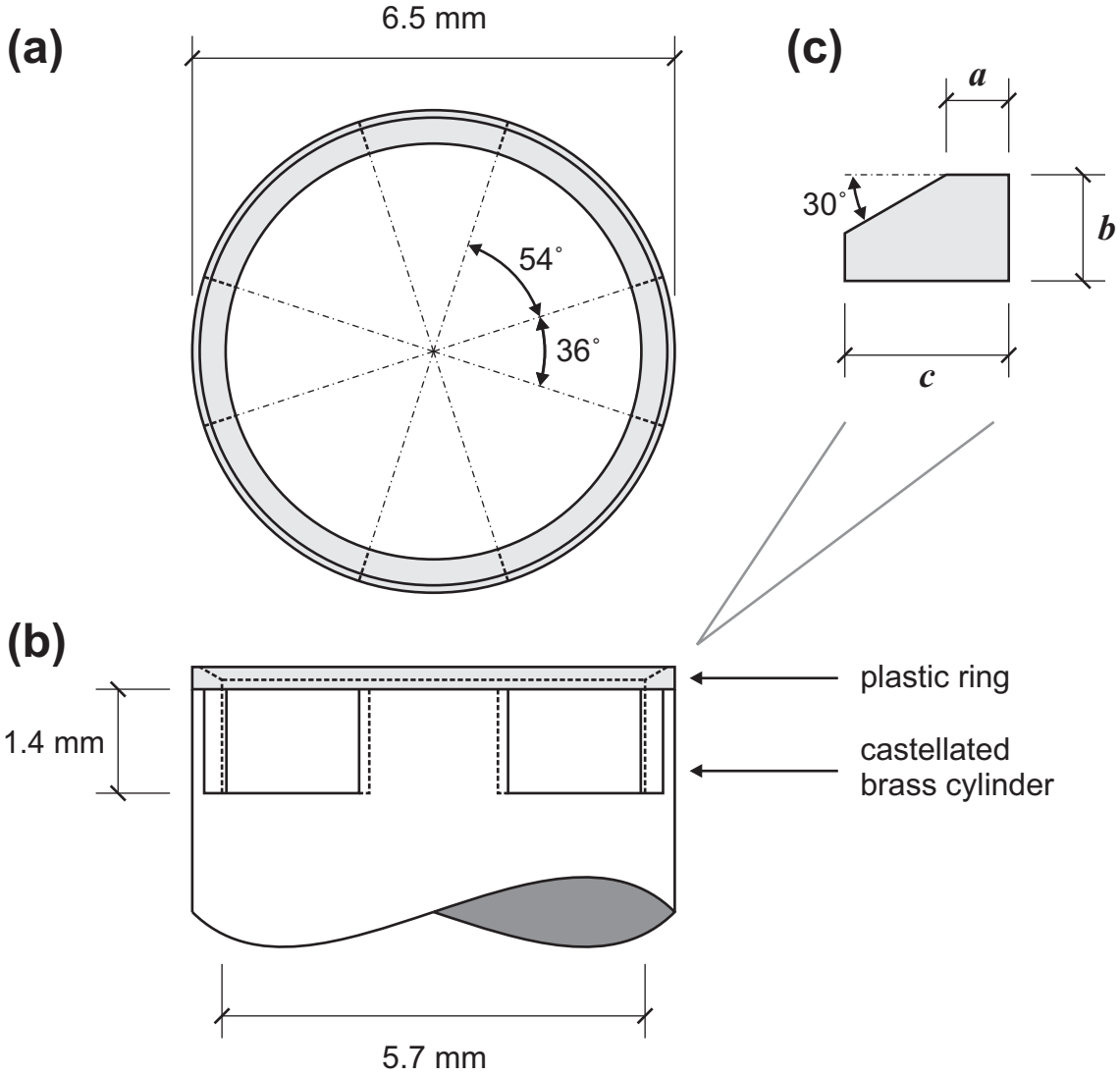

Figure 6.2 – *The lens support: (a) plan, (b) elevation, and (c) the support ring cross-section. (Adapted from Burd et al., 2011).*

Two other supports were used in some early tests on human lenses. A ring support similar to the standard support but of 8 mm outer diameter was used in the first day of tests but this proved to be too large for human lenses, prompting the commissioning of the 6.5 mm version. A dish-type support was trialled with two lenses. It consists of a brass cylinder of 8 mm diameter, with the top milled to a concave spherical surface having a radius of curvature of 10 mm. The dish support allows the lens to be repositioned with reduced risk of damage and decreases the deformation of the lens by the support. However, the contact between the lens and the support is hidden and the support provides less constraint on lens movement, making accurate positioning of the lens more difficult. This, together with the time required to reposition each support when used, meant no subsequent tests were conducted with the

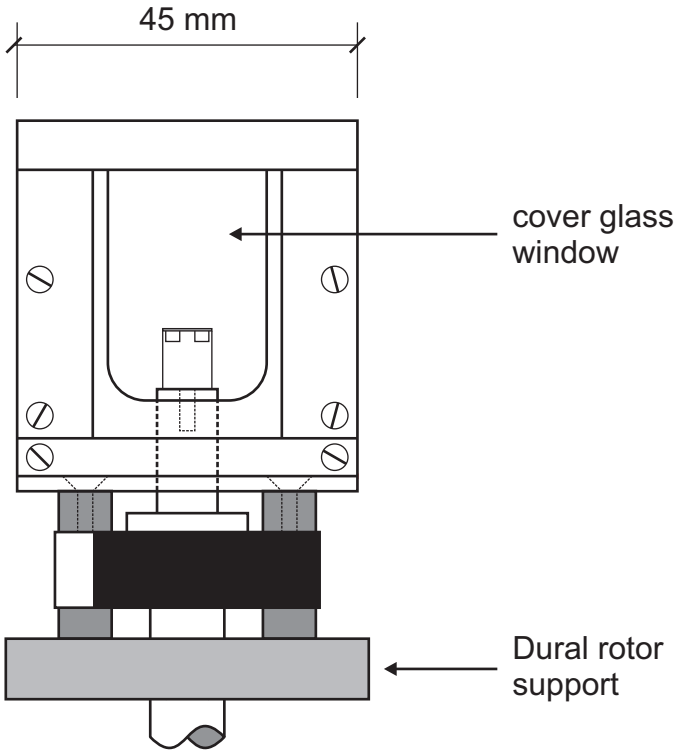

Figure 6.3 – *Front view of the containment box. (Adapted from Burd et al., 2011).*

ring support.

Once a specimen has been positioned on the support, the Perspex containment box is placed over it to prevent contamination of the laboratory by the lens should it scatter aerosols or come off the support during spinning. The containment box is also required so a humid environment can be maintained around the lens to limit any drying during the test procedure. The side of the box facing the camera has an open window. A microscopy cover glass (thickness #1: about 140μm) is slid into place over this window to provide a minimally distorted view of the specimen. The box has a removable clear lid to allow illumination of the lens from above. The inner sides of the box are lined with filter paper, kept moist during the testing to enhance the humidity within the box; the paper also improves the illumination of the specimen. The base of the box is covered in aluminium foil to reflect light onto the underside of the specimen. A piece of black card is mounted at the rear of the box to provide a dark background for the photographs. It is angled slightly downward with an overhanging flap at the top to reduce direct illumination from the flash. The width of the card is just enough to fill the frame of the photograph as a greater width diminishes the illumination of the periphery of the specimen. On the first day of tests on human lenses a larger box

was used, but this was cut down to the size indicated in figure 6.3 to allow the flashgun to be brought closer for enhanced illumination. The smaller box size is also advantageous for maintaining humidity.

6.3 Image acquisition

The data collected from the spinning lens test consist of digital photographs of the specimen, taken using a camera controlled by the program LENSCAM run on a connected laptop PC. A custom electronic timing system synchronizes the exposure of the photographs so they capture the specimen when the rotor is at the eight 'window orientations' (described in section 6.2.2 above) which provide the most useful views through the lens support. These aspects of the apparatus were developed by the author.

6.3.1 The camera

The photographs are acquired with a Nikon D70 digital single lens reflex camera fitted with a Nikon Micro-Nikkor 55 mm macro lens and three Nikon PK-13 extension rings. The camera is mounted on a two axis travelling microscope stand with additional fittings to adjust the third axis and tilt. For human lenses the macro lens is set to its most extended position, then the whole camera is moved using the travelling microscope stand to bring the sample into focus. This gives an image magnification of 1.95, and a resolution of 4 μm per pixel. Thicker specimens, such as porcine lenses, require a different camera lens position to photograph the whole lens.

The camera is controlled from a Windows XP laptop via a USB-1 connection. The custom program LENSCAM provides a graphical user interface to interact with the camera. It primarily allows the operator to initiate the capture of a batch of photographs, but also controls the downloading and naming of the resultant files and allows changes to the camera settings such as the digital ISO. Its image viewer can be used to check the downloaded photographs, but since photographs are usually only downloaded after a complete series of

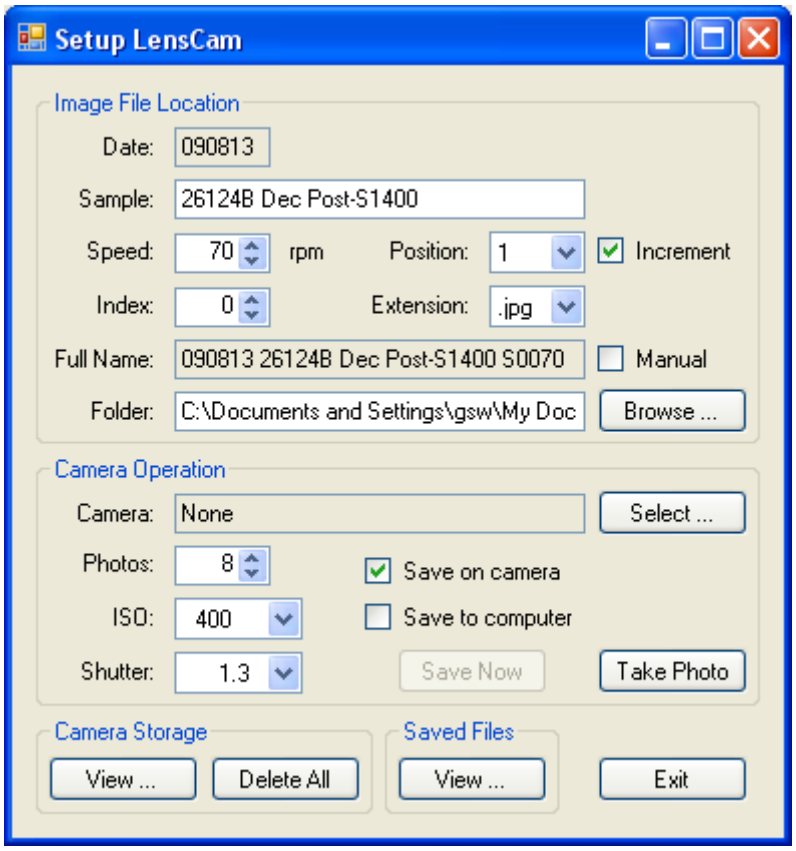

Figure 6.4 – *The principal* LENSCAM *dialog.*

tests on a lens, the thumbnails available via the camera storage dialog are more useful for checking for problems during the test.

The camera is generally used at aperture stop f/22 with a digital ISO of 400. It is set to a long exposure (typically 1.3 seconds) to ensure the specimen has time to reach the current target orientation, even when rotating at low speeds. The specimen is unilluminated for almost all of the exposure, with a flash triggered at a point in the exposure interval which depends on the flash controller (see section 6.3.2). To avoid extraneous light during the long exposure, the room lights are turned off during testing and a cardboard shroud is placed over the apparatus. The communication time with the laptop together with the exposure time dictate that successive photographs are taken at least 5 seconds apart. The photographs are recorded as 3008×2000 pixel, 24 bit colour, JPEG format images. The JPEG format is used in preference to the raw Nikon NEF format as it allows faster camera operation when connected to the computer, with no apparent loss of useful information.

6.3.2 The illumination and timing system

The illumination system controls the timing and duration of the actual exposure to light that forms the digital photograph, during the period when the camera shutter is open. The specimen is illuminated by a flashgun (Nikon Speedlight SB 800) positioned directly above the containment box of the spinning rig, aligned with a marked line to achieve good and consistent lighting. It is used at its lowest-intensity and hence shortest-duration setting which gives a flash of approximately 24 μs (Nikon). For a typical lens rotating at 1000 rpm, this is about 12 μm or 3 pixels of movement at the lens equator during the exposure.

The timing of the flash is controlled by an electronic system based around a programmable microcontroller chip (Microchip PIC16F876; referred to as the PIC below). The flash controller is housed in a metal box with three switches for manual input and seven light emitting diodes to display information, as illustrated in figure 6.5. A schematic of the timing system circuitry is included in Appendix B. The PIC is controlled by a short program written by the author. The assembly language of the PIC was used so that the program can rely on the instruction cycles of the PIC for precise timing of the flash. The program essentially operates so that when the flash controller receives the standard flash signal from the camera it delays passing this signal on to the flashgun until signals from the sensors on the spinning rig indicate the rotor is at the current target orientation. The timing system receives inputs from a binary-coded decimal dial, the camera, the flashgun, and the sensors monitoring the orientation disc and the reset flywheel. It provides outputs to the flashgun (the principal output) and the camera. Seven light-emitting diodes (the display LEDs) provide information on the state of the flash controller.

The binary-coded decimal (BCD) switch (see figure 6.5 and appendix figure B.1) allows the selection of different modes of operation for the timing system. When set to a position from 0 to 7 the timing system is in ‘fixed mode’ in which the current target orientation of the rotor is the same as the dial position. When the dial is in position 8 the timing system is in ‘increment mode’ in which the current target is initially set to orientation 0, but is incremented each time the flashgun is triggered, with orientation 0 following 7. This is the setting used for testing lenses on the rig to provide one photograph at each of the window

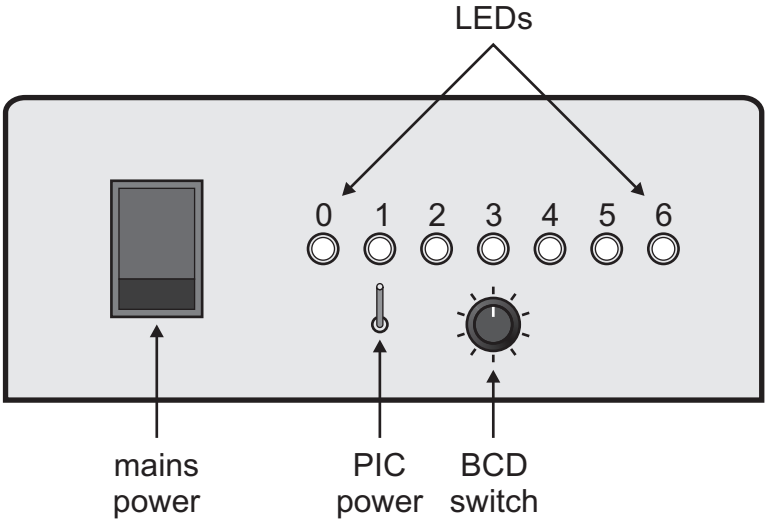

Figure 6.5 – *The front panel of the flash controller box.*

orientations. When the dial is in position 9 the timing system is in 'immediate mode' in which the flashgun is triggered with minimal delay after receiving the flash signal from the camera. Thus the rotor orientation is ignored in this mode.

The camera communicates with the timing system via the standard flash interface. A camera-to-flashgun cable (Nikon SC-29) was cut in half and the exposed ends fitted with three pin plugs to connect with the timing system box. The camera signals for the flashgun to fire by activating a thyristor (or equivalent) between the fire and ground terminals of the first section of cable. This signal is diverted to the PIC and primes it to trigger the flashgun once the rotor is in the correct position. To trigger the flashgun it activates its own thyristor (Philips 2N5064, see figure B.1) between the fire and ground pins of the second segment of cable. The third pin of the cable relays the 'ready' signal from the flashgun to the camera, though the Nikon D70 camera appears to operate the same regardless of this signal.

In order to correctly time the firing of the flashgun, the PIC keeps track of the position of the rotor by counting the rising-edge signals from the orientation sensor monitoring the orientation disc (figure 6.6). This signal occurs each time one of the eight slots cut into the orientation disc passes between the emitter and receiver of the sensor. To ensure that these signals coincide with the window orientations of the lens support it is necessary to rotate the orientation disc to the correct position every time the lens support is removed and replaced on the rotor. The count maintained by the PIC is reset to zero every time a rising-edge signal is

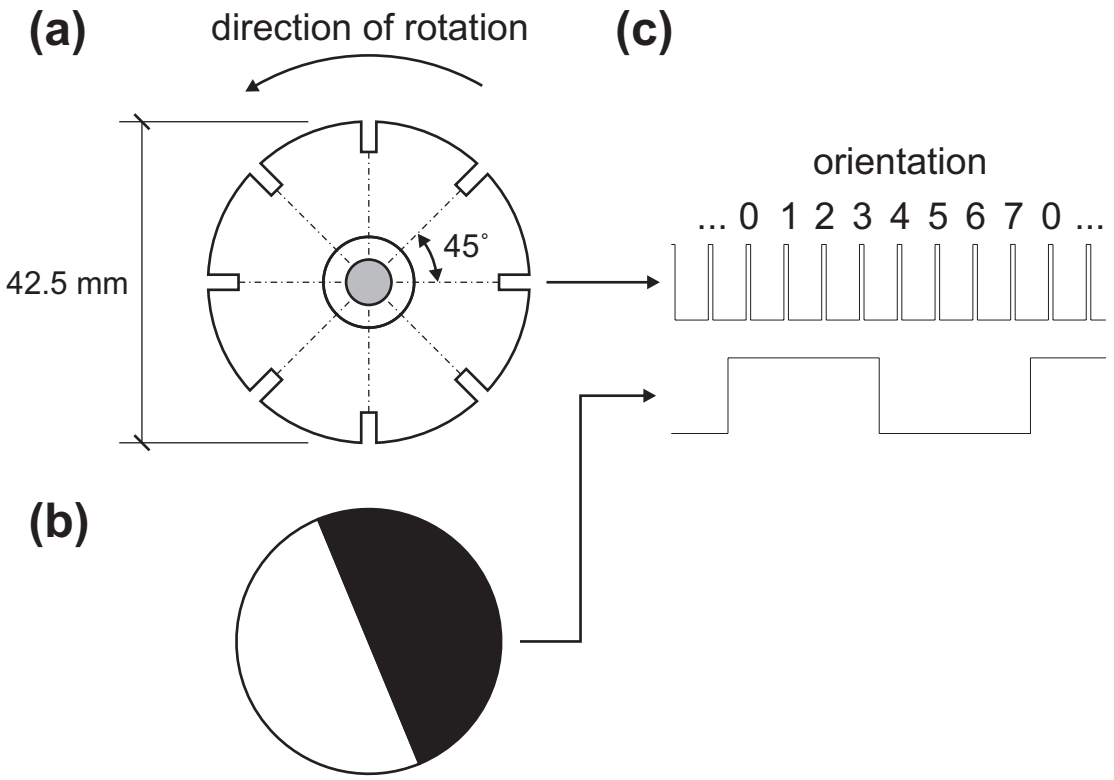

Figure 6.6 – *The synchronization mechanism: (a) the orientation disc, (b) the reset flywheel, and (c) the resultant signals and corresponding orientations.*

received from the sensor monitoring the reset flywheel to ensure that spurious signals cannot cause a persistent error in the calculated position.

There is a delay of approximate duration $\delta T_F = 70\,\mu$s between triggering the flashgun and the actual exposure, as judged from photographs of the support rotating at a range of speeds. If the PIC were to simply trigger the flashgun when it received the signal from the orientation disc the delay would cause a small but noticeable difference in the orientation of the support in photographs taken at different rotational speeds. To avoid this difference in orientations the PIC calculates the correct time to trigger the flashgun, making use of the timing of the previous two orientation signals. To correctly trigger the flashgun for orientation N, the PIC times (in instruction cycles of $1\,\mu$s) the interval $\delta T_S = T_{N-1} - T_{N-2}$ between the arrival of orientation signal $N-2$ at time T_{N-2} and orientation signal $N-1$ at time T_{N-1}. The PIC then triggers the flashgun at time $T_{N-1} + \delta T_S - \delta T_F$ so that the illumination provided by the flashgun occurs with the arrival of orientation signal N regardless of the speed of rotation.

At low speeds the rotor moves with sufficient variability in speed that this approach becomes unreliable, so below 115 rpm the PIC simply triggers the flashgun when the target

Table 6.1 – *Meaning of the timing system LEDs.*

		binary-coded decimal position		
		0 – 7	8	**9**
		fixed mode	increment mode	immediate mode
LED	0	target orientation, bit 0		flashgun ready signal
	1	target orientation, bit 1		reset flywheel signal
	2	target orientation, bit 2		orientation disc signal
	3	off	on	off
	4	off	off	on
	5	always off		
	6	always on once the PIC has initialized		

orientation signal is received. The particular threshold speed of 115 rpm is selected because it corresponds to the point at which the PIC register used to record δT_S overflows before the arrival of orientation signal $N-1$, providing a simple speed test within the PIC program. At such slow rotation speeds the rotor moves a negligible amount during the flashgun delay, δT_F; there is still, however, a residual discrepancy of 0.004 rad on average between the orientation of the support in photographs taken using this mode compared to those taken at higher rotor speeds using the delay adjustment mode. This is enough to be noticed, but has very little effect on the shape of the lens outline captured in the photographs. The remaining discrepancy is probably due to small differences in the angles between the orientation disc slots, with the result that at speeds above 115 rpm the predicted arrival of the signal from a given slot corresponds to a consistent rotor orientation but does not agree exactly with the actual arrival of the signal.

Information on the current state of the timing system is provided by the row of the seven display LEDs. The meaning of some of the LEDs depends on the position of the dial, as summarized in table 6.1. When the dial is fixed mode or increment mode (positions 0 to 8) the three leftmost LEDs indicate the rotor orientation at which the flash will next be fired (in binary, with the least significant bit to the left). When the dial is in position 9 these LEDs instead display the state of the microcontroller inputs to allow diagnosis of problems; the leftmost displays the ready signal from the flashgun, the second displays the signal from the rotation optical sensor, and the third displays the signal from the position optical sensor.

The fourth LED from the left is on when the flash controller is in increment mode, the fifth is on when the flash controller is in direct mode, the sixth is unused and never on, and the seventh is always on once the microcontroller has successfully initialized. This information is summarized in table 6.1.

6.4 Experimental procedures

The basic unit of the spinning test is a sequence of eight photographs taken of a specimen while the rotor is spinning at a given speed (the principal value being 1000 rpm). One photograph is taken when the rotor is at each of the eight orientations dictated by the flash controller set to increment mode. The process of adjusting the speed to the correct value and taking eight photographs generally takes about two minutes.

For comparison with the photographs at the test speed, eight reference photographs of the specimen are taken at low speed (always at 70 rpm). Ideally the specimen would be completely stationary for the reference photographs; this would, however, require a different method to orient the rotor. In practice the difference between a stationary state and spinning at 70 rpm is negligible, smaller than the uncertainty in force at test speeds due to the 5 rpm precision of the speed reading (see section 7.3.2).

The lens is tested first with the capsule intact, then the capsule is removed and the lens is retested. The sequence of speeds used varies between lenses. The time taken is an issue of importance in the choice of test regime. It has not been established if the quality of the lenses changes systematically over time

6.4.1 Initial state and preparation of lenses

The human lenses subjected to the spinning test are received from the Bristol Eye Bank where the iris, ciliary body, zonular fibres, and lens are removed as a unit from the eye globe. They are transported in Sigma Megacell Minimum Essential Medium Eagle (M4067) with Sigma Antibiotic-Antimycotic Stabilized (A5955) at ambient temperature. In the testing laboratory the lenses are kept in the same medium and at room temperature (generally 21-22˚C). The

lenses are usually tested in the order in which they have been labelled by the Bristol Eye Bank.

When a lens is selected for testing it is tipped into a Petri dish, along with its medium. Any extraneous tissues are removed. An ophthalmic spear is brushed against the lens equator to catch hold of remaining zonular fibres. Any zonular fibres which adhere to the spear are stretched away from the lens by lifting and slightly rotating the spear and then cut close to the lens with surgical scissors, care being taken to avoid any damage to the lens capsule. This process is repeated until no more zonular fibres are caught by the spear around the whole lens equator.

6.4.2 The test on the intact lens

Once the lens has been isolated it is transferred to the lens support using ophthalmic spears. The lens is positioned with the anterior side up; the correct orientation can readily be judged as the anterior-equator distance is smaller than the posterior-equator distance. Fluid remaining on the lens is absorbed with a dry ophthalmic spear. The position of the lens is adjusted until it appears well centred when the support is manually rotated. Once suitably positioned, the Perspex box is placed over the lens, the flashgun moved into place above it, the room lights are turned off and testing is begun. In some cases fluid remains on the lens, interfering with the subsequent test. This is generally only apparent once the resulting photographs are analysed, but when fluid is noticed during the test, it is halted and the lens is dried before recommencing (see section 8.1.1 for further discussion of fluid on the lens).

The test starts with a set of reference photographs of the undeformed lens, then sets of photographs are taken at a sequence of increasing test speeds, with another set of reference photographs taken after each speed. The number of speeds applied has varied over the programme of tests. All lenses are subjected to tests at 700 and 1000 rpm (sequence A1 in table 6.2). The latter speed is used to conform with the tests conducted by Fisher (1971). The former speed induces apparent body forces of about half the magnitude of the latter; it was originally included to increase the chance of usable results when the reliability of the test was unknown and has been retained to apply a consistent preconditioning to the lenses.

Table 6.2 – *Sequences of speeds applied to intact lenses.*

sequence	**speeds (rpm)**										
A1	70	700	70	1000	70						
A2	70	700	70	1000	70	1400	70				
A3	70	700	70	1000	70	1400	70	1680	70		
A4	70	700	70	1000	70	1400	70	1730	70		
A5	70	700	70	1000	70	1400	70	1730	70	2000	70
photo set	A_{R1}	A_{T1}	A_{R2}	A_{T2}	A_{R3}	A_{T3}	A_{R4}	A_{T4}	A_{R5}	A_{T5}	A_{R6}

The majority of lenses have also been tested at 1400 rpm to ensure that older, stiffer lenses experience sufficient deformation for analysis (sequence A2 in table 6.2). Two lenses were also tested at 1680 rpm for comparison with tests at this speed conducted at Laser Zentrum Hannover (sequence A3). Finally, for a number of lens pairs one of the pair are also subjected to speeds up to 2000 rpm to induce more substantial strains in the capsule, to enable better analysis of the response of this component (sequence A4 and A5).

The resulting sets of photographs are referred to in the text by the label given in the last line of table 6.2, with 'R' standing for 'reference' and 'T' standing for 'test'. Following the spinning test, some of the lenses were repositioned on the support with the posterior pole uppermost and reference photographs taken. This provides additional information of the lens geometry, in particular regarding the deformation caused by the support.

6.4.3 The test on the decapsulated lens

Following the tests on the intact lens, it is placed back in the Petri dish and taken to a dissecting microscope, under which the capsule is carefully removed with two pairs of forceps. One pair of forceps is used to pull up a 'tent' of capsule on the anterior surface but away from the pole, then both pairs are used to tear the capsule and remove it from the lens. Occasionally some of the lens cortex comes away with the capsule, usually a thin strip running roughly from pole to pole, widening at the equator. The test is performed as usual in such cases as the damage is only superficial. However, the tests from such damaged lenses are not used for subsequent analysis in the current work (see section 8.1.1 for further discussion of damage

Table 6.3 – *The main sequences of speeds applied to decapsulated lenses.*

sequence	**speeds (rpm)**								
B1	70	700	70	1000	70				
B2	70	700	70	1000	70	1400	70		
B3	70	700	70	1000	70	1400	70	1680	70
photo set	B_{R1}	B_{T1}	B_{R2}	B_{T2}	B_{R3}	B_{T3}	B_{R4}	B_{T4}	B_{R5}

to the lens).

Once the capsule is removed, the lens is replaced on the support and positioned in essentially the same way as the intact lens, though generally with fewer manipulations since without the capsule the lens is much more fragile. In the absence of the capsule the lens tends to deform more in the vicinity of the support during the test. The deformation appears greater where the castellations of the support meet the support ring apparently due to a surface tension effect. This causes a slight disruption to the axisymmetry of the lens.

The same initial sequence of speeds is applied to the decapsulated lens as was applied when intact. A lens subjected to sequence A1, A2, or A3 when intact is subjected to the equivalent sequence when decapsulated (B1, B2, or B3 in table 6.3), while a lens subjected to A4 or A5 when intact is subjected to B2 when decapsulated. When these tests are complete, most lenses are subjected to some additional tests to examine time dependent behaviour, listed in table 6.4. First, three sets of photographs are taken while the lens is being spun to measure progressive deformation due to the sustained forces; these are followed by three sets of reference photographs to measure progressive recovery. Final sets of test and reference photographs are taken to assess the change in the response of the lens over the course of the experiment, with the possibility of the surface of the lens drying out being a particular concern. The timing of these photographs is not chosen precisely due to the manual nature of the speed control and photograph initiation; however, the time each photograph is taken is recorded in the resultant file. All these tests are conducted at the highest speed to which each lens has been subjected while decapsulated. If it was tested with sequence B1 then the additional tests are made at 1000 rpm (sequence C1 in table 6.4), while if subjected to sequence B2 the additional tests are made at 1400 rpm (sequence C2). Lenses tested with the

sequence	**speeds (rpm)**							
C1	1000	1000	1000	70	70	70	1000	70
C2	1400	1400	1400	70	70	70	1400	70
photo set	C_{T1}	C_{T2}	C_{T3}	C_{R1}	C_{R2}	C_{R3}	C_{T4}	C_{R4}

Table 6.4 – *Sequences of additional speeds applied to decapsulated lenses.*

longer sequence B3 are not subjected to these additional tests.

Just as for the intact lenses, some of the decapsulated lenses were repositioned with the posterior pole uppermost and a set of reference photographs were taken of this orientation. The primary test used in the subsequent calculation of lens stiffness is the first test at 1000 rpm on the decapsulated lens (B_{T2} in table 6.3).

6.4.4 The test on the isolated nucleus

A further test was performed on the nuclei of 27 lenses following the decapsulated test. To isolate a central portion of the lens, it is submerged in water (rather than physiological medium) and occasionally gently agitated with an ophthalmic spear. This causes the outer layers lens fibre cells to gradually swell up and slough off over a period of about an hour (the precise timing was dictated by the duration of the tests conducted on the whole lenses). Once the remaining lens has a diameter of about 6–7 mm it generally displays greater resistance to the swelling and sloughing process. This resilient portion is assumed to correspond to the lens nucleus. When an increased resilience is observed any remaining partially attached material is gently brushed away with an ophthalmic spear and the nucleus is returned to the lens support for further testing. Since the diameter is considerably smaller than a full lens and the position of the ring support is more restrictive, higher spinning speeds are applied to provide clear deformation. Initial tests on the nucleus used test speeds of 1000, 2000, and 3000 rpm (sequence D1 in table 6.5). The 1000 rpm test was discontinued to reduce the time required to conduct the test, producing sequence D2. The higher speeds of rotation and greater difficulty in placing the nucleus symmetrically on the support mean it is prone to come off during the test. This occurred for a number of lenses when spun at 3000 rpm,

Table 6.5 – *Sequences of speeds applied to nuclei.*

sequence	**speeds (rpm)**						
D1	70	1000	70	2000	70	3000	70
D2	70	2000	70	3000	70		
D3	70	2000	70				
D4	70	2000	70	2450	70	3000	70
photo set	D_{R1}	D_{T1}	D_{R2}	D_{T2}	D_{R3}	D_{T3}	D_{R4}

resulting in the accidentally truncated sequence D3. An intermediate speed of 2450 rpm was introduced in sequence D4 to increase the chance that stiffer nuclei would be sufficiently deformed for analysis. (A speed of 2450 rpm induces forces of about 1.5 times those induced at 2000 rpm).

It must be noted that the lengthy exposure of the nucleus to non-isotonic water casts some doubt on the relevance to the undisturbed nucleus. Also, if the isolated portion of the lens is returned to water following testing further swelling and sloughing does occur over time, so its geometry cannot be considered to mark some exact boundary.

6.4.5 Calibration photographs

In order to determine the scale of the photographs taken of the lenses, sets of calibration photographs are taken before, and usually after, each day of testing. A steel ball bearing is used as the subject of these photographs. Its diameter, as measured by a micrometer, is 7.93 mm, approximately the same as the equator of the lens, but considerably thicker from pole to pole. The same procedure is used for photographing the ball bearing as for the reference photographs of a lens, including the speed of 70 rpm.

The ball bearing photographs are also used to determine the position of the lens support and in particular the top of the support ring which is often obscured when photographing a lens. However, the presence of the ball bearing reduces the illumination of the support, so additional photographs of the empty stand are taken in case they are needed.

7

The spinning lens test: Analysis

The analysis of the spinning lens test requires some quantification of the deformation of the lens as captured in the photographs, and a method of inferring material properties from that deformation. In the approach adopted here the reference photographs are processed to obtain an initial geometry used to simulate each lens test. A target outline for the lens is obtained in a similar manner from the photographs taken during the high-speed test under examination. A simulation of the individual test is produced using the finite element method and an iterative optimization process is used to find the material parameters with which the simulated spinning lens best reproduces the target outline.

7.1 Background

The analysis applied in the original spinning lens test of Fisher (1971) took two measurements from each lens photograph (the anterior axial thickness and the equatorial diameter), and used an approximate analytical model of the test to determine the stiffness of the cortex and nucleus of the lens. The prospect of improving the analysis, primarily by making use of the huge increase in available computing power, was envisioned by Dr Burd and Dr Judge prior to the start of this study. Both the analysis of the lens photographs and the model of the test used to infer lens stiffness values have been markedly improved in the current project.

The author has written the MATLAB based image processing tools used to obtain data

from the photographs, principally the initial lens geometry and the target outline used in the simulation of the test. These tools include gradient-based edge and curve detection (sections 7.2.2 to 7.2.4) to locate features of a photograph, image correlation to detect camera movement between pairs of photographs (section 7.2.6), and an implementation of basis splines along with the process for fitting them to the lens outline (section 7.2.7). The meshing tool `Mesh2d` (Engwirda, 2007), obtained from an online MATLAB code repository, is used to generate triangular meshes. Additional procedures to translate the resulting mesh into the correct form for simulation are the work of the author.

The hyperelastic finite-element program used to perform the simulation of the tests is OXFEM_HYPERELASTIC, written by Dr Burd with this and other ophthalmic modelling in mind. The author uses this as the basis for OXFEM_SEARCHER, which relies on the same source code to perform forward finite-element calculations, but incorporates a number of iterative procedures used in the analysis of the spinning lens test. The most significant of these is the optimization process used to determine material parameters which best match the experimental results (section 7.6), but also include the search for an unstressed geometry used in trials involving the application of gravity (section 7.3.3) and the search for consistent constraints at the interface between the lens and the support ring when sliding is permitted (section 7.4.2). The author made some additions to the core OXFEM_HYPERELASTIC program, such as new material models used to apply heterogeneous stiffness distributions in the lens substance and the alternative solution scheme '`newton2`' for use with OXFEM_SEARCHER (see section 5.4.1).

7.2 Image processing

The photographs obtained in the test are processed using a number of custom MATLAB functions. Three general procedures are employed: detection of horizontal and vertical edges such as the side of the support, detection of curves such as the outline of the lens, and correlation between regions in two photographs to account for camera movement. The principal result from analysing each photograph is a set of finely spaced points lying on the outline

of the lens, with gaps where the lens is obscured by the support. These points are collected and used to generate cubic splines which describe a smoothed and averaged outline, which are in turn used to generate a finite-element mesh and the target outline used to estimate the material parameters implied by the test.

7.2.1 Summary of the image processing procedure

Two sets of reference photographs and one set of spinning photographs are used to analyse a single test, for example the analysis of test B_{T2} of table 6.3 makes use of the photographs from B_{R2}, B_{T2}, and B_{R3}. Those outline points obtained from the reference photographs (B_{R2} and B_{R3} continuing the example) are combined and used to generate the reference geometry of the lens, while those obtained from the photographs of the actual spinning test (B_{T2}) determine the target outline used in the optimization process. A set of calibration photographs from the same day as the test in question are also used, primarily to determine the length scale of the photographs.

The steps in the processing of the photographs from test B_{T2} are summarized below. For a different test, the number subscripts are adjusted accordingly. The general procedure used for each step is given in square brackets. These procedures are explained in detail in subsequent subsections. The set of reference photographs taken after the test (from B_{R3}) are the primary reference set, used to find the support position as well as points on the lens outline; the set taken before the test (from B_{R2}) are the secondary reference set, used only to find points on the lens outline.

Calibration (performed once for each day of tests)

- For each photograph in the calibration set
    - find the top and sides of the support base [edge detection]
    - find the top and sides of the support ring [edge detection]
    - find the ball bearing sides [curve detection]
- Calculate the axis of rotation, the photograph scale, the ring radius, and the offset of the support ring above the support base

Support locations of the primary reference set

- For each photograph from B_{R3} find the top and sides of the support base [edge detection]
- Calculate the positions of the axis of rotation and the support ring (using the calibration data for the latter)

Lens outlines of the primary reference set

- For each photograph from B_{R3} find points on the lens outline above the support ring [curve detection]
    - find the sides of the castellation window or windows [edge detection]
    - find points on the lens outline below the support ring [curve detection]

Lens outlines of the secondary reference set

- For each photograph from B_{R2}
    - find the offset from the corresponding photograph of B_{R3} [image correlation]
    - find points on the lens outline above the support ring [curve detection]
    - find the sides of the castellation window or windows [edge detection]
    - find points on the lens outline below the support ring [curve detection]

Lens outlines of the test set

- For each photograph from B_{T2}
  - find offset from the corresponding photograph of B_{R3} [image correlation]
  - find points on the lens outline above the support ring [curve detection]
  - find the sides of the castellation window or windows [edge detection]
  - find points on the lens outline below the support ring [curve detection]

Spline and mesh generation

- Generate the top reference spline approximating all the outline points above the ring support from B_{R2} and B_{R3}
- Generate the bottom reference spline approximating all the outline points below the ring support from B_{R2} and B_{R3}
- Generate the top target spline approximating all the outline points above the ring support from B_{T2}
- Generate the bottom target spline approximating all the outline points below the ring support from B_{T2}
- Construct a triangular finite-element mesh from the top and bottom reference splines

7.2.2 Gradient based edge and curve detection

The features of interest in the photographs are transitions from the illuminated lens or support to the dark background. Ideally the background would be uniformly black and the lens and support distinctly brighter, but in reality some parts of a lens (especially a decapsulated lens) do not reflect much light towards the camera; meanwhile, some background areas can be bright due to scattered light, especially near well lit parts of the lens and when the cover slip window is not perfectly clean. In light of these circumstances, the transitions from the lens or support to the background are detected by first calculating an approximation to the

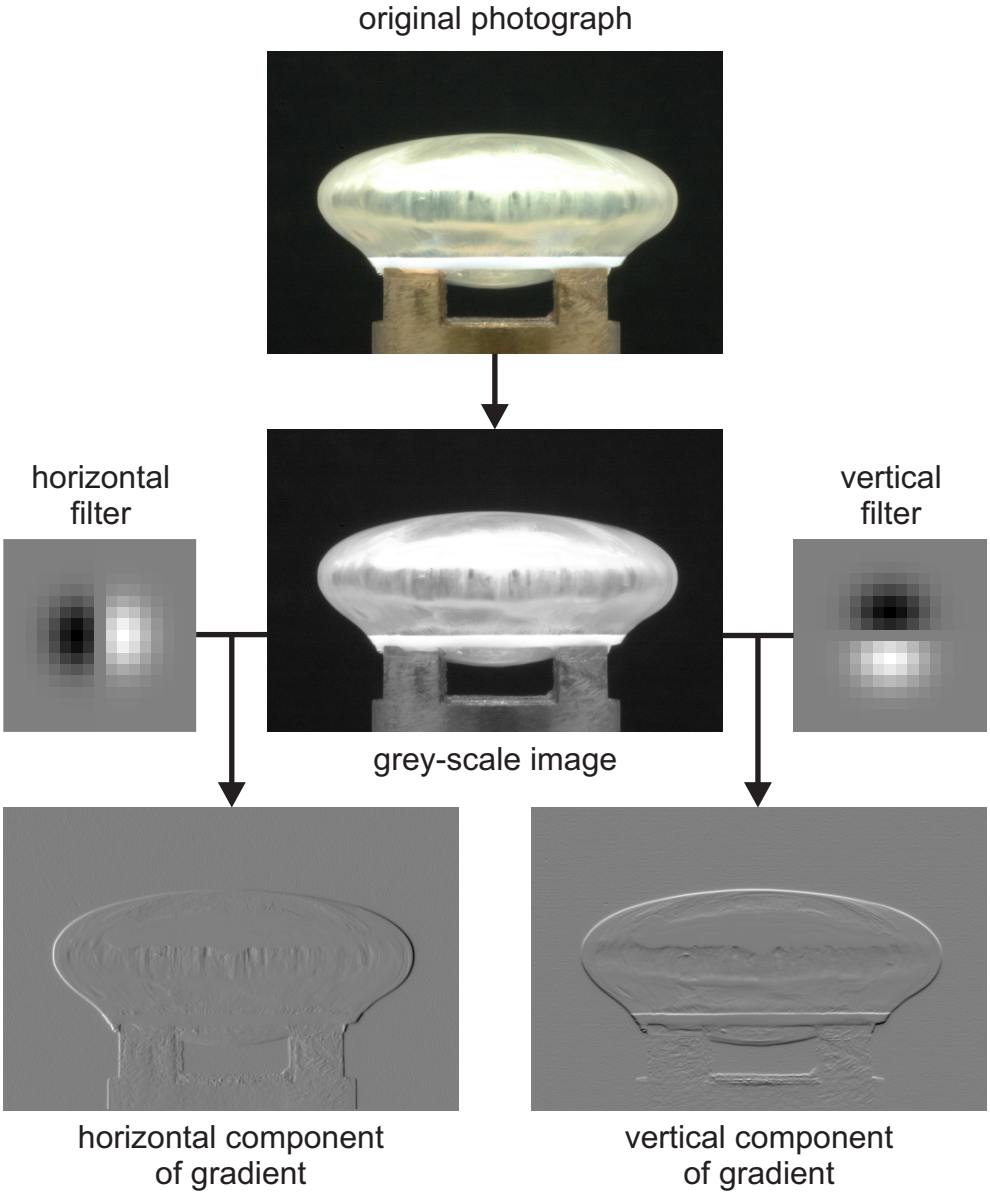

Figure 7.1 – *The process used to calculate the components of the gradient for each photograph. The filters illustrated are the effective filters obtained by combining the derivative-of-Gaussian and Gaussian components; for a standard deviation of two pixels they are 17 by 17 pixels.*

gradient of the pixel intensity, then finding the location where the component of the gradient orthogonal to the edge or curve reaches a peak. This approach is preferable to a simple intensity threshold or a gradient threshold as it is more tolerant of variations in illumination over the photograph and less prone to changes in illumination between photographs causing apparent movement of stationary edges.

To calculate the gradient, the photograph is first converted from colour to grey-scale. An approximation to each Cartesian component of the gradient of the grey-scale image is

calculated by convolving it with a derivative-of-Gaussian filter in the direction of the component and a Gaussian filter in the orthogonal direction, using the built-in MATLAB function `conv2`. This filtering is close to ideal for the detection of step edges (Canny, 1986). A standard deviation of two pixel lengths is used for both filters, though this is increased to up to three pixel lengths if the image quality is poor (a blurred edge is more easily detected with a larger standard deviation, but this makes the edge location less precise).

There are small-amplitude peaks throughout the dark background as it is not uniform, while internal details produce more prominent peaks within the lens and support regions. The actual peaks of interest lie between the two and will exceed all of the background peaks, but not necessarily all the internal peaks. The manner in which the peak of interest is identified depends somewhat on whether it is part of a straight edge or a curve, as discussed below.

7.2.3 Edge detection

Analysis of the lens requires locating a number of nearly vertical and horizontal edges of the lens support, as outlined in section 7.2.1. These edges are all found in the same general way, so the method of finding the left edge of the support will be used as an example. In this case it is known roughly where in the photograph the edge will fall and it is expected that the horizontal component of the gradient will achieve a high value for a column of pixels lying along the edge. The search is limited to a horizontal domain that spans the possible locations of the edge. At each pixel position along that domain, the edge intensity is calculated as the median value of the horizontal component of the gradient over a vertical band (100 pixels near the bottom of the image in this case). The edge in question is taken to be the left-most peak in the edge intensity which exceeds a proportion (0.3 in this case) of the maximum peak in the domain. Using the median value reduces the influence of small but intense anomalies in comparison to a true edge, taking the left-most peak ensures that peaks within the support region will not be considered, and the restriction to 0.3 of the maximum edge intensity excludes the small-amplitude peaks present in the background.

For the calibration photographs it is necessary to find the radius of the support ring and its height above the support base so that these values can be used in determining lens outline.

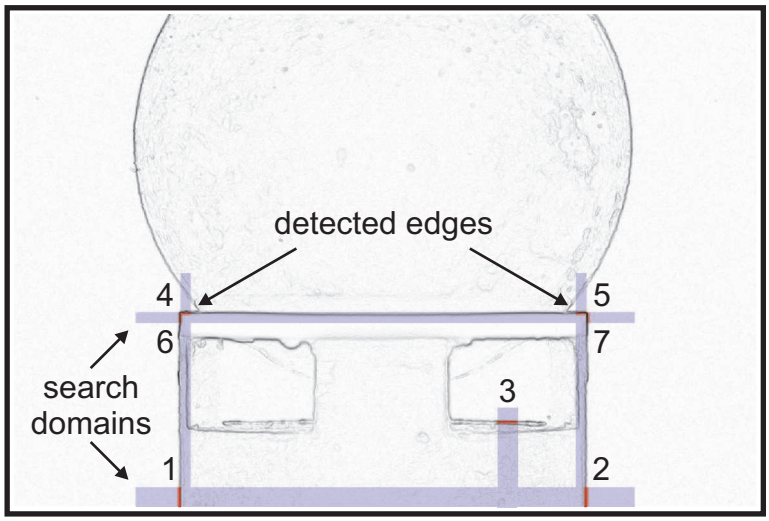

Figure 7.2 – *Detection of edges of the support base. The search domains (blue) and detected edges (red) are displayed with the corresponding gradient magnitude image of a calibration photograph (zero gradient shown as white and the maximum gradient shown as black). The edges are detected in the order indicated by the numbers.*

The process is illustrated in figure 7.2). First, edge detection is used to find the left and right sides of the support base (1 and 2 in figure 7.2) in each of the eight photographs, and the axis of rotation is taken to be the mean of all sixteen values. The top of the support base is sought along the line midway between the left and right sides if the orientation of the castellations provide a single central window, or 500 pixels to the right if they provide two windows (3 in figure 7.2). The top of the support ring is sought at its left and right extremes using the position of the support base as a guide (4 and 5 in figure 7.2), and the left and right sides of the support ring are sought just below these heights (6 and 7). The former values are used to calculate the mean height of the support ring above the support base which is needed for the simulation of the test. The latter values were originally used calculate the mean radius of the support ring, but the current method assumes a fixed radius for all tests using a given support.

For the primary reference photographs, the axis of rotation and the top of the support base are found in the same manner as for the calibration. The mean height of the support ring above the support base in the calibration photographs is used to determine the position of the support ring in the primary reference photographs, as the top is generally obscured by the lens in the reference photographs.

7.2.4 Curve detection

A curve detection algorithm developed by the author is used to find the outline of the lens and the calibration ball bearing in respective photographs. An example of the process for the lens is depicted in figure 7.3.

To find the outline of the lens, an origin is selected on the axis of rotation at the height of the top of the support ring. The outside of the lens is sought along rays emanating from the origin at finely spaced angles ($\frac{\pi}{1000}$ radians apart). This approach is adopted as the lens outline will subsequently be described by a cubic spline defined over polar coordinates.

The position of the outside of the lens along any particular ray is taken to be the last substantial peak in the component of the gradient orthogonal to the outline. The orthogonal direction is determined by extrapolating the outline from previously found outline points when there are enough of these, or by assumption when there are not. A peak counts as substantial when it exceeds a proportion (generally 0.4) of the maximum peak over the domain examined. The gradient values along the ray are calculated at points 0.1 of a pixel length apart using bicubic interpolation from the surrounding square of 16 pixels. The domain examined is restricted to the portion of the ray within 60 pixel lengths of the extrapolated outline, partly to make the process faster, but also to avoid some of the irrelevant internal edges.

The outline of the lens is found separately in four sections: the part above the support ring to the left of the axis (section 1 in figure 7.3 a), the part above the support ring to the right of the axis (section 2), the part below the support ring to the left of the axis (section 3), and the part below the support ring to the right of the axis (section 4). The first point found in section 1 lies on the axis of rotation, with subsequent points sought in an anti-clockwise direction. For the first 15 points the horizontal component of the gradient is used to find the outline, after which extrapolation is used to determine the direction, using up to 30 prior points. Additional outline points are found for section 1 until the next point would be within 20 pixels of the top of the support ring. The same procedure is used for section 2, except that it extends in a clockwise direction from the axis of rotation. The positions of the sections of the lens outline below the support ring depends on the orientation of the support castellations.

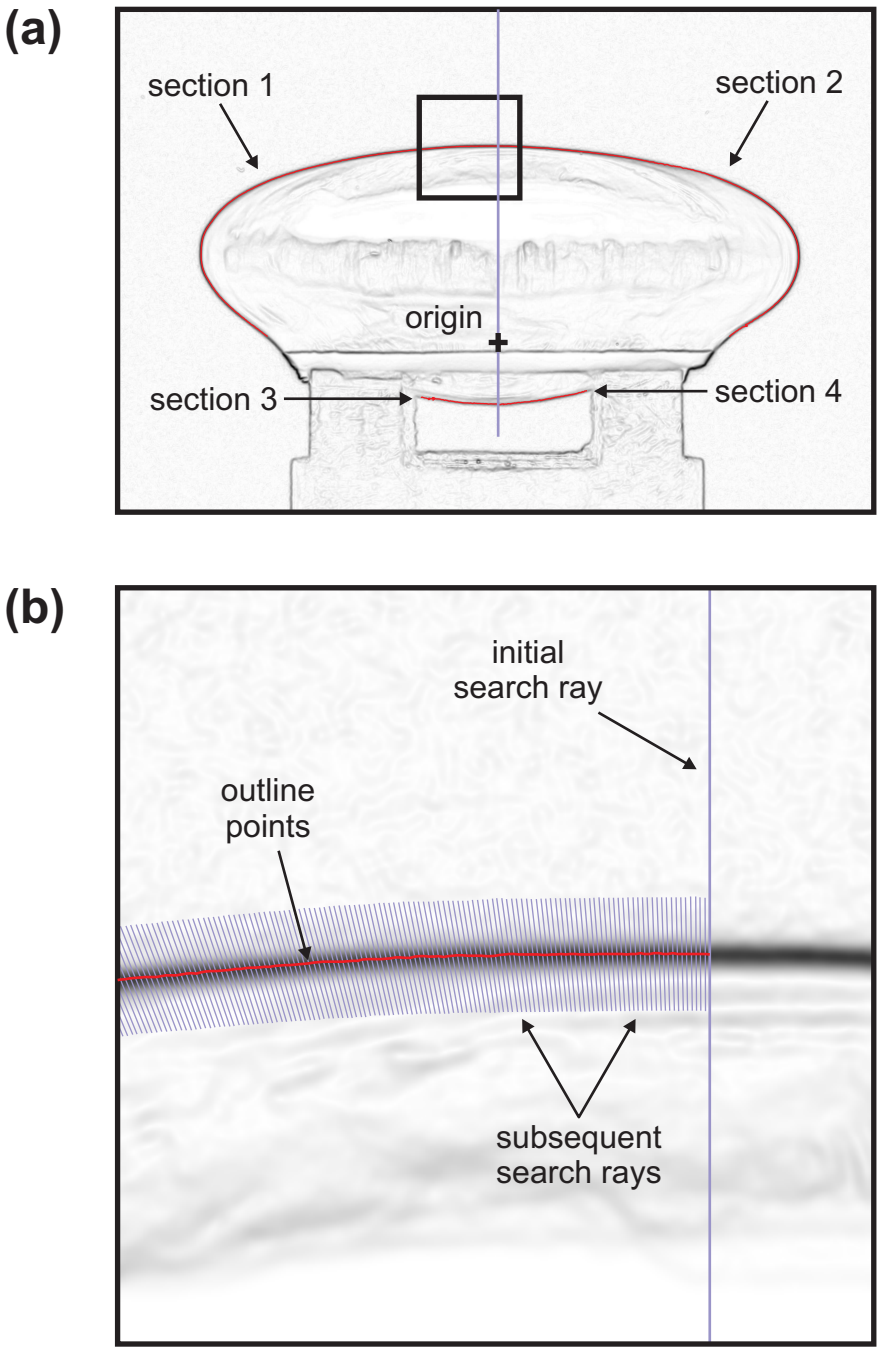

Figure 7.3 – *Detection of the lens outline: (a) The sections of the detected lens outline (red) displayed with the corresponding gradient magnitude image from the second photograph of test A_{R3} for the decapsulated 33-year lens L038A (zero gradient shown as white, the maximum gradient shown as black). (b) A close-up view of the start of section 1 of the outline, including the search rays along which the outline was sought; the corresponding region is marked by a black square in figure (a).*

When there is a central window sections 3 and 4 are found in the same way as sections 1 and 2, with two variations: the first point is sought on a downward directed line segment with the domain restricted to the section of the photograph above the support base, and the process is halted when the next outline point is within 150 pixels of the top of the support ring, or within 20 pixels of the side of the window (found using edge detection as in section 7.2.3). When there are two windows, section 3 lies within the left window and section 4 lies within the right window. The first points of these sections are no longer on the axis of rotation, but are found in a similar way by first determining the first ray that will pass through the lens outline at least 20 pixels from the inner side of the window in question, with the inner side of the window also found using edge detection.

7.2.5 Calibration procedure

The outline of the ball bearing in the calibration photographs (described in section 6.4.5) is identified in a manner similar to the lens (described in section 7.2.4) to determine the appropriate length scale to use in the photographs.

For the outline of the calibration ball bearing an origin is selected on the axis of rotation, half way between the top of the image and the top of the support ring. This lies roughly at the centre of the ball bearing. The top of the ball bearing lies above the frame of the photograph, while the portion of the ball bearing below the support ring is ignored as it is generally poorly illuminated. As with the lens, the outline of the ball bearing is found separately in four sections corresponding to the four quadrants relative to the chosen origin. In each section, the first point of the outline of the ball bearing is found along a horizontal ray from the origin rather than a vertical ray, but the process is otherwise similar to the process for the lens. Once all the outline points have been found a circle is fitted to them using an initial algebraic approximation, followed by a total least squares optimization.

In photographs taken before the 24th of July 2008 the reflective surface of the ball bearing means its actual edges have little contrast with the background, so it is best to determine the scale by hand. In these cases each photograph is imported into CORELDRAW and a circle is constructed that coincides as well as possible with the ball-bearing edge, most clearly

identified by dust on the surface.

Whichever method is used to find the circles, the diameter in pixel lengths of each is recorded and the mean diameter from the eight calibration photographs is calculated. This value is used in conjunction with the diameter of the ball bearing measured with a micrometer to determine the appropriate conversion from pixel lengths to millimetres. An initial test using gridded paper suggested there was little photographic distortion so the same scaling is used for both axes and throughout the photographs.

7.2.6 Image correlation

Image correlation is used to account for camera movement between photographs taken at the same rotor orientation. Only the support region is used for the calculation as the lens itself is expected to differ between photographs. To calculate the offset between two photographs the correlation between the two photographs is calculated in a region including all of the support below the lens for different pixel offsets between the two photographs. Once an offset has been found which gives a local maximum in the correlation that value is assumed to represent the camera movement which occurred between the two photographs. The first correlation calculation is made for no offset, then subsequent calculations are made at offsets forming an orthogonal spiral, to limit the number of calculations needed if the optimum offset is small.

For each photograph from the secondary reference set and the spinning set, the pixel offset relative to the corresponding photograph of the primary reference set is found. This offset is then used to effectively bring the photograph into alignment with the primary reference photograph before obtaining the lens outline. In this way all three of the photograph sets should have the same effective axis of rotation and support ring position.

7.2.7 Lens outline splines

The image processing described above results in a set of points lying on the outline of the lens in each photograph examined. The points are occasionally erratic where the edge is not clear and there is some variation in the lens shape at each orientation, especially around the

lens equator. The further analysis of the spinning lens test, in particular the finite-element simulation, requires a smooth axisymmetric representation of the lens. A number of general forms to describe lens outlines have been published: Fisher (1971) uses an ellipse; Burd et al. (2002) use a combination of polynomials and circular arcs; Chien et al. (2006) use a parametric description combining polynomial and trigonometric terms; Urs et al. (2010) use a truncated Fourier series in polar coordinates. None of these methods seems ideal for the present study, and all would require adaptation to take account of the presence of the lens support which interrupts the smooth surface of the lens.

Polar coordinates seem a natural choice for describing a curve surrounding the origin such as the lens outline, while a cubic spline representation has the advantage of being smooth and adaptable without introducing high order terms. For these reasons cubic splines specified in polar coordinates are used to describe the lens outline. The break in smoothness caused by the presence of the lens support is handled by using a 'top spline' for the outline above the support ring and an independent 'bottom spline' for the outline below. Figure 7.4 depicts an example of a pair of lens splines fitted to a set of outline points.

For the simulation of the spinning test to be fully axisymmetric the axis of rotation must coincide with the axis of symmetry of the lens. This is ensured by requiring the two splines to be symmetric about the axis of rotation. This means that only the portions of the splines to the right of the axis need to be considered, with all the outline points lying on the left of the axis reflected onto the right before determining the forms of the splines.

The top and bottom splines each have a zero slope condition where they meet the axis of rotation as required for symmetry, and have fixed end points at the outside and inside corners of the ring support respectively (see figure 7.4). In reality lenses meet the support at variable locations below these corners, but a fixed end position is much simpler to formulate for the splines and seems a reasonable approximation (originally it was assumed that the material adhering to the side of the support was fluid, not lens substance, but this does not appear to be true in general). The top spline is given seven internal knots with equal angular intervals between them; the first knot is placed at half of this interval from the axis (that is, a full interval from its own reflection if the spline were continued symmetrically past the axis),

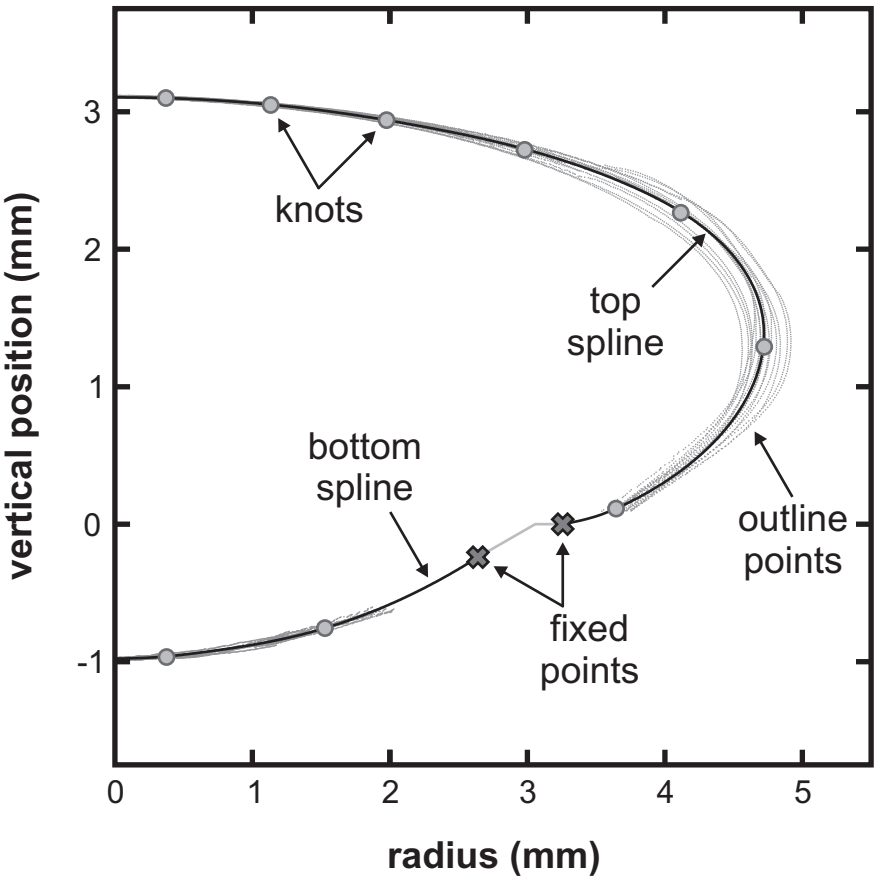

Figure 7.4 – *The top and bottom splines for the decapsulated 33-year lens L038A, together with the outline points used to generate the splines, all plotted in cylindrical coordinates.*

while the last knot is placed at one-eight of the interval from the fixed end point. This small final interval allows the spline to adapt to the required shape near the support without causing significant distortion in the remainder of the curve. The bottom spline is given two internal knots since it covers a smaller domain; the angular interval from each end point to the closest knot is half the interval between the two knots (again, the knot closest to the axis is a full interval from its own reflection).

Finding the specific spline which best fits the set of polar outline points in an ordinary least squares sense is most easily formulated using a set of basis splines, $\{\mathrm{B}_i(\theta)\}$. For a given spline order, sequence of knot positions, and end constraints the basis splines are a set of such splines which have minimal support, that is which are each nonzero over the smallest domain possible while maintaining internal smoothness. Any spline with the same order, knot positions, and end constraints can be expressed as a linear combination of the

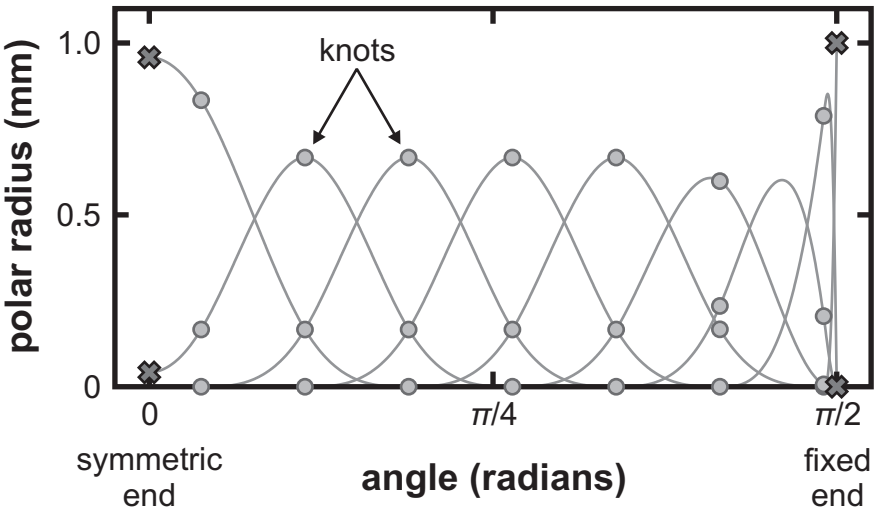

Figure 7.5 – *The basis splines used to generate the top spline of the lens outline. The basis splines all have zero slope at the symmetric end and all but one have zero value at the fixed end.*

basis splines. Thus for such a spline, $\mathrm{S}(\theta)$, there are coefficients, $\{c_i\}$, such that

$$\mathrm{S}(\theta) = \sum c_i \mathrm{B}_i(\theta) \quad . \tag{7.1}$$

Evaluating the spline at a sequence of values $\{\theta_j\}$ can be cast in the form of matrix multiplication: if $\mathbf{s} = \big(\mathrm{S}(\theta_j)\big)$, $\mathbf{B} = \big(b_{ij}\big) = \big(\mathrm{B}_i(\theta_j)\big)$ and $\mathbf{c} = (c_i)$ then $\mathbf{s} = \mathbf{Bc}$. This means that the coefficients of the spline which best fits a set of outline points $\{(\theta_j,\ r_j)\}$ can be found using the pseudo-inverse of the matrix $\mathbf{B}$: if $\mathbf{r} = \big(r_j\big)$, then $\mathbf{c} = \mathbf{B}^{+}\mathbf{r}$. This is a simple operation in MATLAB.

The fixed end condition adds a small complication to this calculation. Only one of the basis splines, B_k say, will have a nonzero value at the fixed end so its coefficient can be determined without reference to the outline points, but the outline points must then be adjusted so the correct coefficients are determined for the remaining basis splines. If the fixed end point is at $(\theta_E,\ r_E)$ then the coefficient of the nonzero basis spline is $c_k = r_E/\mathrm{B}_k(\theta_E)$ and the adjusted radius values are $r'_j = r_j - c_k \mathrm{B}_k(\theta_j)$.

The splines of the reference geometry are calculated from all the outline points identified in both sets of reference photographs. The top reference spline makes use of all these points which lie above the support ring, while the bottom reference spline makes use of all the points which lie below the support ring. Both sets of reference photographs are used on the assumption that the average between the two is a reasonable representation of the hypo-

thetical undeformed state of the lens midway through the spinning test. The splines of the spinning configuration are calculated from all the outline points identified in the single set of spinning photographs in a similar manner.

7.2.8 Lens mesh generation

The top spline and bottom spline found for the reference configuration are used to generate the mesh used as the reference state for the finite-element simulation of the spinning lens test. The construction of the mesh is performed by the MATLAB-based meshing tool `Mesh2d` (Engwirda, 2007). An example of the resulting mesh is illustrated in figure 7.6. `Mesh2d` takes a set of regions defined by boundary polygons and returns a triangular mesh within these regions, with a number of options to control the size of the triangles produced. Three regions of the lens are specified for `Mesh2d` to mesh: region 1 corresponds to the nucleus region used in model D (see section 7.5.2), region 2 is the main cortex region between the nucleus and the lens outline, and region 3 is a small area around the contact with the support ring. Regions 1 and 2 are distinguished so that the discontinuity in shear stiffness which occurs in model D coincides with element boundaries. Region 3 is included so that a smaller element size can be specified in this potentially problematic area. All the curved sections of these regions are approximated by connected line segments as required by the `Mesh2d`. The line segments used are twice as long as the desired element size at the given boundary to provide some flexibility to the meshing tool in node placement while remaining close to the intended geometry.

Once `Mesh2d` has created a mesh for the three regions it is further modified using custom MATLAB functions. All the nodes lying at the exterior of the nucleus or the cortex are adjusted so that they lie exactly on the original curves defining those outlines, rather than on the line segments supplied to `Mesh2d`, and the three-noded triangles generated by `Mesh2d` are upgraded to the fifteen-noded elements used in OXFEM_HYPERELASTIC by adding the required edge and internal nodes. The final mesh is written to a file in a format understood by OXFEM_HYPERELASTIC. The final mesh uses fifteen-noded triangular elements as these perform well in axisymmetric finite-element simulation of nearly incompressible materials

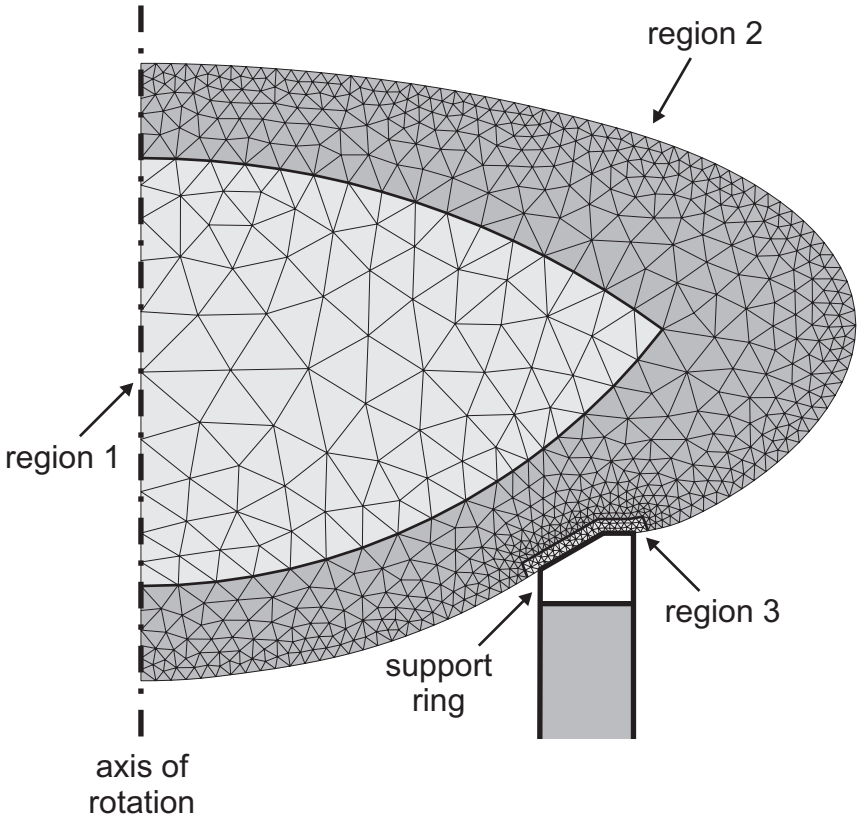

Figure 7.6 – *The mesh generated for analysis of test AT2 of the decapsulated 33-year lens L038A. The three regions are described in the text. This mesh has 1420 elements and 11665 nodes.*

compared to elements with fewer nodes, as discussed in section 5.4.2. The meshes used in the analysis have approximately 12000 nodes.

The element density is determined by specifying the maximum length of the element edges within each region, and separately on the outer boundary, when calling `Mesh2d`. The maximum length is also limited by the length of the line segments used to specify the regions, which constrains the spacing on the nucleus-cortex boundary. The meshes used for the analysis consist of approximately 1400 elements and 12000 nodes. This was found to be a sufficient number that further mesh refinement had negligible effect on the results of the analysis (see section 8.3.1 for an examination of mesh refinement).

7.3 The body forces acting on the lens

The analysis of the spinning lens test is conducted in the non-inertial frame of reference rotating with the lens. In this frame of reference the lens experiences an apparent centrifugal body force. Additionally, the lens is deformed from its unstressed configuration by a gravitational body force throughout the testing procedure. The centrifugal body force is crucial to the analysis of the spinning lens test, while the gravitational body force is a minor complication which has been examined but ultimately ignored. Both body forces are proportional to the local density of the lens which is assigned a value based on past studies.

7.3.1 The density of the lens

The current study has made no attempt to measure the density of the lenses subjected to testing; instead the analysis was performed using a single density value of $1058.98\,\mathrm{kg\,m^{-3}}$ for all lenses. This is the value for a 40-year lens according to the linear age-density regression given by Burd et al. (2006), which uses data from Bellows (1944). The full relationship, calculated for lenses between 20 and 70 years, is

$$\rho = c_0 + c_1 A \quad , \tag{7.2}$$

where $c_0 = 1013.5\,\mathrm{kg\,m^{-3}}$, $c_1 = 1.137\,\mathrm{kg\,m^{-3}\,yr^{-1}}$ and A is the age of the lens in years. This amounts to roughly a 5 % increase in density from the youngest to the oldest lenses. If this were incorporated into the analysis the stiffness values calculated for lenses older than 40 years would be slightly higher to compensate for the increased body force, while value for younger lenses would be correspondingly lower. This is complicated somewhat by the spatial variation of density within each lens, which is also not incorporated into the analysis of the spinning lens test. This variation arises due to the differing protein concentrations through the lens, so follows the form of the refractive index gradient which also depends on the local protein concentration. Using values given by Augusteyn (2010) it can be calculated that the outer cortex is approximately 5 % less dense than the centre of the lens. The differences in density with age and position are sufficiently small and inexact that the use of a single density value seems reasonable.

7.3.2 The centrifugal body force

In its rotating frame of reference the lens experiences an apparent centrifugal body force, $\mathbf{f}_C$, which depends on the density of the lens substance, ρ, the angular velocity of rotation, ω, and the horizontal displacement from the axis of rotation, $\mathbf{r}$, according to

$$\mathbf{f}_C = \rho\omega^2\mathbf{r} \quad . \tag{7.3}$$

The option to include such a radial force in OXFEM_HYPERELASTIC was implemented by Dr Burd prior to the start of the current study. For a spinning test at 1000 rpm, the centrifugal body force experienced by the lens varies from $0\,\mathrm{N\,m^{-3}}$ at the axis of rotation to about $50,000\,\mathrm{N\,m^{-3}}$ at its equator. In the reference tests the lens is slowly rotating at 70 rpm, corresponding to a centrifugal body force which varies from 0 to about $250\,\mathrm{N\,m^{-3}}$ through the lens. This latter force is minuscule so is ignored in the analysis.

The lens is indeed largely axisymmetric and placed on the support so that its centre of mass is close to the axis of rotation so the most substantial components of force and deformation are axisymmetric in form. However, slight misalignment will lead to a net horizontal force on the lens proportional to the distance of misalignment. If the centre of mass of an axisymmetric object is displaced from the axis of rotation in some direction, $\mathbf{r}_M$, then the centrifugal body force acting at a given point in the object can be decomposed into two parts, one depending on the horizontal displacement of the point from the axis of symmetry and one depending on $\mathbf{r}_M$. That is

$$f_C = \rho\omega^2(\mathbf{r} - \mathbf{r}_M) + \rho\omega^2\mathbf{r}_M \quad . \tag{7.4}$$

The first is the axisymmetric component of the centrifugal body force and the second is the misalignment component. Over the whole object the former is purely axisymmetric and contributes no net force, while the latter contributes no net axisymmetric component, but does contribute a net force of

$$\mathbf{F}_M = m\omega^2\mathbf{r}_M \quad , \tag{7.5}$$

where m is the mass of the object. In the case of the lens, this force must be opposed at the contact between the lens and the support, or the lens will ultimately slide off the support.

Provided the deformations due to the misalignment component are small they will be effectively removed by the averaging procedure applied to the lens outline (see section 5.2.7), so will not affect the estimate of the stiffness as calculated from the axisymmetric component of the body force.

7.3.3 The gravitational body force

The lens is deformed by a gravitational body force throughout the test. The conventional gravitational acceleration is $9.810\,\mathrm{m\,s^{-2}}$, yielding a body force of about $10,000\,\mathrm{N\,m^{-3}}$ which is comparable to the volume average of the magnitude of the radial body force. The option to include a vertical body force in OXFEM_HYPERELASTIC was implemented by Dr Burd prior to the start of the current study. However, as the gravitational body force is present in both the reference and spinning states it cannot be applied in a straightforward manner in the simulation.

To include the effect of gravity it is necessary to replace the reference geometry that was obtained from the experiment with a 'prior geometry', undeformed by either gravity or spinning. An option to find such a prior geometry has been implemented in OXFEM_SEARCHER by the author. When this option is used, a number of loading stages are specified as 'prior stages'. Before conducting the full simulation, a routine seeks an appropriate prior geometry, Γ_P, which deforms to the input geometry, Γ_I, when subjected to the loads and displacements specified in the prior stages, $\mathcal{P}$ (for the gravity case, $\mathcal{P}$ consists of the gravitational body force $\mathbf{f}_g$ and zero displacement conditions at the support and axis). The first trial geometry, Γ_0, is found by subjecting Γ_I to the opposite of the loads and displacements of $\mathcal{P}$. The routine then iterates, applying $\mathcal{P}$ to the current trial geometry Γ_i to obtain the deformed trial geometry Γ_i'. An improved trial geometry is found by comparing Γ_i' to Γ_I, adjusting the nodal positions according to

$$\mathbf{n}_{i+1} = \mathbf{n}_i + \left(\mathbf{n}_I - \mathbf{n}_i'\right) \quad , \tag{7.6}$$

where $\mathbf{n}_x$ is the position of a given node from Γ_x. The process terminates when all the nodes of Γ_i' are sufficiently close to the corresponding node of Γ_I (within $1\,\mu$m typically), or once a specified number of iterations are completed. In either case the trial geometry which

gave the smallest maximum discrepancy between the nodes of Γ_i' and Γ_I is selected as the prior geometry Γ_P and is then subjected to all the loading stages in turn, including those not specified as prior stages (the radial body force in the case of the spinning test).

When this form of analysis is performed, the ultimate material parameters obtained are similar to those from an analysis in which gravity is neglected, as would be expected if the lens model is behaving in a roughly linear fashion. For example the shear modulus calculated using model H for a 12-year lens (label L037A) is 180 Pa ignoring gravity and 188 Pa including gravity, a 4.4 % difference. This is small compared to the overall variations between lenses and any effect will be largest with a soft lens such as this due to the large deformations it experiences.

Since each set of material parameters requires a new iterative calculation to find the appropriate prior geometry, which must be repeated each time the material parameters are modified, the inclusion of the effect of gravity slows the optimization procedure considerably without a significant benefit to compensate. For this reason the standard analysis of the decapsulated lenses is performed without considering gravity.

7.4 Contact conditions at the support

The presence of the support must be incorporated in some manner into the simulation of the spinning test. At minimum the lens must be prevented from freely moving vertically to provide a unique solution. An accurate characterization of the effect of the ring on the radial movement of the lens is also desirable as it influences the overall accuracy of the test. In principle the behaviour of the lens where it makes contact with the support could range from frictionless sliding to fully-fixed adherence.

The current spinning lens test is not well suited to determining the true behaviour of the lens in the vicinity of the support. Tracking surface details between the reference and the spinning photographs could provide the information required; however, only serendipitous details are available and these are rare on the transparent lens. As such, they cannot be used to reliably determine the average axisymmetric behaviour of the lens. If the lens does slide

it may only occur over a region of the support; also, a difference between the movement of a surface detail and the simulated movement at that position may arise from the non-axisymmetric misalignment force rather than an incorrectly simulated support.

Faced with this uncertainty each lens is analysed using two support conditions: the fixed support constraint (F) where the nodes that start on the support are held in their initial position throughout the test, and the sliding support constraint (S), where the nodes can effectively slide along the support. It is presumed that the true behaviour lies somewhere between these two possibilities.

7.4.1 The fixed constraint (F)

The fixed constraint restricts all the nodes located at the contact with the support ring. The nodes are prevented from moving either parallel to the support surface or orthogonal to it. This is a simple option to specify in OXFEM_HYPERELASTIC. The solution procedure simply holds each node at its initial radial and vertical position and calculates the reaction force required to maintain this.

The fixed constraint essentially represents a high friction interface. Since gravity is not explicitly included in the simulation (see section 5.4.3) the orthogonal reaction force may be directed towards the support ring without implying an adhesive interface, though no check is made that the reaction force remains within the range permitted by gravity and friction alone.

7.4.2 The sliding constraint (S)

The sliding constraint allows the nodes located at the contact with the support ring to move freely in the tangential direction, but prevents them moving in the orthogonal direction. When spinning is simulated the freedom to move means that the appropriate constraints for some nodes will change between the initial and the final configuration. A method to handle this complication has been implemented in OXFEM_SEARCHER by the author.

The approach adopted is as follows. The geometry of the support interface is specified as a pair of line segments, $\bar{S}$ and $\bar{T}$, corresponding to the slope and the top of the support ring.

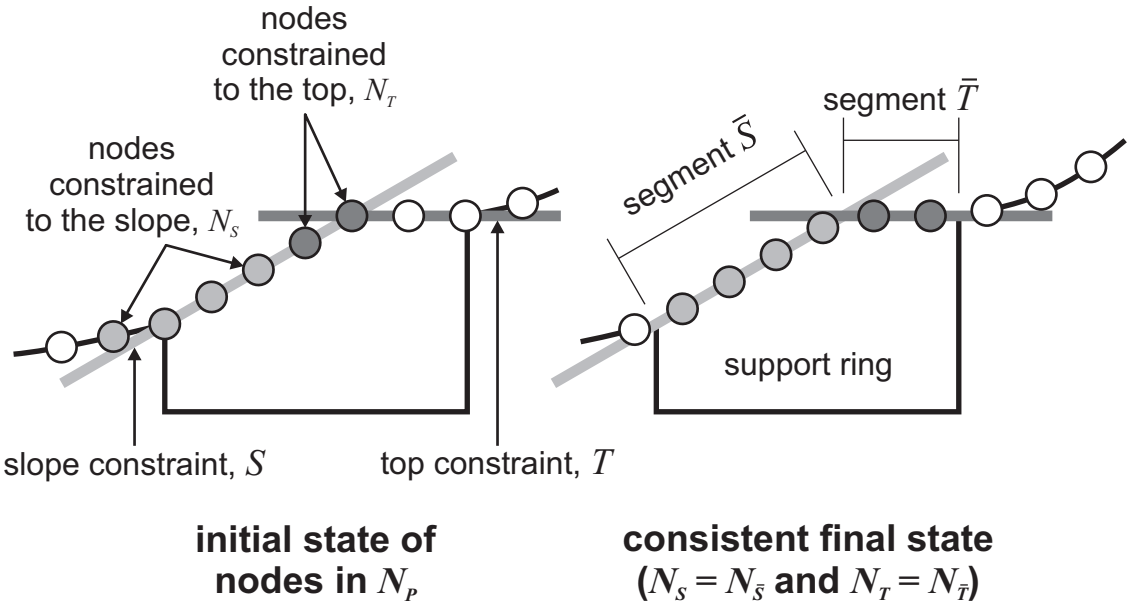

Figure 7.7 – *A schematic of the handling of the sliding constraint. The constrained nodes (N_S, light grey; N_T, dark grey) are forced onto the respective constraint lines (S, light grey; T, dark grey) during the simulation. The final state depicted is consistent with the given constraints because the unconstrained nodes are not in the constraint region while each constrained node lies on the correct line segment ($\bar{S}$ or $\bar{T}$). In reality there are many more nodes in contact with the support ring.*

Nodes can be constrained so that at the end of the simulation of the spinning test they lie on the line S passing through $\bar{S}$, or the line T passing through $\bar{T}$ (see figure 7.7). Such a line constraint can induce a reaction force orthogonal to the constraint line, but not parallel to it.

Constrained nodes are free to move parallel to the line during the simulation, even if they go beyond the corresponding segment, so an iterative process is used to determine the correct nodes to constrain. A set of potentially constrained nodes, N_P, is specified consisting of nodes at the surface of the lens on or near the support interface, and two disjoint subsets of this set, N_S and N_T, are given. The simulation is performed with the nodes of N_S constrained to the line S, and the nodes of N_T constrained to the line T. When the simulation is completed, the final position of each node in N_P is checked. If a node lies orthogonal to the line segment $\bar{S}$ then that node is assigned to a subset $N_{\bar{S}}$, and likewise for $\bar{T}$ and $N_{\bar{T}}$ (though if a node is orthogonal to both segments it is only assigned to the latter subset). If the constraints imposed on the nodes agree with their final positions, that is if $N_S = N_{\bar{S}}$ and $N_T = N_{\bar{T}}$ (with a small tolerance in node position allowed, generally $1\,\mu$m), then the initial constraints are consistent with the deformation and the simulation is accepted as the correct

outcome. Otherwise, the simulation is repeated with the subsets specifying the constraints updated to $N_S = N_{\bar{S}}$ and $N_T = N_{\bar{T}}$.

Between four and six simulations are generally required before consistent constraints are found. This approach ensures the final configuration of the last simulation has suitable constraints and is in equilibrium. However, the intermediate steps of the simulation no longer reflect a physically meaningful progression as nodes may be constrained to points away from the support interface prior to the final step.

An alternative approach in which the nodal constraints are updated following each step of the simulation has also been trialled, as this maintains the physical relevance of the intermediate steps and avoids the need for multiple attempts at the simulation. The principal difficulty is the sudden appearance of substantial unbalanced forces at nodes whenever their constraints change. This is ameliorated by allowing additional steps when required to bring the simulation back towards equilibrium. However, the resulting simulation is potentially as slow as the iterative procedure due to the large number of additional steps required. It is also more prone to failure than the iterative procedure so has not been adopted.

7.5 Stiffness models of the decapsulated lens

Calculation of lens stiffness from the spinning lens test requires some assumptions, since the test only supplies limited information at the surface of the lens. The neo-Hookean model used to describe the lens substance (see section 5.3.2) requires two parameters, μ and κ, equivalent at small strains to the linear-elastic shear modulus and bulk modulus respectively. The lens is generally taken to be nearly incompressible since its water content is over 60 % (Fisher and Pettet, 1973). This is supported by the observation that the total lens volume does not change during accommodation (Hermans et al., 2009). Hence the value of κ can be assumed to be large compared to μ and need not be determined specifically. On the other hand, indentation tests (Heys et al., 2004; Weeber et al., 2007) suggest dramatic variations of shear modulus between the inner and outer regions of the lens, so characterizing μ for a given lens will require at least two parameters if it is to capture this heterogeneity.

With this in mind each lens is analysed using three stiffness models: a homogeneous lens (model H), a model with distinct nucleus and cortex regions (model D), and a model with stiffness varying continuously from the centre to the outside of the lens following an exponential curve (model E). The first is used as it is the simplest stiffness model available, while the second and third are used so that the expected heterogeneity can be examined. Further parameters would be possible, such as a value describing the degree of anisotropy related to the alignment of the lens fibre cells, but it is unlikely that the spinning lens test alone can be used to determine more than two parameters reliably.

7.5.1 The homogeneous lens model (H)

The lenses are analysed first using the assumption that they have the same value of shear modulus, μ, throughout. This is the simplest model of the lens stiffness. Its primary use is to provide a check that the two parameter models do actually achieve a better match to the experimental results.

Instead of specifying the bulk modulus directly a new material, `matNEO_HOOKE_REL`, in which the bulk modulus is specified relative to the shear modulus was created for OXFEM_HYPERELASTIC by the author. For a relative bulk modulus, κ', the actual bulk modulus is given by $\kappa = \kappa'\mu$. This arrangement makes it simpler to ensure that the lens remains nearly incompressible for large values of μ while avoiding poorly conditioned finite-element calculations for small values of μ. For the analysis of the spinning lens test a relative bulk modulus of 100 was used. This ratio is equivalent to a consistent linear-elastic Poisson's ratio of 0.495. The same form of relative bulk modulus is adopted in the heterogeneous models D and E.

7.5.2 The distinct nucleus and cortex model (D)

In the distinct nucleus and cortex model (D) the lens is divided into two regions with potentially different values of shear modulus, the inner nucleus and the outer cortex, each of which is homogeneous. This model is proposed as there is evidence for a demarcation in a number of properties between the nucleus and the cortex, especially in older lenses. The formation

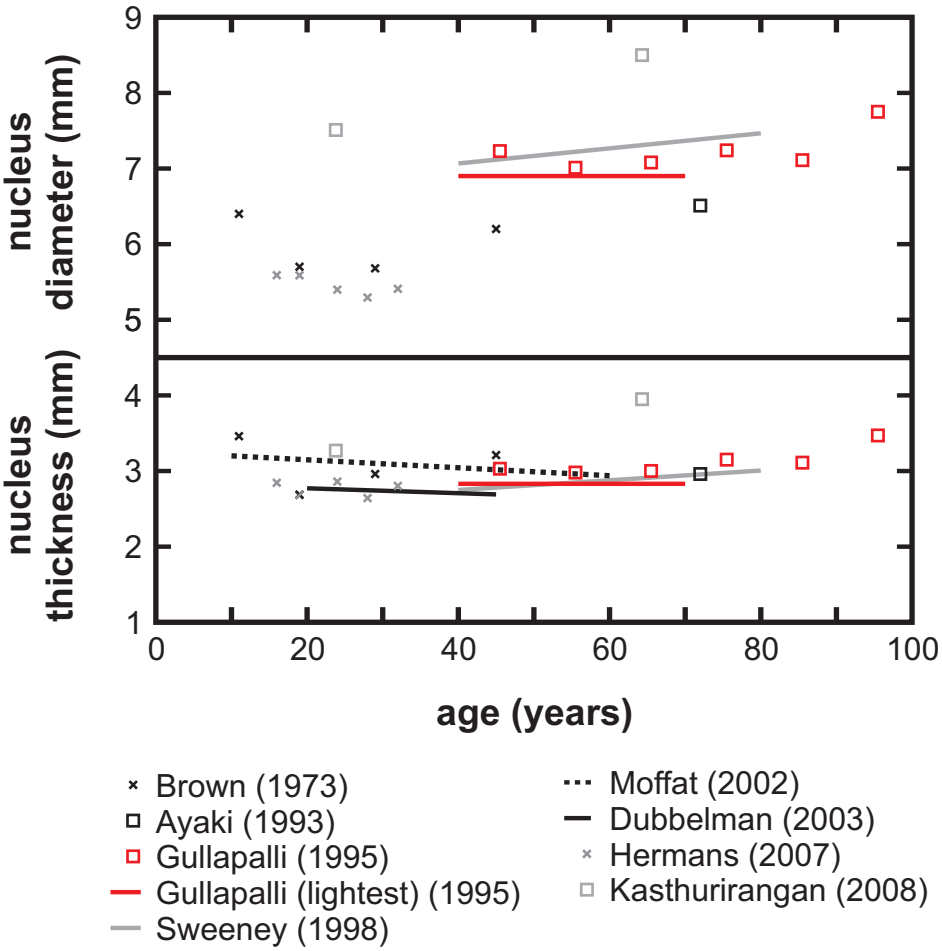

Figure 7.8 – *Published nucleus diameter and thickness measurements. Crosses represent the measurement of one subject, boxes represent averages from a set of subjects of similar age and lines represent a trend or mean over a range of ages.*

of isolatable nuclear cataracts (Gullapalli et al., 1995) is the most directly relevant to lens stiffness, but the existence of a barrier to diffusion (Sweeney and Truscott, 1998) and the change in light scatter seen in slit-lamp photographs (Brown, 1973) also suggest a sudden rather than gradual transition between the inner and outer regions of the lens. A separate nucleus was also assumed in the analysis of the original spinning lens tests of Fisher (1971), so its adoption in the current test allows comparison with the previous results.

Existing values for the dimensions of the nucleus vary depending on how it is defined and measured. Published data include measurements from Scheimpflug photography (Brown, 1973; Dubbelman et al., 2003; Hermans et al., 2007), direct measurement of extracted cataractous nuclei (Ayaki et al., 1993; Gullapalli et al., 1995), *ex vivo* diffusion measurements (Sweeney and Truscott, 1998; Moffat and Pope, 2002), and *in vivo* magnetic resonance based

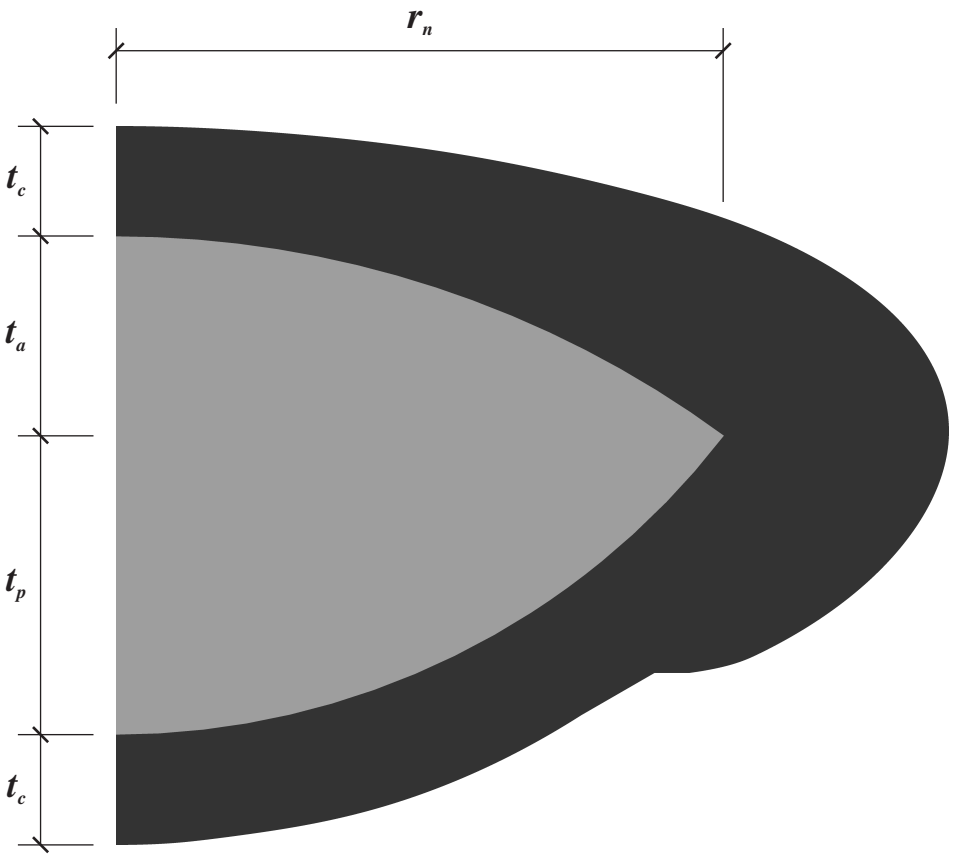

Figure 7.9 – *The form of heterogeneity in model D. The dimensions of the nucleus are the same for all lenses, with $r_n = 3.45$ mm, $t_a = 1.132$ mm, $t_p = 1.698$ mm; the thickness of the cortex, t_c, depends on the particular lens. (Adapted from Burd et al., 2011).*

measurement of refractive index (Kasthurirangan et al., 2008). These are plotted for comparison in figure 7.8. The values reported by Gullapalli et al. (1995) for the lightest (least severe) class of cataract, 2.83 mm thickness and 6.90 mm diameter, are adopted for model D as they come from direct measurements, are related to material stiffness, and lie near the centre of the whole collection of values. This last fact also suggests that it need not be a concern that the measurements come from unhealthy lenses. The dimensions reportedly showed no age dependence for the set of lenses measured, which were all older than 40 years. For simplicity and consistency the same dimensions are also used in model D for lenses younger than 40 years.

The form of the nucleus is illustrated in figure 7.9. Following Burd et al. (2002), the nucleus is assumed to be formed by the intersection of two spheres (or the area between two arcs in the cross-section). The distance from the anterior pole to the plane of the nucleus equator, t_a, is fixed at two thirds of the distance from the posterior pole to the plane of

the nucleus equator, t_p, to roughly agree with the lens as a whole when positioned on the support. This fixes the respective values as $t_a = 1.132\,\text{mm}$ and $t_p = 1.698\,\text{mm}$. The nucleus is located within the lens such that the midpoint of the nucleus along the axis coincides with the midpoint of the whole lens.

A body with two substances such as this can be modeled by dividing the finite-element mesh into two areas and using a different material for each area. However, a new material, `matNEO_HOOKE_REL_ARC`, was created for OXFEM_HYPERELASTIC by the author. This material takes as parameters the relative bulk modulus, the nuclear shear modulus, the cortical shear modulus, and subsidiary values defining the shape and position of the nucleus. When assigning shear modulus values to the Gauss points used in the finite-element formulation the appropriate value is selected according to whether the point in question lies within the nuclear or the cortical region, as defined by the subsidiary material parameters. Such a formulation makes it possible to vary the nucleus geometry without requiring a new mesh. It is preferable in a finite-element calculation for such discontinuities to fall on element boundaries and only one nucleus shape is used, so in practice the standard nucleus geometry is included within the lens meshes used to analyse the spinning lens tests (as discussed in section 7.2.8).

7.5.3 The exponential stiffness model (E)

The exponential stiffness model (E) prescribes that the stiffness varies continuously from the centre of the lens to the outside, following an exponential curve. This allows for a closer correspondence than the distinct model to the results obtained from indentation tests (Heys et al., 2004; Weeber et al., 2007), and avoids the need to dictate the nucleus geometry. As for model D above, there are two free parameters which characterize the stiffness of the lens.

The centre of the lens lies on the axis at the midpoint between the anterior and posterior poles. To compute the value of stiffness at any point in the lens a line segment from the centre to the lens exterior passing through the point in question is considered (see figure 7.10). If ζ is the distance from the midpoint to the point in question and ζ_0 is the length of the whole

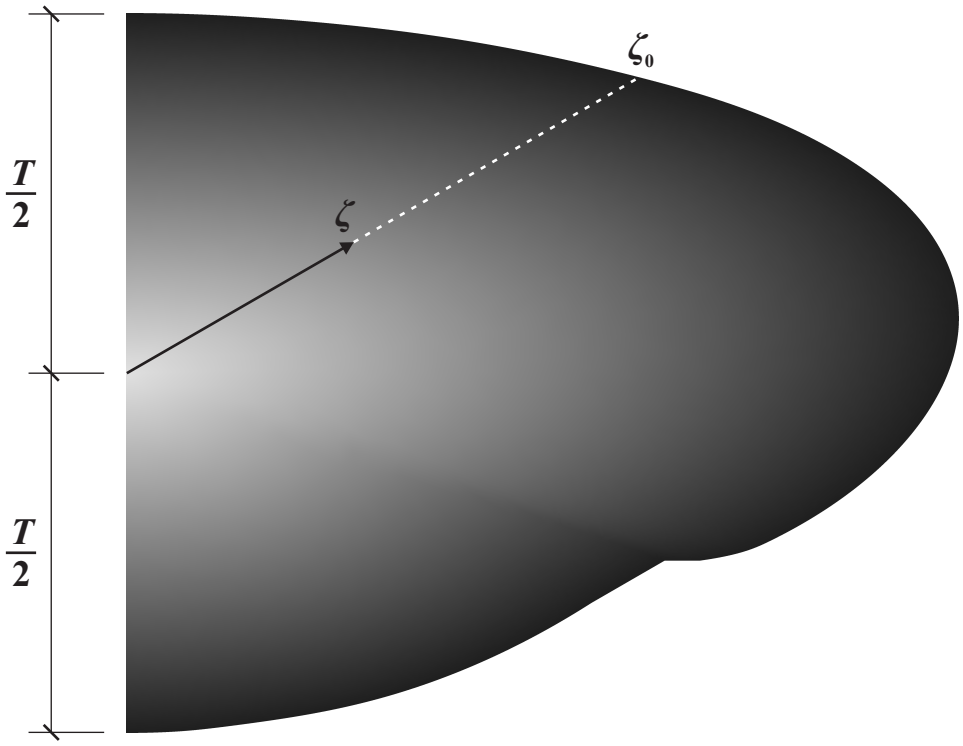

Figure 7.10 – *The form of the exponential model E. The central point where the shear modulus equals μ_0 lies on the axis at the midpoint between the anterior and the posterior poles. The shear modulus equals μ_1 over the whole exterior of the lens. (Adapted from Burd et al., 2011).*

line segment, then the relative distance is

$$\hat{\zeta} = \frac{\zeta}{\zeta_0} \quad . \tag{7.7}$$

At the centre of the lens $\hat{\zeta} = 0$, while at the exterior $\hat{\zeta} = 1$. The neo-Hookean shear modulus, μ, is then given by the exponential equation

$$\mu = \mu_0^{1-\hat{\zeta}} \mu_1^{\hat{\zeta}} \quad , \tag{7.8}$$

where μ_0 is the central shear modulus and μ_1 is the peripheral shear modulus. This arrangement produces a model with concentric shells of equal stiffness each geometrically similar to the lens exterior, roughly corresponding to the layers of equal-age tissue in the lens. In the spinning lens test the exterior of the lens is deformed by the presence of the support, which leads to a small distortion of the calculated stiffness from a realistic shell structure along the lines from the lens centre to the support. This is a minor issue and is not addressed.

A new material, `matNEO_HOOKE_REL_EXP`, was created for OXFEM_HYPERELASTIC by the author to allow the use of model E when simulating the spinning lens test. This mate-

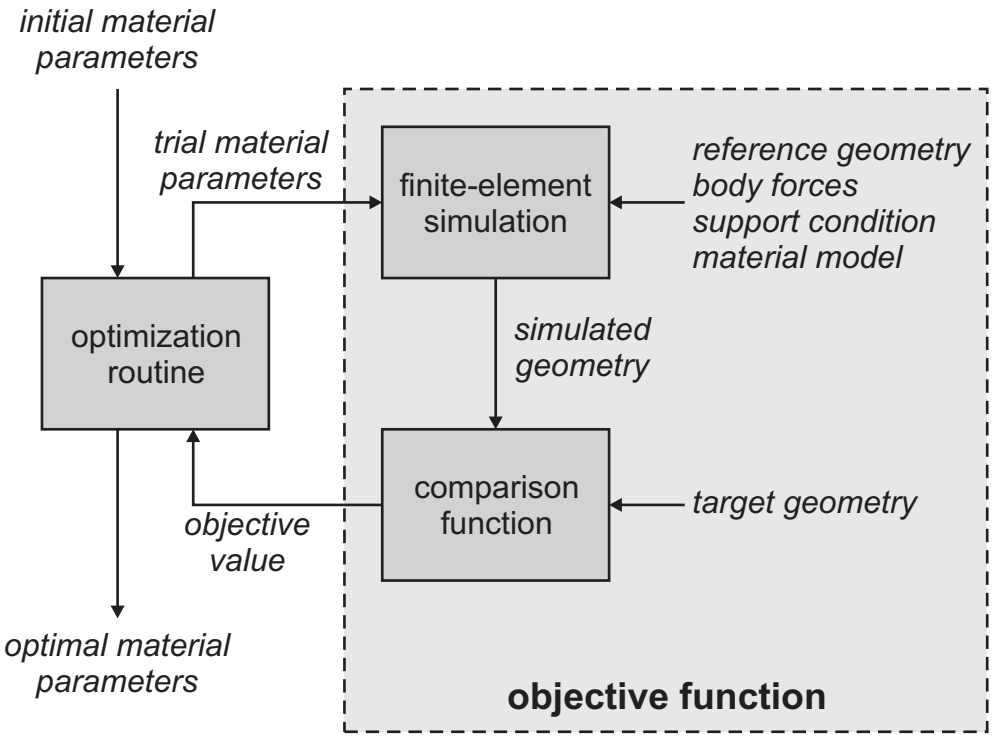

Figure 7.11 – *An overview of the iterative search for material parameters.*

rial takes as parameters the relative bulk modulus, the central shear modulus, the peripheral shear modulus, and the position of the centre point. It also requires a separate specification of all the nodes which lie on the surface of the lens in order to calculate the length ζ_0. When assigning shear modulus values to the Gauss points used in the finite-element formulation, the appropriate value of μ is calculated for each point.

7.6 Estimation of material parameters

An iterative optimization procedure is used to determine which material parameters best reproduce the results of the actual experiment. The objective function used in the optimization procedure has two components: the finite-element simulation which takes the material parameters and calculates the expected geometry during the spinning test, and a comparison function which takes the calculated geometry and determines how close it is to the geometry measured in the actual experiment, as illustrated in figure 7.11.

The value of the objective function is used by an optimization routine, specifically the

Nelder-Mead method (Nelder and Mead, 1965), to determine the material parameter values for which the simulation most closely corresponds to the experiment. These optimal material parameters provide an estimate of the true values.

7.6.1 Geometry comparison functions

A comparison function takes information about the outline of the simulated lens and compare it to the corresponding information about the target outline obtained from the experiment. If the simulation matches the experiment, the value of the comparison function should be zero, and if not it should be a positive value which corresponds in some way to the degree of disagreement. The simulation provides details of the displacements experienced at each node, but such displacement information is not available from the experiment (even at the surface) as it is not possible to track the movement of specific points in the photographs. Thus the comparison function must depend only on the overall shape of the spinning lens outline in the experiment and the simulation.

Two comparison functions have been implemented in OXFEM_SEARCHER. The first is the extrema comparison function, Q_E, which uses only the maximal radius and thickness of the lens outline. This corresponds to the method used in the original spinning lens test (Fisher 1971). The value of the comparison function is

$$Q_E = \sqrt{(R_S - R_T)^2 + (T_S - T_T)^2} \quad , \tag{7.9}$$

where R_S and R_T are the maximal simulated radius and maximal target radius respectively, and T_S and T_T are corresponding thickness values. The target values are calculated from the splines fitted to the experimental spinning lens outline (see section 7.2.7).

The second comparison function is the enclosed-area comparison function, Q_A, which calculates the area between the experimental and simulated outlines. This approach makes use of much more of the available information so is the comparison function used in the analysis of the current spinning lens test. The simulated outline is the piecewise linear curve, C_S, formed by joining the displaced positions of adjacent surface nodes. This is compared to the target outline, C_T, a similar curve formed from points lying on the splines fitted to the experimental spinning lens outline. The points of the target outline are selected with a spac-

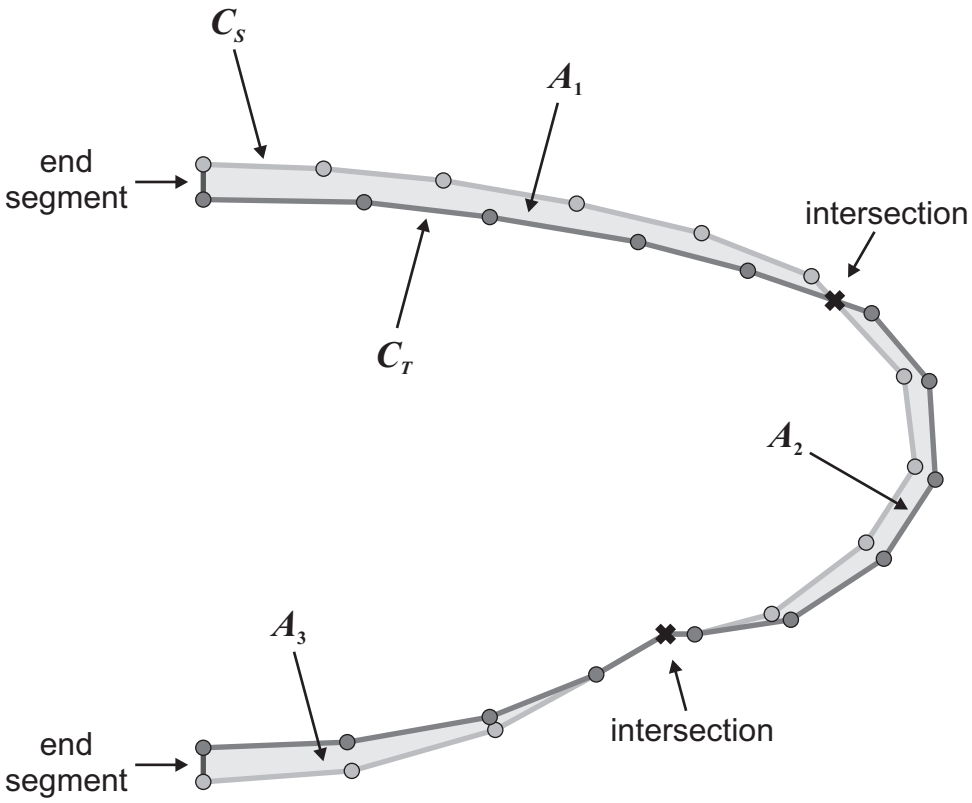

Figure 7.12 – *A schematic for the enclosed-area comparison function,* Q_A*. For clarity the simulated outline,* C_S*, and target outline,* C_T *have been simplified. The region enclosed by the two outlines and the end segments is comprised by three simple polygons with signed areas* A_1*,* A_2*, and* A_3*, so* $\mathrm{Q}_A = |A_1| + |A_2| + |A_3|$*.*

ing similar to the nodes of the simulation mesh. The method of calculation is summarized in figure 7.12.

The two curves, C_S and C_T, together with line segments connecting their endpoints, form a polygon. It is a simple matter to compute the signed area of such an object from its vertex locations. A two-dimensional polygon with vertices at a sequence points $\{\mathbf{x}_i\}$ in which the first and last points are equal has a signed area of

$$A = \frac{1}{2}\sum_i \mathbf{x}_i \times \mathbf{x}_{i+1} \quad . \tag{7.10}$$

However, it is the unsigned area that is required for the comparison function and the two area values differ since the polygon intersects itself. To calculate the unsigned area, each intersection between C_S and C_T is found so the original polygon can be decomposed into multiple simple polygons, for which the unsigned area is simply the absolute value of the signed area. The full comparison function is the sum of the unsigned areas of the constituent simple polygons. That is, if the simple polygons have signed areas $\{A_j\}$ then the value of

the enclosed-area comparison function is

$$\mathrm{Q}_A = \sum_j \left| A_j \right| \quad . \tag{7.11}$$

If the curve which describes the outline of the reference geometry of the lens is C_R then the value of Q_A is bounded above by Q_{A_0}, the area enclosed between C_R and C_T. This allows the definition of $\hat{\mathrm{Q}}_A$, a dimensionless measure of how well the optimization process matches the target outline:

$$\hat{\mathrm{Q}}_A = \frac{\mathrm{Q}_A}{\mathrm{Q}_{A_0}} \quad . \tag{7.12}$$

The value of $\hat{\mathrm{Q}}_A$ can range from 0 for an exact match between C_S and C_T to 1 if the undeformed outline C_R is the closest match that can be achieved. This permits a comparison of the quality of the fit achieved for lenses which experience deformation of substantially different magnitudes.

Additional comparison functions have been considered. One option is to calculate the volume enclosed between the surfaces obtained by rotating the curves C_S and C_T about the axis. This would be preferable if there was a substantial difference in volume enclosed by the two surfaces, but this is not the case. Instead, the considerably greater weight that would be given to discrepancies at the equator is undesirable as there is just as much confidence in the measurements at the pole as at the equator.

Another option is to base the comparison on the full set of outline points for both the reference and spinning configurations, rather than using the splines fitted to them. This requires interpolation between nodes to find an appropriate displacement to apply to each reference configuration point, as well as interpolation between spinning configuration points to find an appropriate target position. Such a comparison function has been implemented using MATLAB and found to give comparable results to the much simpler process using the fitted splines, so the latter are used in the analysis.

7.6.2 The optimization routine

The principal search method used in analysing the spinning lens test is an implementation of the direct-search Nelder-Mead method. For a search over n parameters, this method starts

with $n+1$ points forming a simplex in the parameter space to be explored. It constructs a new trial point in the parameter space from the points in the current simplex based on a number of heuristics. If the value of the objective function at the trial point is better than that at the worst point in the simplex then the former is included in the simplex and the latter is removed. The method terminates if it fails to find a better point, or if the ranges of the parameter and objective values at the current simplex points are sufficiently small. For the current analysis the latter termination condition is set to be a ratio of 1.005 between the maximum and minimum of each material parameter and 1.001 between maximum and minimum objective function value. Depending on how close the starting values are to the optimum the method generally requires 10–20 iterations for a single material parameter (for stiffness model H) or 30–60 iterations for two material parameters (for stiffness models D and E). An option is included in OXFEM_SEARCHER which allows the Nelder-Mead search to be conducted in logarithm space. In this case the standard trial point constructions are applied to the logarithm of the simplex parameter values, then the exponential is taken to find the corresponding point in regular parameter space. This is advantageous as the effect of changing a stiffness parameter is generally proportional to the relative change in value rather than the absolute change; it also prevents the algorithm exploring non-physical negative stiffness values.

The Nelder-Mead method was selected and implemented in OXFEM_SEARCHER before the final form of the comparison function was set. It was chosen in preference to a gradient-based approach because the latter would require finite-difference approximations to the gradient which are slow due to the finite-element calculation, and could be potentially problematic should the objective function lack smoothness at small scales. The Nelder-Mead method performs sufficiently well that the implementation of alternative optimization methods has not been warranted.

The only other search routine which has been implemented is a simple grid search which computes the objective function over a specified grid of values in the material parameter space. The principal use of the grid search is to determine the overall shape of the objective function rather than the location of the optimum. As with the Nelder-Mead method, the grid

search can be conducted in logarithm space, so that the material parameter values at the grid points form a geometric rather than an arithmetic sequence.

8

The spinning lens test: Results

The principal results of the spinning lens test are the stiffness parameters obtained by applying the analysis described in chapter 7 to a set of 29 lenses which produced good quality tests when decapsulated. These lenses are referred to as lens set $\mathcal{G}$. Details of the tested lenses and a preliminary description of their response to the spinning test are reported in section 8.1, including the criteria used to select the lenses of set $\mathcal{G}$. The values of stiffness parameters of lens set $\mathcal{G}$, calculated using the various forms of the spinning test analysis, are reported in section 8.2. An analysis of the reliability of the main results is provided in section 8.3. Finally, a comparison of the current results with the values obtained in the previous tests of Fisher (1971), Heys et al. (2004), Heys et al. (2007) and Weeber et al. (2007) is given in section 8.4.

8.1 The tested lenses

A total of 119 lenses from donors aged from 12 to 87 years were received from the Bristol Eye Bank between the 23rd of August 2007 and the 13th of August 2009. Of these, 71 were subject to a standard spinning test described in chapter 6. Nine lenses were not tested either due to major damage to the lens or the absence of the author when they were received. The remaining 39 lenses were obtained during the early stages of the project and were used to refine the test procedure and experiment with differing supports and lighting arrangements.

Individual lenses are referred to by a label consisting of 'L', followed by a three digit number referring to the donor, then a suffix of 'A' or 'B' to distinguish the two lenses from the same donor (for example lens L038A). The donor numbers differ from those assigned by the Bristol Eye Bank, but maintain the same order. A summary of the received lenses and the tests performed on them is given in table 1 of appendix A.2. The 29 lenses of the good quality set $\mathcal{G}$ are aged between 12 and 58 years with a mean of 40.3 years. They were enucleated at the Bristol Eye Bank 18 ± 5 hours after death (mean$\pm$s.d.) and tested 74 ± 17 hours after death. All lenses in set $\mathcal{G}$ were tested within five days of the death of the donor. Additional details and the stiffness parameters calculated for these lenses are given in table 2 of appendix A.2. Three lenses are consistently used as examples in this chapter, the 33-year lens L038A, the 43-year lens L039B, and the 50-year lens L056B.

8.1.1 Selection of the good quality tests ($\mathcal{G}$)

The set of lenses, $\mathcal{G}$, from which the main results were obtained constitute a relatively small proportion of the lenses received from the Bristol Eye Bank. The majority of the lenses that were subjected to testing but excluded from $\mathcal{G}$ suffered from apparent swelling; a number were also excluded due to problems during the experiment: either damage caused to the lens substance or the presence of fluid on the surface of the lens when tested following the removal of the capsule.

Swelling and aspect ratio Lenses are prone to swelling following death. If the tissue of the cortex becomes swollen its mechanical response may differ from that *in vivo*. Due to the constraint of the capsule, swelling tends to increase the axial thickness of a lens, T, and decrease the equatorial diameter, D. The aspect ratio of a lens is defined by

$$\alpha = \frac{D}{T} \quad . \tag{8.1}$$

This provides a rough proxy for the degree of swelling of each lens. According to Augusteyn (2008), an isolated adult lens with an intact capsule typically has an aspect ratio between 2.2 and 2.3, with $\alpha < 2.0$ suggestive of swelling in lenses older than 20 years. Younger lenses

tend to have a lower aspect ratio even when not swollen (a typical 15-year lens would have an aspect ratio of 1.93 according to Fisher, 1971).

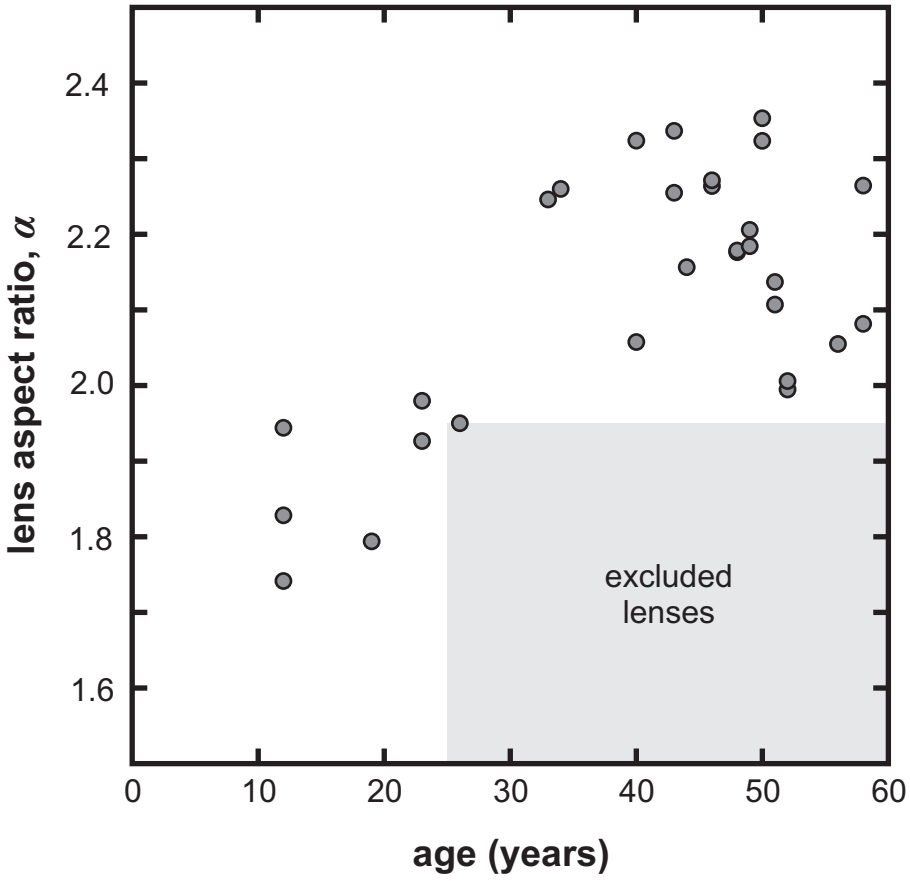

***Figure 8.1** – Aspect ratios of the lenses in set $\mathcal{G}$. Lenses with age and aspect ratio falling in the grey region are excluded from $\mathcal{G}$ on the assumption that they have become swollen following death.*

In the current study the aspect ratio is used to judge if swelling has occurred, though the threshold value is relaxed to an aspect ratio of 1.95 and only applied to lenses older than 25 years due to the uncertain influence of positioning the lens on the support ring. Being smaller and softer, young lenses are more liable to experience a decrease in aspect ratio due to the support. Twenty-one lenses were excluded from set $\mathcal{G}$ due to an aspect ratio indicative of swelling. The aspect ratios of the lenses of set $\mathcal{G}$ are shown in figure 8.1.

The aspect ratio is calculated from the photographs of the first intact reference test (A_{R1} in table 6.2). In these photographs the capsule intact and the lens has not been subjected to any spinning. In five cases (including L029B, L052B, and L055B from set $\mathcal{G}$) the aspect ratios are calculated from alternative reference photographs due to the presence of fluid in

A_{R1}. The diameter and thickness used to calculate the aspect ratio are obtained from the splines fitted to the lens outlines identified from the photographs (see section 7.2.7).

Lens damage When conducting the spinning lens test, damage to a lens most frequently occurs during the removal of the capsule. Generally a cohesive strip of cortex fibre cells come away with the capsule leaving a depression in the surface of the lens substance running in the meridional direction. Damage can also occur when positioning the lens on the support, either by applying too much pressure or allowing the lens to fall.

All lenses which suffered apparent damage or were dropped a substantial distance were excluded from set $\mathcal{G}$. Eleven lenses with an acceptable aspect ratio were excluded on this basis. Two lenses (L054B, 52 years, and L055A, 51 years) show some surface unevenness but were not excluded from set $\mathcal{G}$ as they were not clearly damaged and were otherwise of good quality.

Surface fluid The presence of fluid on the surface of the lens prevents accurate analysis of the spinning test as it obscures the true outline of the lens and tends to move to the equator when the lens is spun. Ophthalmic spears are used to absorb fluid from the lens surface when it is positioned on the support ring, but in some cases fluid remains. When subjected to spinning at 1000 rpm or faster, fluid on the lens generally forms a characteristic bulge at the lens equator which can be readily identified from the photographs of the test.

There are 10 tests which were of otherwise acceptable quality in which surface fluid is evident on the lens and was not corrected during the test. These lenses are therefore excluded from lens set $\mathcal{G}$ as a reliable analysis is impossible. Where fluid is only present during the initial tests on the intact lens this does not affect the usefulness of the main test on the decapsulated lens, though the calculation of the aspect ratio sometimes requires a combination of two reference tests to construct a full fluid-free profile in these cases.

8.1.2 Load-deformation responses

When a lens is subjected to spinning the apparent centrifugal body force is proportional to the square of the speed of rotation. The total radial load experienced by the lens also depends on

its geometry, which differs between lenses and as a consequence of loading. The differences in geometry are, however, modest so the square of the speed of rotation provides a useful approximation to the relative load to which the spinning lens is subjected at each stage of the test sequence. This approximate relative load is most naturally expressed as a proportion of the load during the main test at 1000 rpm. That is the relative radial load for a test at rotational frequency f is given by

$$\hat{F} = \frac{f^2}{f_0^2} \quad , \tag{8.2}$$

where f_0 is the reference rotational frequency of 1000 rpm.

Spinning stretches the lens equatorially and flattens it axially, so the equatorial diameter, D, and the axial thickness, T, provide two convenient measures of the magnitude of the deformation experienced by the lens. The values at a given stage in the testing sequence are readily obtained from the lens outline splines derived from the photographs taken during that test (see section 7.2.7). The value of D or T from a given test are indicated with the corresponding subscript from table 6.2 or 6.3 so D_{R1} is the diameter during the first reference test, either with or without the capsule present.

The equatorial stretch, λ_E, at a given point in the testing sequence is the current diameter divided by the diameter during the initial reference test. So, for example, the stretch during the test $\mathrm{B_{T2}}$ is

$$\lambda_E = \frac{D_{\mathrm{T2}}}{D_{\mathrm{R1}}} \quad . \tag{8.3}$$

A simple relationship between load and deformation can be examined by comparing the relative radial load to the equatorial stretch.

Examples of this load-deformation response are given for the three lenses L038A, L039B and L056B in figures 8.2, 8.3, and 8.4 respectively. L038A and L039B were tested with sequences A1 and B1 from tables 6.2 and 6.3, while L056B was tested with sequences A2 and B2. For a fixed lens and capsule state the loading slopes remain approximately the same for each test speed, as do the unloading slopes, indicating that the lens responds in close to a linear manner over the range of speeds used. In each case the removal of the capsule results in a less stiff response for the equatorial diameter.

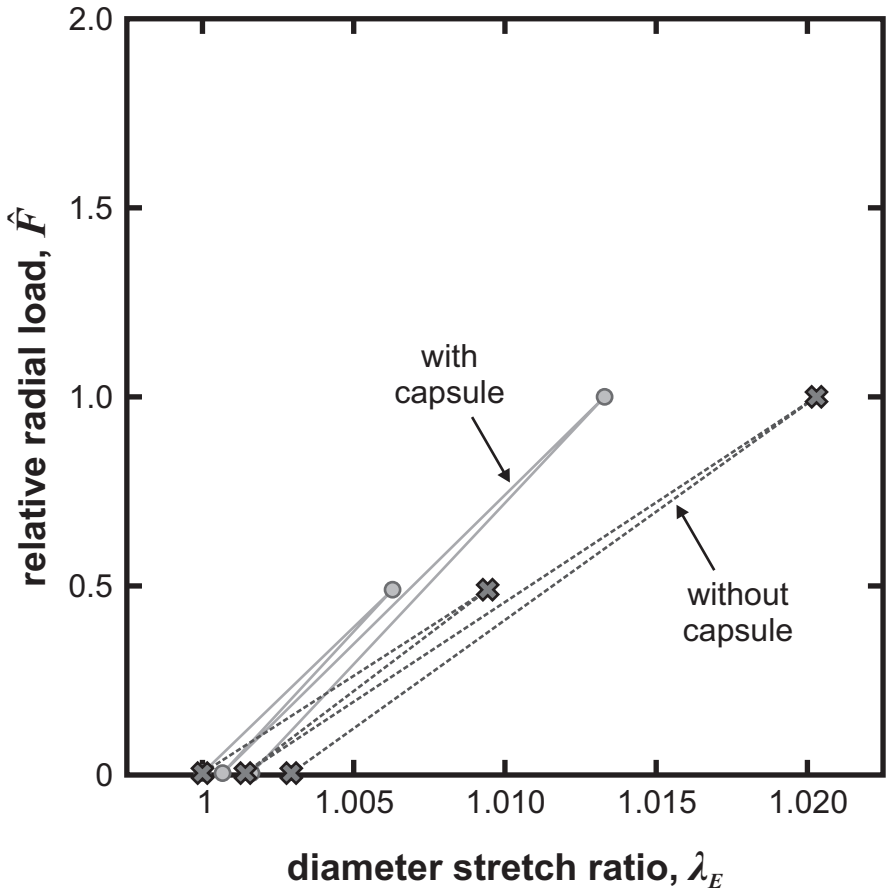

Figure 8.2 – *The response of the diameter of a 33-year lens. The stretch values are for the lens labelled L038A which was subjected to test sequence A1 (with capsule) and B1 (without capsule).*

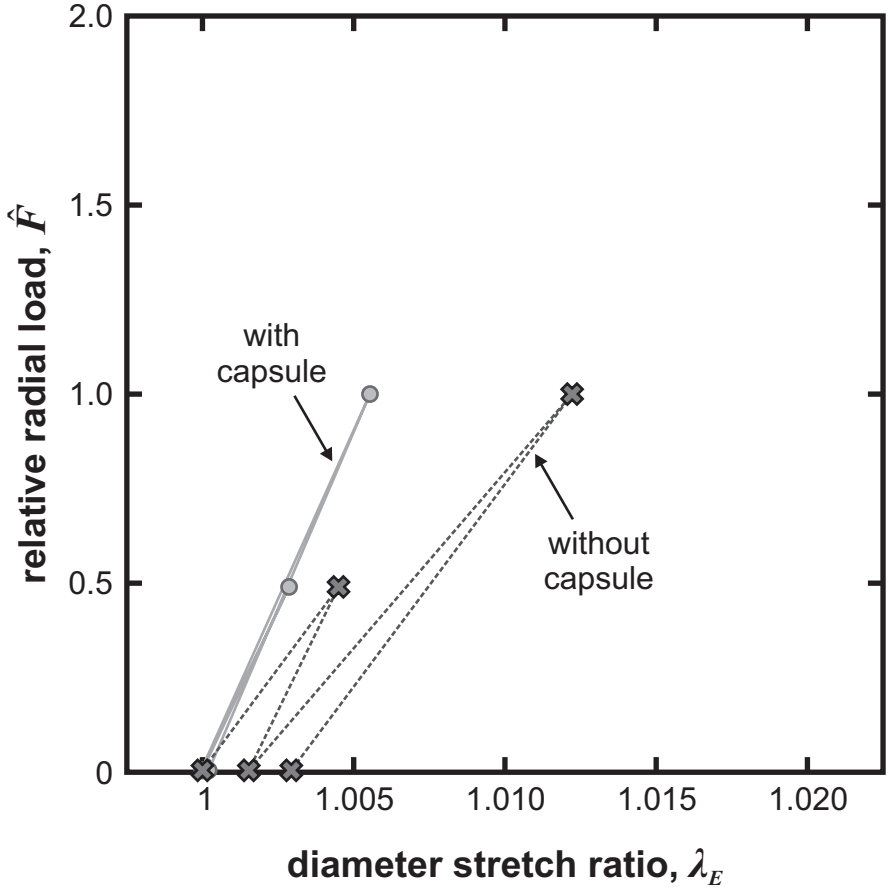

Figure 8.3 – *The response of the diameter of a 43-year lens. The stretch values are for the lens labelled L039B which was subjected to test sequence A1 (with capsule) and B1 (without capsule).*

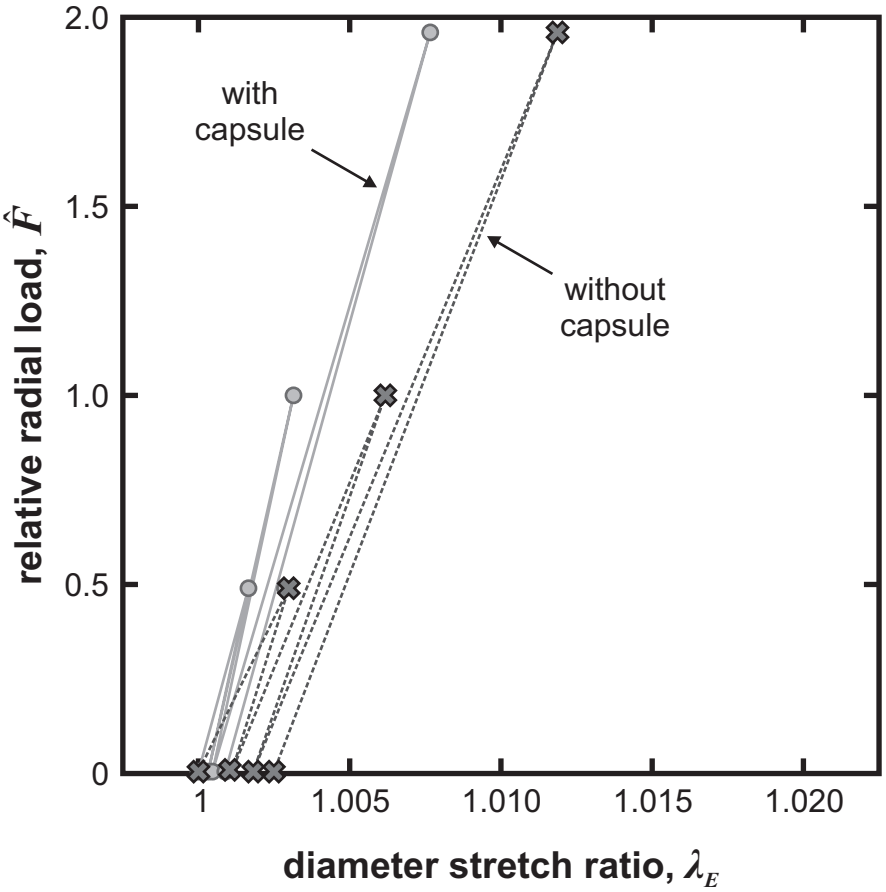

Figure 8.4 – *The response of the diameter of a 50-year lens. The stretch values are for the lens labelled L056B which was subjected to test sequence A2 (with capsule) and B2 (without capsule).*

These three lenses also display unrecovered deformation following each spinning test. That is, the equatorial diameter is greater in the reference test following a spinning test than in the preceding reference test. The unrecovered deformation is considerably larger once the capsule has been removed from the lens. The lack of recovery indicates that lenses are not deforming in a fully elastic manner. The magnitude of the unrecovered deformation after spinning at 1000 rpm can be characterized as λ_U, the change in diameter between reference tests divided by the change in diameter during the spinning test. That is

$$\lambda_U = \frac{D_{\mathrm{R3}} - D_{\mathrm{R2}}}{D_{\mathrm{T2}} - D_{\mathrm{R2}}} \quad . \tag{8.4}$$

The mean value of λ_U for the tests on the lenses of $\mathcal{G}$ in the decapsulated state is 0.14. The origin of the residual deformation is not clear from the current tests. It may result from some combination of the following:

i. a slow viscoelastic or poroelastic response of the lens material (as measured by Weeber et al., 2005; 2007)

ii. the gradual failure of the material in the vicinity of the support

iii. unrecovered slippage of the lens at the support.

The current analysis of the spinning lens test examines the response on the assumption that it is purely elastic as this is the dominant aspect and is also presumed to be of most relevance to the behaviour of the lens during *in vivo* accommodation. The main analysis of the spinning test uses an average of the reference tests before and after the test in question in order to diminish the influence of the unrecovered deformation (see section 7.2.7).

8.1.3 Comparison of intact and decapsulated tests

In the current study the stiffness parameters describing the lens substance are derived from the tests on decapsulated lenses, in contrast to the spinning lens test of Fisher (1971) in which the capsule was left intact. The effect of using the decapsulated lenses can be assessed by comparing the changes in diameter, D, and thickness, T, induced by spinning first with and then without the capsule. For the intact lens, the changes in D and T experienced during the test $\mathrm{A_{T2}}$ (at 1000 rpm) are given by

$$\delta D_A = D_{\mathrm{T2}} - \frac{1}{2}\left(D_{\mathrm{R2}} + D_{\mathrm{R3}}\right) \quad \text{and} \quad \delta T_A = T_{\mathrm{T2}} - \frac{1}{2}\left(T_{\mathrm{R2}} + T_{\mathrm{R3}}\right) \quad . \tag{8.5}$$

The mean of the reference values is used for consistency with the main analysis in which the reference geometry is calculated from the combination of both reference tests. For the decapsulated lens the changes in each dimension, δT_B and δD_B, are calculated equivalently for test $\mathrm{B_{T2}}$. The ratios between the intact and the decapsulated cases for the changes in each dimension are

$$\gamma_T = \frac{\delta T_A}{\delta T_B} \quad \text{and} \quad \gamma_D = \frac{\delta D_A}{\delta D_B} \quad . \tag{8.6}$$

The changes in diameter and thickness plotted in figure 8.5 show a substantial and age-varying difference between the values with capsule present and those when it has been removed. The measurements for the 49-year lens L029A with capsule intact are not available due to the presence of fluid on the lens during that test.

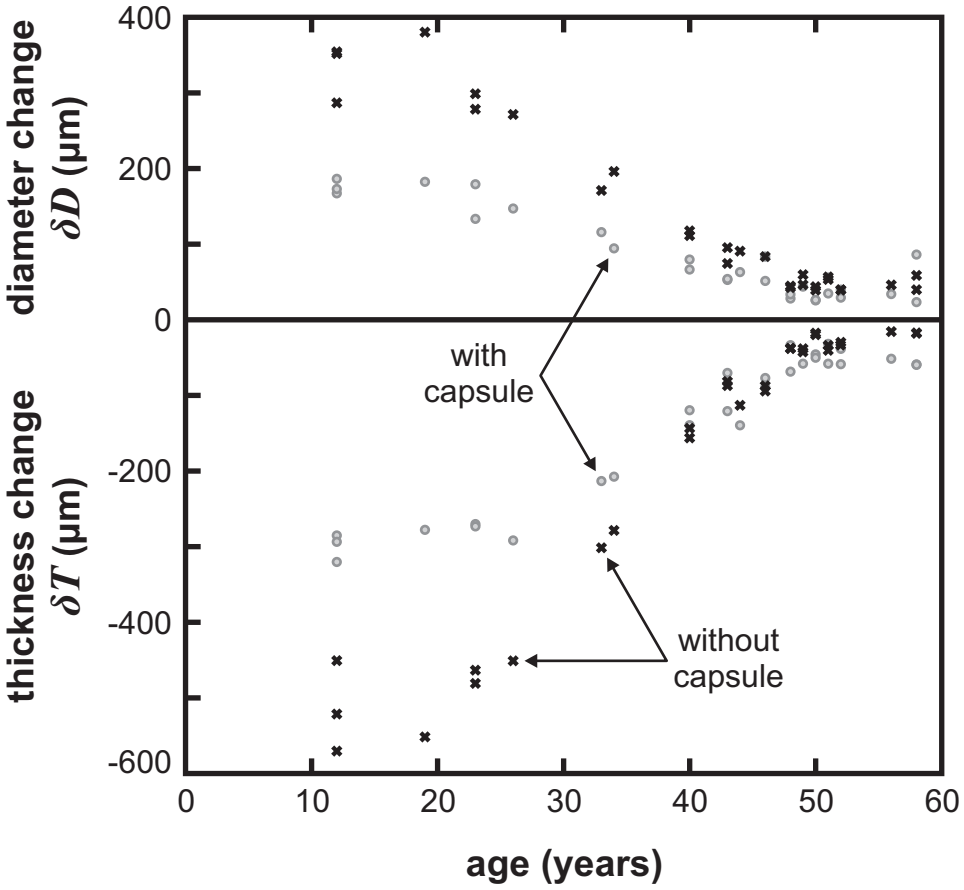

Figure 8.5 – *The change in thickness and diameter of intact and decapsulated lenses. The values are δT_A, δD_A, δT_B, and δD_B for the lenses of set $\mathcal{G}$. The changes experienced by the 49-year lens L029A with intact capsule are not included due to the presence of fluid on the lens during that test.*

The effect of the capsule varies considerably between lenses, with γ_T ranging from 0.5 to 4.5 and γ_T ranging from 0.5 to 1.6. The capsule has a consistently restrictive effect on the younger lenses, with $\gamma_T < 1$ and $\gamma_D < 1$ for all 11 lenses aged 40 years or less. The value of γ_T tends to increase with age, and also becomes more variable among older lenses. For the lenses aged over 40 years $\gamma_T > 1$ for 12 of the 17 cases; thus the presence of the capsule often enhances the axial compression of these older lenses. The value of γ_D also tends to increase with age, but $\gamma_D > 1$ for only 3 of the 17 lenses aged over 40 years, so in the majority of cases the capsule restricts the equatorial deformation of the lens substance to some extent.

The variability seen in the effect of the capsule indicates that it should be removed in order to obtain accurate measurements of the stiffness of the lens substance from the spinning test. Since the capsule has markedly different effects on lenses of different ages this is particularly important when attempting to characterize relation between age and stiffness.

The stiffness values reported by Fisher (1971) make no allowance for the presence of the capsule during the spinning test, so the differences observed here between tests with and without the capsule cast serious doubt on the accuracy of those values from the original spinning test.

8.2 Stiffness parameters for the lens substance

The stiffness of the lens substance has been calculated for the lenses of set $\mathcal{G}$ by applying the analysis procedures described in chapter 7. The principal results are those obtained from the test conducted at 1000 rpm on the decapsulated lens (test B_{T2} of table 6.3). The two alternative support constraints (fixed (F) or sliding (S); see section 7.4) and the three alternative stiffness models (homogeneous (H), distinct nucleus (D), and exponential (E); see section 7.5) mean that six different descriptions of the stiffness of the lens substance are generated from each test. The homogeneous stiffness values can provide only a very approximate representation of the lens. Which of the remaining four representations of the lens are useful must be determined. The properties of the analysis procedure and the optimal values of the objective function, Q_A (used in the analysis of the test), are assessed for this purpose.

8.2.1 Six descriptions of lens stiffness

The three stiffness models all indicate a substantial increase in the stiffness of the lens substance over the range of ages tested, with the most dramatic increase starting after about 30 years (see figures 8.6 to 8.11). The model D and model E both indicate that the stiffness of the inner region of the lens (characterized by μ_N for model D and μ_0 for model E) experiences a particularly rapid increase from this age. The values of the stiffness parameters for model E are generally more extreme than those for model D since they correspond to the most extreme values within the lens. The stiffness of the outer region of the lens (characterized by μ_C for model D and μ_1 for model E) shows a moderate increase up to about 40 years in both heterogeneous stiffness models, after which it remains roughly constant or begins to

decline after about 50 years. It seems unlikely that the decline reflects the physiological state of the lens. Possibly it arises from the limitations of the stiffness models when representing the very large difference in the stiffness calculated for the inner and outer regions of the older lenses.

8.2.2 Comparison of support constraints

During the simulation of the spinning test the sliding constraint S provides a smaller restriction on the movement of the lens than the fixed constraint F. Hence the stiffness for which the simulated lens most closely matches the target outline would be expected to be higher with constraint S. This is indeed the case, as can be seen by comparing the values calculated for stiffness model H. The shear modulus, μ, calculated using constraint S is on average 1.12 times the stiffness calculated using the fixed constraint. This difference is small compared to the span of stiffness values exhibited by lenses of different ages, which encompasses a 20-fold range.

A more dramatic effect of the choice of support constraint is seen in the partition of the stiffness between the inner and the outer regions among young lenses (compare figure 8.8 with 8.9 and figure 8.10 with 8.11). For lenses younger than 30 years, the inner stiffness (μ_N or μ_0) is much greater under the sliding constraint S than the fixed constraint F, while the outer stiffness (μ_C or μ_1) is lower despite the overall increase in stiffness indicated by model H. This same tendency is seen in the older lenses but to a lesser extent. Uncertainty regarding the true conditions at the support leads to a large uncertainty in the stiffness distribution within the younger lenses. The ratio of μ_N calculated using constraint S to μ_N calculated using constraint F has a geometric mean of 3.4 for the seven lenses younger than 30 years, with the 12-year lens labelled L043B having the maximum ratio of 4.8. The ratio of the μ_C values has a geometric mean of 0.65 and a minimum ratio of 0.48, which also occurs in the same lens.

As discussed in section 7.4, the photographs of the spinning test provide little direct information that could be used to determine which constraint is the more appropriate for modelling the contact with the support. However, the optimization procedure produces an

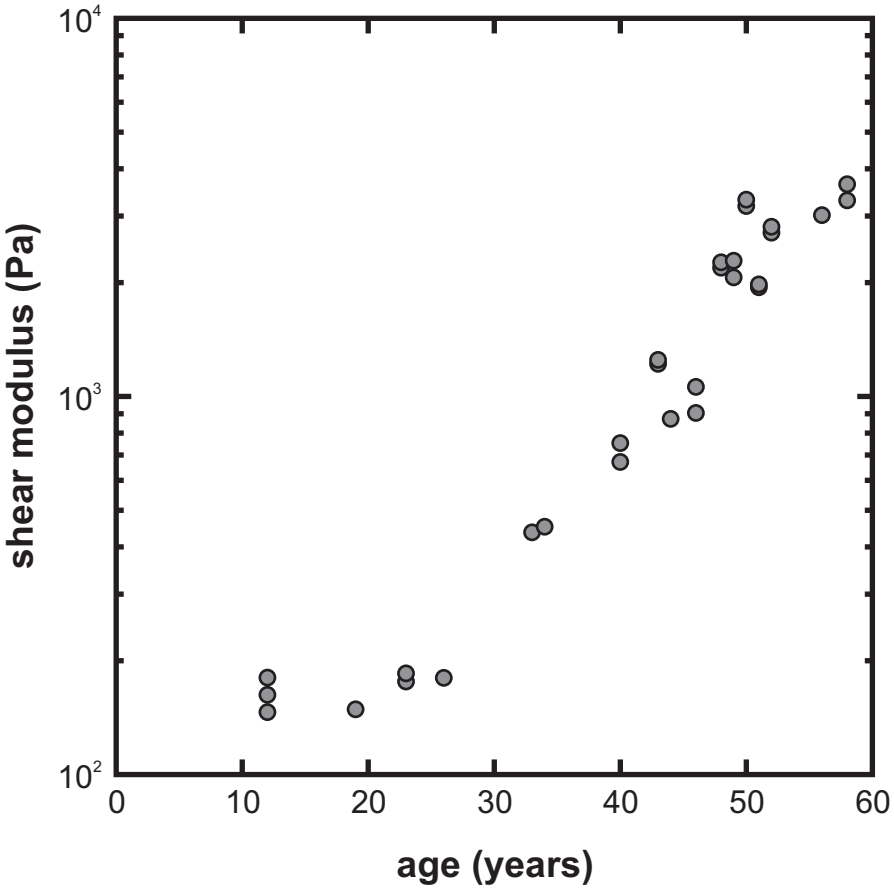

Figure 8.6 – *The model H stiffness values for lens set $\mathcal{G}$ using constraint F.*

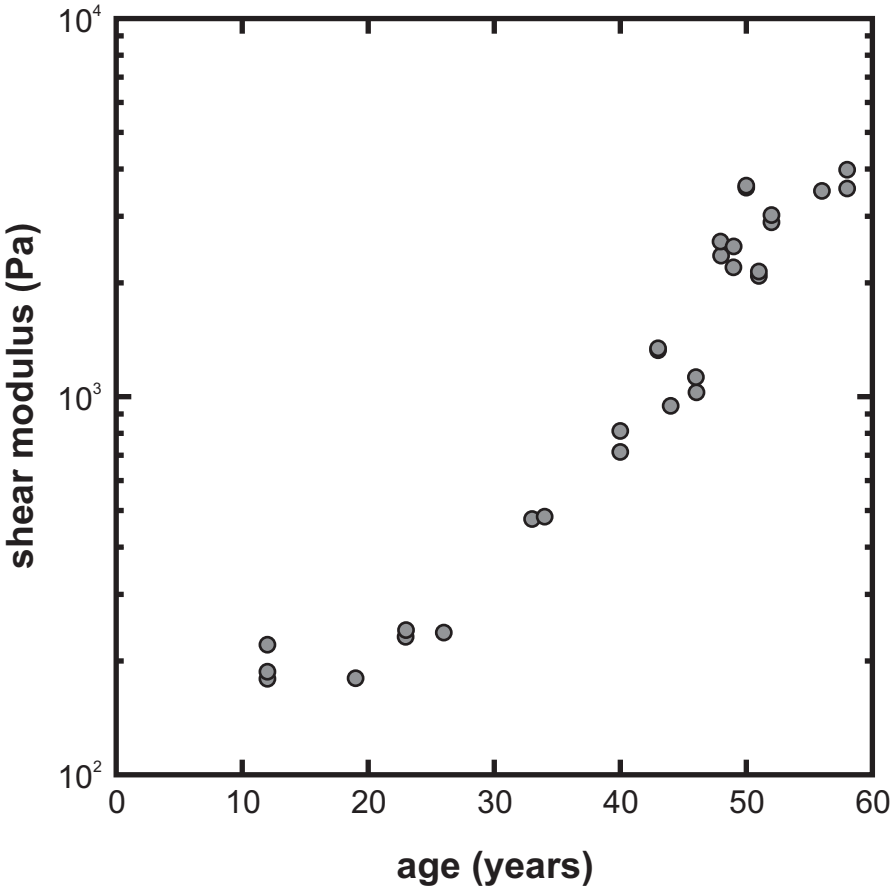

Figure 8.7 – *The model H stiffness values for lens set $\mathcal{G}$ using constraint S.*

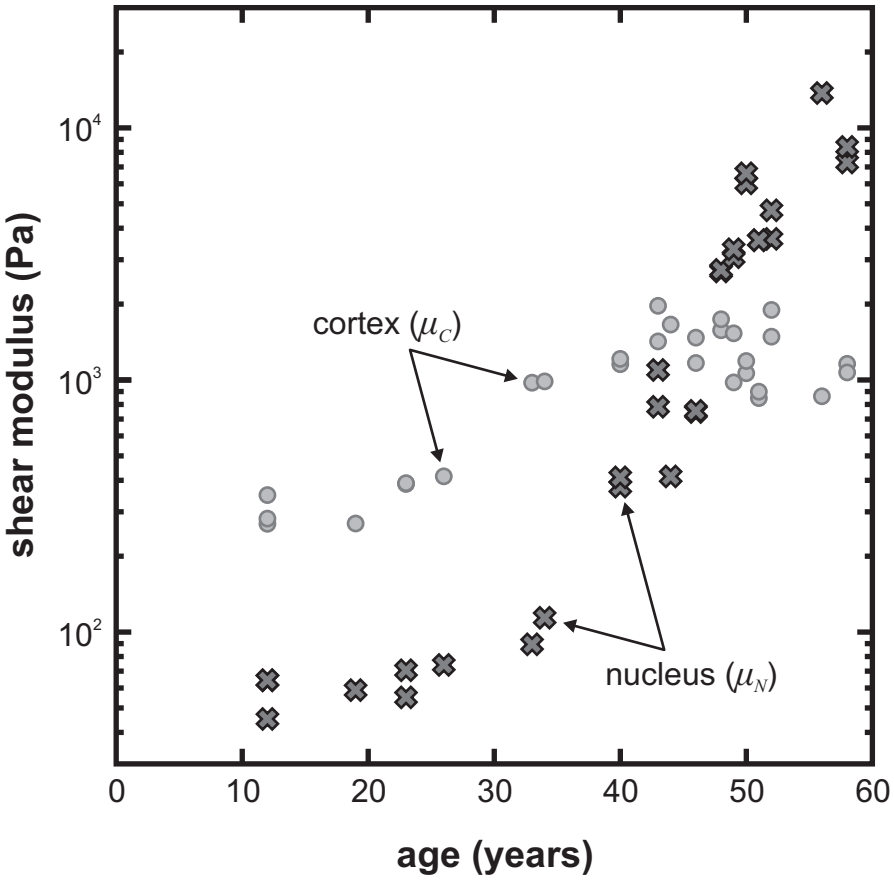

Figure 8.8 *– The model D stiffness parameters for lens set $\mathcal{G}$ using constraint F.*

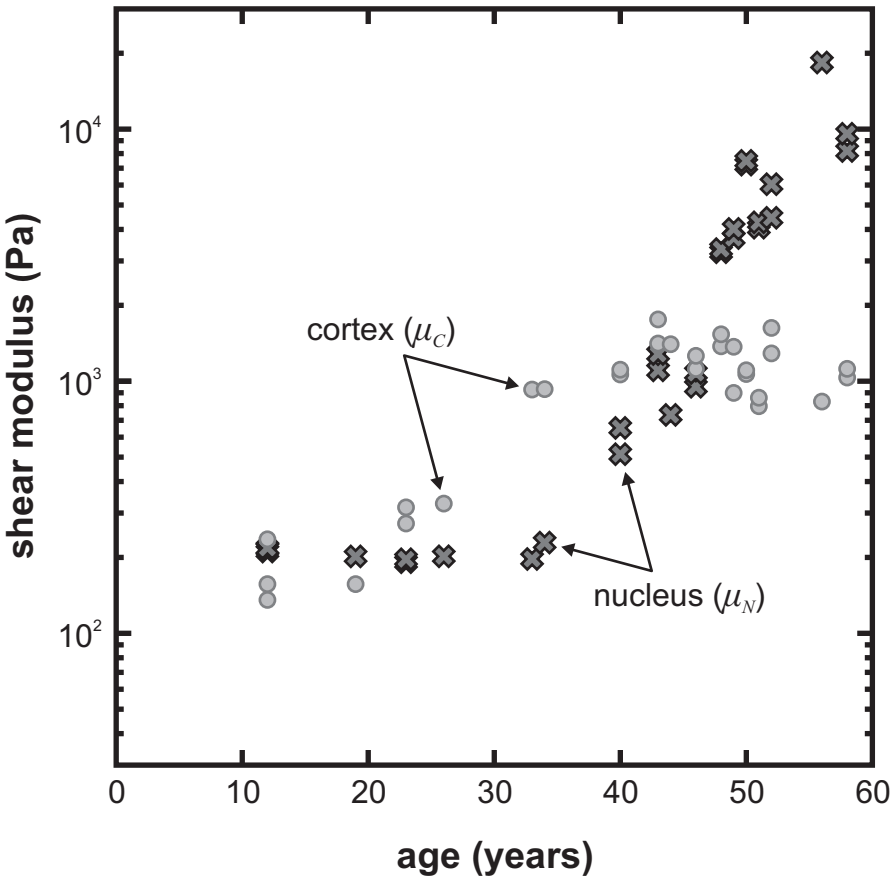

Figure 8.9 *– The model D stiffness parameters for lens set $\mathcal{G}$ using constraint S.*

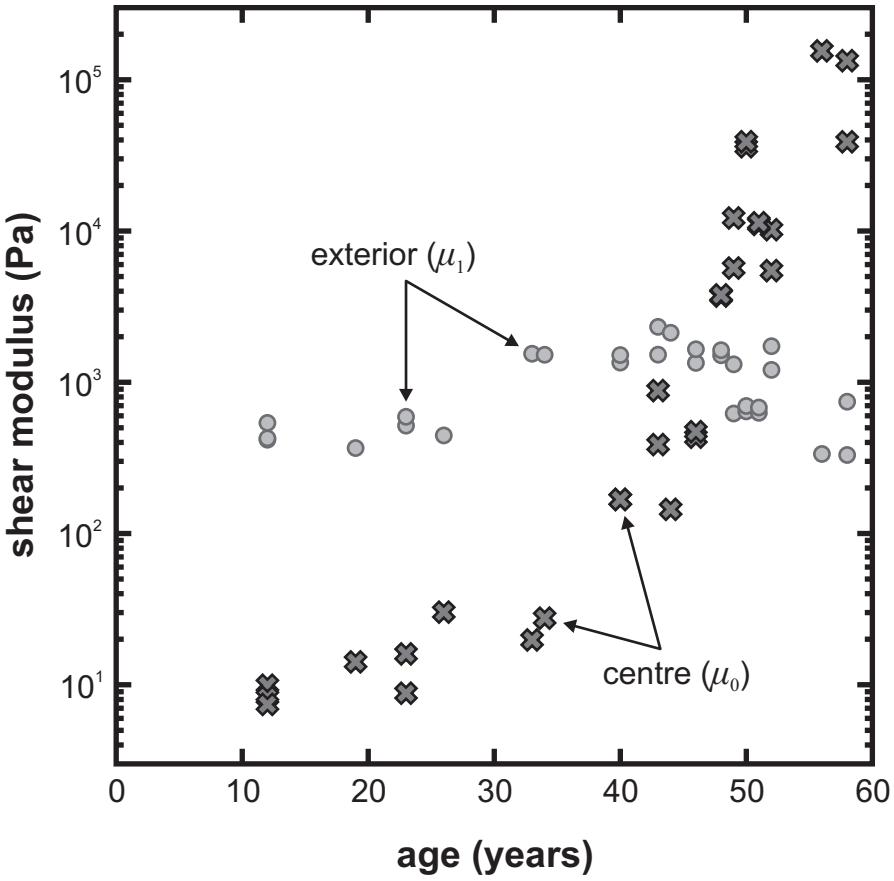

Figure 8.10 – *The model E stiffness parameters for lens set $\mathcal{G}$ using constraint F.*

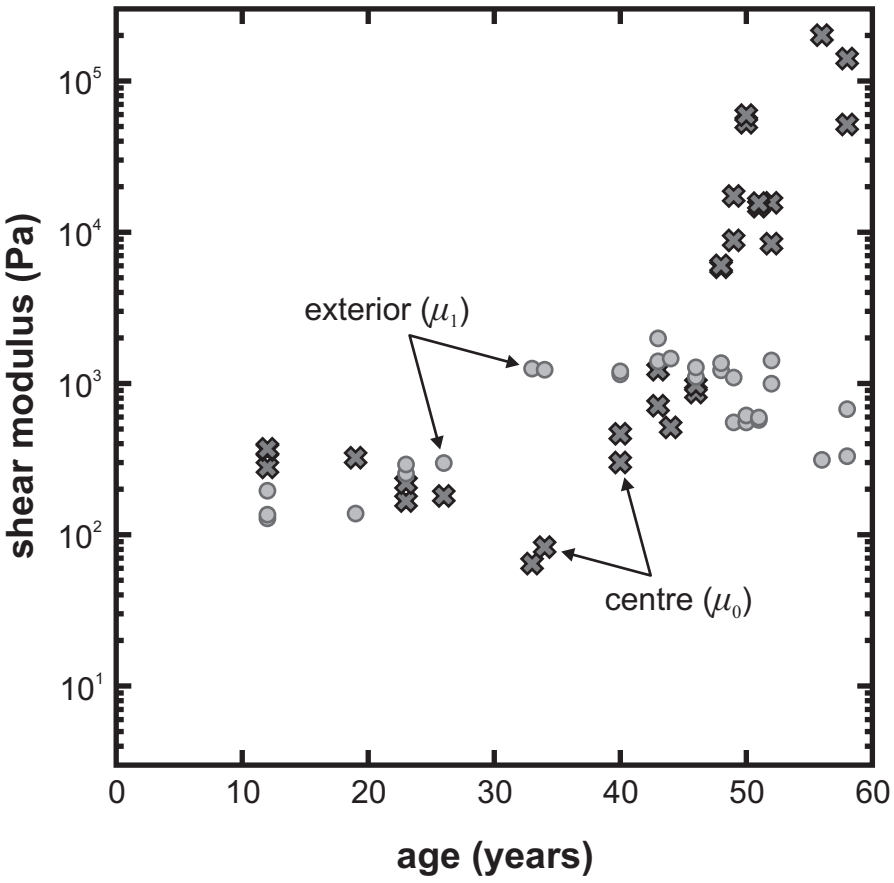

Figure 8.11 – *The model E stiffness parameters for lens set $\mathcal{G}$ using constraint S.*

assessment of how well the experiment was reproduced by each constraint for each lens in the form of the optimum objective function value. If the quantity Q_C is defined as the ratio of the optimal objective function value obtained using constraint S to that obtained using constraint F, then a value of Q_C that is less than one indicates that constraint S provides a better match, while a value greater than one indicates that constraint F provides a better match. This ratio must be treated with caution as it will to some extent correspond to how well the given constraint compensates for other deficiencies within the simulation, which has no bearing on how accurate the constraint and corresponding stiffness values are. It does, however, provide a means of assessing the two support conditions systematically.

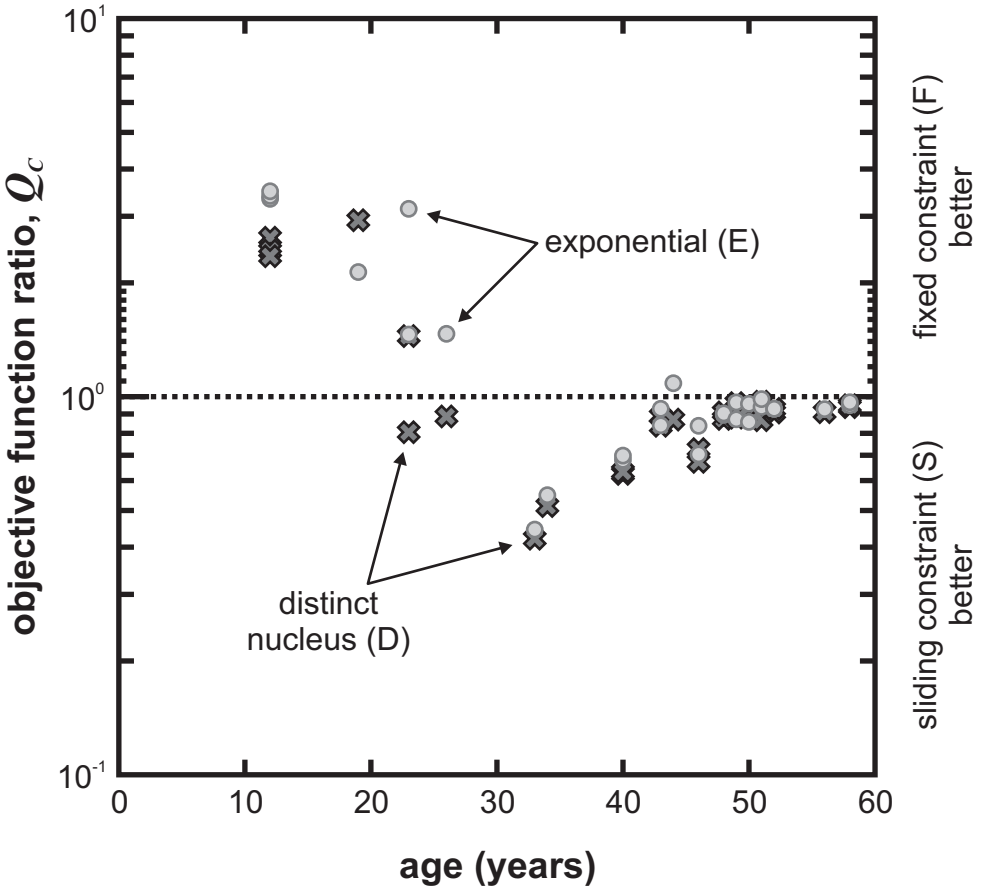

Figure 8.12 – *The ratio, Q_C, of the constraint errors for lenses of set $\mathcal{G}$. The values are the ratio of the optimum objective function value obtained using constraint S to that obtained using constraint F. The results for both model D and model E are included.*

An examination of the objective function values for the two constraints produces a largely consistent outcome: the constraint F provides a better match to the experiment for 12 of the 14 analyses applied to lenses younger than 30 years, while constraint S provides a better

match for 43 of the 44 analyses applied to lenses of 30 years or older. This is illustrated in figure 8.12. It is plausible that the younger, softer lenses would be more constrained by the support ring as they sit lower and deform significantly around the support under the effect of gravity.

The most appropriate conditions at the support probably lie somewhere between the extremes of constraint F and constrain S for each lens, but in the absence of better information it is assumed that the stiffness parameters obtained using the fixed constraint are the most representative for lenses younger than 30 years while the parameters calculated using the sliding constraint are the most representative for lenses of 30 years or older. The combination of using results calculated with constraint F for lenses younger than 30 years and constraint S for lenses of 30 years or older is referred to as using the preferred support constraints. The preferred support constraints are used in section 8.2.4 below when computing age-stiffness relations for a typical lens from the individual measurements. Using the preferred support constraints also avoids the physically unlikely situation that the inner portion of young lenses decreases in stiffness until an age of about 35 years, which is what adopting support constraint S in conjunction with stiffness model E would imply (see figure 8.11).

8.2.3 Comparison of stiffness models

An examination of the stiffness profiles predicted by the three models for three example lenses (figures 8.13, 8.14, and 8.15) shows that stiffness models D and E predict similar stiffness profiles given the constraints of their respective forms, while model H provides a value intermediate between these extremes (rather than, for example, approximating the cortex value of model D).

The largest departure between the heterogeneous stiffness models in these examples is seen in the central region of the 50-year old lens labelled L056B, where model E indicates a value 8 times that of model D. This is an understandable limitation of the spinning lens test. When the centre of the lens is substantially stiffer than the outer region the simulated behaviour of the spinning lens will not depend heavily on the exact stiffness at the centre. Once the deformation at the centre of the lens is small compared to the deformation in the

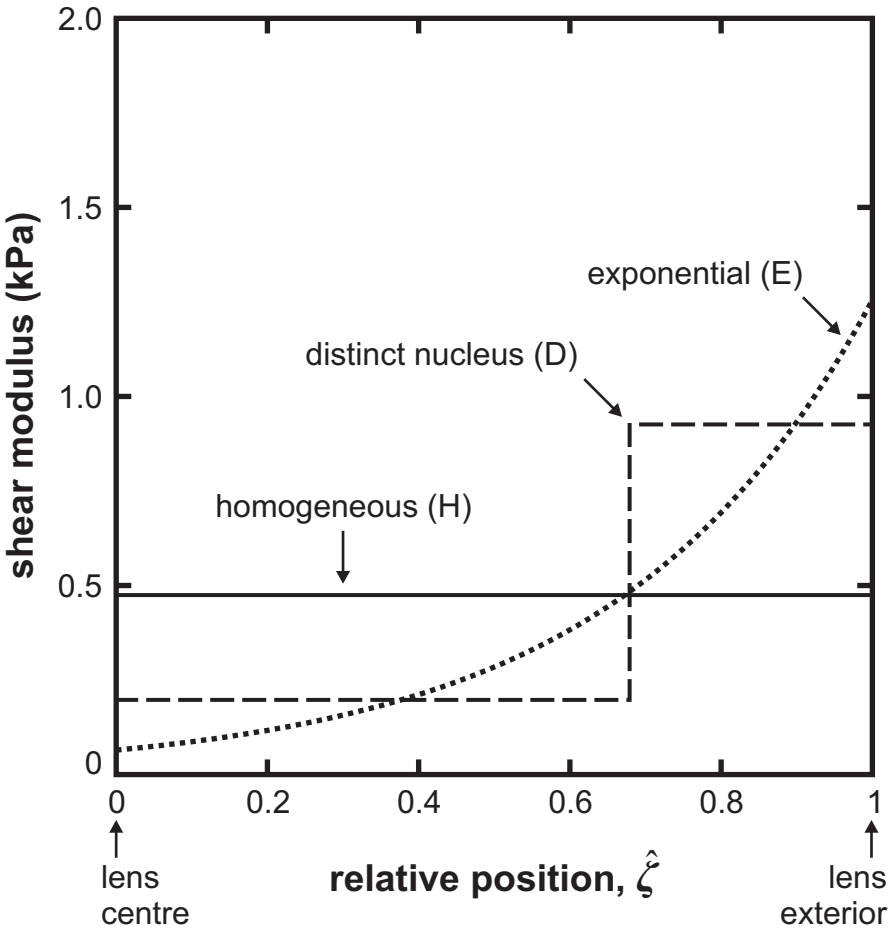

Figure 8.13 – *Three stiffness profiles for a 33-year lens. The profiles were calculated for the lens labelled L038A using constraint S. The step change of model D is at the mean relative position of the transition from the nucleus to the cortex.*

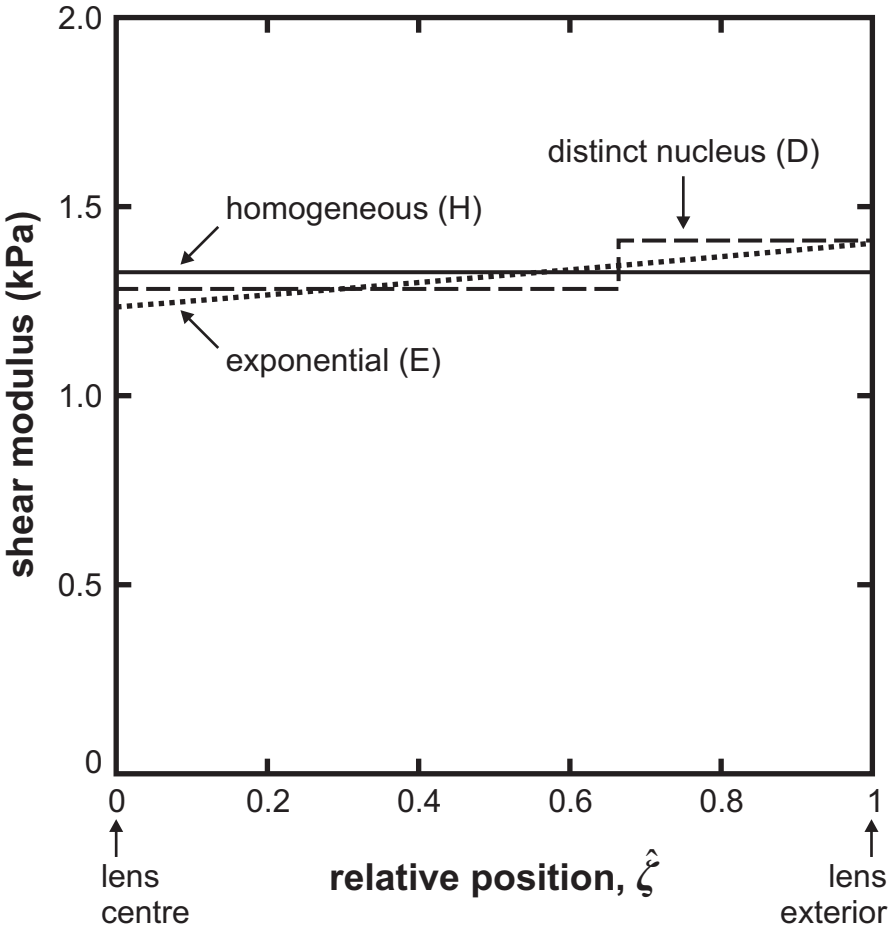

Figure 8.14 – *Three stiffness profiles for a 43-year lens. The profiles were calculated for the lens labelled L039B using constraint S. The step change of model D is at the mean relative position of the transition from the nucleus to the cortex.*

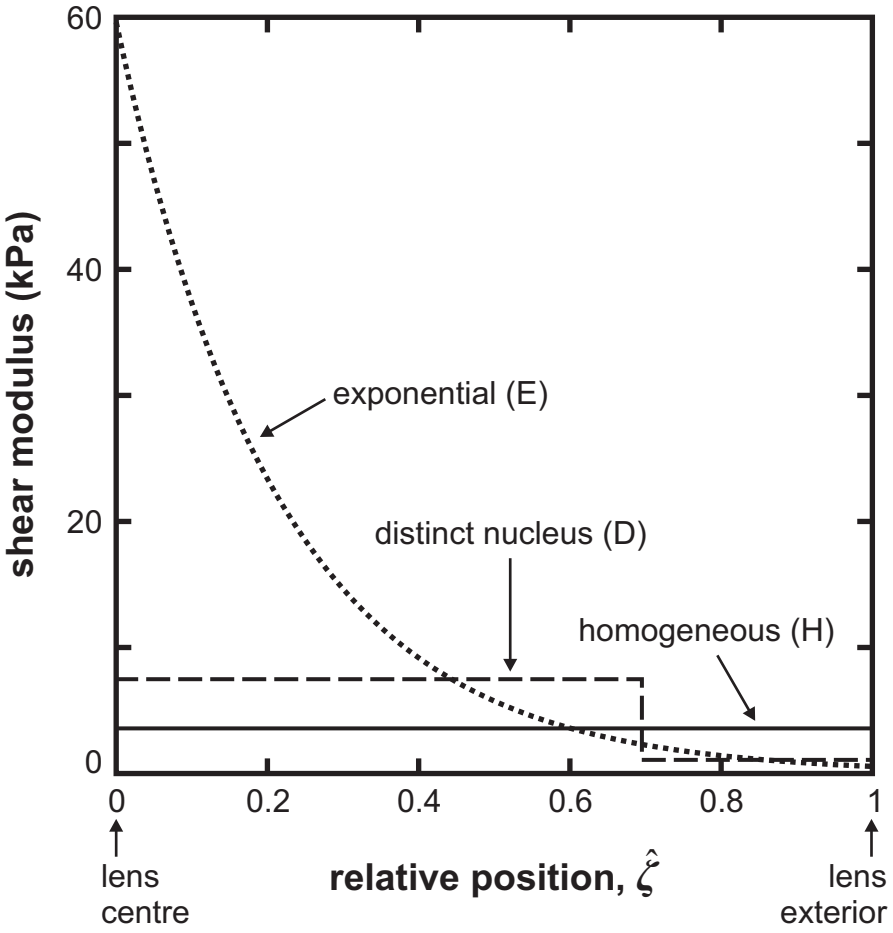

Figure 8.15 – *Three stiffness profiles for a 50-year lens. The profiles were calculated for the lens labelled L056B using the constraint S. The step change of model D is at the mean relative position of the transition from the nucleus to the cortex. The vertical scale differs from figures 8.13 and 8.14 to encompass the much higher stiffness values at the centre of the lens.*

outer region even a large increase in the central stiffness will only have a small effect on the overall deformation. When the optimization process is applied to such a lens it will tend to provide appropriate stiffness values for the outer and intermediate regions of the lens, while the central value will be dictated by the form of the stiffness model. In the case of model E this can produce a central stiffness value much greater than the actual value. If the intermediate region of the lens is substantially stiffer than the outermost region then the exponential function will rise rapidly as the lens centre is approached. Model D is more conservative in that it may also produce an inaccurate central stiffness value when the centre is much stiffer than the cortex, but the value will tend to be within the range of values which are actually present in the lens rather than extrapolating beyond them.

This limitation of the spinning lens test is significant when making use of the stiffness

values directly, such as when making comparisons with values calculated using other tests. However, it is less of a problem when the stiffness values are used for modelling of the whole lens, as in that case the sensitivity of the model results is comparable to the sensitivity of the spinning test.

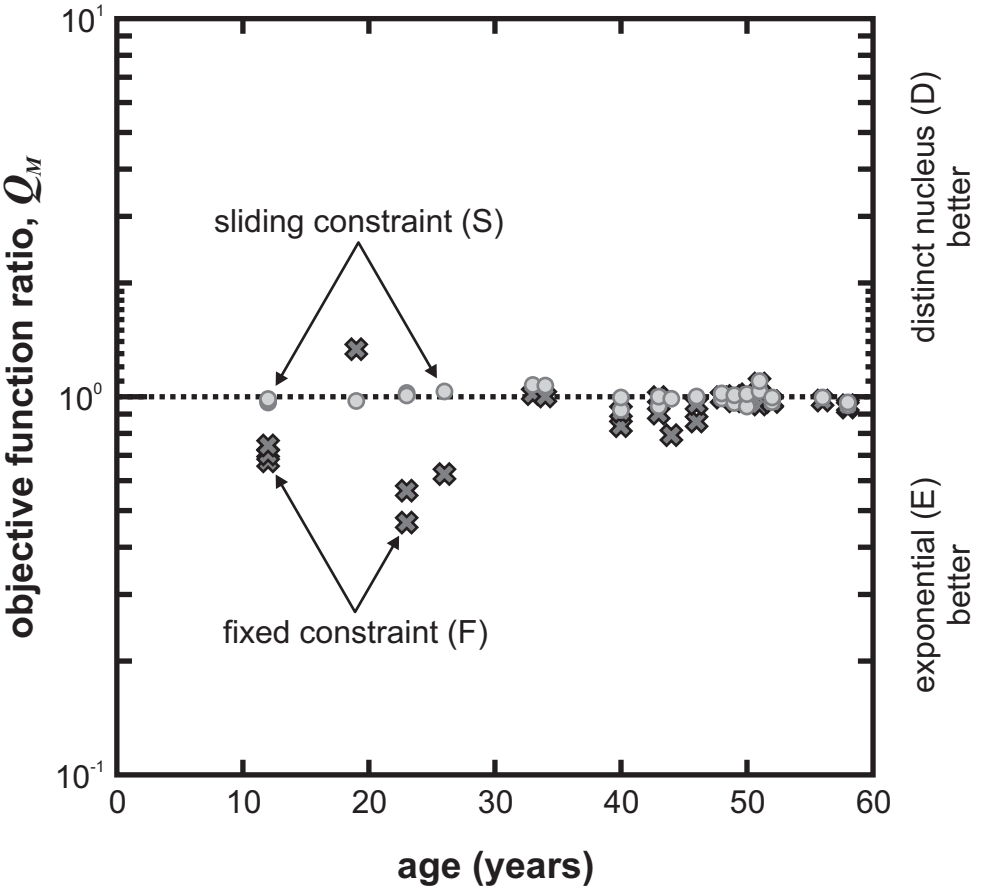

Figure 8.16 – *The ratio, Q_M, of the stiffness model errors for lenses of set $\mathcal{G}$. The values are the ratio of the optimum objective function value obtained using model E to that obtained using model D. The results for both constraint F and constraint S are included.*

The relative performance of the respective stiffness models can be examined in the same manner as the support constraints in section 8.2.2. If the quantity Q_M is defined as the ratio of the optimal objective function value obtained using model E to that obtained using model D, then a value of Q_M that is less than one indicates that model E provides a better match, while a value greater than one indicates that model D provides a better match. As illustrated in figure 8.16, there is no apparent difference in the performance of the two stiffness models when support constraint S is used, but model E generally performs better when constraint F is used. In section 8.2.2 it is concluded that constraint F should be preferred for in the lenses

younger than 30 years while constraint S should be preferred for older lenses. Limiting the consideration to the preferred support constraints indicates that stiffness model E should be preferred for the younger lenses, and both stiffness models are equally good for the older lenses. The generally better performance of model E among the younger lenses is an indication that the form of the nucleus assumed in model D may be inappropriate for these lenses, either because there is not a mechanically distinct nucleus at all, or because its size or shape is incorrect.

8.2.4 Age-stiffness relations for the lens

The relations between age and the parameters of the three stiffness models H, D, and E can be summarized effectively by calculating a function of best fit. Since the parameter values range over several orders of magnitude performing such a fit in log-space is appropriate. Examination of figures 8.6 to 8.11 suggests a linear fit in log-space (equivalent to a weighted exponential fit) would generally provide a poor representation of the stiffness parameters, but that a piecewise linear function with two segments can serve well. Such a function describing a general stiffness parameter μ_x takes the form

$$\log_{10}\mu_x = \begin{cases} b_1\,(A - A_0) + c & A \leq A_0 \\ b_2\,(A - A_0) + c & A > A_0 \end{cases}, \tag{8.7}$$

where A is the age variable and A_0, b_1, b_2 and c are the four function parameters determined by the fitting process. The parameters b_1 and b_2 are the slopes of the two linear segments, A_0 corresponds to the age of transition from one linear segment to the other, and c is the value of $\log_{10}\mu_x$ at this age.

On the basis of the discussion in section 8.2.2, the stiffness parameter values used for each lens in the fitting procedure are composed of those calculated using the fixed support constraint F for lenses younger than 30 years, and those calculated using the sliding support constraint S for lenses of 30 years and older. The MATLAB utility `cftool` was used to calculate the best-fitting parameters and the corresponding 95 % confidence intervals for the fitted function.

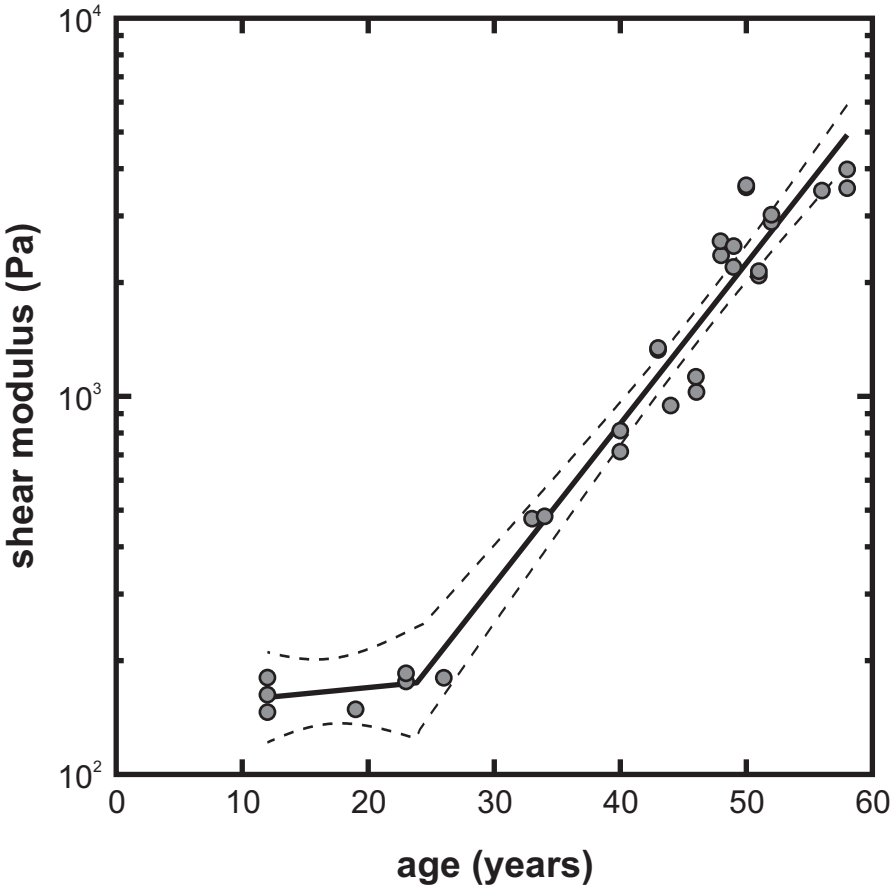

Figure 8.17 – *The age-stiffness relation for model H. A piece-wise linear function is fitted to the shear modulus values calculated for model H using the preferred support constraints of each lens. The dashed lines indicate the 95% confidence bounds for the fitted function calculated by* `cftool`*.*

Table 8.1 – *The parameters of the model H age-stiffness relation. The function parameters of equation 8.7 are calculated for the homogeneous stiffness model (H) with the preferred support constraints. The values are for an age, A, specified in years and the homogeneous shear modulus, μ, specified in pascals. The parameters and 95% confidence intervals are calculated by the* MATLAB *utility* `cftool`*.*

	value	**95% interval**
A_0	23.843	18.7 – 29.0
b_1	0.00322	-0.0139 – 0.0204
b_2	0.04242	0.0367 – 0.0481
c	2.2421	2.08 – 2.40

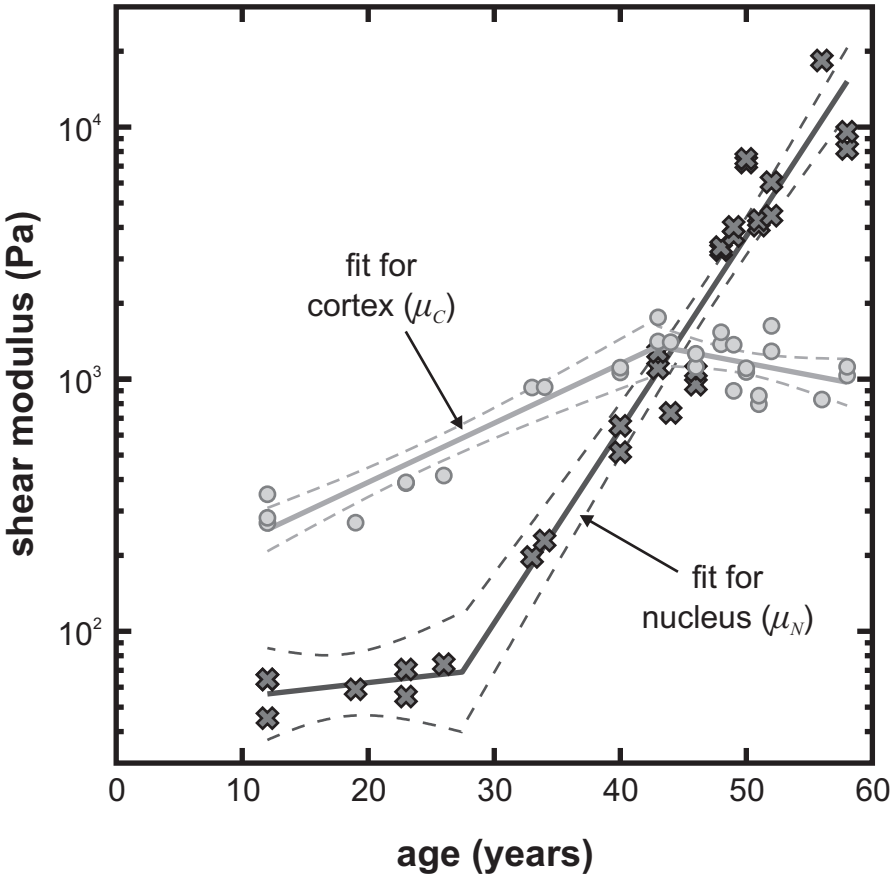

Figure 8.18 – *The age-stiffness relations for model D. Piece-wise linear functions are fitted to the stiffness parameters calculated for model D using the preferred support constraints of each lens. The dashed lines indicate the 95% confidence bounds for the fitted function calculated by* `cftool`*.*

Table 8.2 – *The parameters of the model D age-stiffness relation. The parameters of equation 8.7 are calculated for the distinct nucleus stiffness model (D) with the preferred support constraints. The values are for an age, A, specified in years and stiffness parameters, μ_N and μ_C, specified in pascals. The parameters and 95% confidence intervals are calculated by the* MATLAB *utility* `cftool`*.*

	nucleus (μ_N)		**cortex (μ_C)**	
	value	**95% interval**	**value**	**95% interval**
A_0	27.451	22.9 – 32.0	43.000	39.0 – 47.1
b_1	0.00562	-0.0162 – 0.0275	0.02348	0.0189 – 0.0280
b_2	0.07671	0.0661 – 0.0874	-0.00932	-0.0212 – 0.0026
c	1.8379	1.58 – 2.10	3.1286	3.05 – 3.20

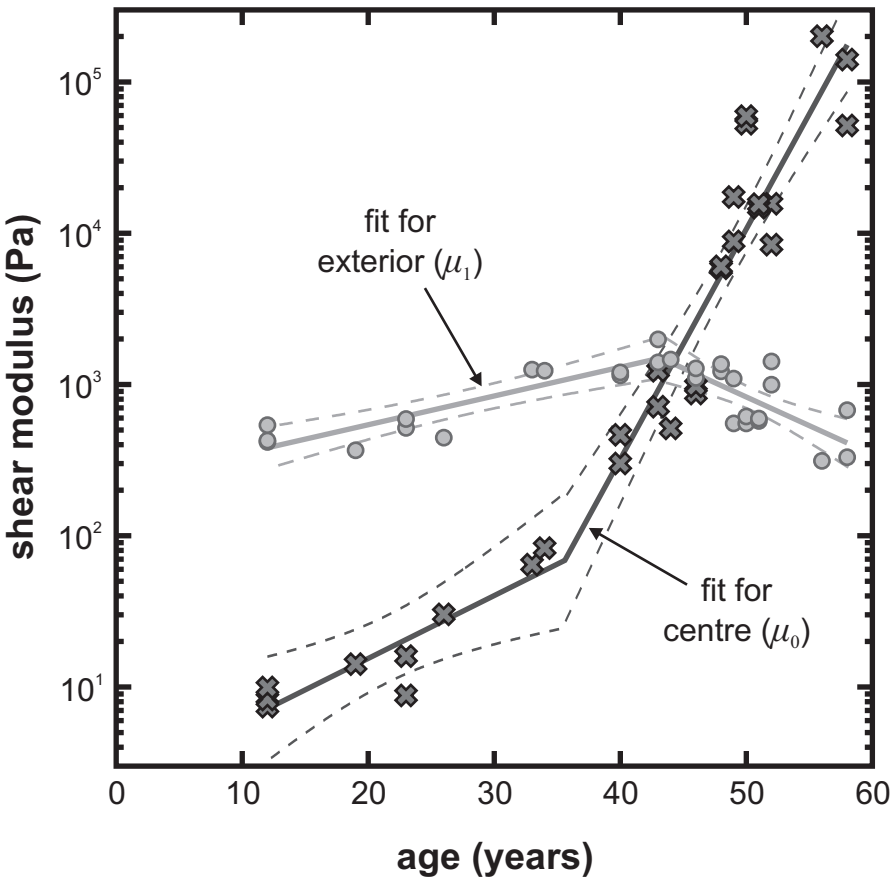

Figure 8.19 – *The age-stiffness relations for model E. Piece-wise linear functions are fitted to the stiffness parameters calculated for model E using the preferred support constraints of each lens. The dashed lines indicate the 95% confidence bounds for the fitted function calculated by* `cftool`*.*

Table 8.3 – *The parameters of the model E age-stiffness relation. The parameters of equation 8.7 are calculated for the exponential stiffness model (E). The values are for an age, A, specified in years and stiffness parameters, μ_0 and μ_1, specified in pascals. The parameters and 95% confidence intervals are calculated by the* MATLAB *utility* `cftool`*.*

	centre (μ_0)		**exterior (μ_1)**	
	value	**95% interval**	**value**	**95% interval**
A_0	35.594	30.1 – 41.1	43.166	39.5 – 46.8
b_1	0.04154	0.0140 – 0.0690	0.01910	0.0120 – 0.0263
b_2	0.15222	0.1228 – 0.1816	-0.03796	-0.0566 – -0.0193
c	1.8357	1.20 – 2.47	3.1772	3.07 – 3.28

The individual shear modulus values for model H and the corresponding age-stiffness relation are plotted in figure 8.17, while the values of the relation parameters and corresponding confidence intervals are presented in table 8.1. Likewise, the model D and model E parameter values and age-stiffness relations are plotted in figures 8.18 and 8.19, while the corresponding relation parameters given in tables 8.2 and 8.3. The age-stiffness relations for model D and model E indicate that younger lenses have a softer inner region than outer region, while for older lenses the reverse is the case. Both age-stiffness fits suggest that this transition occurs at an age of about 44 years.

8.3 The reliability of the measurements

The spinning lens test is a delicate operation on a fragile material and the analysis required to interpret the results is substantial, so the reliability of the measurements is open to question. The most prominent issues are addressed below. The influence of the form of the mesh is examined by comparing the results of more refined meshes. An assessment of the repeatability of the test and a check that the lens substance responds in a roughly linear manner are made by examining some of the tests conducted at speeds other than 1000 rpm. The precision with which the analysis can determine the stiffness parameters is examined for three example lenses with differing stiffness profiles. The influence of any swelling among the lenses is assessed by comparing lenses with a range of aspect ratios. Finally, the possibility that drying of the lens affects its mechanical response is checked by examining the response of three lenses to secondary tests conducted about ten minutes after the main test at 1000 rpm.

8.3.1 Mesh refinement

The form, and particularly the density, of mesh used for a finite element analysis has some effect on the outcome. For accuracy the analysis should be performed with a mesh that is sufficiently dense that further subdivision of the elements will result in no appreciable change. In the current work, extreme accuracy of the finite element analysis is not required as other aspects of the analysis process introduce unavoidable uncertainties. In order to

Table 8.4 – *The results obtained using more refined meshes. A refinement factor of 1 corresponds to the refinement used in the main analysis of the spinning lens test. The analyses were performed for lens L038A using stiffness model D and support constraint F.*

refinement factor	**number of elements**	**max. element edge** (mm)	μ_N (Pa)	μ_C (Pa)
1	1420	0.500	8.89×10^1	9.77×10^2
2	3478	0.250	8.91×10^1	9.78×10^2
3	7697	0.167	8.92×10^1	9.76×10^2

demonstrate that the mesh densities used in the current analysis are sufficiently dense, the analysis of lens L038A using stiffness model D and support constraint F was repeated with more refined meshes. The results are summarized in table 8.4.

The small differences seen in the stiffness parameters calculated using the three meshes examined are less than 0.5 %, so are negligible compared to other sources of uncertainty (for example the precision of the optimization procedure discussed in section 8.3.3 below). Thus the mesh density used in the analysis is adequate for the purpose.

An area of particular concern within the mesh is the equator of the nucleus in model D, as a sharp angle such as this can lead to stress concentration and cause an over-stiff response from the finite element simulation. The very small changes seen in the results when the whole mesh is refined suggest that any inaccuracy of the simulation in this area in the unrefined mesh has little influence on the overall behaviour of the lens.

8.3.2 Analyses at other speeds

In addition to the main tests at 1000 rpm, similar analyses have been performed for additional tests for some lenses from the set $\mathcal{G}$. The majority of the lenses of 40 years or older were tested at 1400 rpm to ensure they experienced large enough deformations for useful analysis (test $\mathrm{B2_{T3}}$ and $\mathrm{B3_{T3}}$ in table 6.3), though in five cases these tests were not conducted. Additionally, the lenses younger than 40 years experience sufficient deformations when spun at 700 rpm to render those tests useful (test $\mathrm{B1_{T1}}$); indeed the large deformations such young lenses experience at 1000 rpm may exaggerate some inaccuracies of the analysis, such as the assumption that the lens behaves as a neo-Hookean material and the selected constraints

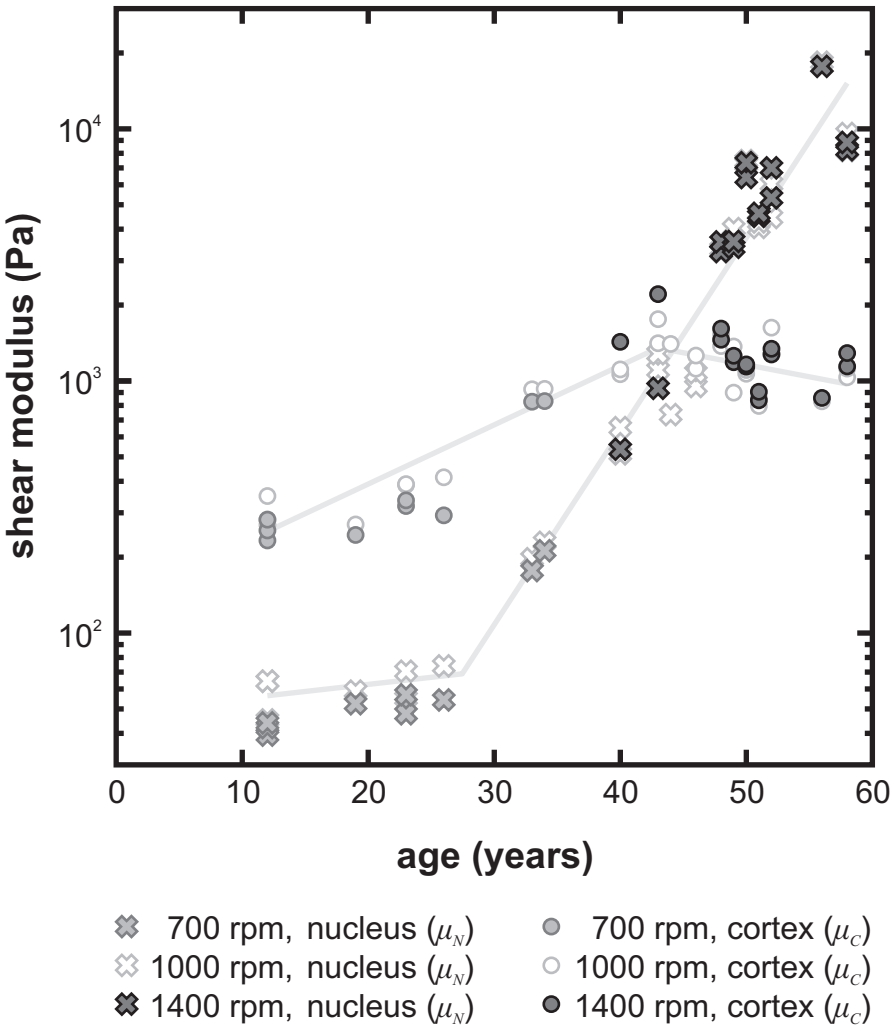

Figure 8.20 – *A comparison of stiffness parameters calculated at different speeds. The parameters are for model D using the preferred support constraint for each lens. Values have been calculated for 9 lenses at 700 rpm (test* B_{T1}*), 29 lenses at 1000 rpm (test* B_{T2}*), and 15 lenses at 1400 rpm (test* B_{T3}*).*

imposed at the contact with the support.

The stiffness parameters obtained from the analysis of these additional tests broadly agree with the parameters obtained from the main test at 1000 rpm, as illustrated in figure 8.20 for stiffness model D. For this analysis the stiffness parameters obtained from the 700 rpm tests are all lower than those from the corresponding 1000 rpm tests, with the value for μ_N being 0.81 of the main result on average, and the value for μ_C being 0.85 of the main result on average. The behaviour at 1400 rpm does not differ from that at 1000 rpm in the same systematic manner. The average value of μ_N at 1400 rpm coincides with that at 1000 rpm and the value for μ_C at 1400 rpm is 1.07 times the value at 1000 rpm on average.

The variation in the calculated stiffness parameters for the tests at different speeds is

relatively small compared to the change in the parameters with age, and even compared to the effect of changing the support constraint used in the analysis. The response of the substance of the older lenses appears to be essentially linear up to 1400 rpm, while the substance of the younger lenses may be displaying a slightly non-linear response, though the form of the experiment does not enable this to be distinguished from a preconditioning effect, as the test at 700 rpm always preceded the test at 1000 rpm.

8.3.3 Precision of the optimization procedure

The optimization procedure provides a precise value for the stiffness parameters which best reproduce the observed behaviour a given lens during testing. Such precision is not actually justified due to the substantial approximations and assumptions incorporated into the simulation of the spinning test. An estimate of all the plausible stiffness parameters implied by the observed behaviour of the lens can be made by examining the form of the objective function in the vicinity of the optimum. The set of points in parameter-space where the objective function is close to the optimal value can be considered plausible since a small improvement in the simulation of the spinning test could alter the objective function enough to make such a point the optimum.

The threshold of the objective function value below which a point can be considered plausible depends on the accuracy of the simulation. This can be approximated by the optimal value: if the simulation closely matches the observed behaviour then it is more likely that it corresponds closely to the experimental situation (though it is always possible that two inaccuracies compensate for each other to some extent). Thus the region of plausible stiffness parameters can be estimated as the region for which the objective function lies between the optimal value and some multiple of the optimal value.

Contours of the objective function in parameter-space are illustrated for the 33-year lens L038A in figure 8.21. The optimal stiffness parameters for this lens using stiffness model D and support constraint S are $\mu_N = 0.19\,\text{kPa}$ and $\mu_C = 0.93\,\text{kPa}$, so the nucleus is considerably softer than the cortex. In these circumstances the stiffness of the nucleus is not tightly constrained by the spinning lens test. If an objective function value of 1.2 times the optimum

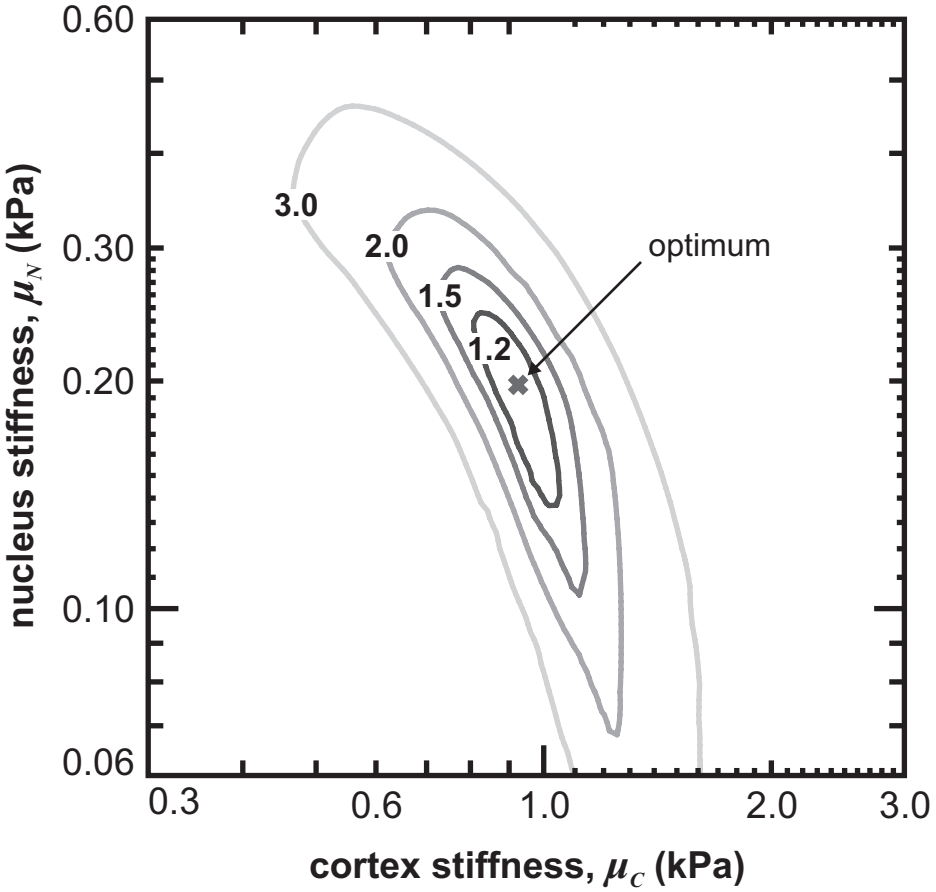

Figure 8.21 – *Contours of the objective function for a 33-year lens. The contours were calculated for the lens labelled L038A, analysed using model D and constraint S. The contour values are relative to the optimum value of the objective function (*Q_A*= 0.059 mm*^{2}*;* $\hat{Q}_A$ *= 0.075).*

is taken to delineate the region of plausible stiffness values, then μ_N can be assumed to lie between 0.13 and 0.24 kPa, about a two-fold range (see figure 8.21). For a given nucleus stiffness, the optimal cortex stiffness varies somewhat, with an increase in μ_N being compensated for by a slight decrease in μ_C and *vice versa*. Using the same objective function contour as for the nucleus, μ_C should lie between 0.8 and 1.1 kPa, a considerably tighter interval.

The 43-year lens labelled L039B has a substantially poorer optimum objective function value than L038A when analysed using the stiffness model D and support constraint S, leading to a considerably larger region within which the objective function is below 1.2 times the optimum, as depicted in figure 8.22. The calculated stiffness parameters of this lens are $\mu_N = 1.28$ kPa and $\mu_C = 1.41$ kPa, so it is roughly homogeneous. For such a lens the stiffness of the nucleus is somewhat more constrained by the spinning test than the cortex. In this case

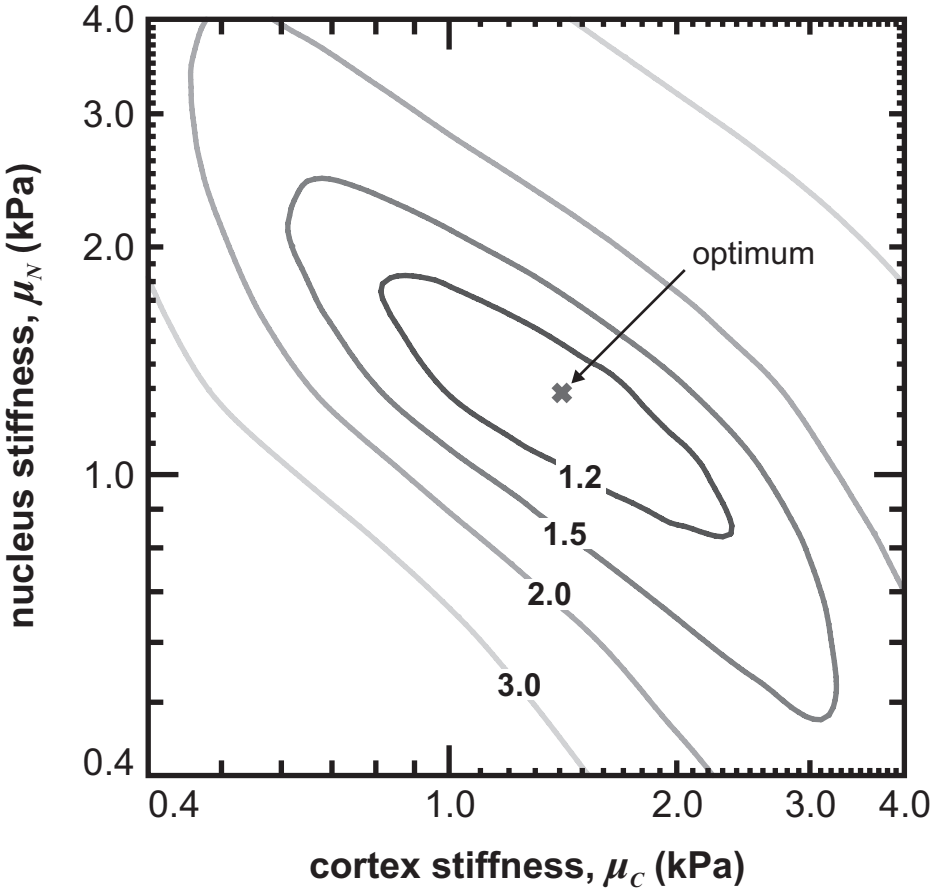

Figure 8.22 – *Contours of the objective function for a 43-year lens. The contours were calculated for the lens labelled L039B, analysed using model D and constraint S. The contour values are relative to the optimum value of the objective function (*Q_A*= 0.060 mm*^{2}*;* $\hat{Q}_A$ *= 0.186).*

μ_N can be assumed to lie between 0.80 and 1.9 kPa, while μ_C can be assumed to lie between 0.8 and 2.4 kPa.

When the nucleus is considerably stiffer than the cortex the spinning lens test once again provides less constraint on the former value than on the latter, as can be seen in the case of the 50-year lens labelled L056B in figure 8.23. This lens has stiffness parameters of $\mu_N = 7.48$ kPa and $\mu_C = 1.07$ kPa calculated using stiffness D and support constraint S. For this lens the region within 1.2 times the optimum objective function value gives a range for μ_N from 6 to 9 kPa, and a range for μ_C from 0.9 and 1.2 kPa.

As can be seen in the above examples, the spinning lens test is not sufficient to tightly constrain the parameters of a heterogeneous stiffness model. Fortunately the parameters change sufficiently with age that the the trend can be discerned despite the likelihood that individual measurements are somewhat scattered. A more problematic aspect of the loose

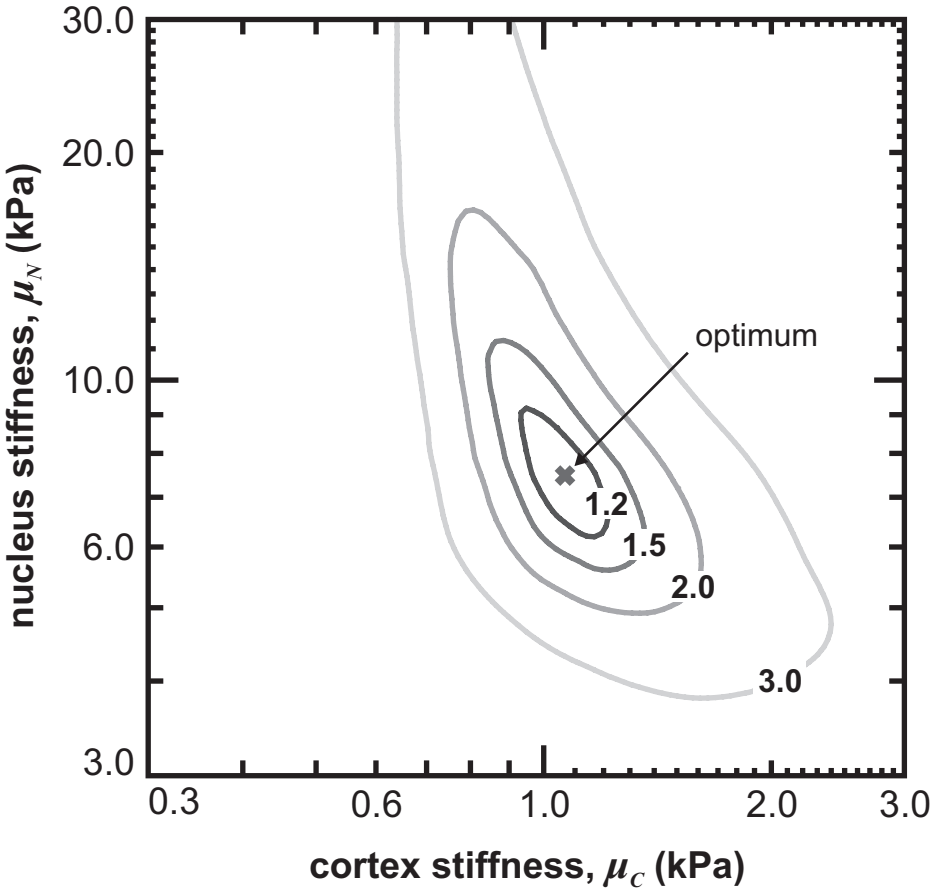

Figure 8.23 – *Contours of the objective function for a 50-year lens. The contours were calculated for the lens labelled L056B, analysed using model D and constraint S. The contour values are relative to the optimum value of the objective function (*Q_A*= 0.011 mm*^{2}*;* $\hat{Q}_A$ *= 0.104).*

constraints is that a modest change in the model used to simulate the test can lead to a large relative change in the calculated stiffness profile, as seen with the younger lenses when subjected to different support constraints (see section 8.2.2).

8.3.4 Swelling of the lenses

It is possible that some of the lenses included in the main lens set $\mathcal{G}$ have altered mechanical properties due to the absorption of fluid. The aspect ratio, α, of lenses tends to decrease when they swell (see section 8.1.1), so this can be used as a proxy for swelling. If fluid is absorbed by the lens substance it is likely to first be apparent in the cortex, so the parameter μ_C calculated for stiffness model D is the mechanical property of greatest concern. Both the aspect ratio and μ_C have a positive correlation with age for the lenses of set $\mathcal{G}$, so identifying any separate contribution from swelling is problematic.

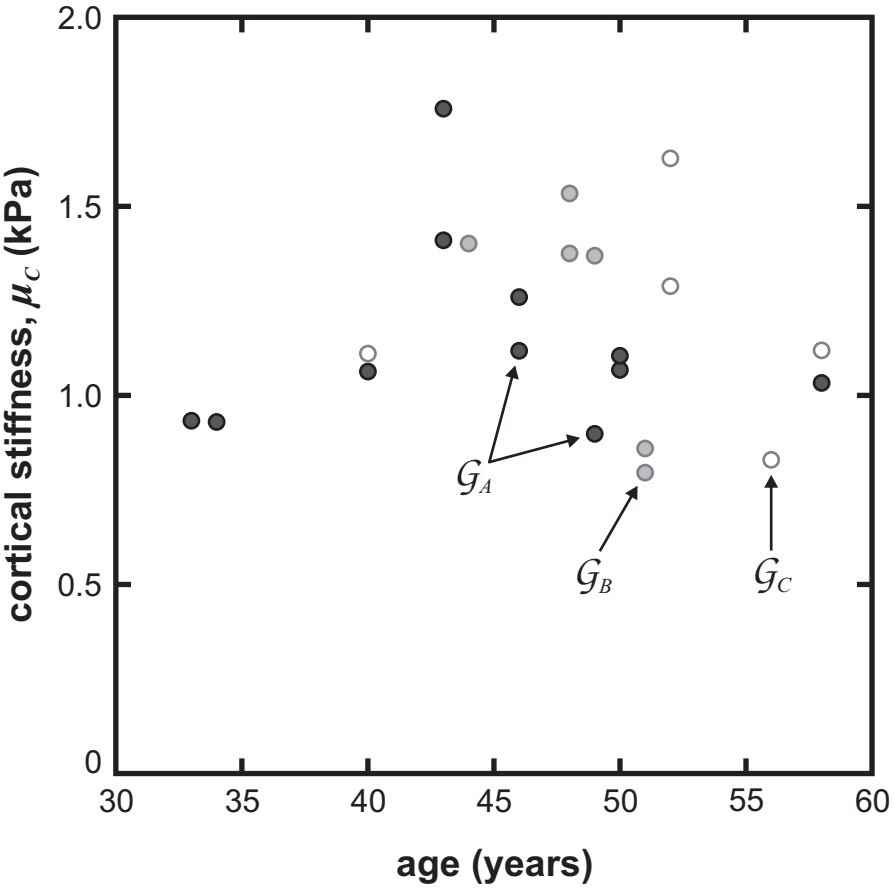

Figure 8.24 – *An examination of lens swelling. The cortical stiffness, μ_C, (calculated for model D using constraint S) is plotted for lenses older than 30 years, grouped by aspect ratio, α. Only lenses older than 30 years are included. The lenses of $\mathcal{G}_A$ satisfy $\alpha \geq 2.2$, those of $\mathcal{G}_B$ satisfy $2.1 \leq \alpha < 2.2$, and those of $\mathcal{G}_C$ satisfy $\alpha < 2.1$.*

The lenses for which $\alpha \geq 2.2$ are assumed to be unaffected by swelling as they are well within the expected range for unswollen lenses. These lenses are grouped together as a subset, $\mathcal{G}_A$. The 11 lenses of subset $\mathcal{G}_A$ are aged between 33 and 58 years, so are best compared with other lenses in this age range (no lens in set $\mathcal{G}$ is aged over 58 years). The 11 lenses aged 33 years or more which are not in $\mathcal{G}_A$ are assigned to two further subsets, $\mathcal{G}_B$ consisting of the 6 lenses for which $2.1 \leq \alpha < 2.2$, and $\mathcal{G}_C$ consisting of the 5 lenses for which $\alpha < 2.1$, which are the lenses most likely to be affected by swelling. There is no evident distinction in the cortical stiffness of the lenses in these three subsets as illustrated in figure 8.24. This suggests that any influence of swelling on the mechanical response of these older lenses is small compared to the variability in the measurement between individual specimens.

A similar examination of the seven lenses younger than 33 years is not informative as

Table 8.5 – *An examination of lens drying. The stiffness parameters for model D using constraint S are calculated from two tests on each of the example lenses. The comparison test is the first on the decapsulated lens at the same speed as the final test (see tables 6.3 and 6.4).*

		comparison test				final test			
lens	**age** (years)	**test**	μ_N (kPa)	μ_C (kPa)	**time** (min)	**test**	μ_N (kPa)	μ_C (kPa)	**time** (min)
L038A	33	$B1_{T2}$	0.19	0.93	8	$C1_{T4}$	0.21	1.00	19
L039B	43	$B1_{T2}$	1.28	1.41	8	$C1_{T4}$	1.27	1.57	20
L056B	50	$B2_{T3}$	7.35	1.16	9	$C2_{T4}$	7.06	1.27	18

the aspect ratio of these lenses is more variable, both with age and due to the softness of the lenses. It is therefore not possible to identify any younger lenses which are clearly not swollen to provide a comparison. This unfortunately leaves unanswered the question of whether some or all of the younger lenses are affected by swelling.

8.3.5 Drying of the lens

Despite the measures taken to limit drying of the lens during the test it may have some effect on the stiffness measurement. The final test performed on the decapsulated lens (C_{T4} in table 6.4) provides a means of assessing the effect of drying to some extent, as it is generally performed after the lens has been exposed to the air for about twice as long as the main test (B_{T2}). The stiffness parameters obtained from the final tests for lenses L038A, L039B, and L056B are presented in table 8.5, along with the parameters obtained from the first test conducted at the same speed (1000 rpm for lenses L038A and L039B, and 1400 rpm for lens L056B).

It can be anticipated that drying will tend to increase the stiffness of the exterior of the lens. This is indeed reflected in the stiffness parameters obtained for the example lenses where the cortex is about 1.09 times stiffer in the final test than in the comparison test at the same speed. The difference cannot be unambiguously attributed to the drying of the lens since the unrecovered deformation seen in figures 8.2, 8.3, and 8.4, or preconditioning effects may also play a role in the changing response of the lenses. It does, however, suggest that drying has at most a modest effect on the stiffness parameters obtained from the main

tests when compared to the substantial variation seen between lenses.

8.4 Comparisons with published measurements

The relationships presented in section 8.2.4 provide three descriptions how the stiffness of a typical lens changes with age: the model H age-stiffness relation based on the homogeneous model of the lens, the model D age-stiffness relation based on the distinct nucleus model, and the model E age-stiffness relation based on the exponential stiffness model. These can be compared to the results reported by Fisher (1971), Heys et al. (2004), Heys et al. (2007), and Weeber et al. (2007), with the choice of model for comparison depending on the form of the reported data.

Two main factors complicate comparisons between the tests. First, the comparisons depend on the accuracy of the constitutive model adopted for the lens substance, as this is used to relate the different sorts of measurements to common mechanical parameters. Second, the description of the heterogeneity of the lens differs between the tests, requiring selection of appropriate values for comparison. The spinning lens test is suited to characterizing the response of the whole lens rather than the stiffness at particular points, so these values will only broadly follow the locally measured stiffness values.

8.4.1 Comparison with Fisher (1971)

In the original spinning lens test of Fisher (1971) the lens is assumed to consist of a nucleus and cortex as in the current model D. However, the nucleus is simplified to a sphere by Fisher (1971), unlike the more realistic shape employed in model D. Figure 8.25 provides a comparison of the stiffness values reported for the nucleus and cortex by Fisher (1971) with those obtained from the model D age-stiffness relation (see figure 8.18 and table 8.2).

The general forms of the curves are similar: the stiffness of the nucleus changes little up to 30 years then increases substantially, while the increase in the stiffness of the cortex is greater in the earlier period and levels off or declines slightly from 40 years. However, the magnitude of the changes, especially in the nucleus, are much greater in the model D relation.

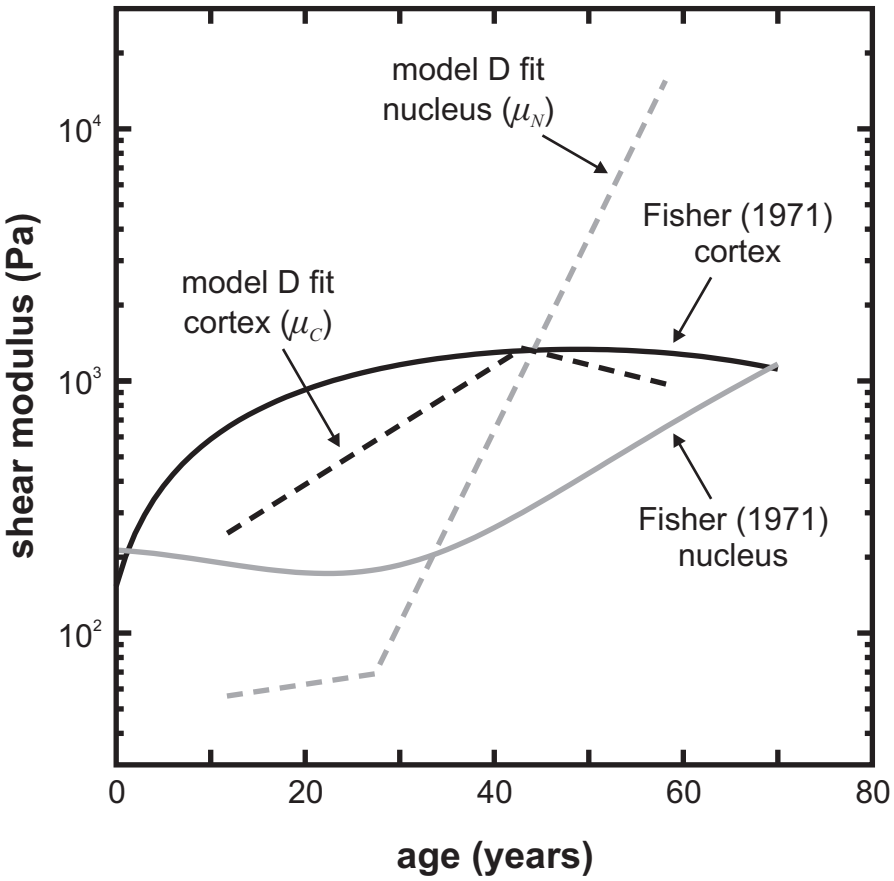

Figure 8.25 – *A comparison with the stiffness values of Fisher (1971). The model D age-stiffness relations (dashed lines) are compared to the age-stiffness relations for the nucleus and the cortex reported by Fisher (1971) (solid curves). The latter curves have been translated from Young's modulus to shear modulus assuming incompressibility and plotted on a $\log_{10}$ scale.*

The relative stiffness of the two components is also substantially different, with the model D relation suggesting that the nucleus becomes stiffer than the cortex after 44 years (during the development of presbyopia), rather that at 70 years (well after presbyopia is established).

The lower stiffness in younger lenses seen in the model D relation could be anticipated given that the analysis used by Fisher (1971) did not incorporate the restrictions on the deformation of the lens imposed by the lens capsule and the lens support. Such restrictions will naturally have a greater influence on the value of the stiffness calculated for softer young lenses. Additionally, the more dramatic changes calculated for the nucleus in the current work can be explained in part by the different choice of nucleus shape. Fisher (1971) approximated the nucleus by a sphere occupying the full height of the lens so a smaller increase in stiffness with age will have a greater influence on the deformation towards the poles of

the lens than the less extensive nucleus of model D. There are of course a number of other differences which must also influence the alternate stiffness values to some extent, though not in such an obvious way (see chapter 4 and Burd et al., 2006).

8.4.2 Comparison with Heys et al. (2004) and Heys et al. (2007)

Heys et al. (2004) obtained stiffness measurements by applying an indentation test at several locations across each lens. The published age-stiffness relations are apparently derived from measurements at two locations: points 0.5 mm from the lens axis, here labelled point H1, and points 3.5 mm from the lens axis, here labelled point H2. Further stiffness values from point H1 are reported for individual lenses by Heys et al. (2007), but not combined into an age-stiffness relation.

A comparison can be made between the indentation measurements at point H1 and H2 and the corresponding stiffness values from the age-stiffness relations calculated for model D and model E. In reality the indentation results depend to a degree on the stiffness of the material in the whole volume deformed during the test; however, for simplicity it is assumed that the value at a fixed point within this volume is representative. The indentation probe had a diameter of 0.4 mm and this was inserted a typical distance of 0.75 mm into the substance during the measurement. Thus the centre of the deformed volume, and therefore points H1 and H2, all lie some way below the lens equator. For ease of comparison with model E, points H1 and H2 are assumed to lie on the plane passing through the midpoint of the lens (according to values given by Rosen et al., 2006 this plane generally lies about 0.4 mm below the equatorial plane for an isolated lens, so this is a reasonable approximation).

For model D, point H1 corresponds to the nucleus region while point H2 corresponds to the cortex region, though it lies very close to the border with the nucleus. For model E, it is necessary to determine the relative distance, λ, from the lens midpoint to the measurement points. Rosen et al. (2006) report a linear relation for the equatorial diameter of isolated lenses:

$$D = 8.7 + 0.0138A \quad , \tag{8.8}$$

where A is the age of the lens in years and D is the diameter in millimetres. It is assumed

that this is also a reasonable approximation for the diameter of the lens in the plane passing through the midpoint since the diameter does not vary rapidly in this region. On this basis, the relative distances for points H1 and H2 are taken to be

$$\hat{\zeta}_{H1} = \frac{1}{D} \quad \text{and} \quad \hat{\zeta}_{H2} = \frac{7}{D} \quad , \tag{8.9}$$

where D is given by equation 8.8.

The various values for the stiffness at point H1 are presented in figure 8.26. The model D age-stiffness relation agrees reasonably well with the relation given by Heys et al. (2004), with the former being on average 1.4 times stiffer. The model E fit gives a more rapid increase in stiffness with age at point H1 than the other relations. It suggests lenses aged around 20 years are about half the stiffness indicated by the relation reported by Heys et al. (2004), and that lenses aged around 50 years are about three times stiffer. As discussed in section 8.2.3, the stiffness values implied by model E near the centre of older lenses are not reliable since the spinning lens test is not sensitive to the value once the inner region becomes much stiffer than the outer region.

The stiffness values reported by Heys et al. (2007) for lenses younger than about 35 years are considerably greater than the values from either Heys et al. (2004) or the current age-stiffness relations. The principal difference reported between Heys et al. (2004) and Heys et al. (2007) is that the former tested lenses previously frozen at $-70\,^{\circ}\mathrm{C}$, while the latter tested fresh lenses. The current spinning test also uses fresh lenses so this factor does not explain the substantial difference seen between the current measurements and those of Heys et al. (2007) in figure 8.26. Interestingly, the stiffness values reported by Heys et al. (2007) for point H1 (close to the centre of the lens) in these younger lenses are similar to the cortical stiffness values, μ_C, of the model D age-stiffness relation. This may be an indication that for lenses with a very soft interior the testing of Heys et al. (2007) was somehow influenced more by the stiffness of the outer region of the lens than by the inner region. The indentation procedure used by both Heys et al. (2004) and Heys et al. (2007) is force controlled, so the full indentation distance in lenses with a soft inner region would be considerably greater than the reported typical value of 0.75 mm, and possibly enough that the outer region of the lens had a substantial effect. This does not explain why the same effect is not seen in Heys et al.

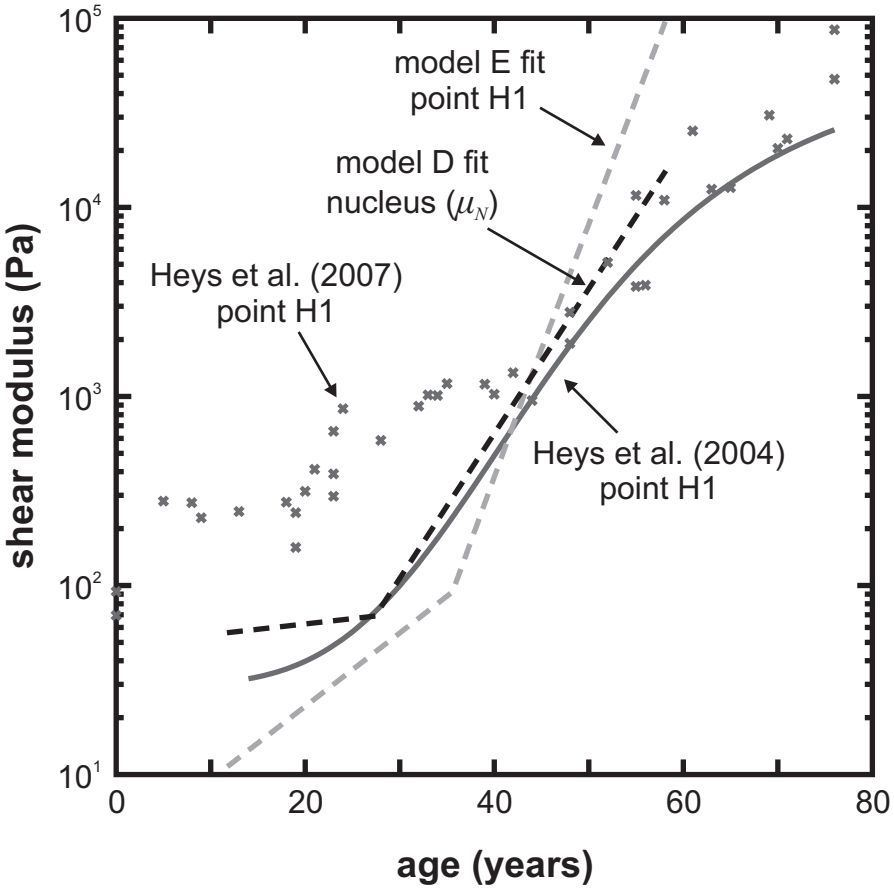

Figure 8.26 *– A comparison with the inner stiffness values from Heys et al. (2004) and Heys et al. (2007). The values of the model D and E age-stiffness relations at point H1 (dashed lines) are compared to a corresponding relation reported by Heys et al. (2004) (solid line) and measurements reported by Heys et al. (2007) (crosses).*

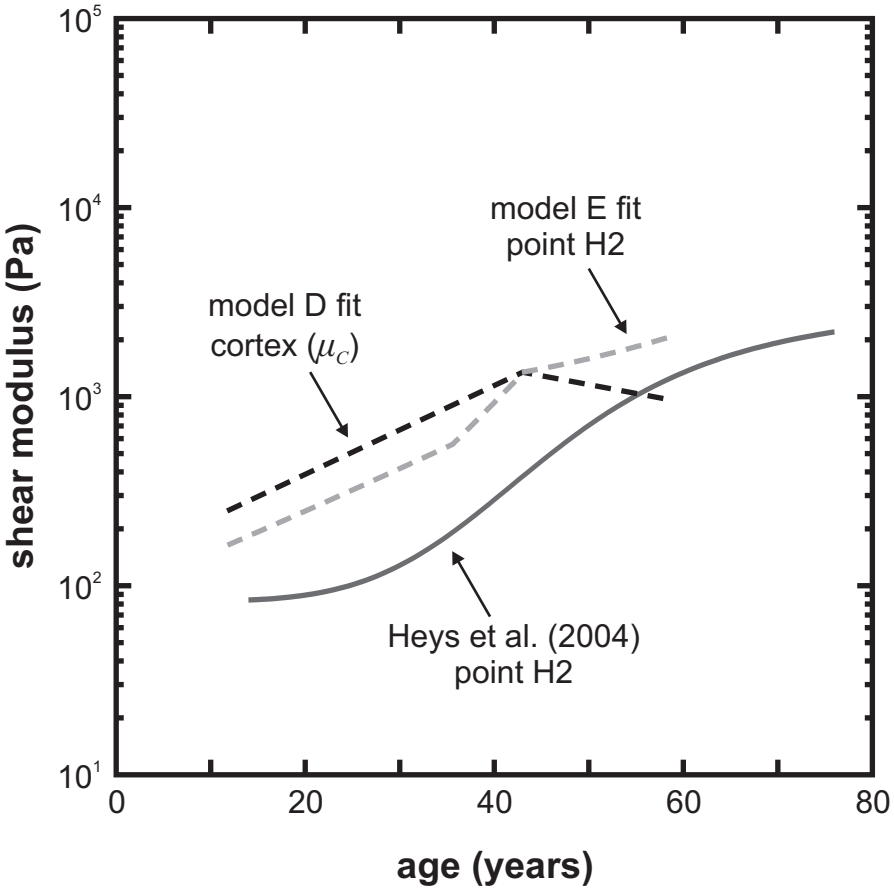

Figure 8.27 *– A comparison with the outer stiffness values from Heys et al. (2004). The values of the model D and E age-stiffness relations at point H2 (dashed lines) are compared to a corresponding relation reported by Heys et al. (2004) (solid line).*

(2004).

Both the model D and model E age-stiffness relations suggest considerably higher stiffness values at point H2 than the relation reported by Heys et al. (2004), as shown in figure 8.27. The model D fit suggests lenses aged up to 45 years are about four times stiffer at point H2 than the Heys et al. (2004) relation, while the model E fit suggests they are about three times stiffer. The discrepancy diminishes for older, stiffer lenses. A possible cause of the disagreement lies in the the analysis of the indentation test which ignores proximity of the boundary of the sample (see section 2.1.4). The analysis of the spinning lens test also entails considerable uncertainty in the appropriate stiffness values for young lenses due to the contact with the support (see section 8.2.2). However, the variation in the stiffness values calculated at point H2 using the two support constraints is modest; most of this uncertainty relates to the stiffness calculated towards the centre of the lens.

8.4.3 Comparison with Weeber et al. (2007)

Weeber et al. (2007) provide a description of the stiffness profile from the axis of the lens to 4 mm and for ages from 20 to 70 years calculated by fitting a surface to the individual stiffness measurements from 10 lenses (see section 2.1.5). The profile for a given age can be compared to the corresponding stiffness profiles obtained from the model D and model E age-stiffness relations. The lenses tested by Weeber et al. (2007) were sectioned at the equatorial plane. At each test point the probe was inserted 0.5 mm into the lens substance before performing the oscillatory test so, just as for Heys et al. (2004), the stiffness values correspond to a point posterior of the equatorial plane. It is assumed for the purposes of comparison that the measurements reported by Weeber et al. (2007) correspond to points located on the plane through the midpoint of the lens, as discussed in section 8.4.2. For model D the transition from the nucleus to the cortex is calculated to occur at a radius of 3.10 mm in this plane. Consistent with section 8.4.2, the relative position for a given location in this plane is taken to be

$$\hat{\zeta} = \frac{2r}{D} \quad , \tag{8.10}$$

where r is the distance from the lens axis and D is the age-varying diameter given by equa-

tion 8.8.

Within the limitations of the respective representations the stiffness profiles reported by Weeber et al. (2007) and the current age-stiffness relations are broadly similar at least for the inner region of the lens, as shown in figures 8.28 and 8.29.

The stiffness of the nucleus of model D lies within (or at 50 years close to) the range covered by the corresponding portion of the profile for the same age from Weeber et al. (2007). The same is not true for the cortex, where at several ages the model D stiffness is well outside the range covered by the whole indentation profile of the same age. The stiffness of the cortex region of model D shows a far smaller increase with age than the indentation tests, largely due to the slight decline in stiffness after 43 years in the former. The discrepancy between the profiles towards the outside of the lens may reflect uncertainty in the behaviour at the interface between the lens and its holder when performing indentation, although unlike Heys et al. (2004) a trephine was not employed and the effect of the lens shape was included in the analysis of Weeber et al. (2007).

In the interior of younger lenses, the form of model E allows closer agreement with the profiles of Weeber et al. (2007) than the form of model D. If the stiffness of the inner region of the lens is well represented by the indentation profiles then the capacity of model E to more closely match that form provides an explanation for its better performance at matching the experimental results of the spinning lens test for lenses younger than 30 years, as seen in section 8.2.3. In the interior of the older lenses, model E departs more dramatically from the indentation profiles than model D in a similar manner to the comparison with Heys et al. (2004) at point H1 discussed in section 8.4.2. In the outer region of the lens the difference between the indentation profiles and model E is similar to the difference seen in the cortex for model D, with the results from the spinning test showing considerably smaller variation with age, especially for older lenses.

8.4.4 Summary of comparisons

The stiffness values calculated for the inner region of the lens using both model D and model E bear more similarity to the results reported for the indentation tests of Heys et al.

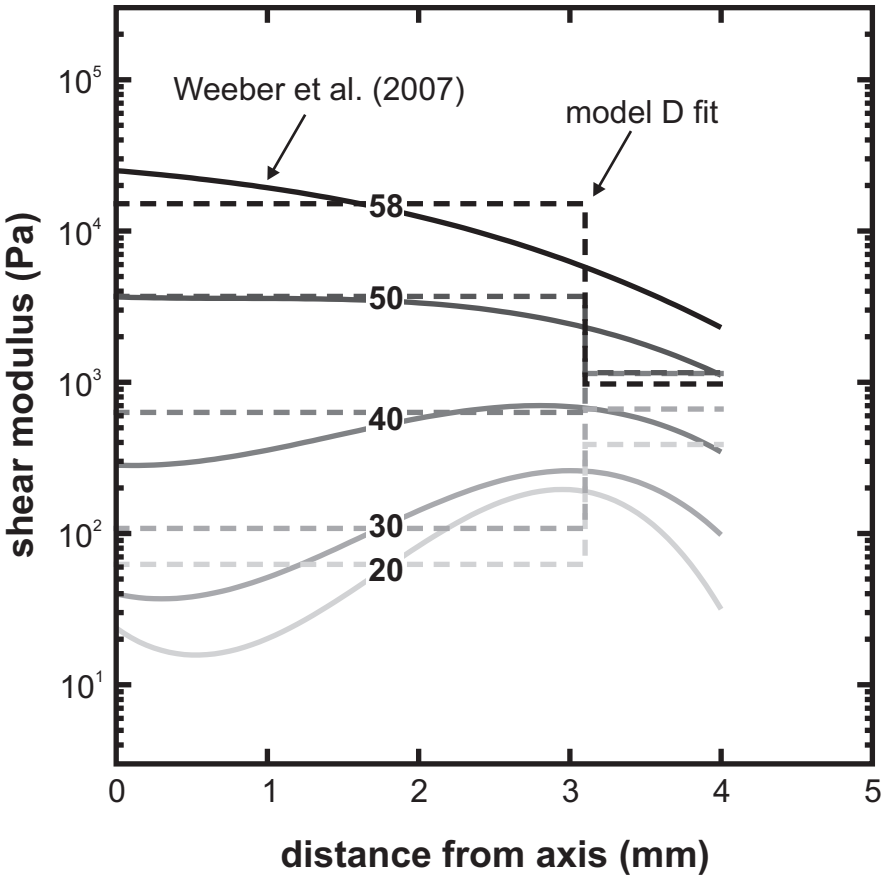

Figure 8.28 *– A comparison between the profiles from the model D age-stiffness relation (dashed lines) and equivalent profiles from Weeber et al. (2007) (solid curves).*

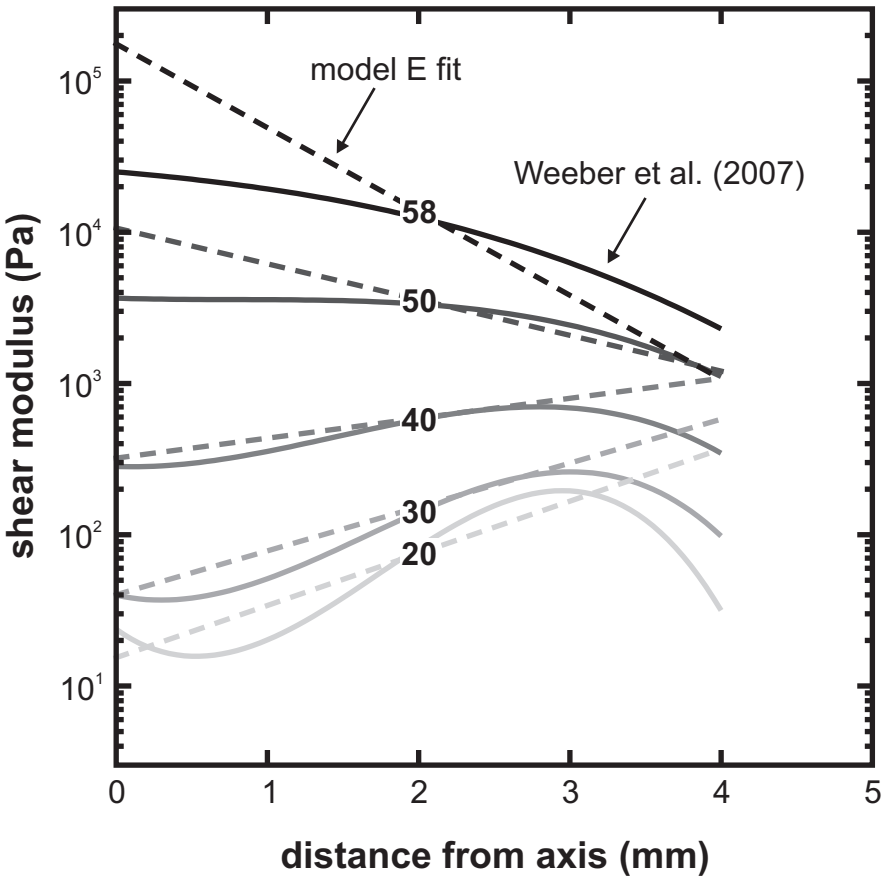

Figure 8.29 *– A comparison between profiles from the model E age-stiffness relation (dashed lines) and equivalent profiles from Weeber et al. (2007) (solid curves).*

Table 8.6 – *The relative increase in stiffness between 20 and 50 years calculated from the age-stiffness relations obtained in previous and current tests. The values for Glasser and Campbell (1999), Weeber et al. (2005), and Heys et al. (2007) are as described in the caption of figure 2.2.*

	nucleus **or** 0.5 mm	**cortex** **or** 3.5 mm	**whole lens**
Fisher (1971)	2.5	1.4	
Glasser and Campbell (1999)			3.7 or 4.9
Heys et al. (2004)	63	7.9	
Weeber et al. (2005)			6.9
Heys et al. (2007)	10		
Weeber et al. (2007)	229	14.1	
model H relation			13
model D relation	59	3.0	
model E relation	335	6.4	

(2004) and Weeber et al. (2007) than to the original spinning test of Fisher (1971). This applies both to the low stiffness values obtained for younger lenses and the dramatic increase in stiffness with age. The differences between the spinning tests are consistent with the expected results of improvements made to the current version which suggests that the values obtained for the nucleus in the original spinning test are not accurate. The comparison between model E and both indentation tests indicates that it is unlikely to provide realistic stiffness values for the inner region of lenses beyond about 45 years, as was also suggested in section 8.2.3. The model D age-stiffness relation should therefore be preferred for describing such lenses.

The situation for the outer region of the lens is more ambiguous. The stiffness values obtained in the current spinning test largely lie between those of the original spinning test of Fisher (1971) and the indentation tests, but closer to the former. However, the rate of increase in stiffness up to about 40 years is similar to the indentation tests. The current spinning test is likely to be better able to determine the stiffness of the outer region of the lens than indentation tests as this is usually where the uncertainties of a spinning test are smallest and the uncertainties of an indentation tests are greatest. The spinning test of Fisher (1971) does not have the same advantage due to the presence of the capsule.

The stiffening indices introduced in section 2.1.7 are repeated in table 8.6 with the addition of the values from the model H, D, and E age-stiffness relations. These values provide a summary of the increase in stiffness over the ages during which presbyopia develops. The values confirm the impressions given by figures 8.25 to 8.29. For the inner region of the lens, the model D fit is similar to Heys et al. (2004) while the model E fit indicates considerably more stiffening than even Weeber et al. (2007). For the outer region of the lens the model D fit lies between Fisher (1971) and Heys et al. (2004), while the model E fit is similar to Heys et al. (2004).

Three test methods characterize the mechanical response of the lens substance by a single value: Glasser and Campbell (1999), Weeber et al. (2005), and model H. These tests each mobilize the lens substance in a different manner so the evident non-homogeneity of the lens substance will naturally lead to different outcomes from each method. This can be expected to extend to the calculated change in stiffness with age, since Model D and E suggest that this also varies with position. Over the range of ages tested in the current work, the typical values for shear modulus obtained using model H are on average about 40 % of the equivalent values obtained from figure 5 of Weeber et al. (2005). The differences the the change in stiffness with age for these tests can be most easily compared using the values reported in table 8.6. Model H indicates a greater increase in stiffness over this range than Weeber et al. (2005), and greater still than Glasser and Campbell (1999). For lenses younger than about 24 years, though, model H indicates very little change in stiffness.

9

Modelling accommodation

The measurements of the stiffness of the lens substance using the spinning lens test presented in chapters 6, 7, and 8 are primarily intended for use in computational models of *in vivo* accommodation. Such models allow an improved and more quantitative understanding of the development of presbyopia, and also permit an examination of the efficacy of treatments intended to reverse it. In this chapter models of the accommodation mechanism at 29 and 45 years are described, making use of the age-stiffness models described in section 8.2.4. The treatment of the capsule is also novel, attempting to mimic the behaviour suggested by Burd (2009) and also incorporating a possible effect of residual stresses in the lens, suggested by Dr Burd. The remaining details of the models reflect previously published methods. The finite element method, outlined in chapter 5, is used to simulate the process of disaccommodation in the models, and their resulting mechanical and optical performance is examined and compared to *in vivo* measurements. The 45 year model is further adapted to explore the possibility of using a laser treatment to increase the flexibility of the lens substance and thereby increase the amplitude of accommodation.

9.1 Models for 29 and 45 years

The accommodation apparatus is examined at two ages within the range covered by the age-stiffness models calculated in section 8.2.4. The ages of 29 and 45 years are adopted as they

have been used in a number of previously published models (for example Burd et al. 2002; Hermans et al. 2008a). At 29 years the eye has a subjective accommodation amplitude of about 8 D, sufficient for most tasks. By 45 years this has typically fallen to 4 D, indicating considerable changes in the behaviour of the accommodation apparatus over this interval. This is also about the age at which loss of accommodation amplitude generally becomes a practical difficulty.

9.1.1 Model geometry

Distinct geometries are used for the 29 and 45 year accommodation models, denoted by the labels A29 and A45 respectively. The two geometries are derived from a number of *in vivo* measurements of the lens, using a mixture of the methods and data sources of Burd et al. (2002) and Hermans et al. (2008a). Each model is composed of the lens substance, the capsule and an idealized representation of the zonular fibres. The whole accommodation apparatus is essentially axisymmetric and is modelled as such. The initial configuration of each model is constructed to correspond to the fully-accommodated state for a typical lens of the same age. The finite-element mesh used for model A29 is illustrated in figure 9.1; the mesh used for model A45 is of the same general form but with differing dimensions. The principal differences from previous models of accommodation are the application of the stiffness values obtained from the current spinning lens test in modelling the lens substance, and the manner in which the lens capsule is modelled.

Lens shape The exterior shape of the lenses of A29 and A45 are taken from the models of the same age presented by Hermans et al. (2008a). In this formulation the axisymmetric outline of each lens is divided into four segments each of which is described by a conic section. The parameters of the conic sections were chosen to agree with selected published measurements of *in vivo* lenses (Strenk et al., 1999; Dubbelman and van der Heijde, 2001; Dubbelman et al., 2005; Rosen et al., 2006), and are also constrained to ensure a smooth transition between the segments. For both ages the fully-accommodated shapes specified by Hermans et al. (2008a) are adopted. The geometry of the 29 year lens is stated to correspond to 8 D of accommodation, and that of the 45 year lens to 4 D of accommodation.

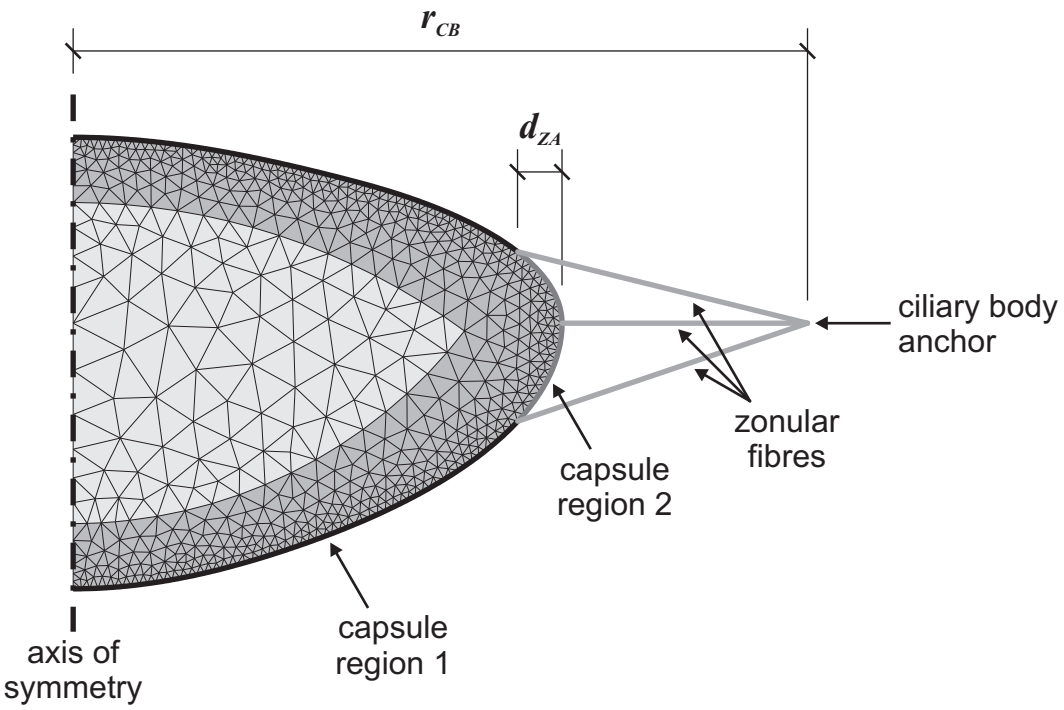

Figure 9.1 – *The mesh used to simulate accommodation for the 29-year model A29. The measurements r_{CB} and d_{ZA} determine the geometry of the zonular fibres. For the distinction between capsule region 1 and capsule region 2, see the text.*

Capsule The capsule is modelled as a thin membrane conforming to the exterior of the lens substance. It is assumed to fully adhere to the underlying lens substance during deformation. The capsule is divided into two regions, as illustrated in figure 9.1. These regions are distinguished in order to reflect plausible effects of residual stresses in the lens when it is fully accommodated without requiring an explicit inclusion of such stresses in the model, as discussed in detail below. The method of modelling the effect of residual stresses were proposed by Dr Burd and implemented by the author.

There is understandably no information available on residual stresses in the lens *in vivo*; however, Pedrigi et al. (2007) report a residual strain of about 3 % in the anterior capsule within partially dissected eye globes. The presence of residual stresses would have little impact on the model of the lens substance due to its approximately linear behaviour, but may have a significant effect on the behaviour of the capsule due to geometric non-linearity. One likely implication of residual stresses is the presence of an equatorial zone in which the

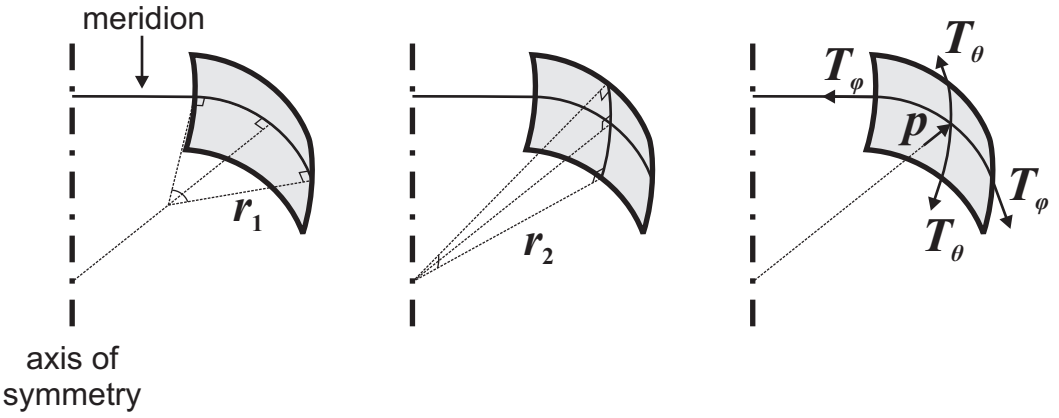

Figure 9.2 – *A small element of an axisymmetric membrane. The principal radii of curvature of the membrane are r_1 and r_2, corresponding to the meridional direction and the orthogonal direction respectively. If the membrane is subjected to a pressure, p, then membrane tractions T_φ and T_θ arise.*

capsule is slack in the circumferential direction. This possibility arises from consideration of the simplest residual stress for the lens, in which the lens substance experiences a uniform pressure balanced by residual stresses in the capsule.

If an axisymmetric membrane such as the capsule is inflated by a uniform pressure, p, then its state of stress can be determined directly from its geometry. At a given point the membrane tractions in the meridional and circumferential directions are given by

$$\begin{aligned} T_\varphi &= \frac{pr_2}{2} \\ T_\theta &= \frac{pr_2}{2}\left(2-\frac{r_2}{r_1}\right) \quad , \end{aligned} \tag{9.1}$$

where r_1 and r_2 are the principal radii of curvature, as illustrated in figure 9.2, (see for example Irvine, 1981). The centre of curvature corresponding to r_2 must lie on the axis of symmetry since those lines normal to the membrane that pass through equivalent points on adjacent meridians intersect on that axis. The second equation of 9.1 requires the circumferential membrane traction to be negative wherever $r_2 > 2r_1$. This geometric condition holds for typical lens geometries in a band about the equator. Since the capsule cannot sustain compressive loads it is liable to become buckled in this region. If this occurs, subsequent stretching of the capsule will not engage its circumferential stiffness until the buckling has been removed.

It has not been established that the capsule does become buckled in a band about the

equator. However, the results of the spinning lens test suggest that the capsule offers an unexpectedly small constraint on the lens substance around the equator. The equatorial displacements for the tests on intact lenses at 1000 rpm are in all cases at least 47 % of the displacements obtained in the corresponding decapsulated tests, with 60 % being typical (see figure 8.5). This is substantially higher than the value of 21 % found by Burd et al. (2006) using a finite-element model of the spinning lens test applied to a 22 year lens (with stiffness values from Fisher, 1971). Circumferential buckling about the equator is tentatively adopted as a contributor to this observation, and further is assumed to apply *in vivo*.

OXFEM_HYPERELASTIC does not allow for residual stresses in the initial configuration, so the effect of a buckled region is achieved by imposing a slack condition in the circumferential direction in capsule region 2 of figure 9.1 (between the anterior and posterior zonular fibres). In this region the strain area-density function does not depend on the stretch ratio in the circumferential direction, λ_2, but becomes

$$\Psi_{2D} = \begin{cases} \frac{t_0 E}{2}(\lambda_1 - 1)^2 & \lambda_1 \geq 1 \\ 0 & \lambda_1 < 1 \end{cases} . \tag{9.2}$$

This corresponds to the second and fourth components in equation 5.4. Capsule region 2 is limited to the region between the anterior and posterior zonular attachments for both the A29 and the A45 model. This is somewhat smaller than the zone for which equation 9.1 would imply compressive circumferential stresses. This reduced region is adopted because the response of the lens to zonular traction is sensitive to the size of the gaps between capsule region 1 and the anterior and posterior zonular attachments. Using equation 9.1 to define capsule region 2 might introduce a substantial but essentially arbitrary difference between A29 and A45 models which would complicate comparisons between them.

Zonular fibres and ciliary body The geometry of the zonular fibres is set in accordance with Burd et al. (2002), since the models of Hermans et al. (2008a) do not include the fibres explicitly. The zonular fibres are substantially idealized in the models, as illustrated in figure 9.1. All fibres start at a point corresponding to the ciliary body, located in the plane of the lens equator and at an age-dependent radius, r_{CB}. They are divided into three groups, the

anterior, equatorial, and posterior zonular fibres, which each meet the lens capsule at distinct attachment points. The equatorial zonular fibres meet the capsule at the lens equator, while anterior and posterior attachment points are taken to lie at an age dependent radial distance, d_{ZA}, inside the lens equator. The equations used to determine r_{CB} and d_{ZA} are those derived by Burd et al. (2002) from the data of Strenk et al. (1999) and Farnsworth and Shyne (1979) respectively:

$$\begin{aligned} r_{CB} &= 6.735 - 0.009A \\ d_{ZA} &= 0.0311 + 0.0124A \quad , \end{aligned} \tag{9.3}$$

where A is the age of the subject in years and r_{CB} and d_{ZA} have units of millimeters. Burd et al. (2002) also used the data of Strenk et al. (1999) to derive an equation for the displacement of the ciliary body that occurs with disaccommodation, as follows:

$$\delta_{CB} = 0.5129 - 0.00525A \quad , \tag{9.4}$$

where once again A is the age of the subject in years and δ_{CB} has units of millimeters. This is the radial displacement applied to the ciliary body anchor of the zonular fibres in order to simulate disaccommodation in the current models.

9.1.2 Material parameters

Lens substance The lens substance is represented in OXFEM_HYPERELASTIC by 15-noded triangular elements, as in the models of the spinning lens test. It is modelled as a neo-Hookean continuum, as described in section 5.3.2. The three alternative stiffness models (homogeneous, H; distinct nucleus, D; exponential, E) used in the analysis of the spinning lens test are applied to the models of accommodation. The stiffness parameters for the 29-year and 45-year materials are calculated from age-stiffness relations given in section 8.2.4; these values are tabulated in table 9.1 and illustrated in figure 9.3. Each of the stiffness models is used in conjunction with the lens geometry of corresponding age, leading to six main models of accommodation: A29H, A29D, A29E, A45H, A45D, and A45E. In addition two mixed-age models are considered: model B29D is identical to A29D except that the stiffness parameters of the lens substance correspond to those of a 45-year lens, while

Table 9.1 – *The parameter values for stiffness models H, D and E at ages 29 and 45. The values are calculated from the age-stiffness relations of section 8.2.4.*

material age	**model H**	**model D**		**model E**	
(years)	μ (kPa)	μ_N (kPa)	μ_C (kPa)	μ_0 (kPa)	μ_1 (kPa)
29	0.28996	0.09052	0.63113	0.03646	0.80662
45	1.37922	1.52775	1.28991	1.85118	1.28106

model B45D is identical to A45D except that stiffness parameters of the lens substance correspond to those of a 29-year lens. These models are used to assess the influence of the differing stiffness of the lens substance independent of the other changes which occur with age.

All the stiffness models are defined in the same manner as for the spinning lens test. In particular the geometry of the nucleus in model D has the form given in section 7.5.2 rather than the form specified by Hermans et al. (2008a).

The bulk modulus, κ, of the material is set to 1000 times the shear modulus. This differs from the factor of 100 used for the models of the spinning lens test as on the one hand the models of accommodation do not have a numerically challenging region like the contact with the lens support, while on the other hand the presence of the capsule makes maintaining the correct lens volume more important in obtaining the correct mechanical response.

Capsule The capsule is represented in OXFEM_HYPERELASTIC by 5-noded membrane elements. It is modelled using the elastic membrane constitutive model specified by equation 5.3 in section 5.3.3. This requires the specification of the thickness of the unstrained capsule, t_0, its Young's modulus, E, and its in-plane Poisson's ratio, ν_{2D}. In all the current models the thickness is set to a single spatially varying profile reported by Barraquer et al. (2006), namely that of lens group A, which is reproduced in figure 9.4. Lens group A consists of lenses aged from 30 to 42 years, with a mean age of 36 years. Of the three available age groups, this is the most appropriate for both the 29-year models and the 45-year models. The process of assigning the varying thickness values is handled automatically within OXFEM_HYPERELASTIC when a lens-capsule material is specified. Linear interpolation is used to set the thickness at points between those plotted by Barraquer et al. (2006).

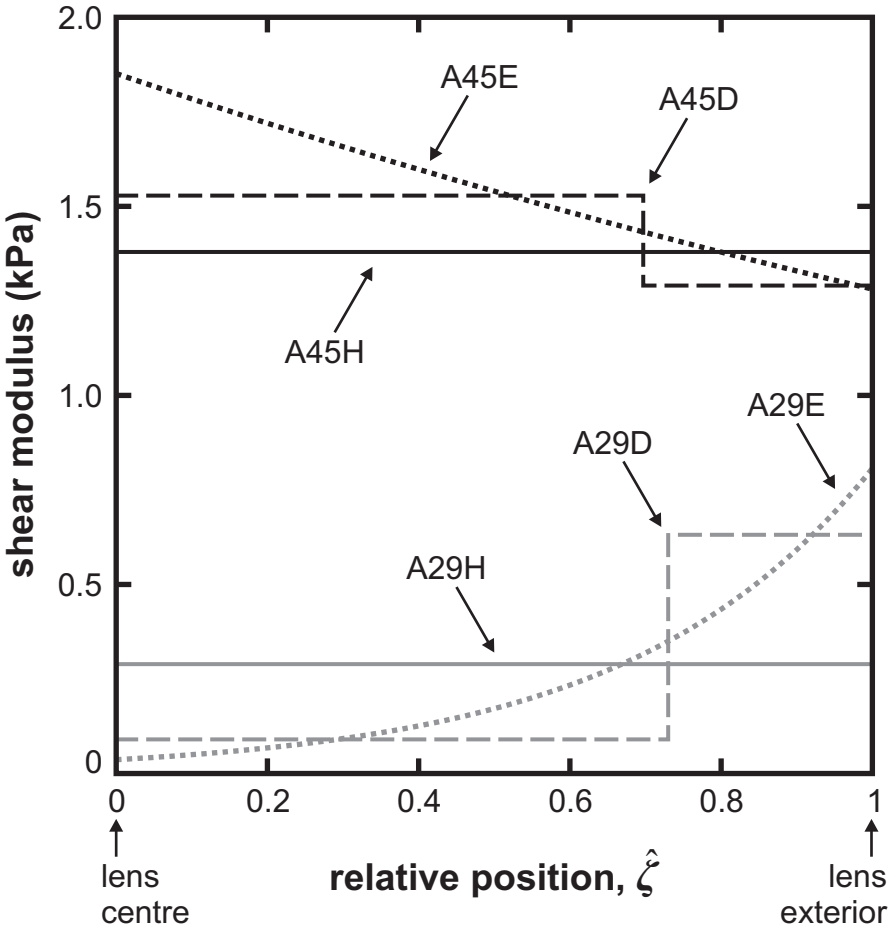

Figure 9.3 – *Stiffness profiles for the six stiffness models. The position of the step indicated for A29D and A45D is the average location of the transition from nucleus to cortex.*

The Young's modulus and in-plane Poisson ratio of the capsule are chosen to reconcile the uniaxial tests of Krag and Andreassen (2003a) with the biaxial tests of Fisher (1969), in a manner proposed by Dr Burd and calculated by the author. In the former test, the circumferential Young's modulus of the capsule was essentially measured directly. The secant values obtained at 10 % strain are described by the piece-wise linear function

$$E = \begin{cases} b\,(A - A_0) + c & A \leq A_0 \\ c & A > A_0 \end{cases}, \tag{9.5}$$

where $A_0 = 35$ years, $b = 30\,\text{kPa year}^{-1}$, and $c = 1450\,\text{kPa}$. In the biaxial test of Fisher (1969) the Young's modulus was found to decline from about 6 MPa in childhood to about 3 MPa by 60 years. These values are considerably higher than those of Krag and Andreassen (2003a), as illustrated in figure 9.5. The calculation used by Fisher (1969) makes the assumption

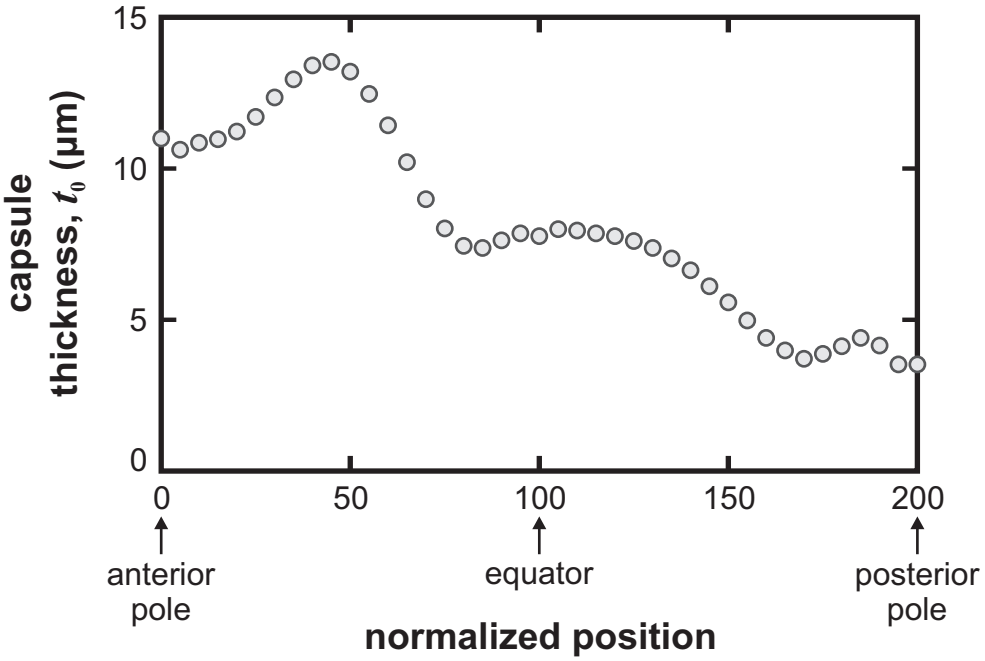

Figure 9.4 – *The thickness of the capsule along a meridian of the lens. The values are for lens group A and a normalized position, both as defined by Barraquer et al. (2006). (Adapted from figure 7 of Barraquer et al., 2006).*

that the in-plane Poisson's ratio is equal to the volumetric Poisson's ratio (measured to be about 0.47). This choice of in-plane Poisson's ratio is only justified if the capsule behaves isotropically, an unlikely situation given the laminar arrangement seen in young capsule specimens (Krag and Andreassen, 2003a). If the assumption of full isotropy is dispensed with then the measurements of Fisher (1969) can be used to determine an in-plane Poisson's ratio which is consistent with the Young's modulus measurements of Krag and Andreassen (2003a).

The response of a linear-elastic membrane to uniform biaxial loading does not depend on the Young's modulus or the in-plane Poisson's ratio independently, but on the combined value $\frac{E}{1-\nu_{2D}}$. Thus, if E_F is the Young's modulus of the capsule determined by Fisher (1969) using an in-plane Poisson's ratio of ν_F, then the same experimental biaxial response would be obtained with the Young's modulus, E, equal to that measured by Krag and Andreassen (2003a) provided the corrected in-plane Poisson's ratio is given by

$$\nu_{2D} = 1 - (1 - \nu_F)\frac{E}{E_F} \quad . \tag{9.6}$$

Figure 9.6 displays the values of ν_{2D} which would reconcile each measurement plotted in

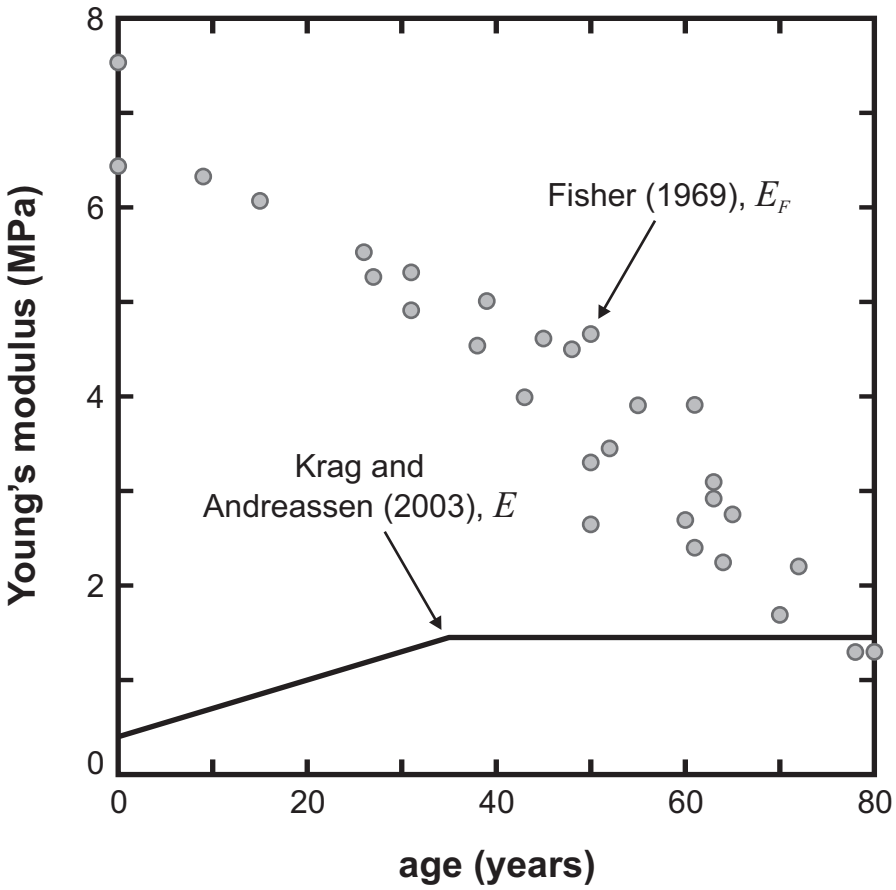

Figure 9.5 *– A comparison of measurements of capsule stiffness. The values, E_F reported by Fisher (1969) are from a biaxial test and the relation, E, reported by Krag and Andreassen (2003a) is from a uniaxial test.*

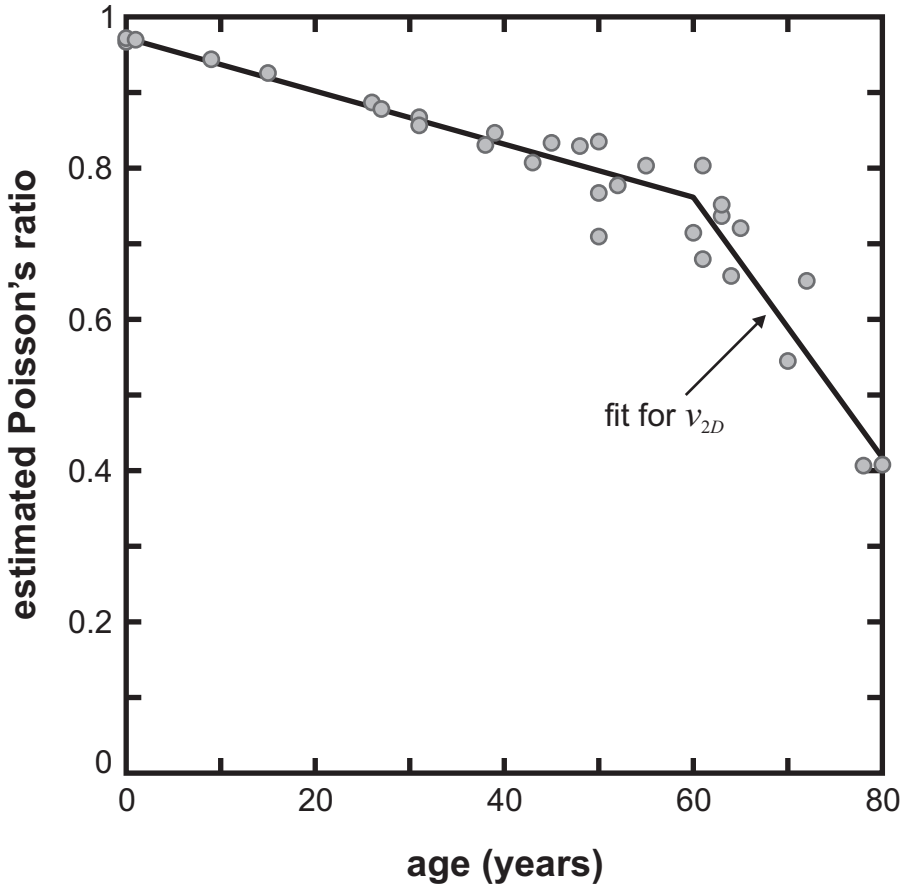

Figure 9.6 *– The in-plane Poisson's ratio of the capsule model. The circles are the values which reconcile the Young's modulus values reported by Fisher (1969) with equation 9.5. The line is a piecewise-linear fit to the points.*

Table 9.2 – *The parameters used in the elastic-membrane constitutive model of the capsule.*

	t_0 (mm)	E (kPa)	ν_{2D}
A29	Barraquer et al. (2006)	1270	0.870339
A45	lens group A profile	1450	0.814195

figure in figure 8 of Fisher (1969) with the Young's modulus implied by equation 9.5. A piece-wise linear function is fitted to the points to estimate ν_{2D} and obtain values for use in the 29-year and 45-year lens models. This function is given by

$$\nu_{2D} = \begin{cases} b_1 (A - A_0) + c & A \leq A_0 \\ \\ b_2 (A - A_0) + c & A > A_0 \end{cases} , \tag{9.7}$$

where A_0 was chosen to be 60 years by inspection, and the fitting process yielded the values $b_1 = -0.003509\,\text{year}^{-1}$, $b_2 = -0.017224\,\text{year}^{-1}$, and $c = 0.76156$. The parameter values calculated from equation 9.5 and 9.7 used in model A29 and model A45 are given in table 9.2.

Zonular fibres The zonular fibres are represented in OXFEM_HYPERELASTIC by 2-noded bar elements. They are modelled using the neo-Hookean bar constitutive model described in section 5.3.4. The published values for the stiffness of the zonular fibres span a broad range, from 350 kPa reported by Fisher (1986) to a typical value of 1.5 MPa reported by van Alphen and Graebel (1991). It seems the most reliable way to obtain a realistic response from the lens is to apply the method used by Burd et al. (2002). In this approach it is assumed that the relative abundance of zonular fibres is in the ratio 6:1:3 for the anterior, equatorial, and posterior groups respectively, while the overall stiffness of the zonular fibres must be such that the ciliary body displacement given by equation 9.4 induces a displacement at the lens equator, δ_{LE}, consistent with the measurements reported by Strenk et al. (1999). To achieve these outcomes the total cross-sectional area, A_0, is set to 0.6, 0.1, and $0.3\,\text{mm}^2$ for the respective groups, while the shear modulus of the zonular material, μ, is adjusted until the target displacement is obtained at the lens equator. The value of μ is the same for all three groups. The product $A_0\mu$ is physically meaningful in this scheme, while the constituent parameters are not.

Table 9.3 – *The parameters of the zonular fibre groups used in the neo-Hookean bar constitutive model. The same values are adopted in all the present lens models.*

	A_0 (mm^2)	μ (kPa)
anterior	0.6	763.1
equatorial	0.1	763.1
posterior	0.3	763.1

In the current set of simulations a single model, A29D, is used to determine the stiffness of the zonular fibres, then this value is applied in all other models. The target equatorial displacement for this lens is $\delta_{LE} = 0.2903\,\text{mm}$, also taken from Burd et al. (2002). This value is obtained from a linear fit to the data of Strenk et al. (1999). The resulting parameters used for the zonular fibres of all the accommodation models are given in table 9.3.

9.1.3 Physical response of the models

The process of disaccommodation is simulated in the models by radially displacing the ciliary body anchor of the zonular fibres by the amount specified by equation 9.4: 0.36065 mm for the 29-year models and 0.27665 mm for the 45-year models. The effect of this displacement is calculated using OXFEM_HYPERELASTIC. The lens becomes radially stretched and axially compressed, and the radius of curvature of the lens surface at the anterior and posterior poles increases. It is the increase in the radii of curvature which is central to disaccommodation as these changes decrease the optical power of the lens. Figures 9.7 and 9.8 illustrate the disaccommodated shape of model A29D and A45D, while table 9.4 summarizes the main physical measurements of these models in their initial accommodated and final disaccommodated states. The same data for all the accommodation models are given in the appendix in table D.1. The change in lens radius, δ_{LE}, of the models, particularly the 45 year models, is somewhat exaggerated by the local stretching in the vicinity of the equatorial zonular fibre group. If the traction on the capsule were less concentrated this effect would be diminished.

The radii of curvature, r_A and r_P, of the anterior and posterior surfaces of the lens are calculated for the accommodated and disaccommodated lens states. Since the surfaces are not spherical there is some ambiguity in the values. In the current work r_A and r_P are calculated

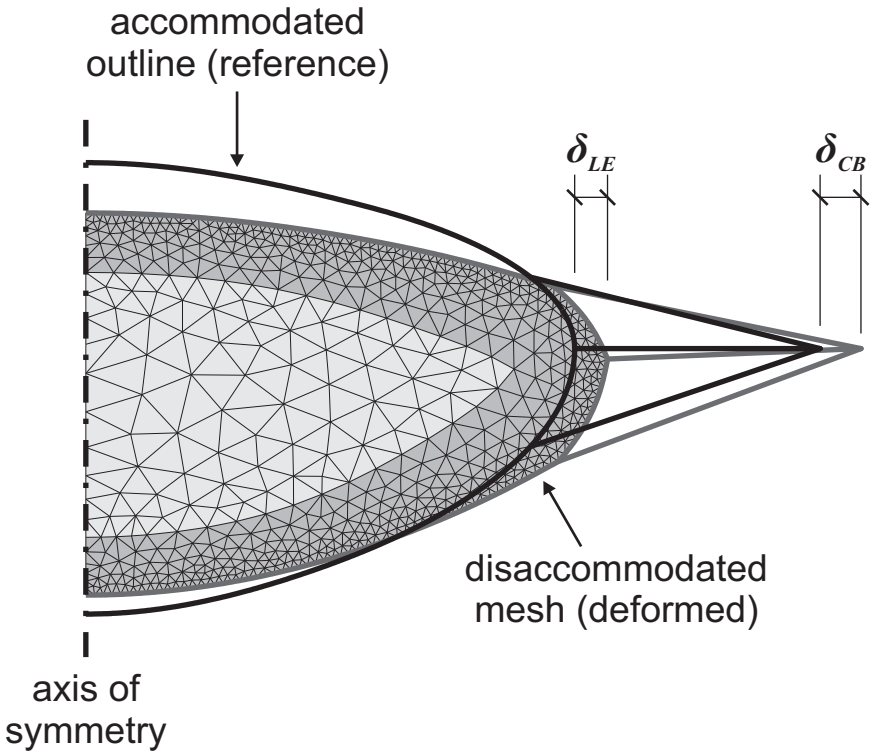

Figure 9.7 – *The disaccommodated state of model A29D. The radial displacement of the ciliary body, δ_{CB}, is 0.36065 mm, while the resultant radial displacement of the lens equator, δ_{LE}, is 0.2903 mm.*

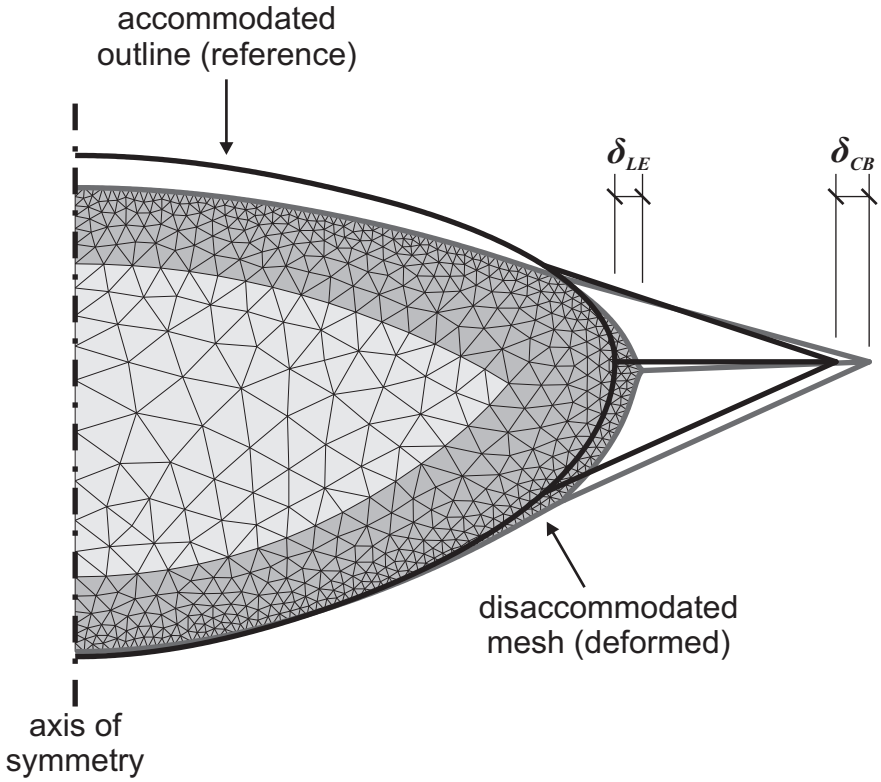

Figure 9.8 – *The disaccommodated state of model A45D. The radial displacement of the ciliary body, δ_{CB}, is 0.27665 mm, while the resultant radial displacement of the lens equator, δ_{LE}, is 0.2306 mm.*

Table 9.4 – *The physical effect of disaccommodation on A29D and A45D.*

		ciliary radius r_{CB} (mm)	**lens radius** r_{LE} (mm)	**lens thickness** d_L (mm)	**anterior radius** r_A (mm)	**posterior radius** r_P (mm)
A29D	**initial**	6.47	4.31	3.98	7.10	-5.09
	final	6.83	4.60	3.37	12.49	-7.28
	change	0.36	0.29	-0.61	5.40	-2.19
A45D	**initial**	6.33	4.49	4.17	8.13	-5.32
	final	6.61	4.72	3.86	9.93	-6.04
	change	0.28	0.23	-0.31	1.80	-0.73

by fitting a circular arc to the nodes of the finite-element model located on the surface up to 1.5 mm from the axis of symmetry. The contribution of the individual nodes is weighted in proportion to their distance from the axis, so the result is equivalent to fitting a spherical cap to the surface of revolution. A total least squares procedure is used to find the radius and centre of the best fitting arc. This method is adopted in preference to calculating the local curvature at the axis as the larger zone is relevant to the optical performance of the lens. The further refinement of determining the appropriate zones for arc fitting by considering the optical effect of a realistic pupil is, however, not felt to be warranted. The fitting zones would then vary in size with both age and accommodation state, and would differ at the anterior and posterior surfaces. While providing more precise optical results such a method would complicate comparison of the physical differences between models and between accommodation states. The calculated radii of curvature are signed values leading to the posterior curvature to have a negative value, in accordance with the usual convention in optics.

The calculated radii of curvature and the changes with disaccommodation of models A29D and A45D are reported in table 9.4. These values are in good agreement with the *in vivo* measurements of Dubbelman et al. (2005), except for the change in the posterior curvature of model A29D which experiences a greater magnitude of change than most of the *in vivo* measurements. This may reflect an inaccuracy of the distribution of traction between the anterior and posterior segments of the capsule in the model.

The change in thickness of both lens models are much greater than the measurements of Dubbelman et al. (2003) using Scheimpflug photography, and towards the high end of

the ranges obtained by Strenk et al. (1999), Jones et al. (2007), and Hermans et al. (2009) using magnetic resonance imaging. If this change in thickness is excessive it may reflect that the model has either an excessive radial movement of the lens equator, or an incorrect final shape in the equatorial region of the lens due to the particular form of the capsule and zonular fibres. Since the former was chosen to agree with the data of Strenk et al. (1999), the latter possibility is most likely.

Another discrepancy between the models and the measurements of Dubbelman et al. (2003) is found in the change in thickness of the cortex along the axis of the lens. The Scheimpflug photographs suggest that typically just over 10 % of the thickness change occurs within the cortex, including in lenses of 43 and 49 years. In model A29D almost 20 % of the thickness change occurs within the cortex, even though the shear modulus of the cortex is about seven times greater than that of the nucleus. This behaviour and the larger than expected change in total axial thickness are also seen in the model of Weeber and van der Heijde (2008). Decreasing the shear modulus of the nucleus further does not bring the model much closer to the experimental measurements. Once the nucleus is much softer than the cortex the high bulk modulus of the lens substance means that the axial compression of the nucleus is primarily limited by the confinement provided by the cortex around the lens equator. This suggests that to match the behaviour reported by Dubbelman et al. (2003) the form of the stiffness model would need to change. Three possible changes are:

i. to distinguish between the cortex in the axial region (where the ends of the lens fibre cells meet) and the cortex in the equatorial region (where the outer layer includes immature lens fibre cells)

ii. to introduce anisotropy into the constitutive model of the cortex, reflecting the alignment of the lens fibre cells

iii. to use a poroelastic model for the lens substance, permitting fluid to flow from the nucleus to the cortex in the vicinity of the axis.

The observation of Hermans et al. (2007) that the volume of the nucleus is conserved during accommodation argues against the last of these. These three options are all beyond the scope

Table 9.5 – *The diameter-load response of groups of lenses tested in a mechanical stretcher by Manns et al. (2007), converted to mm N^{-1}.*

lens groups from Manns et al. (2007)				
lens group	**mean age** (years)	**age range** (years)	**mean response** ($mm\,N^{-1}$)	**response range** ($mm\,N^{-1}$)
group 1	14.0	8 – 19	7.0	5.0 – 10.3
group 2	39.5	38 – 41	3.7	2.8 – 4.4
group 3	62.7	55 – 70	4.6	3.0 – 6.4

of the current work.

The total radial force required at the ciliary body anchor to induce the required displacement is 104 mN for A29D and 82 mN for A45D. The average change in the diameter of the lens for a given load is $5.6\,mm\,N^{-1}$ for each lens. These values can be compared to results from Manns et al. (2007), who applied a mechanical stretcher to partially dissected eyes in order to approximate *in vivo* accommodation. The reported diameter-load response of the three groups of human lenses that were tested are given in table 9.5 (converted to units of $mm\,N^{-1}$). The experimental values are of a similar magnitude to the values from the models. The diameter-load response of model A29D lies between the mean response of the younger group 1 and older group 2. Model A45D is bracketed in age by group 2 and group 3 but these two groups both show a generally stiffer response than the accommodation model. The measurements from the mechanical stretcher include the effect of circumferential stresses developed in the ciliary body which are not present in the accommodation model, so are not directly comparable.

The previous computational models of Burd et al. (2002) and Hermans et al. (2008a) both require a somewhat smaller total radial force than the current models. Reducing the Poisson's ratio of the capsule in the current models to 0.47 (in line with the previous models) decreases the total radial force to 47 mN for A29D and 52 mN for A45D, values which are similar to those of Hermans et al. (2008a) when using the data of Heys et al. (2004) for the stiffness of the lens substance. This indicates that it is the higher biaxial stiffness of the current model of the capsule which results in the higher total radial force.

In general *in vivo* measurements of the lens display considerable variation between individuals and often come from a relatively small number of measurements. This means a

degree of latitude should be permitted when comparing models of accommodation to mean or typical experimental measurements. However, the models are themselves constructed using parameters generally equal to mean or typical values, so should lie towards the centre of a population of measurements, rather than towards an extreme.

9.1.4 Optical response of the models

The physical changes induced in the accommodation models produce optical changes. The optical power of the lens models can be calculated using the thick lens formula:

$$P_L = \frac{n_L - n_A}{r_A} + \frac{n_V - n_L}{r_P} - \frac{d_L}{n_L}\frac{(n_L - n_A)(n_V - n_L)}{r_A r_P} \quad , \tag{9.8}$$

where d_L, r_A, and r_P are the thickness, anterior radius of curvature and posterior radius of curvature obtained from the simulated lens in a given state, while n_L, n_A, and n_V are the refractive indices of the lens substance, the aqueous humour and the vitreous humour respectively. The values of the refractive indices are adopted from the schematic eye of Bennett and Rabbetts (1998) and given in table 9.6. The value assigned to the lens is an effective refractive index which for typical lens geometries gives approximately the same optical power as the gradient refractive index which actually exists within the lens.

The relationship between the optical power of the lens and displacement of the ciliary body anchor are plotted in figure 9.9 for the six main lens models. All the models of the 29-year lens exhibit a change in power which is more than double the models of the 45-year lens. All three stiffness models for the lens substance produce similar optical outcomes for the relatively homogeneous 45-year models. The two heterogeneous stiffness models for the 29-year models also produce similar optical outcomes, while model H results in an optical power change which is about 1 D smaller. This suggests that the spatial variation in stiffness of the lens has some impact on the optical performance, but that the precision achieved using the spinning lens test analysed using a heterogeneous stiffness model is sufficient for this relatively simple assessment of the accommodation mechanism.

Within the small variation exhibited by the different stiffness models it is noticeable that lower stiffness values in the central region of the lens consistently correlate with greater changes in power. At 29 years model E is the stiffness model with the lowest central stiffness

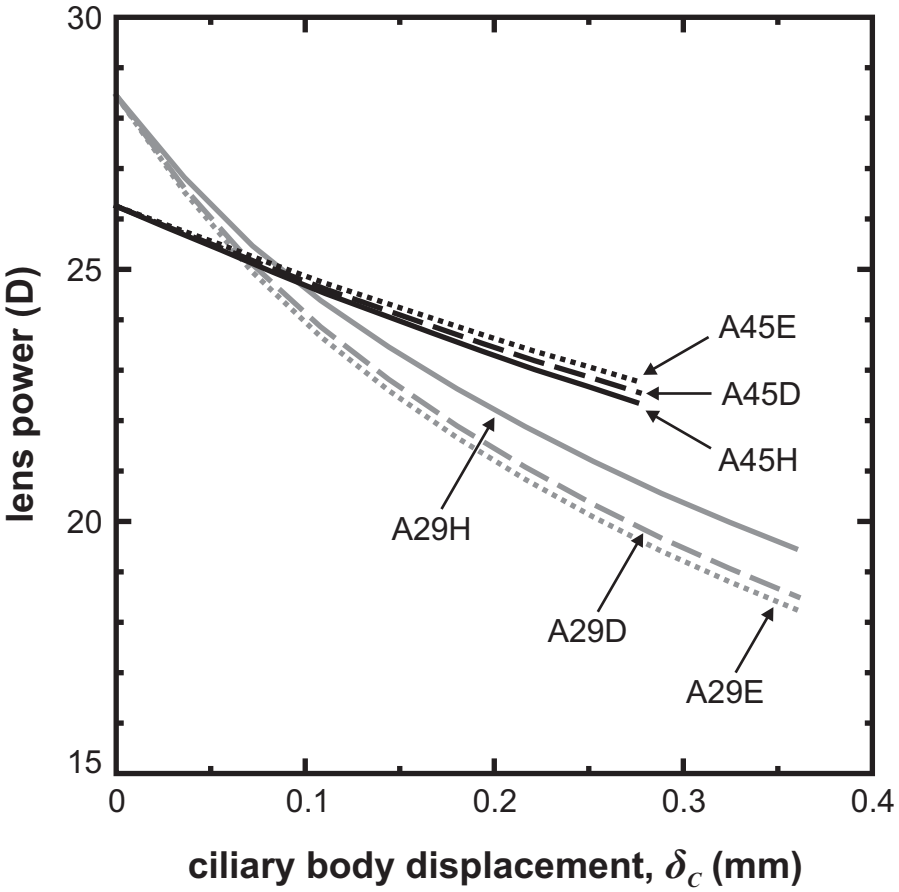

Figure 9.9 – *The optical power of the modelled lenses in response to the displacement of the ciliary body anchor.*

and provides the greatest change in power, followed by model D then model H. At 45 years model H is the stiffness model with the lowest central stiffness and provides the greatest change in power, followed by model D then model E.

Weeber and van der Heijde (2007) obtained broadly equivalent results when comparing the homogeneous stiffness data of Weeber et al. (2005) to the heterogeneous stiffness data of Weeber et al. (2007). At 20 and 40 years the heterogeneous stiffness values indicate the centre was the softest location within the lens, and the models using that data resulted in a change in lens power which was about 0.5 D greater than the corresponding models using the homogeneous stiffness data. At 60 years, though, the heterogeneous stiffness data indicate that the centre of the lens is about 15 times stiffer than the exterior and the model using that data change in lens power which was about 3 D smaller than the homogeneous case.

Figure 9.10 compares the optical power of the mixed-age models B29D and B45D to the corresponding single-age models A29D and A45D. The change in optical power of the

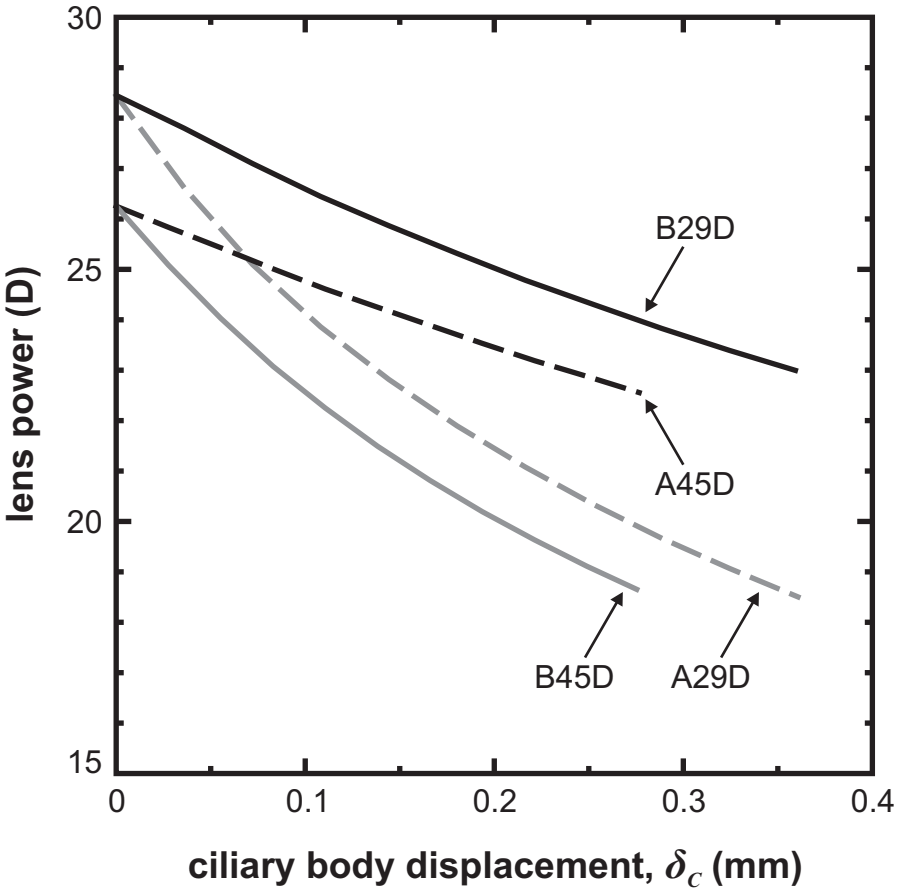

Figure 9.10 – *The optical power of the mixed-age model lenses in response to the displacement of the ciliary body anchor.*

mixed-age models most closely resembles the single-age model with the same lens substance parameters. This indicates that the decline in performance from A29D to A45D is mostly due to the differences in the lens substance rather than the differences in geometry and capsule stiffness of the two models. Most of the decline in performance not explained by the lens substance can be largely accounted for by the difference in the displacement applied to the ciliary muscle anchor. In the models this displacement is prescribed according to age; in reality, however, this may also partly depend on the stiffness of the lens if the outward movement of the ciliary body is impeded by the constraint of the lens and zonular fibres.

To compare the optical performance of the accommodation models to clinical data it is necessary to place them in the context of the whole eye. This is achieved here by modifying the schematic eye of Bennett and Rabbetts (1998), which specifies three optical surfaces (the cornea, the anterior lens surface and the posterior lens surface) and the image plane of the retina. To assess the effect of a particular accommodation model in a particular state, the

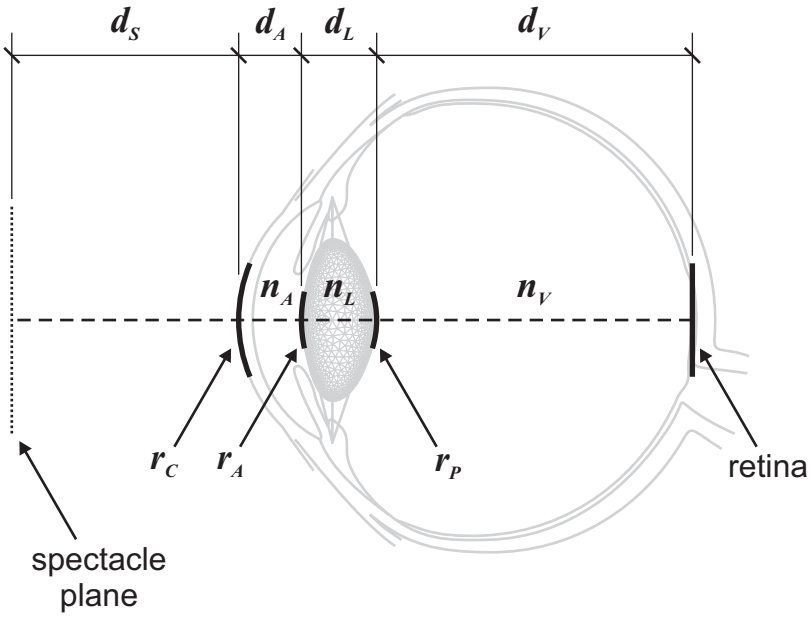

Figure 9.11 – *A modified schematic eye, adapted from the schematic eye of Bennett and Rabbetts (1998).*

Table 9.6 – *The values used for the modified schematic eye.*

parameter	value
d_S (mm)	12.0
$d_A + d_L$ (mm)	7.3
d_L (mm)	from model
A29 d_V (mm)	17.369
A45 d_V (mm)	16.986

parameter	value
r_C (mm)	7.8
r_A (mm)	from model
r_P (mm)	from model
n_A	1.336
n_L	1.422
n_V	1.336

original lens of the schematic eye is replaced by the modelled lens, positioned so that its posterior pole is in the same position as for the original lens. A schematic eye, modified by the inclusion of model A29D, is illustrated in figure 9.11. The values d_S, $d_A + d_L$, r_C, n_A, n_L, and n_V are all taken from Bennett and Rabbetts (1998), and are listed in table 9.6. The values of d_L, r_A, and r_P are calculated from a particular state of the accommodation model of interest. The length of the vitreous, d_V, and therefore the position of the retina, is chosen so that each lens in its fully-accommodated state achieves the accommodation specified by Hermans et al. (2008a) (8 D for A29 and 4 D for A45), as measured from the spectacle plane. That is, an object 125 mm from the spectacle plane will form an image on the retina for the reference geometry A29, while an object 250 mm from the spectacle plane will do the same for the reference geometry A45.

Table 9.7 – *The accommodation amplitude of the models of accommodation, including the mixed-age models B29D and B45D. The amplitude is measured with respect to the spectacle plane.*

	A_S (D)
A29H	7.50
A29D	8.15
A29E	8.32
B29D	4.88

	A_S (D)
A45H	3.15
A45D	2.99
A45E	2.84
B45D	5.70

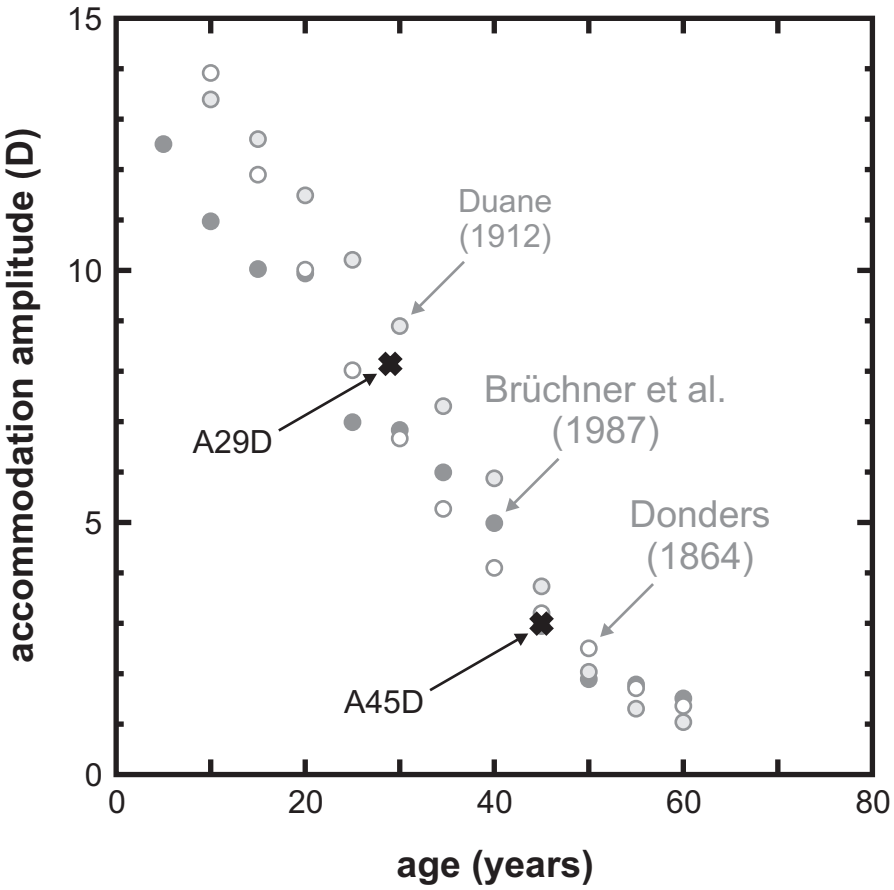

Figure 9.12 – *The objective accommodation amplitude, A_S, calculated for models A29D and A45D, and the subjectively measured accommodation amplitude calculated for individuals of different ages in three studies (Donders, 1864; Duane, 1912; Brückner et al., 1987), averaged over 5-year intervals. (The latter adapted from figure 1 of Weale, 1990).*

The accommodation amplitude for the eye is calculated with reference to the spectacle plane, in accordance with usual clinical practice (Bennett and Rabbetts, 1998). For each accommodation model, the object point which is conjugate to the retina is calculated for its fully-accommodated state and its fully-disaccommodated state. If these near and far points lie respectively at positions l_N and l_F with respect to the spectacle plane, then the accommo-

dation amplitude of the model is

$$A_S = \frac{1}{l_F} - \frac{1}{l_N} \quad . \tag{9.9}$$

Figure 9.12 displays the objective accommodation amplitude calculated for models A29D and A45D in comparison to clinical measurements of subjective accommodation. Both models lie close to the clinical measurements of similar age. This suggests that the accommodation amplitude of the models is actually excessive, since subjective measurements generally overestimate the objective value by about 1.75 D due to the effect of depth of field in subjective measurements (Hamasaki et al., 1956). If the capsule or zonular fibres were modified to more closely match the *in vivo* measurements of the change in lens thickness as mentioned in section 9.1.3, a smaller accommodation amplitude for both models would also be expected, bringing the values closer to the expected results.

Despite the slightly excessive amplitudes of accommodation, the 29-year and 45-year models appear to capture the development of presbyopia. The difference in optical performance of the two lens models is largely explained by the increase in the stiffness of the lens substance, supporting the view that this is the major contributor to presbyopia.

9.2 Modelling accommodation after laser lentotomy

One proposed method for treating presbyopia is the use of a laser to modify the lens substance to increase its flexibility, a process termed lentotomy. The light of a pulsing femtosecond laser system can be precisely focused within the lens so that nonlinear absorption processes at the focal point cause local optical breakdown of the tissue (Schumacher et al., 2009). The repeated application of the laser in a specified pattern can produce partial or complete separation of the lens substance at surfaces within the lens, essentially creating a series of cuts (Stachs et al., 2009). Schumacher et al. (2009) used this technique on isolated human lenses to create a ‘steering-wheel pattern’, made up of the constituent cuts illustrated in figure 9.13. This modification of the lens substance was found to increase the deformation experienced by treated lenses when subjected to a spinning test. The form of the steering-wheel pattern is primarily influenced by the need to avoid treating the optically active central

portion of the lens, since the cuts introduce significant light scatter within the lens tissue which would affect visual performance *in vivo*. The peripheral portion of the lens also remains untreated since the presence of the iris *in vivo* prevents laser access.

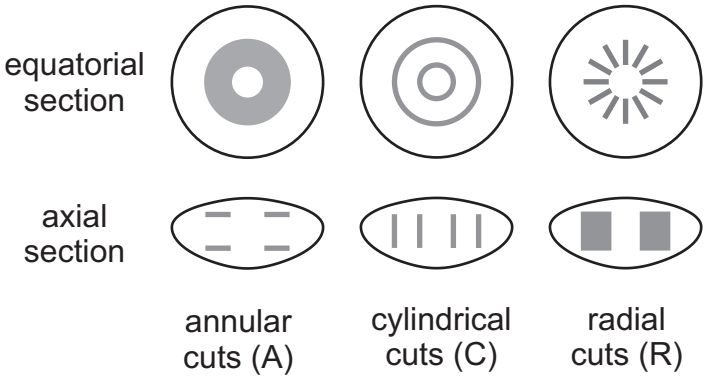

Figure 9.13 – *The three types of cuts which make up the 'steering-wheel pattern' of lentotomy used by Schumacher et al. (2009).*

In order to examine the possible effects of the steering-wheel pattern on *in vivo* accommodation, model A45H from section 9.1 is modified to represent the presence of the various cuts. The 45-year lens is used as this is the anticipated age for lentotomy treatment. The stiffness model H is chosen as the homogeneous value differs little from stiffness model D at this age, and the absence of a distinct nucleus considerably simplifies the process of specifying the presence of lentotomy cuts within the lens.

9.2.1 Modelling lentotomy cuts

A typical single femtosecond laser pulse focused within the lens ablates the material approximately contained within a spheroid with an axial length of about 20 μm aligned with the lens axis and a equatorial diameter of about 5 μm. The material in this zone is vaporized, forming a gas bubble which subsequently dissolves into the surrounding fluid. The lens is left with an ablation zone in which the usual solid constituents of the lens substance have been disrupted. These individual ablation zones created in the lens by laser lentotomy are too small to represent explicitly in a typical finite-element model of the lens. Instead, the effect on the macroscopic behaviour of the lens substance in the regions subjected to ablation are approximated by adjusting the material properties of all of the lens substance in that region.

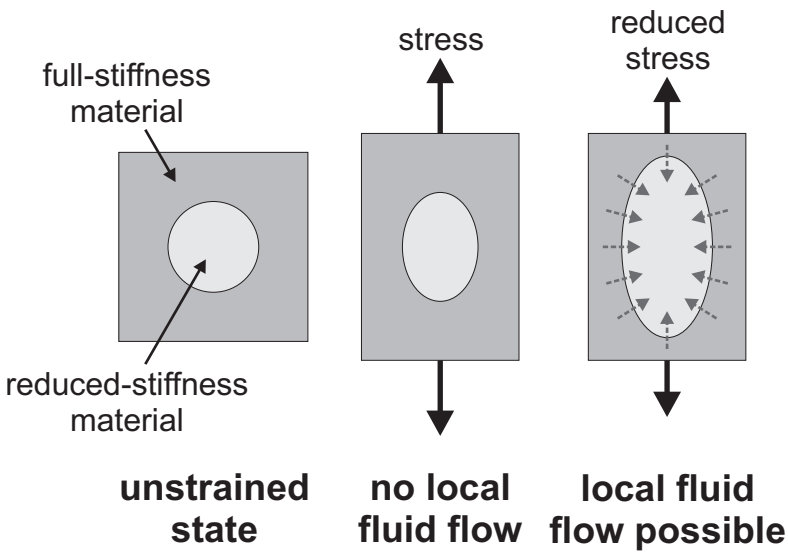

Figure 9.14 – *The influence of fluid flow on the efficacy of a lentotomy ablation zone. A small ablation zone of low stiffness has limited effect if no fluid flow is possible, but becomes more influential if fluid can move from the surrounding tissue into the ablation zone.*

When modelling the lentotomy cuts it is not sufficient to simply determine the region directly modified by ablation and reduce its stiffness accordingly. The neo-Hookean constitutive model treats the macroscopic lens substance as an amorphous nearly-incompressible solid. However, this is unsuitable for characterizing the behaviour of the tissue at the scale of the ablation zone. At this level the lens fibres provide an ordered structure and the possibility of local fluid flow (presumably enhanced by lentotomy) means that the deformation of the solid component of the tissue need not conserve volume locally.

Figure 9.14 illustrates the possible difference in behaviour depending on whether fluid is free to flow into the reduced-stiffness ablation zone. With no fluid flow the ablation zone decreases the overall stiffness of the material, but its effect is limited by the restriction on its volume. When fluid flow is possible the potential for the ablation zone to expand in preference to the stiffer surrounding tissue allows a larger influence on the overall stiffness. There is little information available to inform a constitutive model that might capture these details so instead it is necessary to use models which can approximate the macroscopic deformation of the lens substance without attempting to represent the details of the behaviour at the ablation zones.

Annular and cylindrical cuts In order to model the annular and cylindrical cuts the stiffness of the surrounding area of the lens substance is reduced substantially. The reduced-stiffness region is a strip 0.1 mm wide, centred on each cut. In this region the shear modulus, μ, of the lens substance is 10 % of the value in the uncut lens. The same bulk modulus, κ, is assigned to the reduced-stiffness region as the original material so that the lens as a whole remains nearly incompressible.

The reduced-stiffness region extends well beyond the zone directly affected by ablation since the nearly-incompressible nature of the material would otherwise heavily limit the effect that a cut could have on the overall deformation of the lens. For a very thin incompressible region the deformations parallel to the cut surface must essentially match the deformations in the neighbouring full-stiffness material, which implies that deformations in the orthogonal direction are also similar due to conservation of volume. Thus the effect of such a cut would be limited to reducing shear stresses. Local fluid flows would avoid this limitation, but these cannot be modelled directly with OXFEM_HYPERELASTIC.

Radial cuts The radial cuts of the proposed lentotomy pattern break the axisymmetry of the lens. A full three dimensional model is not possible using OXFEM_HYPERELASTIC, so an approximation which maintains axisymmetry is adopted. The radial cuts are assumed to be sufficiently numerous that the variation in material properties in the circumferential direction does not need to be imposed at the macroscopic level, but instead can be modelled by introducing anisotropy into the constitutive model.

The principal effect on the *in vivo* lens of numerous radial cuts is expected to be a reduction of the tensile stiffness of the material in the circumferential direction, provided local fluid flow allows the volume of the low-stiffness zones to increase in preference to the surrounding full-stiffness tissue. The cuts will also reduce the resistance to shearing in parallel directions, but since the lens only deforms axisymmetrically this is not a property which needs consideration. Finally, the presence of the radial cuts will slightly reduce the stiffness of the lens material radially and axially since the volume of full-stiffness tissue has been reduced by ablation.

The material of the radially cut region of the lens is modelled with an anisotropic con-

stitutive model derived from a strain-energy function that is a modified version of the neo-Hookean material discussed in section 5.3.2. The strain-energy function of an isotropic hyperelastic material can only depend on the three invariants of the right Cauchy-Green tensor, $\mathbf{C}$ (Holzapfel, 2000). These invariants are

$$\begin{aligned} I_1 &= \mathrm{tr}\,(\mathbf{C}) \\ I_2 &= \frac{1}{2}\left(\mathrm{tr}\,(\mathbf{C})^2 - \mathrm{tr}\left(\mathbf{C}^2\right)\right) \\ I_3 &= \det(\mathbf{C}) = J^2 \quad . \end{aligned} \tag{9.10}$$

The strain energy of the neo-Hookean material depends only on I_1 and I_3. The strain-energy function of a transversely isotropic material can additionally depend on the two pseudo-invariants of the combination of the right Cauchy-Green tensor and the unit vector, $\mathbf{a}_0$, aligned with the direction of anisotropy (in the material configuration) (Holzapfel, 2000). These pseudo-invariants are

$$\begin{aligned} I_4 &= \mathbf{a}_0 \cdot \mathbf{C}\mathbf{a}_0 \\ I_5 &= \mathbf{a}_0 \cdot \mathbf{C}^2\mathbf{a}_0 \quad . \end{aligned} \tag{9.11}$$

The pseudo-invariant I_4 is the square of the stretch ratio in the direction of the anisotropy. For a transversely isotropic material consisting of parallel fibres in a matrix the strain-energy function is generally formed as the sum of an isotropic strain-energy function representing the matrix and an anisotropic function representing the additional strain-energy of the fibres. The current situation is similar, with the neo-Hookean material playing the role of the matrix. However, for the radial cuts, the anisotropic component contributes a decrease in the strain energy, and must be chosen so that the strain energy does not become negative for any state of strain. A suitable function for the anisotropic component has the following form

$$\Psi_\alpha = \begin{cases} -\frac{\alpha\mu}{2}\left(\hat{I}_4 + 2\hat{I}_4^{-\frac{1}{2}} - 3\right) & \hat{I}_4 \geq 1 \\ 0 & \hat{I}_4 < 1 \end{cases} , \tag{9.12}$$

where $\hat{I}_4 = J^{-\frac{2}{3}}\mathbf{a}_0 \cdot \mathbf{C}\mathbf{a}_0$ is the fourth pseudo-invariant of the isochoric component of the right Cauchy-Green strain tensor and μ is the shear modulus of the isotropic component of

the strain energy. The parameter α takes a value between 0 and 1, with 0 corresponding to isotropy and 1 corresponding to no initial stiffness in the direction of $\mathbf{a}_0$. The second Piola-Kirchhoff stress and the stiffness of the material are dictated by the first and second derivatives of the strain energy function with respect to $\mathbf{C}$.

$$\begin{aligned}
\frac{\partial \Psi_\alpha}{\partial \mathbf{C}} &= -\frac{\alpha\mu}{3}\left(1-\hat{I}_4^{-\frac{3}{2}}\right)\left(3J^{-\frac{2}{3}}\mathbf{a}\otimes\mathbf{a}-\hat{I}_4\mathbf{C}^{-1}\right) \\
\frac{\partial^2 \Psi_\alpha}{\partial \mathbf{C}^2} &= -\frac{\alpha\mu}{36}\left[27J^{-\frac{4}{3}}\hat{I}_4^{-\frac{5}{2}}\mathbf{a}\otimes\mathbf{a}\otimes\mathbf{a}\otimes\mathbf{a}-6\left(\hat{I}_4-\hat{I}_4^{-\frac{1}{2}}\right)\frac{\partial \mathbf{C}^{-1}}{\partial \mathbf{C}}\right. \\
&\quad \left.+J^{-\frac{2}{3}}\left(2+\hat{I}_4^{-\frac{3}{2}}\right)\left(\hat{I}_4\mathbf{C}^{-1}\otimes\mathbf{C}^{-1}-3\left(\mathbf{C}^{-1}\otimes\mathbf{a}\otimes\mathbf{a}+\mathbf{a}\otimes\mathbf{a}\otimes\mathbf{C}^{-1}\right)\right)\right] \qquad (9.13)
\end{aligned}$$

In OXFEM_HYPERELASTIC, the response of the anisotropic material is calculated by first obtaining the isotropic response from equation 5.2, then augmenting this with the anisotropic component obtained from the equations 9.13.

For the radial cuts $\mathbf{a}_0$ is the unit vector in the circumferential direction, the isotropic shear modulus, μ, of the region subjected to cuts is set to 0.9 times the value in the uncut region, and α is set to 0.5, so the stiffness in the circumferential direction is initially half the value in the axial and radial directions. The bulk modulus, κ, which appears in equation 5.2 is given the same value in the region subjected to radial cuts as the uncut region.

9.2.2 Lentotomy geometry

A 45-year lens geometry, assigned the label C45, is used to model the effect of lentotomy. This geometry is illustrated in figure 9.15. The exterior of the lens and the zonular fibres of C45 are identical to the geometry of A45, while the region subjected to laser ablation is divided into multiple materials which can be assigned properties corresponding either to a cut or an uncut state.

Eight models of accommodation following lentotomy are considered, all using the same finite-element mesh. Three are each subjected to one of the individual components of the steering-wheel pattern: C45H-A has annular cuts, C45H-C has cylindrical cuts, and C45H-R has radial cuts. Three are subjected to pairs of components: C45H-AC has both annular and cylindrical cuts, C45H-AR has both annular and radial cuts, and C45H-CR has both cylindrical and radial cuts. The full steering-wheel pattern is present in model C45H-ACR.

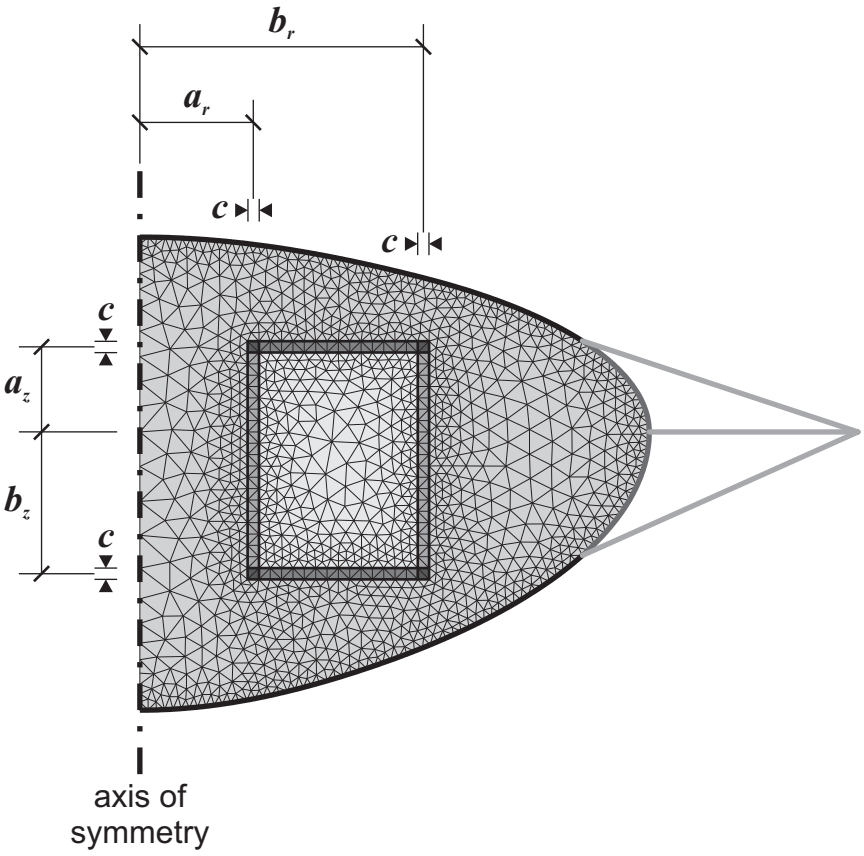

Figure 9.15 – *The mesh used used to simulate accommodation following lentotomy. The cylindrical cuts are at radii of $a_r = 1.0$ mm and $b_r = 2.5$ mm. The anterior annular cut is $a_z = 0.75$ mm anterior of the lens equator and the posterior annular cut is $b_z = 1.25$ mm posterior from the lens equator. The width of the reduced-stiffness region surrounding each cut is $c = 0.1$ mm and also extends 0.05 mm beyond the end of the cut. The radial cuts occupy the region bordered by the annular and cylindrical cuts.*

Finally, model C45H-F is an extreme case in which the whole cutting region is assigned a shear modulus that is 10 % of the value in the uncut region.

9.2.3 Effect on accommodation

The performance of each lentotomy model is assessed in the same manner as the models with native lenses in section 9.1.4. Figure 9.16 plots the optical power of the lens during the process of disaccommodation in models A45H, C45H-A, C45H-R and C45H-F, as these models showed the most clearly distinct responses.

The accommodation amplitude of all the models are provided in table 9.8; complete details are tabulated in appendix D. The effects of the annular and cylindrical cuts are modest, with annular cuts causing a slight reduction in accommodation amplitude and cylindrical

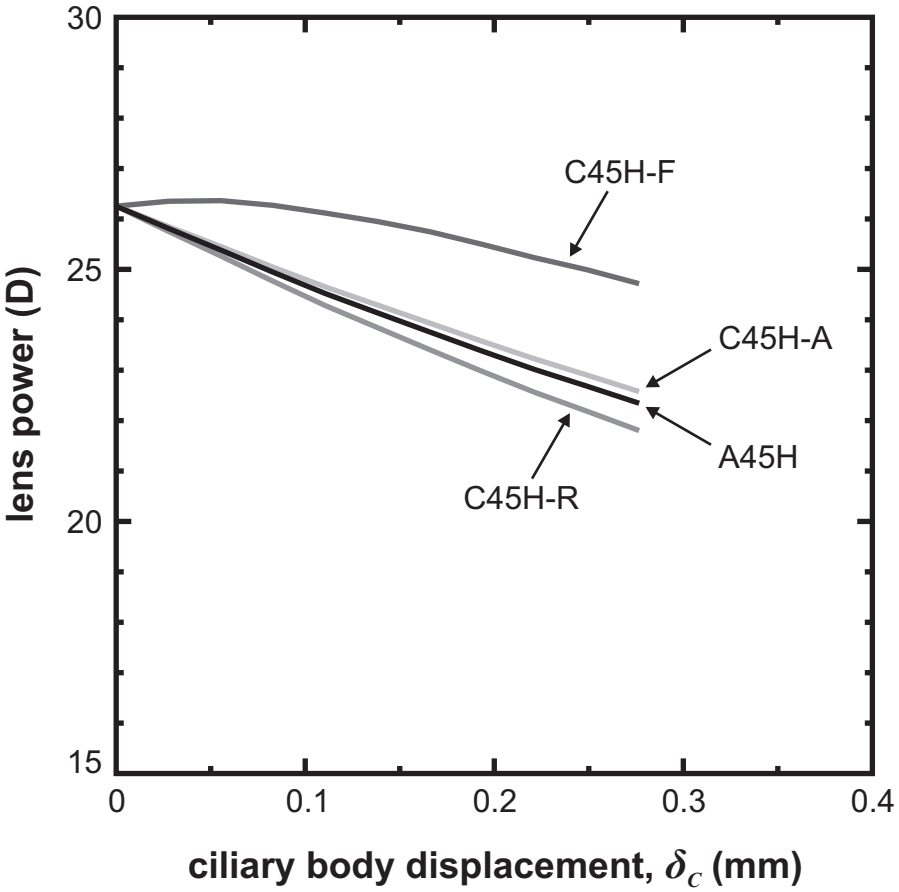

Figure 9.16 – *The optical power of models with different lentotomy cuts. Model A45H is not subjected to lentotomy, C45H-A includes annular cuts, model C45H-R includes radial cuts), and model C45H-F has a reduced stiffness throughout the cutting region.*

Table 9.8 – *The accommodation amplitude, A_S of the models of lentotomy compared to the corresponding untreated model A45H. The change in accommodation amplitude, ΔA_S, is with respect to the untreated lens. The amplitude is measured with respect to the spectacle plane.*

	A_S (D)	ΔA_S (D)
A45H	3.15	
C45H-A	3.00	-0.16
C45H-C	3.22	0.06
C45H-R	3.55	0.40
C45H-F	1.47	-1.68

	A_S (D)	ΔA_S (D)
C45H-AC	3.04	-0.11
C45H-AR	3.36	0.21
C45H-CR	3.56	0.40
C45H-ACR	3.36	0.20

cuts causing a slight increase. The radial cuts cause a moderate improvement in performance, providing 0.4 D of additional accommodation amplitude. This is not sufficient to be clinically useful, though it is enough to encourage further investigation of similar cutting patterns to optimize the performance. The combination of all of the steering-wheel cuts in model C45H-ACR is less effective than the radial cuts alone.

Softening the whole cutting region has a large detrimental effect on accommodation. Model C45H-F induces greater compression on the axis of the lens during disaccommodation than A45H which on its own would be favourable for accommodation amplitude. However, the influence of the soft region is greater further from the axis, resulting in a smaller decrease in the optical power during disaccommodation. The requirement that the axial region of the lens substance remains untreated means that a good cutting pattern must primarily enhance the transmission of force from the equatorial region where the zonular fibres act to the untreated axial region, but not induce larger deformations in the intermediate region. This increased transmission of force is exactly what the present model of the radial cuts achieves by reducing the constraining effect of the circumferential stiffness.

The method adopted for modelling the cuts may not capture important effects within the lens substance, so the limited influence of the steering-wheel pattern on accommodation amplitude suggested by the current models could be misleading. In particular the 0.1 mm width assigned to the reduced-stiffness regions of the annular and cylindrical cuts is apparently insufficient to significantly overcome the limitations imposed by the neo-Hookean constitutive model. On the other hand the effect of the most promising component of the pattern, the radial cuts, may be exaggerated by the form of the anisotropic representation. This constitutive model introduces changes in the response of the lens substance which do not exist in the simple reduced-stiffness representation of the annular and cylindrical materials. The major detrimental effect of model C45H-F is less subject to question and provides a useful indication that simply increasing flexibility within the lens does not necessarily lead to improved accommodation amplitude.

One aspect of lentotomy which the current model cannot address at all is the possibility that the cuts induce a change in the fully-accommodated state of the lens. If the capsule is in a state of tension when the lens is fully accommodated, as suggested by Pedrigi et al. (2007), then using lentotomy to making the lens substance more flexible would allow the capsule to deform it towards a more spherical form with higher optical power. Increasing the power of the lens when accommodated is preferable to decreasing the power of the lens when disaccommodated, as the disaccommodated state is usually appropriate for distance

vision without treatment. In order to model this behaviour it would be necessary to explicitly include residual stresses in the fully-accommodated lens.

9.3 Summary of results

The models of the natural accommodation apparatus presented in this chapter use the new age-stiffness relations given in chapter 8 to describe the lens substance and also treat the lens capsule in a substantially different manner than previous models. The single-age models (A29H, D, E and A45H, D, E) provide a reasonable representation of the accommodation mechanism and the decline in accommodation amplitude with age, while the mixed-age models (B29D and B45D) indicate that the bulk of this decline is due to the increase in stiffness of the lens substance. This suggests that treatments directed at the lens substance, such as lens refilling and laser lentotomy, have the potential to restore some measure of accommodation. There is good agreement between the models and a number of independent experimental measurements, such as the force required to induce disaccommodation. However, some aspects, particularly the change in the thickness of the lens during disaccommodation, indicate that the current models incorporate some substantial inaccuracies.

One of the models of the natural accommodation apparatus (A45H) has been adapted to investigate the potential of laser ablation to treat presbyopic lenses. The models suggest that a series of radial cuts is the most effective of the patterns considered, providing a modest increase of 0.4 D in the amplitude of accommodation. Further improvement may be possible by adjusting the location of the cuts. It is not clear how well the modelled cuts represent the actual effect of laser ablation within the lens. This is unavoidable without further experimental work, as the mechanical behaviour of the lens substance at the scale of the laser ablations is not known in any detail. In particular, a poroelastic constitutive model of the lens substance may be required to properly describe the effect of the laser ablation.

10

Concluding remarks

10.1 Summary of work

The work described in this dissertation consists of the development of an improved method of determining the stiffness of the substance of human lenses based on the spinning lens test devised by Fisher (1971), the use of the improved test to obtain new data characterizing the relationship between age and the stiffness of the lens substance, and the development of models of the *in vivo* accommodation mechanism, making use of the new data, to investigate the development of presbyopia and to assess the efficacy of laser lentotomy as a treatment of presbyopia.

The spinning lens test provides an excellent means of applying known body forces to the fragile lens substance in order to determine its mechanical response. The original spinning lens tests conducted by Fisher (1971) suffered from a number of limitations, including the presence of the capsule in the tests, the modest accuracy of the photographic measurements, and the substantial approximations introduced in the calculations used to obtain stiffness values. Nevertheless, the reported stiffness values have been widely used to inform the understanding of accommodation and the development of presbyopia. The form of the spinning lens test presented in this dissertation addresses these limitations by testing the lens after the capsule has been removed, using a more precise photographic system, and adopting a detailed computational model of the test to determine the stiffness of the lens substance.

The current series of tests has established that the behaviour of a spinning lens with intact capsule differs substantially from the behaviour of the same lens when the capsule has been removed, and that the typical difference in behaviour varies with the age of the lens. Thus obtaining accurate results from the spinning lens test either requires the removal of the capsule, the approach adopted in the current work, or the inclusion of the capsule in the analysis of the spinning lens test, an approach liable to introduce its own uncertainties or inaccuracies.

The photographic system developed for the current series of tests ensures the deformation of the outline of the lens is recorded with high precision. In particular the synchronization of the photographs with the rotor orientation removes one source of random errors from the experiment.

The analysis of the spinning lens test makes use of custom image processing software to determine the location of the lens outlines in the sequences of photographs obtained during the experiment. These outlines are used to construct a finite-element model of each test, from which the stiffness parameters are obtained by applying an iterative inverse method. This approach requires an assumption regarding the form of the heterogeneity of stiffness within the lens. Three alternatives have been considered: a homogeneous model, a model with distinct nucleus and cortex, and a model with an exponential stiffness profile. Because of this imposition the data obtained are appropriate for determining the behaviour of the lens as a whole, such as when *in vivo* accommodation, rather than for determining the stiffness at a particular point within the lens.

The stiffness data obtained from the current spinning lens test indicate that the stiffness of the lens substance increases dramatically with age. When the distinct nucleus and cortex model is adopted, the stiffness of the former is calculated to increase 59-fold between 20 and 50 years, while the stiffness of the latter is calculated to increase 3-fold over the same range of ages. The change seen in the nucleus is far greater than found using the original spinning test (Fisher, 1971), but comparable to the results obtained applying indentation tests to sectioned lenses (Heys et al., 2004; Weeber et al., 2007).

The new stiffness data obtained from the spinning lens test have been integrated into mod-

els describing the mechanism of accommodation for typical subjects aged 29 and 45 years. These models also incorporate a novel method of modelling the capsule. The physical and optical changes displayed by the models have been compared to a range of published measurements. The degree of agreement between models and measurements is mixed. Several aspects compare well, but some, such as the change in the thickness of the lens, differ noticeably from *in vivo* data. The accommodation amplitude and its decline with age are similar to clinical results, suggesting that the models are broadly representative of the accommodation mechanism and the development of presbyopia. An investigation of the effect of the increase in the stiffness of the lens substance with age was conducted. This demonstrated that the difference in stiffness is the dominant cause of the decline in accommodation amplitude from the 29-year model to the 45-year model. This provides some support for a largely lens-based explanation for the development of presbyopia.

A model of the 45-year accommodation mechanism has been adapted to represent the effect of applying a laser lentotomy to the lens substance. The components of the 'steering-wheel pattern' (Schumacher et al., 2009) and their combination were examined in separate models. These models suggest that the most effective component is the set of radial cuts, which could provide a modest increase of about 0.4 D in accommodation amplitude. This might be further enhanced by optimizing the location of the cuts. However, there remains considerable uncertainty in how best to represent the effects of laser lentotomy, primarily due to the lack of information on the mechanics of the lens substance at the small scale at which the lentotomy process operates.

10.2 Future directions

The principal data presented in this dissertation are obtained from the tests conducted on lenses following the removal of the capsule. Lenses were also tested with the capsule intact and in a number of cases the nucleus of the lens was isolated and tested. The photographs from these tests can be analysed using the same general method presented here to obtain further information. Tests on an intact lens can be used to examine the behaviour of the

capsule by making use of the stiffness of the lens substance reported for the given lens in this dissertation. This has not been attempted as part of the current analysis as it is not at present clear how to treat the capsule in such a model. Tests on an isolated nucleus can be used to examine the stiffness of the inner portion of the lens without the obscuring effect of the cortex, making use of the tools developed by the author. This work has been conducted by Mr Chai while at the University of Oxford as a visiting student in the summer of 2010, and compiled in an unpublished report.

The current experimental apparatus could be improved in a number of respects. A lens support with a wider outer radius would allow more of the lens outline to be visible at all orientations of the rotor. The containment box could be further reduced in size and equipped with active temperature and humidity controls. It may also be preferable to replace the current flashgun with a set of suitable LEDs built into the containment box to illuminate the specimen from multiple directions. Automation of the speed of the rotor and the initiation of photography would allow more precisely defined spinning regimes and facilitate investigation of the time-dependent properties of the lens. This would require a different system to trigger the camera as the control from the laptop PC is slow and imprecise. Finally, a system allowing a magnified image of the lens to be viewed throughout the experiment would assist the identification of poorly aligned specimens and the presence of fluid.

One limitation of the current analysis is the difficulty in determining the appropriate constraint to apply at the contact between the lens and the support. This leads to uncertainty in the distribution of stiffness within young lenses in particular. This could be addressed by modifying the test to allow direct measurement of the displacements of the lens in that vicinity. A set of markers or a random pattern on the surface of the lens would allow individual points to be tracked, rather than just the position of the lens outline. For this approach to be accurate the small discrepancies in angular orientation between reference and high-speed tests would also have to be addressed. If this method of tracking were extended to the whole surface of the lens a more precise method of matching analysis to experiment would be possible, though it is not clear to what extent this would improve the accuracy of the test.

There remains a great deal of scope for improving the modelling of the accommodation

apparatus, though this largely depends on the collection of additional data on the geometry and mechanics of the system. The models presented in this dissertation highlight two aspects which would benefit from further consideration.

The first is the method adopted for representing the capsule, which is derived from a quite speculative synthesis of a number of observations. A study examining how a range of alternative capsule models perform compared to the available *in vivo* measurements of the behaviour of the accommodation apparatus may be informative for future modelling. A rigorous implementation of residual stresses in the lens substance and capsule is also desirable. This is of particular relevance to laser lentotomy as the presence of residual stresses in the treated lens substance would lead to changes in the accommodated geometry of the lens, in addition to the changes in the disaccommodated geometry investigated in this dissertation.

The second aspect is the discrepancy noted between the accommodation models and the Scheimpflug photography of Dubbelman et al. (2005) regarding the compression of the nucleus and cortex along the axis of the lens during disaccommodation. It is not clear how the discrepancy would be resolved; however, investigation of the *in vivo* deformation may shed additional light on the behavior of the lens substance.

Appendix A

Safety statement

Mechanics of Presbyopia Project, University of Oxford

Version 3 incorporating limited updates by G. S. Wilde on 21th of April 2011

(Version 2 by H. J. Burd and S. J. Judge on 6th of May 2008)

A.1 Safety issues

The principal Health and Safety issue associated with the project is the (very small) possibility that lenses supplied to the project may be infected (for example with HIV or hepatitis B). This provides a potential hazard to the researchers handling the tissue. The likely exposure route would be percutaneous or by splashing of the eyes or mucous membranes.

A.2 Minimize risk at source

Standard protocol at the Bristol Eye Bank excludes donors with indications of eye infections, and who (for reasons of lifestyle *etc.*) are judged to belong to a relatively high-risk group with respect to HIV or hepatitis. Tests for HIV and hepatitis are conducted but the results will not be routinely available to us at the time we test the lenses as we need to be able to test lenses as soon as possible after death (previous work by others has shown that it may not be straightforward to prevent post-mortem changes in lens properties). In the highly unlikely event of a positive result an appropriate indication of the hazard would be communicated to us. It should be noted that the standards adopted at the eye bank are sufficiently rigorous to ensure the safety of corneas harvested for transplant purposes.

A.3 Adopt appropriate personal protection

Dissection and tissue handling will be conducted by operators wearing lab coats and good quality (for example Touch'n'Stuff) nitrile gloves. Gloves will be changed regularly and when thought to be contaminated. Protective eyewear will be provided for operators without spectacles and worn when possible. Operators will be registered with the University's Occupational Health Department so they can be offered hepatitis B vaccination.

A.4 Dissection procedure

The lenses will be removed from the donor eyes by the Bristol Eye Bank, and will be supplied with the zonule attached to minimize the risk of inadvertent damage to the lens capsule. Tissue will be handled only by forceps or ophthalmic spears. Prior to spinning the lenses, the zonular fibres (the very fine radial fibres that hold the lens in place and attach to the lens capsule near its equator) and any attached ciliary body tissue are removed with ophthalmic spears and scissors. After the encapsulated lens has been tested on the spinning rig, the capsule is removed. This generally only requires the use of forceps. Before and after use, the pointed instruments will be placed in a separate dish so that the points cannot inadvertently come into contact with the hand of the operator. Scalpels will not be used at any point.

A.5 Design of test rig

The rig has been designed to ensure that the lens is spun within a secure enclosure (see figure A.1), preventing the possibility of any tissue or fluid from the lens going any further than the inside of the enclosure. It is known from the work of Fisher (1971) that encapsulated lenses are not damaged by rotation at 1000 rpm and we wish to have the possibility of using higher speeds with the stiffest lenses.

A.6 Disinfecting test rig and dissecting equipment

After each test session, the top part of the rig (lid, casing, lens mount), dissecting instruments, and all other potentially contaminated surfaces are cleaned with Virkon disinfectant (Du

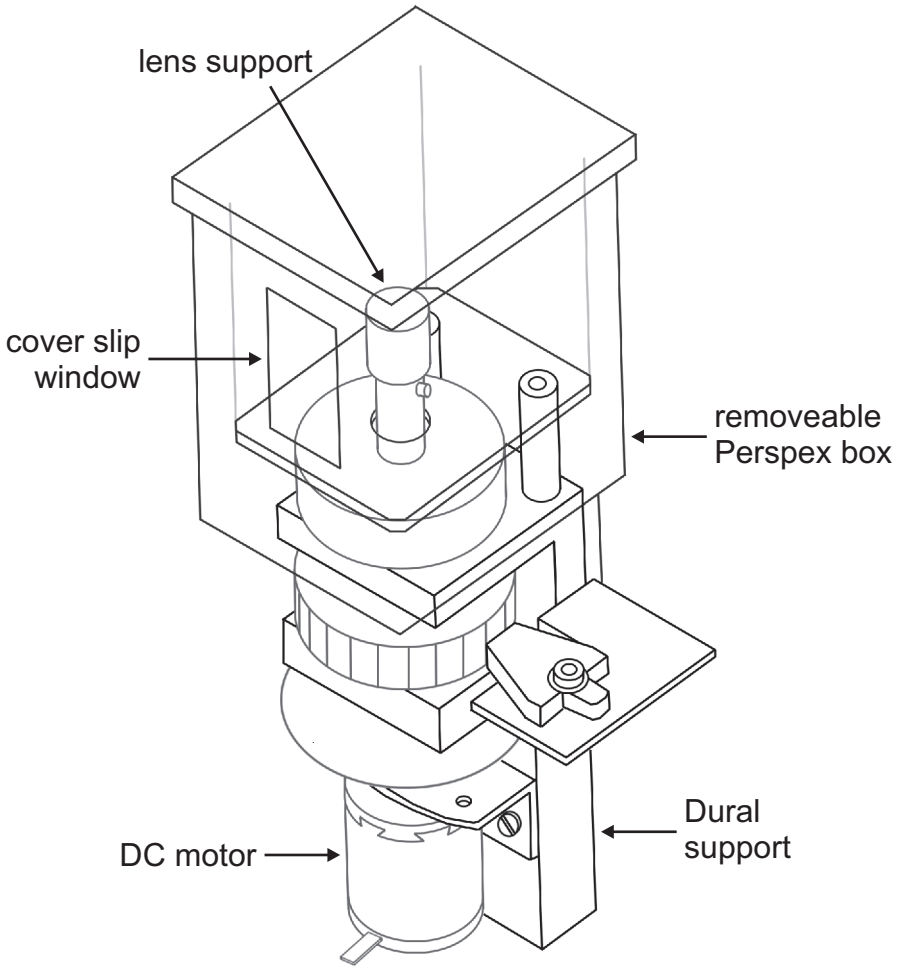

Figure A.1 – *Enclosed test compartment on spinning lens rig.*

Pont), in accordance with the policy of the Botnar Research Centre at which the tests are generally conducted.

A.7 Avoid cross-contamination

Ideally two operators will conduct each test. Dissection and manipulation of the human tissue will be conducted by Operator 1, wearing a lab coat, and gloves. Certain components of the experimental set up (camera, laptop computer, power pack) are regarded as 'clean' and will be operated by Operator 2. Operator 2 will not have physical contact with the lens or dissection equipment.

When only one operator is available all manipulation of the human tissue is conducted

while wearing gloves. Whenever it becomes necessary to handle 'clean' components the gloves are removed and disposed of before doing so. A new pair of gloves is worn if further manipulation of human tissue is necessary.

A.8 Avoid risks to others

Tests will be conducted in a containment level 2 laboratory. Tissue will be tested immediately on delivery to the laboratory. Disposal of human tissue and disposable gloves will be via the clinical waste stream.

A.9 Accidents

1. In the event of an accident resulting in a wound immediately, encourage it to bleed, wash thoroughly with soap and water but **do not scrub**, and cover with waterproof dressing.

2. In the event of contamination of skin, conjunctiva or mucous membrane immediately wash thoroughly.

3. Contact the University Occupational Health Service immediately (01865 282676), or, outside working hours, the on-call microbiologist via the John Radcliffe Hospital (01865 741166).

4. All accidents and incidents must be reported using the accident report book.

A.10 Supervision and training

Dr Harvey Burd, a co-holder of the Wellcome Trust grant funding the work, will take overall responsibility for ensuring that the operators are fully trained and conversant with the risks and precautions. While not medically qualified, he is a chartered civil engineer (MICE) with experience of the importance of rigorous attention to safety procedures in dangerous environments, and he will be able to draw on the expertise of Mr Paul Rosen FRCOS, a practising ophthalmic surgeon who is also a co-holder of the grant.

Appendix B

Flash controller

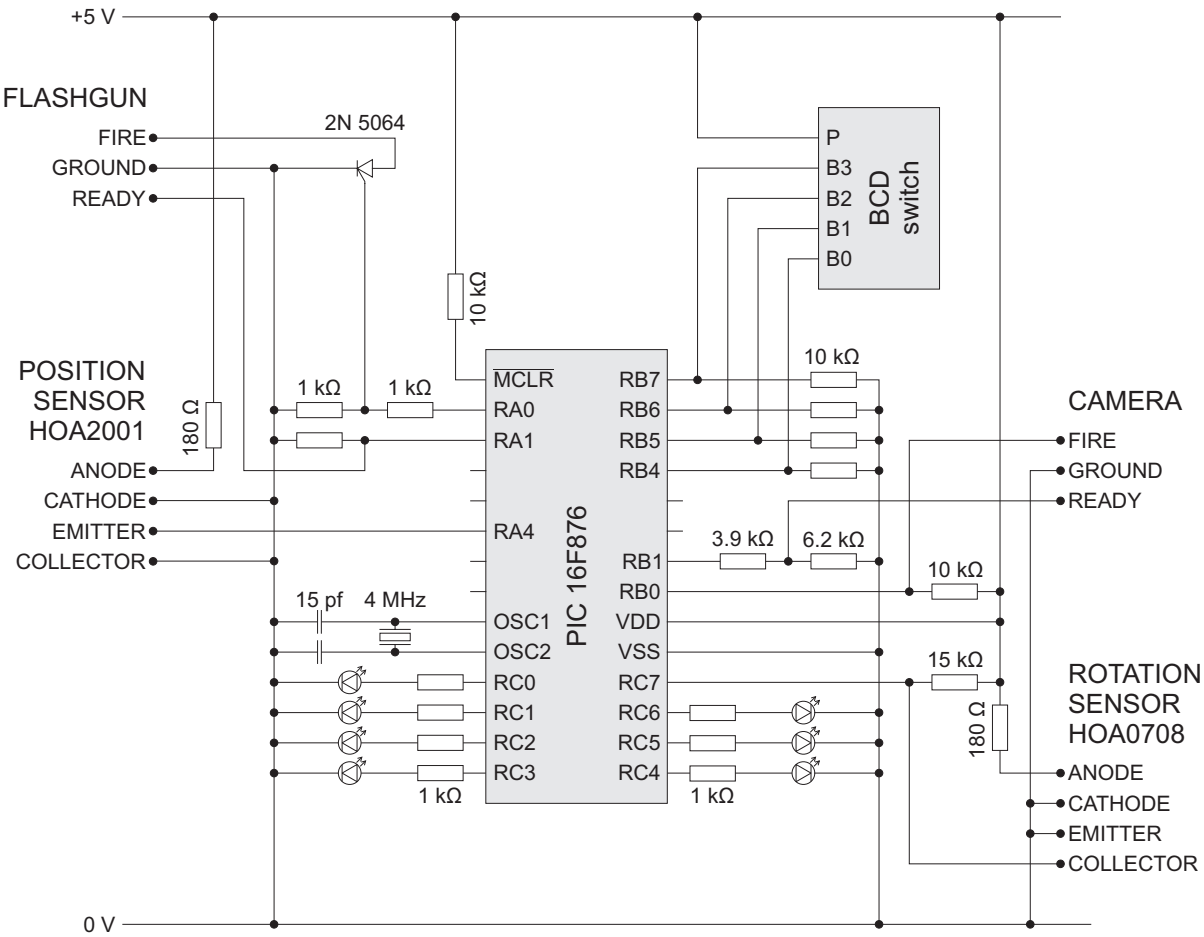

Figure B.1 – *The circuit diagram of the flash controller. Inputs are received from the binary-coded decimal (BCD) switch, the camera, the rotation sensor, the position sensor, and the flashgun. Outputs are provided to the camera and the flashgun.*

Appendix C

Spinning test data

Table C.1 – *Lenses received during preliminary tests.*

Oxford label	**sex**	**age** (years)	**date received**
L001A	M	23	23.08.2007
L001B	M	23	23.08.2007
L002A	M	35	23.08.2007
L002B	M	35	23.08.2007
L003A	F	74	23.08.2007
L003B	F	74	23.08.2007
L004A	F	56	23.08.2007
L004B	F	56	23.08.2007
L005A	F	64	23.08.2007
L005B	F	64	23.08.2007
L006A	M	65	23.08.2007
L006B	M	65	23.08.2007
L007A	F	17	02.11.2007
L007B	F	17	02.11.2007
L008A	M	43	02.11.2007
L008B	M	43	02.11.2007
L009A	F	59	02.11.2007
L009B	F	59	02.11.2007
L010A	M	61	02.11.2007
L011A	M	87	02.11.2007
L011B	M	87	02.11.2007
L012A	M	52	02.11.2007
L012B	M	52	02.11.2007
L013A	M	76	02.11.2007
L013B	M	76	02.11.2007
L014A	M	66	02.11.2007
L014B	M	66	02.11.2007
L015A	M	68	02.11.2007
L015B	M	68	02.11.2007
L016A	M	22	02.11.2007
L016B	M	22	02.11.2007
L017A	M	53	02.11.2007
L017B	M	53	02.11.2007
L018A	M	47	22.02.2008
L018B	M	47	22.02.2008
L019A	M	54	22.02.2008
L019B	M	54	22.02.2008

Table C.2 – *The lenses received for the main spinning lens tests. Aspect ratios were not calculated for lenses L020B, L025B, and L058B because they were damaged or had absent capsules when received. The table continues over four pages.*

Oxford label	**sex**	**age** (years)	**test sequences**	**date of test**	**time since death** (days)	**aspect ratio**, α	**set** $\mathcal{G}$	**swelling**	**damage**	**fluid**
L020A	F	25	*not tested due to absence of capsule*							
L020B	F	25	B1	13.03.2008	2 22:25	–			•	
L021A	F	40	A2 B2	02.04.2008	2 14:42	2.324	•			
L021B	F	40	A2 B2	02.04.2008	2 16:12	2.289				•
L022A	M	26	A1 B1	25.04.2008	2 14:20	1.853		•		•
L022B	M	26	A1 B1	25.04.2008	2 15:01	1.950	•			
L023A	M	49	A2 B2 C2	07.05.2008	1 22:09	2.756			•	
L023B	M	49	*not tested due to damage*							
L024A	M	63	A2 B2 C2	07.05.2008	2 03:35	1.819		•	•	
L024B	M	63	A2 B2 C2	07.05.2008	2 04:42	1.879		•		
L025A	M	37	*not tested due to absence of capsule*							
L025B	M	37	B1	20.06.2008	3 09:33	–			•	
L026A	F	30	A1 B1 C1	20.06.2008	1 12:38	1.895		•		
L026B	F	30	A1 B1 C1	20.06.2008	1 13:37	1.880		•		•
L027A	M	46	A1 B1 C1	16.07.2008	2 15:14	2.264	•			
L027B	M	46	A1 B1 C1	17.07.2008	3 21:01	2.271	•			
L028A	M	31	A1 B1 C1	16.07.2008	2 15:10	2.325			•	
L028B	M	31	A1 B1 C1	16.07.2008	2 18:00	2.212			•	
L029A	M	49	A2 B2 C2	16.07.2008	2 17:19	2.206	•			
L029B	M	49	A2 B2 C2	17.07.2008	3 19:08	2.184	•			

Table C.2 – *(Part ii, continued from previous page.)*

Oxford label	**sex**	**age** (years)	**test sequences**	**date of test**	**time since death** (days)	**aspect ratio**, α	**set** $\mathcal{G}$	**swelling**	**damage**	**fluid**
L030A	M	58	A2 B2 C2	22.07.2008	2 12:20	2.306				•
L030B	M	58	A2 B2 C2	22.07.2008	2 13:36	2.264	•			
L031A	M	21	A1 B1 C1	22.07.2008	2 16:31	2.152			•	•
L031B	M	21	A1 B1 C1	22.07.2008	2 19:25	2.122				•
L032A	F	45	A2 B1	24.07.2008	2 13:49	1.514		•	•	
L032B	F	45	A2 B2 C2	24.07.2008	2 15:06	1.910		•	•	
L033A	F	19	A1 B1 C1	24.07.2008	2 09:08	1.794	•			
L033B	F	19	A1 B1	24.07.2008	2 10:07	1.846				•
L034A	M	43	*not tested due to absence of author*							
L034B	M	43	"							
L035A	M	65	"							
L035B	M	65	"							
L036A	M	53	"							
L036B	M	53	"							
L037A	M	12	A1 B1 C1	16.09.2008	1 22:40	1.944	•			
L037B	M	12	A1 B1 C1	16.09.2008	1 23:40	1.949				•
L038A	F	33	A1 B1 C1	11.11.2008	4 14:11	2.246	•			
L038B	F	33	A5 B1 C1	11.11.2008	4 17:11	2.256				•
L039A	M	43	A1 B1 C1	11.11.2008	4 03:55	2.167			•	
L039B	M	43	A1 B1 C1	11.11.2008	4 04:55	2.255	•			

Table C.2 – *(Part iii, continued from previous page.)*

Oxford label	**sex**	**age** (years)	**test sequences**	**date of test**	**time since death** (days)	**aspect ratio**, α	**set** $\mathcal{G}$	**swelling**	**damage**	**fluid**
L040A	M	23	A1 B1	11.11.2008	4 00:43	1.980	•			
L040B	M	23	A1 B1 C1	11.11.2008	4 01:38	1.926	•			
L041A	M	39	A1 B1 C1	15.01.2009	3 01:21	1.913		•	•	
L041B	M	39	A5 B1 C1	15.01.2009	3 02:21	2.003			•	
L042A	M	40	A4 B1 C1	25.02.2009	2 18:27	1.905		•		
L042B	M	40	A1 B1 C1	25.02.2009	2 19:42	1.917		•		
L043A	M	12	A4 B1 C1	25.02.2009	2 16:05	1.828	•			
L043B	M	12	A1 B1 C1	25.02.2009	2 16:55	1.741	•			
L044A	F	44	A5 B1 C1	19.03.2009	3 14:38	2.111			•	
L044B	F	44	A1 B1 C1	19.03.2009	3 16:08	2.156	•			
L045A	M	45	A2 B2	21.04.2009	3 04:20	1.870		•		•
L045B	M	45	A5 B2 C2	21.04.2009	3 07:45	1.828		•	•	
L046A	F	58	A5 B2 C2 D1	23.04.2009	3 06:48	1.923		•	•	
L046B	F	58	A2 B2 C2 D1	23.04.2009	3 08:38	1.896		•	•	
L047A	M	43	A4 B1 C1 D1	23.04.2009	2 16:55	2.322				•
L047B	M	43	A2 B2 D1	23.04.2009	2 20:20	2.337	•			
L048A	M	48	A5 B2 C2 D1	25.06.2009	2 21:43	2.046				•
L048B	M	48	A2 B2 C2 D3	25.06.2009	3 00:51	2.157				•
L049A	M	60	A5 B2 C2 D2	25.06.2009	2 07:53	1.829		•		•
L049B	M	60	A2 B2 C2 D2	25.06.2009	2 09:15	1.821		•	•	

Table C.2 – *(Part iv, continued from previous page.)*

Oxford label	**sex**	**age** (years)	**test sequences**	**date of test**	**time since death** (days)	**aspect ratio**, α	**set** $\mathcal{G}$	**swelling**	**damage**	**fluid**
L050A	F	48	A5 B2 C2 D3	26.06.2009	2 08:27	2.178	•			
L050B	F	48	A2 B2 C2 D3	26.06.2009	2 09:23	2.176	•			
L051A	M	40	A5 B2 C2 D3	26.06.2009	3 02:36	2.057	•			
L051B	M	40	A2 B2 C2 D3	26.06.2009	3 03:41	1.934		•		•
L052A	F	34	A1 B1	16.07.2009	2 18:20	1.873		•		
L052B	F	34	A2 B2 C2 D3	16.07.2009	2 21:23	2.260	•			
L053A	F	56	A2 B2 D3	24.07.2009	2 17:13	2.055	•			
L053B	F	56	A2 B2 D3	25.07.2009	3 09:41	1.988			•	
L054A	M	52	A2 B2 D3	24.07.2009	3 12:12	2.006	•			
L054B	M	52	A2 B2 D3	25.07.2009	4 01:19	1.995	•			
L055A	M	51	A2 B2 D3	25.07.2009	3 14:35	2.137	•			
L055B	M	51	A2 B2 D3	24.07.2009	2 23:23	2.107	•			
L056A	M	50	A3 B3 D3	29.07.2009	2 14:02	2.323	•			
L056B	M	50	A2 B2 C2 D3	29.07.2009	2 16:16	2.353	•			
L057A	M	58	A3 B3 D3	29.07.2009	2 04:46	2.011				•
L057B	M	58	A2 B2 C2 D3	29.07.2009	2 06:28	2.081	•			
L058A	M	63	A5 B5 D3	12.08.2009	1 19:47	1.816		•		
L058B	M	63	D3	13.08.2009	2 21:12	–			•	
L059A	F	41	A2 B2 D3	12.08.2009	2 07:12	1.913		•		
L059B	F	41	A2 B2 D3	13.08.2009	3 06:25	1.938		•		

Table C.3 – *Equatorial diameter in millimeters of intact lenses of set $\mathcal{G}$ during the sequence of spinning tests up to A_{R4}. The initial intact tests of L052B and L055B were affected by fluid, so additional tests were conducted starting from A_{R2}, which are reported here. Lens L054A was subjected to sequence A2 twice due to technical difficulties in the initial sequence, so the aspect ratio reported in table C.2 is calculated from the first A_{R1} while the diameter from the second is reported here. The aspect ratio reported in table C.2 for lens L029B is calculated using the fluid free portions of the outlines of the lens from A_{R1} and A_{R2}.*

test	A_{R1}	A_{T1}	A_{R2}	A_{T2}	A_{R3}	A_{T3}	A_{R4}
L021A	9.463	9.498	9.462	9.544	9.467	9.628	9.481
L022B	8.732	8.808	8.737	8.890	8.749		
L027A	9.337	9.358	9.327	9.376	9.322		
L027B	9.346	9.375	9.346	9.433	9.354		
L029A	9.425	9.444	9.427	9.472	9.430	9.508	9.433
L029B	*fluid present in all tests*						
L030B	9.812	9.856	9.827	9.933	9.847	9.998	9.859
L033A	8.367	8.468	8.379	8.569	8.395		
L037A	8.352	8.448	8.371	8.573	8.401		
L038A	9.531	9.590	9.537	9.657	9.546		
L039B	9.654	9.682	9.653	9.707	9.656		
L040A	8.591	8.667	8.597	8.732	8.601		
L040B	8.572	8.647	8.578	8.767	8.598		
L043A	8.382	8.469	8.387	8.557	8.393	8.728	8.413
L043B	8.333	8.423	8.335	8.511	8.341		
L044B	9.163	9.190	9.163	9.231	9.173		
L047B	9.543	9.566	9.542	9.598	9.547	9.675	9.556
L050A	9.304	9.321	9.305	9.339	9.308	9.378	9.315
L050B	9.325	9.338	9.322	9.348	9.319	9.400	9.334
L051A	9.015	9.051	9.018	9.085	9.020	9.166	9.035
L052B	–	–	9.502	9.607	9.524	9.766	9.553
L053A	9.308	9.323	9.309	9.345	9.314	9.392	9.312
L054A	9.233	9.254	9.240	9.283	9.246	9.313	9.253
L054B	9.305	9.319	9.307	9.337	9.309	9.366	9.313
L055A	9.225	9.244	9.229	9.268	9.237	9.319	9.246
L055B	–	–	9.221	9.285	9.237	9.337	9.252
L056A	9.324	9.339	9.326	9.353	9.328	9.390	9.330
L056B	9.338	9.353	9.341	9.367	9.342	9.409	9.346
L057B	9.087	9.098	9.088	9.114	9.093	9.156	9.102

Table C.4 – *Axial thickness in millimeters of intact lenses of set $\mathcal{G}$ during the sequence of spinning tests up to A_{R4}. See the caption of table C.3 for discussion of some anomalous tests.*

test	A_{R1}	A_{T1}	A_{R2}	A_{T2}	A_{R3}	A_{T3}	A_{R4}
L021A	4.072	4.015	4.078	3.954	4.069	3.833	4.046
L022B	4.478	4.329	4.464	4.160	4.440		
L027A	4.125	4.082	4.121	4.039	4.110		
L027B	4.115	4.058	4.114	4.017	4.099		
L029A	4.273	4.226	4.271	4.204	4.253	4.167	4.241
L029B	*fluid present in all tests*						
L030B	4.333	4.230	4.306	4.209	4.268	4.170	4.261
L033A	4.664	4.509	4.645	4.359	4.627		
L037A	4.296	4.111	4.268	3.932	4.237		
L038A	4.244	4.135	4.245	4.027	4.235		
L039B	4.281	4.244	4.282	4.208	4.274		
L040A	4.340	4.193	4.331	4.051	4.317		
L040B	4.450	4.302	4.433	4.155	4.417		
L043A	4.585	4.436	4.573	4.273	4.559	3.972	4.529
L043B	4.785	4.638	4.775	4.484	4.764		
L044B	4.249	4.160	4.245	4.093	4.220		
L047B	4.084	4.032	4.098	3.977	4.098	3.854	4.093
L050A	4.271	4.250	4.273	4.240	4.275	4.211	4.271
L050B	4.285	4.253	4.293	4.226	4.296	4.190	4.288
L051A	4.381	4.315	4.383	4.243	4.381	4.082	4.357
L052B	–	–	4.205	3.983	4.176	3.788	4.151
L053A	4.530	4.506	4.535	4.483	4.535	4.433	4.538
L054A	4.687	4.654	4.682	4.621	4.678	4.562	4.673
L054B	4.665	4.650	4.669	4.630	4.667	4.593	4.660
L055A	4.317	4.301	4.317	4.283	4.314	4.249	4.309
L055B	–	–	4.376	4.315	4.370	4.256	4.364
L056A	4.013	3.986	4.012	3.961	4.012	3.914	4.007
L056B	3.968	3.945	3.969	3.922	3.967	3.892	3.962
L057B	4.366	4.333	4.362	4.302	4.360	4.242	4.355

Table C.5 – *Equatorial diameter in millimeters of decapsulated lenses of set $\mathcal{G}$ during the sequence of spinning tests up to B_{R4}. Lens L053A was repositioned following B_{T1}, so values for B_{R1} and B_{T1} are not included here.*

test	B_{R1}	B_{T1}	B_{R2}	B_{T2}	B_{R3}	B_{T3}	B_{R4}
L021A	9.328	9.388	9.341	9.468	9.359	9.623	9.398
L022B	8.567	8.713	8.605	8.900	8.652		
L027A	9.161	9.206	9.165	9.249	9.167		
L027B	9.147	9.196	9.159	9.249	9.171		
L029A	9.379	9.406	9.385	9.449	9.393	9.533	9.416
L029B	9.225	9.256	9.235	9.284	9.240	9.342	9.251
L030B	9.641	9.668	9.650	9.714	9.660	9.828	9.681
L033A	8.241	8.452	8.302	8.726	8.389		
L037A	8.275	8.494	8.344	8.646	8.375		
L038A	9.434	9.523	9.448	9.626	9.462		
L039B	9.538	9.580	9.552	9.654	9.566		
L040A	8.398	8.575	8.451	8.756	8.505		
L040B	8.401	8.586	8.448	8.776	8.506		
L043A	8.286	8.528	8.360	8.748	8.428		
L043B	8.171	8.390	8.225	8.606	8.284		
L044B	9.061	9.121	9.082	9.180	9.095		
L047B	9.349	9.396	9.367	9.448	9.381	9.548	9.401
L050A	9.191	9.211	9.194	9.239	9.199	9.291	9.207
L050B	9.218	9.242	9.225	9.273	9.232	9.324	9.242
L051A	8.899	8.960	8.914	9.034	8.931	9.151	8.955
L052B	9.446	9.532	9.468	9.677	9.495	9.846	9.530
L053A	–	–	9.175	9.227	9.186	9.285	9.196
L054A	9.100	9.124	9.108	9.150	9.113	9.196	9.123
L054B	9.191	9.211	9.197	9.240	9.203	9.283	9.209
L055A	9.123	9.152	9.131	9.192	9.140	9.275	9.156
L055B	9.089	9.116	9.096	9.154	9.105	9.227	9.119
L056A	9.234	9.259	9.245	9.287	9.252	9.357	9.261
L056B	9.247	9.275	9.258	9.305	9.264	9.357	9.271
L057B	8.958	8.976	8.964	9.006	8.968	9.060	8.976

Table C.6 – *Axial thickness in millimeters of decapsulated lenses of set $\mathcal{G}$ during the sequence of spinning tests up to* B_{R4}*. See the caption of table C.5 for discussion of lens L053A.*

test	B_{R1}	B_{T1}	B_{R2}	B_{T2}	B_{R3}	B_{T3}	B_{R4}
L021A	4.053	3.974	4.043	3.890	4.024	3.745	3.983
L022B	4.337	4.041	4.276	3.791	4.209		
L027A	4.015	3.968	4.013	3.920	4.002		
L027B	4.047	3.993	4.035	3.937	4.028		
L029A	4.140	4.113	4.137	4.093	4.135	4.054	4.125
L029B	4.145	4.124	4.144	4.103	4.140	4.060	4.133
L030B	4.153	4.125	4.134	4.116	4.132	4.093	4.129
L033A	4.370	4.039	4.300	3.699	4.200		
L037A	3.905	3.589	3.845	3.377	3.810		
L038A	4.117	3.942	4.095	3.782	4.072		
L039B	4.241	4.192	4.229	4.144	4.221		
L040A	4.395	4.095	4.326	3.830	4.261		
L040B	4.307	4.010	4.254	3.737	4.182		
L043A	4.381	4.044	4.302	3.737	4.216		
L043B	4.535	4.191	4.475	3.866	4.397		
L044B	4.030	3.966	4.023	3.904	4.010		
L047B	3.950	3.901	3.944	3.848	3.926	3.751	3.902
L050A	4.199	4.179	4.199	4.160	4.197	4.123	4.189
L050B	4.227	4.202	4.221	4.181	4.217	4.141	4.211
L051A	4.236	4.144	4.216	4.046	4.188	3.910	4.149
L052B	4.146	3.963	4.113	3.822	4.087	3.600	4.044
L053A	–	–	4.308	4.293	4.309	4.275	4.306
L054A	4.491	4.468	4.484	4.449	4.480	4.413	4.470
L054B	4.555	4.535	4.549	4.517	4.545	4.491	4.541
L055A	4.250	4.213	4.230	4.185	4.221	4.145	4.212
L055B	4.234	4.216	4.233	4.197	4.228	4.160	4.220
L056A	3.872	3.864	3.872	3.853	3.869	3.830	3.865
L056B	3.878	3.864	3.873	3.851	3.868	3.830	3.862
L057B	4.175	4.164	4.173	4.153	4.169	4.133	4.165

Table C.7 – *Stiffness parameters for lenses of set $\mathcal{G}$ calculated from test B_{T2} (1000 rpm) using support constraint F. If this is the preferred constraint for a given lens it is marked in that column.*

	model H	**model D**		**model E**		**preferred**
	μ (Pa)	μ_N (Pa)	μ_C (Pa)	μ_0 (Pa)	μ_1 (Pa)	**constraint**
L021A	7.52×10^2	4.11×10^2	1.21×10^3	1.71×10^2	1.51×10^3	
L022B	1.80×10^2	7.40×10^1	4.15×10^2	3.02×10^1	4.45×10^2	•
L027A	1.06×10^3	7.54×10^2	1.47×10^3	4.34×10^2	1.65×10^3	
L027B	9.04×10^2	7.46×10^2	1.17×10^3	4.72×10^2	1.34×10^3	
L029A	2.06×10^3	3.30×10^3	9.77×10^2	1.22×10^4	6.21×10^2	
L029B	2.28×10^3	3.07×10^3	1.53×10^3	5.69×10^3	1.31×10^3	
L030B	3.30×10^3	8.41×10^3	1.07×10^3	1.34×10^5	3.30×10^2	
L033A	1.49×10^2	5.88×10^1	2.70×10^2	1.42×10^1	3.67×10^2	•
L037A	1.80×10^2	6.44×10^1	3.50×10^2	7.41×10^0	5.38×10^2	•
L038A	4.37×10^2	8.89×10^1	9.77×10^2	1.97×10^1	1.55×10^3	
L039B	1.22×10^3	1.09×10^3	1.42×10^3	8.81×10^2	1.52×10^3	
L040A	1.76×10^2	7.05×10^1	3.86×10^2	1.60×10^1	5.16×10^2	•
L040B	1.85×10^2	5.50×10^1	3.90×10^2	8.79×10^0	5.91×10^2	•
L043A	1.62×10^2	6.43×10^1	2.68×10^2	9.93×10^0	4.26×10^2	•
L043B	1.46×10^2	4.52×10^1	2.82×10^2	8.26×10^0	4.17×10^2	•
L044B	8.72×10^2	4.14×10^2	1.66×10^3	1.45×10^2	2.13×10^3	
L047B	1.25×10^3	7.83×10^2	1.97×10^3	3.87×10^2	2.33×10^3	
L050A	2.26×10^3	2.73×10^3	1.74×10^3	3.72×10^3	1.63×10^3	
L050B	2.19×10^3	2.69×10^3	1.58×10^3	3.79×10^3	1.51×10^3	
L051A	6.71×10^2	3.77×10^2	1.15×10^3	1.68×10^2	1.35×10^3	
L052B	4.52×10^2	1.14×10^2	9.87×10^2	2.76×10^1	1.52×10^3	
L053A	3.02×10^3	1.38×10^4	8.61×10^2	1.55×10^5	3.36×10^2	
L054A	2.81×10^3	3.63×10^3	1.90×10^3	5.47×10^3	1.73×10^3	
L054B	2.71×10^3	4.71×10^3	1.48×10^3	1.02×10^4	1.21×10^3	
L055A	1.98×10^3	3.59×10^3	8.47×10^2	1.13×10^4	6.28×10^2	
L055B	1.94×10^3	3.58×10^3	8.99×10^2	1.11×10^4	6.82×10^2	
L056A	3.31×10^3	6.03×10^3	1.19×10^3	3.61×10^4	6.97×10^2	
L056B	3.19×10^3	6.60×10^3	1.06×10^3	3.90×10^4	6.42×10^2	
L057B	3.64×10^3	7.29×10^3	1.16×10^3	3.90×10^4	7.43×10^2	

Table C.8 – *Stiffness parameters calculated for some lenses of set $\mathcal{G}$ from test B_{T1} (700 rpm) using support constraint F. If this is the preferred constraint for a given lens it is marked in that column.*

	model H	**model D**		**model E**		**preferred**
	μ (Pa)	μ_N (Pa)	μ_C (Pa)	μ_0 (Pa)	μ_1 (Pa)	**constraint**
L022B	1.54×10^2	5.42×10^1	2.93×10^2	6.08×10^0	5.77×10^2	•
L033A	1.31×10^2	5.24×10^1	2.45×10^2	1.13×10^1	3.54×10^2	•
L037A	1.45×10^2	4.39×10^1	2.81×10^2	5.04×10^0	4.12×10^2	•
L038A	2.97×10^2	8.79×10^1	7.99×10^2	2.54×10^1	1.09×10^3	
L040A	1.69×10^2	5.68×10^1	3.36×10^2	7.56×10^0	5.37×10^2	•
L040B	1.66×10^2	4.78×10^1	3.19×10^2	6.34×10^0	5.08×10^2	•
L043A	1.28×10^2	3.93×10^1	2.55×10^2	9.30×10^0	3.19×10^2	•
L043B	1.19×10^2	4.21×10^1	2.33×10^2	8.89×10^0	3.32×10^2	•
L052B	2.92×10^2	5.78×10^0	1.22×10^3	1.90×10^1	1.18×10^3	

Table C.9 – *Stiffness parameters calculated for some lenses of set $\mathcal{G}$ from test B_{T3} (1400 rpm) using support constraint F. If this is the preferred constraint for a given lens it is marked in that column.*

	model H	**model D**		**model E**		**preferred**
	μ (Pa)	μ_N (Pa)	μ_C (Pa)	μ_0 (Pa)	μ_1 (Pa)	**constraint**
L029A	2.17×10^3	2.96×10^3	1.30×10^3	8.79×10^3	8.92×10^2	
L029B	2.21×10^3	2.90×10^3	1.44×10^3	5.09×10^3	1.27×10^3	
L030B	3.95×10^3	7.14×10^3	1.35×10^3	5.76×10^5	2.20×10^2	
L047B	1.27×10^3	7.46×10^2	2.13×10^3	3.17×10^2	2.65×10^3	
L050A	2.41×10^3	2.99×10^3	1.64×10^3	4.47×10^3	1.55×10^3	
L050B	2.33×10^3	2.67×10^3	1.86×10^3	3.30×10^3	1.83×10^3	
L051A	7.67×10^2	4.09×10^2	1.38×10^3	1.62×10^2	1.70×10^3	
L053A	2.96×10^3	1.35×10^4	8.56×10^2	1.53×10^5	3.31×10^2	
L054A	2.71×10^3	4.33×10^3	1.44×10^3	9.77×10^3	1.15×10^3	
L054B	2.88×10^3	5.68×10^3	1.45×10^3	1.35×10^4	1.16×10^3	
L055A	2.10×10^3	3.92×10^3	8.86×10^2	1.33×10^4	6.38×10^2	
L055B	2.12×10^3	3.98×10^3	9.36×10^2	1.29×10^4	6.99×10^2	
L056A	3.48×10^3	6.02×10^3	1.15×10^3	3.49×10^4	7.18×10^2	
L056B	3.36×10^3	6.32×10^3	1.18×10^3	3.33×10^4	7.58×10^2	
L057B	3.67×10^3	7.55×10^3	1.20×10^3	4.98×10^4	6.86×10^2	

Table C.10 – *Stiffness parameters for lenses of set $\mathcal{G}$ calculated from test B_{T2} (1000 rpm) using support constraint S. If this is the preferred constraint for a given lens it is marked in that column.*

	model H	**model D**		**model E**		**preferred**
	μ (Pa)	μ_N (Pa)	μ_C (Pa)	μ_0 (Pa)	μ_1 (Pa)	**constraint**
L021A	8.11×10^2	6.53×10^2	1.06×10^3	4.65×10^2	1.15×10^3	•
L022B	2.38×10^2	2.02×10^2	3.27×10^2	1.80×10^2	2.98×10^2	
L027A	1.13×10^3	1.08×10^3	1.26×10^3	9.77×10^2	1.28×10^3	•
L027B	1.01×10^3	9.50×10^2	1.12×10^3	8.72×10^2	1.11×10^3	•
L029A	2.17×10^3	4.02×10^3	8.98×10^2	1.74×10^4	5.53×10^2	•
L029B	2.50×10^3	3.70×10^3	1.37×10^3	8.84×10^3	1.09×10^3	•
L030B	3.55×10^3	9.59×10^3	1.03×10^3	1.41×10^5	3.30×10^2	•
L033A	1.80×10^2	2.02×10^2	1.57×10^2	3.23×10^2	1.38×10^2	
L037A	2.21×10^2	2.11×10^2	2.36×10^2	2.79×10^2	1.95×10^2	
L038A	4.75×10^2	1.92×10^2	9.33×10^2	6.19×10^1	1.27×10^3	•
L039B	1.33×10^3	1.28×10^3	1.41×10^3	1.23×10^3	1.40×10^3	•
L040A	2.41×10^2	1.91×10^2	3.16×10^2	1.67×10^2	2.92×10^2	
L040B	2.30×10^2	1.96×10^2	2.72×10^2	2.19×10^2	2.54×10^2	
L043A	1.87×10^2	2.16×10^2	1.57×10^2	3.70×10^2	1.36×10^2	
L043B	1.79×10^2	2.18×10^2	1.36×10^2	3.63×10^2	1.28×10^2	
L044B	9.45×10^2	7.34×10^2	1.40×10^3	5.13×10^2	1.46×10^3	•
L047B	1.34×10^3	1.10×10^3	1.76×10^3	7.13×10^2	1.99×10^3	•
L050A	2.55×10^3	3.34×10^3	1.53×10^3	5.87×10^3	1.36×10^3	•
L050B	2.36×10^3	3.25×10^3	1.38×10^3	6.05×10^3	1.22×10^3	•
L051A	7.14×10^2	5.13×10^2	1.11×10^3	3.01×10^2	1.20×10^3	•
L052B	4.81×10^2	2.29×10^2	9.30×10^2	8.28×10^1	1.23×10^3	•
L053A	3.50×10^3	1.84×10^4	8.30×10^2	2.01×10^5	3.13×10^2	•
L054A	3.02×10^3	4.45×10^3	1.63×10^3	8.41×10^3	1.42×10^3	•
L054B	2.89×10^3	6.04×10^3	1.29×10^3	1.57×10^4	9.97×10^2	•
L055A	2.14×10^3	4.27×10^3	7.96×10^2	1.48×10^4	5.74×10^2	•
L055B	2.08×10^3	4.06×10^3	8.60×10^2	1.56×10^4	5.95×10^2	•
L056A	3.61×10^3	7.23×10^3	1.10×10^3	5.31×10^4	6.15×10^2	•
L056B	3.57×10^3	7.48×10^3	1.07×10^3	5.96×10^4	5.54×10^2	•
L057B	3.98×10^3	8.19×10^3	1.12×10^3	5.16×10^4	6.76×10^2	•

Table C.11 – *Stiffness parameters calculated for some lenses of set $\mathcal{G}$ from test B_{T1} (700 rpm) using support constraint S. If this is the preferred constraint for a given lens it is marked in that column.*

	model H	**model D**		**model E**		**preferred**
	μ (Pa)	μ_N (Pa)	μ_C (Pa)	μ_0 (Pa)	μ_1 (Pa)	**constraint**
L022B	2.11×10^2	1.69×10^2	2.72×10^2	2.06×10^2	2.15×10^2	
L033A	1.56×10^2	1.92×10^2	1.13×10^2	3.38×10^2	1.07×10^2	
L037A	1.60×10^2	1.61×10^2	1.63×10^2	3.75×10^2	1.08×10^2	
L038A	3.47×10^2	1.77×10^2	8.27×10^2	9.13×10^0	1.93×10^3	•
L040A	1.98×10^2	1.56×10^2	2.63×10^2	1.47×10^2	2.27×10^2	
L040B	1.90×10^2	1.65×10^2	2.18×10^2	2.41×10^2	1.65×10^2	
L043A	1.41×10^2	1.77×10^2	1.06×10^2	5.00×10^2	7.96×10^1	
L043B	1.41×10^2	2.30×10^2	6.50×10^1	3.80×10^2	8.88×10^1	
L052B	3.53×10^2	2.12×10^2	8.32×10^2	4.68×10^1	1.36×10^3	•

Table C.12 – *Stiffness parameters calculated for some lenses of set $\mathcal{G}$ from test B_{T3} (1400 rpm) using support constraint S. If this is the preferred constraint for a given lens it is marked in that column.*

	model H	**model D**		**model E**		**preferred**
	μ (Pa)	μ_N (Pa)	μ_C (Pa)	μ_0 (Pa)	μ_1 (Pa)	**constraint**
L029A	2.38×10^3	3.39×10^3	1.19×10^3	1.51×10^4	7.03×10^2	•
L029B	2.39×10^3	3.58×10^3	1.26×10^3	8.06×10^3	1.04×10^3	•
L030B	4.35×10^3	8.26×10^3	1.29×10^3	1.03×10^6	1.81×10^2	•
L047B	1.35×10^3	9.35×10^2	2.21×10^3	5.01×10^2	2.57×10^3	•
L050A	2.65×10^3	3.56×10^3	1.46×10^3	6.68×10^3	1.31×10^3	•
L050B	2.55×10^3	3.26×10^3	1.61×10^3	5.32×10^3	1.49×10^3	•
L051A	8.23×10^2	5.36×10^2	1.43×10^3	2.82×10^2	1.60×10^3	•
L053A	3.19×10^3	1.77×10^4	8.28×10^2	2.09×10^5	3.02×10^2	•
L054A	2.89×10^3	5.32×10^3	1.27×10^3	1.32×10^4	1.04×10^3	•
L054B	3.10×10^3	7.00×10^3	1.33×10^3	1.90×10^4	1.01×10^3	•
L055A	2.28×10^3	4.62×10^3	8.38×10^2	1.72×10^4	5.86×10^2	•
L055B	2.32×10^3	4.50×10^3	9.06×10^2	1.69×10^4	6.38×10^2	•
L056A	3.86×10^3	6.41×10^3	1.14×10^3	5.80×10^4	5.92×10^2	•
L056B	3.74×10^3	7.35×10^3	1.16×10^3	4.99×10^4	6.64×10^2	•
L057B	4.04×10^3	8.84×10^3	1.14×10^3	7.73×10^4	5.88×10^2	•

Table C.13 – *Optimum objective function values for lenses of set $\mathcal{G}$ from stiffness calculations for test B_{T2} (1000 rpm).*

		constraint F			constraint S		
	initial Q_{A_0} (mm^2)	**model H** Q_A (mm^2)	**model D** Q_A (mm^2)	**model E** Q_A (mm^2)	**model H** Q_A (mm^2)	**model D** Q_A (mm^2)	**model E** Q_A (mm^2)
L021A	0.409	0.091	0.064	0.058	0.053	0.040	0.040
L022B	1.159	0.243	0.166	0.104	0.161	0.147	0.152
L027A	0.277	0.044	0.034	0.029	0.026	0.025	0.024
L027B	0.319	0.054	0.050	0.048	0.034	0.034	0.034
L029A	0.195	0.053	0.039	0.039	0.059	0.038	0.038
L029B	0.147	0.023	0.019	0.018	0.027	0.016	0.016
L030B	0.150	0.085	0.065	0.061	0.089	0.061	0.058
L033A	1.457	0.244	0.088	0.117	0.259	0.256	0.250
L037A	1.082	0.231	0.085	0.063	0.224	0.224	0.221
L038A	0.787	0.268	0.139	0.142	0.193	0.059	0.063
L039B	0.320	0.072	0.071	0.071	0.060	0.060	0.060
L040A	1.146	0.277	0.242	0.137	0.207	0.195	0.200
L040B	1.209	0.236	0.145	0.068	0.213	0.210	0.212
L043A	1.367	0.255	0.119	0.084	0.291	0.290	0.279
L043B	1.209	0.258	0.130	0.087	0.306	0.305	0.296
L044B	0.326	0.064	0.035	0.028	0.040	0.030	0.030
L047B	0.250	0.051	0.036	0.032	0.036	0.032	0.030
L050A	0.152	0.030	0.029	0.029	0.031	0.026	0.026
L050B	0.157	0.022	0.019	0.019	0.027	0.017	0.017
L051A	0.406	0.093	0.072	0.060	0.060	0.045	0.042
L052B	0.776	0.247	0.136	0.136	0.177	0.070	0.075
L053A	0.116	0.049	0.025	0.025	0.054	0.023	0.023
L054A	0.131	0.024	0.021	0.020	0.027	0.020	0.019
L054B	0.135	0.027	0.020	0.020	0.031	0.019	0.018
L055A	0.175	0.045	0.026	0.028	0.052	0.025	0.027
L055B	0.164	0.039	0.020	0.019	0.046	0.017	0.018
L056A	0.100	0.035	0.018	0.018	0.039	0.017	0.017
L056B	0.102	0.035	0.011	0.012	0.039	0.011	0.010
L057B	0.097	0.040	0.026	0.025	0.044	0.025	0.024

Table C.14 – *Optimum objective function values from stiffness calculations for test* B_{T1} *(700 rpm)..*

		constraint F			constraint S		
	initial Q_{A_0} (mm^2)	**model H** Q_A (mm^2)	**model D** Q_A (mm^2)	**model E** Q_A (mm^2)	**model H** Q_A (mm^2)	**model D** Q_A (mm^2)	**model E** Q_A (mm^2)
L022B	0.738	0.226	0.128	0.131	0.235	0.235	0.233
L033A	0.777	0.160	0.075	0.057	0.185	0.181	0.185
L037A	0.682	0.164	0.056	0.035	0.175	0.170	0.174
L038A	0.445	0.148	0.084	0.084	0.103	0.071	0.070
L040A	0.651	0.144	0.040	0.088	0.154	0.154	0.152
L040B	0.693	0.152	0.041	0.073	0.168	0.167	0.167
L043A	0.797	0.184	0.075	0.042	0.231	0.220	0.229
L043B	0.813	0.189	0.074	0.066	0.240	0.235	0.236
L052B	0.461	0.170	0.102	0.092	0.138	0.114	0.111

Table C.15 – *Optimum objective function values from stiffness calculations for test* B_{T3} *(1400 rpm).*

		constraint F			constraint S		
	initial Q_{A_0} (mm^2)	**model H** Q_A (mm^2)	**model D** Q_A (mm^2)	**model E** Q_A (mm^2)	**model H** Q_A (mm^2)	**model D** Q_A (mm^2)	**model E** Q_A (mm^2)
L029A	0.355	0.073	0.055	0.054	0.083	0.052	0.051
L029B	0.307	0.040	0.026	0.025	0.051	0.021	0.021
L030B	0.258	0.140	0.093	0.072	0.148	0.090	0.067
L047B	0.490	0.112	0.084	0.077	0.083	0.067	0.063
L050A	0.281	0.038	0.031	0.031	0.048	0.025	0.026
L050B	0.283	0.031	0.029	0.029	0.041	0.025	0.026
L051A	0.705	0.176	0.138	0.116	0.117	0.082	0.076
L053A	0.232	0.098	0.050	0.049	0.106	0.045	0.045
L054A	0.258	0.050	0.030	0.030	0.060	0.028	0.031
L054B	0.249	0.051	0.031	0.031	0.060	0.028	0.028
L055A	0.329	0.091	0.044	0.049	0.106	0.043	0.049
L055B	0.306	0.079	0.041	0.039	0.093	0.036	0.035
L056A	0.200	0.075	0.036	0.034	0.083	0.035	0.034
L056B	0.102	0.036	0.014	0.014	0.041	0.014	0.013
L057B	0.184	0.081	0.048	0.046	0.088	0.046	0.045

Appendix D

Accommodation model data

Table D.1 – *The physical effect of disaccommodation on accommodation models of type A and B.*

		ciliary radius r_{CB} (mm)	**lens radius** r_{LE} (mm)	**lens thick-ness** d_L (mm)	**anterior radius** r_A (mm)	**posterior radius** r_P (mm)
A29H	**initial**	6.47	4.31	3.98	7.10	-5.09
	final	6.83	4.60	3.41	11.78	-6.96
	change	0.36	0.29	-0.57	4.69	-1.87
A29D	**initial**	6.47	4.31	3.98	7.10	-5.09
	final	6.83	4.60	3.37	12.49	-7.28
	change	0.36	0.29	-0.61	5.40	-2.19
A29E	**initial**	6.47	4.31	3.98	7.10	-5.09
	final	6.83	4.60	3.37	12.69	-7.38
	change	0.36	0.29	-0.61	5.60	-2.29
A45H	**initial**	6.33	4.49	4.17	8.13	-5.32
	final	6.61	4.72	3.85	10.06	-6.09
	change	0.28	0.23	-0.32	1.92	-0.78
A45D	**initial**	6.33	4.49	4.17	8.13	-5.32
	final	6.61	4.72	3.86	9.93	-6.04
	change	0.28	0.23	-0.31	1.80	-0.73
A45E	**initial**	6.33	4.49	4.17	8.13	-5.32
	final	6.61	4.72	3.87	9.82	-5.99
	change	0.28	0.23	-0.30	1.68	-0.68
B29D	**initial**	6.47	4.31	3.98	7.10	-5.09
	final	6.83	4.57	3.60	9.64	-5.98
	change	0.36	0.26	-0.38	2.54	-0.89
B45D	**initial**	6.33	4.49	4.17	8.13	-5.32
	final	6.61	4.74	3.64	12.24	-7.28
	change	0.28	0.25	-0.53	4.10	-1.96

Table D.2 – *The physical effect of disaccommodation on the models of lentotomized lenses.*

		ciliary radius r_{CB} (mm)	**lens radius** r_{LE} (mm)	**lens thickness** d_L (mm)	**anterior radius** r_A (mm)	**posterior radius** r_P (mm)
C45H-A	**initial**	6.33	4.49	4.17	8.13	-5.32
	final	6.61	4.72	3.85	9.96	-6.02
	change	0.28	0.23	-0.32	1.83	-0.71
C45H-C	**initial**	6.33	4.49	4.17	8.13	-5.32
	final	6.61	4.72	3.84	10.16	-6.09
	change	0.28	0.23	-0.33	2.02	-0.77
C45H-R	**initial**	6.33	4.49	4.17	8.13	-5.32
	final	6.61	4.72	3.82	10.40	-6.21
	change	0.28	0.23	-0.35	2.27	-0.90
C45H-AC	**initial**	6.33	4.49	4.17	8.13	-5.32
	final	6.61	4.72	3.84	10.04	-6.02
	change	0.28	0.23	-0.33	1.90	-0.70
C45H-AR	**initial**	6.33	4.49	4.17	8.13	-5.32
	final	6.61	4.72	3.82	10.27	-6.13
	change	0.28	0.23	-0.35	2.14	-0.82
C45H-CR	**initial**	6.33	4.49	4.17	8.13	-5.32
	final	6.61	4.72	3.82	10.45	-6.19
	change	0.28	0.23	-0.35	2.31	-0.88
C45H-ACR	**initial**	6.33	4.49	4.17	8.13	-5.32
	final	6.61	4.72	3.82	10.30	-6.11
	change	0.28	0.23	-0.35	2.17	-0.80
C45H-F	**initial**	6.33	4.49	4.17	8.13	-5.32
	final	6.61	4.72	3.80	8.96	-5.54
	change	0.28	0.23	-0.37	0.83	-0.23

Bibliography

Abolmaali, A., Schachar, R. A., and Le, T. (2007). Sensitivity study of human crystalline lens accommodation. *Computer Methods and Programs in Biomedicine*, 85(1):77–90.

Augusteyn, R. C. (2007). Growth of the human eye lens. *Molecular Vision*, 13:252–257.

Augusteyn, R. C. (2008). Growth of the lens: in vitro observations. *Clinical and Experimental Optometry*, 91(3):226–239.

Augusteyn, R. C. (2010). On the growth and internal structure of the human lens. *Experimental Eye Research*, 90(6):643–654.

Ayaki, M., Ohde, H., and Yokoyama, N. (1993). Size of the lens nucleus separated by hydrodissection. *Ophthalmic Surgery*, 24(7):492–493.

Barraquer, R. I., Michael, R., Abreu, R., Lamarca, J., and Tresserra, F. (2006). Human lens capsule thickness as a function of age and location along the sagittal lens perimeter. *Investigative Ophthalmology and Visual Science*, 47(5):2053–2060.

Beers, A. P. A., v. d. H. G. L. (1996). Age-related changes in the accommodation mechanism. *Optometry and Vision Science*, 73(4):235–242.

Bellows, J. G. (1944). *Cataract and Abnormalities of the Lens*. Henry Kimpton, London.

Bennett, A. G. and Rabbetts, R. B. (1998). *Clinical Visual Optics*. Butterworth-Heinemann, Oxford, 3rd edition.

Bonet, J. L. and Wood, R. D. (1997). *Nonlinear Continuum Mechanics for Finite Element Analysis*. Cambridge University Press, Cambridge.

Bourge, J.-L., Robert, A. M., Robert, L., and Renard, G. (2007). Zonular fibers, multimolecular composition as related to function (elasticity) and pathology. *Pathologie Biologie*, 55(7):347–359.

Brückner, R., Batschelet, E., and Hugenschmidt, F. (1987). The Basel longitudinal study on aging (1955-1978). *Documenta Ophthalmologica*, 64:235–310.

Brown, N. A. P. (1973). The change in shape and internal form of the lens of the eye on accommodation. *Experimental Eye Research*, 15(4):441–459.

Burd, H., Judge, S. J., and Flavell, M. J. (1999). Mechanics of accommodation of the human eye. *Vision Research*, 39(9):1591–1595.

Burd, H. J. (2009). A structural constitutive model for the human lens capsule. *Biomechanics and Modeling in Mechanobiology*, 8(3):217–231.

Burd, H. J., Judge, S. J., and Cross, J. A. (2002). Numerical modelling of the accommodating lens. *Vision Research*, 42(18):2235–2251.

Burd, H. J., Wilde, G. S., and Judge, S. J. (2006). Can reliable values of Young's modulus be deduced from Fisher's (1971) spinning lens measurements? *Vision Research*, 46(8-9):1346–1360.

Burd, H. J., Wilde, G. S., and Judge, S. J. (2011). An improved spinning lens test to determine the stiffness of the human lens. *Experimental Eye Research*, 92(1):28–39.

Canny, J. F. (1986). A computational approach to edge detection. *IEEE Transactions on Pattern Analysis and Machine Intelligence*, 8(6):679–698.

Chien, C. M., Huang, T., and Schachar, R. A. (2006). Analysis of human crystalline lens accommodation. *Journal of Biomechanics*, 39(4):672–680.

Chrisfield, M. A. (1991). *Non-linear Finite Element Analysis of Solids and Structures, Volume 1: Essentials*. John Wiley and Sons, Chichester.

Coleman, D. J. (1970). Unified model for accommodative mechanism. *American Journal of Ophthalmology*, 69(6):1063–1079.

Coleman, D. J. and Fish, S. K. (2001). Presbyopia, accommodation, and the mature catenary. *Ophthalmology*, 108(9):1544–1551.

Cowper, G. R. (1973). Gaussian quadrature formulas for triangles. *International Journal for Numerical Methods in Engineering*, 7(3):405–408.

Czygan, G. and Hartung, C. (1996). Mechanical testing of isolated senile human eye lens nuclei. *Medical Engineering and Physics*, 18(5):345–349.

Danielsen, C. C. (2004). Tensile mechanical and creep properties of Descemet's membrane and lens capsule. *Experimental Eye Research*, 79(3):343–350.

Dexl, A. K., Seyeddain, O., Riha, W., Hohensinn, M., Hitzl, W., and Grabner, G. (2011). Reading performance after implantation of a small-aperture corneal inlay for the surgical correction of presbyopia: two-year follow-up. *Journal of Cataract and Refractive Surgery*, 37(3):525–531.

Donders, F. C. (1864). *On the Anomalies of Accommodation and Refraction of the Eye*. New Sydenham Society, London.

Duane, A. J. (1912). Normal values of the accommodation at all ages. *Journal of the American Medical Association*, 59(12):1010–1013.

Duane, A. J. (1922). Studies in monocular and binocular accommodation with their clinical applications. *American Journal of Ophthalmology*, 5(11):865–877.

Dubbelman, M. and van der Heijde, G. L. (2001). The shape of the aging human lens: curvature, equivalent refractive index and the lens paradox. *Vision Research*, 41(14):1867–1877.

Dubbelman, M., van der Heijde, G. L., and Weeber, H. A. (2005). Change in shape of the aging human crystalline lens with accommodation. *Vision Research*, 45(1):117–132.

Dubbelman, M., van der Heijde, G. L., Weeber, H. A., and Vrensen, G. F. J. M. (2003). Changes in the internal structure of the human crystalline lens with age and accommodation. *Vision Research*, 43(22):2363–2375.

Engwirda, D. (2007). Mesh2d v2.3. URL: http://www.mathworks.com/matlabcentral/fileexchange/25555 [accessed 18 February 2008].

Erpelding, T. N., Hollman, K. W., and O'Donnell, M. (2007). Mapping age-related elasticity changes in porcine lenses using bubble-based acoustic radiation force. *Experimental Eye Research*, 84(2):332–341.

Farnsworth, P. N. and Shyne, S. E. (1979). Anterior zonular shifts with age. *Experimental Eye Research*, 28(3):291–297.

Fisher, R. F. (1969). Elastic constants of the human lens capsule. *Journal of Physiology*, 201(1):1–19.

Fisher, R. F. (1971). The elastic constants of the human lens. *Journal of Physiology*, 212(1):147–180.

Fisher, R. F. (1973). Presbyopia and the changes with age in the human crystalline lens. *Journal of Physiology*, 228(3):765–779.

Fisher, R. F. (1977). The force of contraction of the human ciliary muscle during accommodation. *Journal of Physiology*, 270(1):51–74.

Fisher, R. F. (1982). The vitreous and lens in accommodation. *Transactions of the Ophthalmological Societies of the United Kingdom*, 102(3):318–322.

Fisher, R. F. (1986). The ciliary body in accommodation. *Transactions of the Ophthalmological Societies of the United Kingdom*, 105(2):208–219.

Fisher, R. F. and Pettet, B. E. (1972). The postnatal growth of the capsule of the human crystalline lens. *Journal of Anatomy*, 112(2):207–214.

Fisher, R. F. and Pettet, B. E. (1973). Presbyopia and the water content of the human crystalline lens. *Journal of Physiology*, 234(2):443–447.

Garner, L. F. and Smith, G. (1997). Changes in equivalent and gradient refractive index of the crystalline lens with accommodation. *Optometry and Vision Science*, 74(2):114–119.

Glasser, A. (2008). Restoration of accommodation: surgical options for correction of presbyopia. *Clinical and Experimental Optometry*, 91(3):279–295.

Glasser, A. and Campbell, M. C. W. (1998). Presbyopia and the optical changes in the human crystalline lens with age. *Vision Research*, 38(2):209–229.

Glasser, A. and Campbell, M. C. W. (1999). Biometric, optical and physical changes in the isolated human crystalline lens with age in relation to presbyopia. *Vision Research*, 39(11):1991–2015.

Gullapalli, V., Murthy, P., and Murthy, K. (1995). Colour of the nucleus as a marker of nuclear hardness, diameter and central thickness. *Indian Journal of Ophthalmology*, 43(4):181–184.

Hamasaki, D., Ong, J., and Marg, E. (1956). The amplitude of accommodation in presbyopia. *American Journal of Ophthalmology and Archives of American Academy of Optometry*, 33(1):3–14.

Hermans, E. A., Dubbelman, M., van der Heijde, G. L., and Heethaar, R. M. (2006). Estimating the external force acting on the human eye lens during accommodation by finite element modelling. *Vision Research*, 46(21):3642–3650.

Hermans, E. A., Dubbelman, M., van der Heijde, G. L., and Heethaar, R. M. (2007). The shape of the human lens nucleus with accommodation. *Journal of Vision*, 7(10):1–10.

Hermans, E. A., Dubbelman, M., van der Heijde, G. L., and Heethaar, R. M. (2008a). Change in the accommodative force on the lens of the human eye with age. *Vision Research*, 48(1):119–126.

Hermans, E. A., Pouwels, P. J. W., Dubbelman, M., Kuijer, J. P. A., van der Heijde, R. G. L., and Heethaar, R. M. (2009). Constant volume of the human lens and decrease in surface area of the capsular bag during accommodation: an MRI and scheimpflug study. *Investigative Ophthalmology and Visual Science*, 50(1):281–289.

Hermans, E. A., Terwee, T. T., Koopmans, S. A., Dubbelman, M., van der Heijde, G. L., and Heethaar, R. M. (2008b). Development of a ciliary muscle-driven accommodating intraocular lens. *Journal of Cataract and Refractive Surgery*, 34(12):2133–2138.

Heys, K. R., Cram, S. L., and Truscott, R. J. W. (2004). Massive increase in the stiffness of the human lens nucleus with age: the basis for presbyopia? *Molecular Vision*, 10:956–963.

Heys, K. R., Friedrich, M. G., and Truscott, R. J. W. (2007). Presbyopia and heat: changes associated with aging of the human lens suggest a functional role for the small heat shock protein, alpha-crystallin, in maintaining lens flexibility. *Aging Cell*, 6(6):807–815.

Hirunyachote, P. (2003). Mechanism of accommodation of the human eye. Part II project, Department of Engineering Science, University of Oxford.

Hollman, K. W., O'Donnell, M., and Erpelding, T. N. (2007). Mapping elasticity in human lenses using bubble-based acoustic radiation force. *Experimental Eye Research*, 85(6):890–893.

Holzapfel, G. A. (2000). *Nonlinear Solid Mechanics. A Continuum Approach for Engineering*. John Wiley and Sons, Chichester.

Irvine, H. M. (1981). *Cable Strucures*. MIT Press, Cambridge, MA.

Itoi, M., Ito, N., and Kaneko, H. (1965). Visco-elastic properties of the lens. *Experimental Eye Research*, 4(3):168–173.

Jones, C. E., Atchison, D. A., Meder, R., and Pope, J. M. (2005). Refractive index distribution and optical properties of the isolated human lens measured using magnetic resonance imaging (MRI). *Vision Research*, 45(18):2352–2366.

Jones, C. E., Atchison, D. A., and Pope, J. M. (2007). Changes in lens dimensions and refractive index with age and accommodation. *Optometry and Vision Science*, 84(10):990–995.

Kasthurirangan, S., Markwell, E., Atchison, D. A., and Pope, J. M. (2008). In vivo study of changes in refractive index distribution in the human crystalline lens with age and accommodation. *Investigative Ophthalmology and Visual Science*, 49(6):2531–2540.

Koopmans, S. A., Terwee, T., Glasser, A., Wendt, M., Vilipuru, A. S., Kooten, T. G. v., Norrby, S., Haitjema, H. J., and Kooijman, A. C. (2006). Accommodative lens refilling in rhesus monkeys. *Investigative Ophthalmology and Visual Science*, 47(7):2976–2984.

Koretz, J. F., Cook, C. A., and Kaufman, P. L. (2001). Aging of the human lens: Changes in lens shape at zero-diopter accommodation. *Journal of the Optical Society of America A: Optics and Image Science, and Vision*, 18(2):265–272.

Koretz, J. F., Cook, C. A., and Kaufman, P. L. (2002). Aging of the human lens: Changes in lens shape upon accommodation and with accommodative loss. *Journal of the Optical Society of America A: Optics and Image Science, and Vision*, 19(1):144–151.

Koretz, J. F. and Handelman, G. H. (1986). Modeling age-related accomodative loss in the human eye. *Mathematical Modelling*, 7(5-8):1003–1014.

Krag, S. and Andreassen, T. T. (2003a). Mechanical properties of the human lens capsule. *Progress in Retinal and Eye Research*, 22(6):749–767.

Krag, S. and Andreassen, T. T. (2003b). Mechanical properties of the human posterior lens capsule. *Investigative Ophthalmology and Visual Science*, 44(2):691–696.

Krag, S., Olsen, T., and Andreassen, T. T. (1997). Biomechanical characteristics of the human anterior lens capsule in relation to age. *Investigative Ophthalmology and Visual Science*, 38(2):357–363.

Leyland, M. J. and Zinicola, E. (2003). Multifocal versus monofocal intraocular lenses in cataract surgery: a systematic review. *Ophthalmology*, 110(9):1789–1798.

Ljubimova, D., Eriksson, A., and Bauer, S. (2008). Aspects of eye accommodation evaluated by finite elements. *Biomechanics and Modeling in Mechanobiology*, 7:139–150.

Malecaze, F. J., Gazagne, C. S., Tarroux, M. C., and Gorrand, J.-M. (2001). Scleral expansion bands for presbyopia. *Ophthalmology*, 108(12):2165–2171.

Manns, F., Parel, J.-M., Denham, D., Billotte, C., Ziebarth, N., Borja, D., Fernandez, V., Aly, M., Arrieta, E., Ho, A., and Holden, B. (2007). Optomechanical response of human and monkey lenses in a lens stretcher. *Investigative Ophthalmology and Visual Science*, 48(7):3260–3268.

Martin, H., Guthoff, R. F., Terwee, T., and Schmitz, K.-P. (2005). Comparison of the accommodation theories of Coleman and of Helmholtz by finite element simulations. *Vision Research*, 45(22):2910–2915.

Mathews, S. M. (1999). Scleral expansion surgery does not restore accommodation in human presbyopia. *Ophthalmology*, 106(5):873–877.

Menapace, R., Findl, O., Kriechbaum, K., and Leydolt-Koeppl, C. (2007). Accommodating intraocular lenses: a critical review of present and future concepts. *Graefe's Archive for Clinical and Experimental Ophthalmology*, 245(4):473–489.

Moffat, B. A. and Pope, J. M. (2002). Anisotropic water transport in the human eye lens studied by diffusion tensor NMR micro-imaging. *Experimental Eye Research*, 74(6):677–687.

Nelder, J. A. and Mead, R. (1965). A simplex method for function minimization. *The Computer Journal*, 7(4):308–313.

Nishi, O. and Nishi, K. (1998). Accommodation amplitude after lens refilling with injectable silicone by sealing the capsule with a plug in primates. *Archives of Ophthalmology*, 116(10):1358–1361.

Nishi, O., Nishi, K., Nishi, Y., and Chang, S. (2008). Capsular bag refilling using a new accommodating intraocular lens. *Journal of Cataract and Refractive Surgery*, 34(2):302–309.

O'Neill, W. D. and Doyle, J. M. (1968). A thin shell deformation analysis of the human lens. *Vision Research*, 8(2):193–206.

Ott, M. (2006). Visual accommodation in vertebrates: mechanisms, physiological response and stimuli. *Journal of Comparative Physiology A: Neuroethology, Sensory, Neural, and Behavioral Physiology*, 192(2):97–111.

Pardue, M. and Sivak, J. (2000). Age-related changes in human ciliary muscle. *Optometry and Vision Science*, 77(4):204–210.

Parel, J.-M., Gelender, H., Trefers, W., and Norton, E. (1986). Phaco-ersatz: cataract surgery designed to preserve accommodation. *Graefe's Archive for Clinical and Experimental Ophthalmology*, 224(2):165–173.

Patnaik, B. (1967). A photographic study of accommodative mechanisms: changes in the lens nucleus during accommodation. *Investigative Ophthalmology and Visual Science*, 6(6):601–611.

Pedrigi, R. M., David, G., Dziezyc, J., and Humphrey, J. D. (2007). Regional mechanical properties and stress analysis of the human anterior lens capsule. *Vision Research*, 47(13):1781–1789.

Reilly, M. A. and Ravi, N. (2010). A geometric model of ocular accommodation. *Vision Research*, 50(3):330–336.

Ripken, T., Breitenfeld, P., Fromm, M., Oberheide, U., Gerten, G., and Lubatschowski, H. (2006). Fem simulation of the human lens compared to ex-vivo porcine lens cutting pattern: a possible treatment of presbyopia. In *Proceedings of the SPIE*, volume 6138.

Rosen, A. M., Denham, D. B., Fernandez, V., Borja, D., Ho, A., Manns, F., Parel, J.-M., and Augusteyn, R. C. (2006). In vitro dimensions and curvatures of human lenses. *Vision Research*, 46(6-7):1002–1009.

Schachar, R. A. (1992). Cause and treatment of presbyopia with a method for increasing the amplitude of accommodation. *Annals of Ophthalmology*, 24(12):445–447, 452.

Schachar, R. A., Huang, T., and Huang, X. (1993). Mathematic proof of Schachar's hypothesis of accommodation. *Annals of Ophthalmology*, 25(1):5–9.

Schumacher, S., Oberheide, U., Fromm, M., Ripken, T., Ertmer, W., Gerten, G. J., Wegener, A. R., and Lubatschowski, H. (2009). Femtosecond laser induced flexibility change of human donor lenses. *Vision Research*, 49(14):1853–1859.

Sloan, S. W. and Randolph, M. F. (1982). Numerical prediction of collapse loads using finite element methods. *International Journal for Numerical and Analytical Methods in Geomechanics*, 6(1):47–76.

Sorkin, T. (2005). The stiffness of the ocular lens. Third year research project, Department of Physiology, University of Oxford.

Stachs, O., Martin, H., Behrend, D., Schmitz, K.-P., and Guthoff, R. F. (2006). Three-dimensional ultrasound biomicroscopy, environmental and conventional scanning electron microscopy investigations of the human zonula ciliaris for numerical modelling of accommodation. *Graefe's Archive for Clinical and Experimental Ophthalmology*, 244:836–844.

Stachs, O., Schumacher, S., Hovakimyan, M., Fromm, M., Heisterkamp, A., Lubatschowski, H., and Guthoff, R. F. (2009). Visualization of femtosecond laser pulse-induced microincisions inside crystalline lens tissue. *Journal of Cataract and Refractive Surgery*, 35(11):1979–1983.

Strenk, S. A., Semmlow, J. L., Strenk, L. M., Munoz, P., Gronlund-Jacob, J., and DeMarco, J. K. (1999). Age-related changes in human ciliary muscle and lens: a magnetic resonance imaging study. *Investigative Ophthalmology and Visual Science*, 40(6):1162–1169.

Strenk, S. A., Strenk, L. M., and Koretz, J. F. (2005). The mechanism of presbyopia. *Progress in Retinal and Eye Research*, 24(3):379–393.

Sweeney, M. H. J. and Truscott, R. J. W. (1998). An impediment to glutathione diffusion in older normal human lenses: a possible precondition for nuclear cataract. *Experimental Eye Research*, 67(5):587–595.

Urs, R., Ho, A., Manns, F., and Parel, J.-M. (2010). Age-dependent Fourier model of the shape of the isolated ex vivo human crystalline lens. *Vision Research*, 50(11):1041–1047.

van Alphen, G. W. H. M. and Graebel, W. P. (1991). Elasticity of tissues involved in accommodation. *Vision Research*, 31(7-8):1417–1438.

van de Sompel, D., Kunkel, G. J., Hersh, P. S., and Smits, A. J. (2010). Model of accommodation: contributions of lens geometry and mechanical properties to the development of presbyopia. *Journal of Cataract and Refractive Surgery*, 36(11):1960–1971.

von Helmholtz, H. (1855). Ueber die accommodation des auges. *Albrecht von Graefes Archiv für klinische und experimentelle Opthalmologie*, 1(2):1–14.

Weale, R. A. (1990). Evolution, age and ocular focus. *Mechanisms of Ageing and Development*, 53(1):85–89.

Weeber, H. A. (2002). Influence of the stress-free shape of the lens on accommodation. *Investigative Ophthalmology and Visual Science*, 43(12):ARVO Meeting abstract no. 410.

Weeber, H. A., Eckert, G., Pechhold, W., and van der Heijde, R. G. L. (2007). Stiffness gradient in the crystalline lens. *Graefe's Archive for Clinical and Experimental Ophthalmology*, 245(9):1357–1366.

Weeber, H. A., Eckert, G., Soergel, F., Meyer, C. H., Pechhold, W., and van der Heijde, R. G. L. (2005). Dynamic mechanical properties of human lenses. *Experimental Eye Research*, 80(3):425–434.

Weeber, H. A. and van der Heijde, R. G. L. (2007). On the relationship between lens stiffness and accommodative amplitude. *Experimental Eye Research*, 85(5):602–607.

Weeber, H. A. and van der Heijde, R. G. L. (2008). Internal deformation of the human crystalline lens during accommodation. *Acta Ophthalmologica*, 86(6):642–647.

Wilson, R. S. (1997). Does the lens diameter increase or decrease during accommodation? Human accommodation studies: a new technique using infrared retro-illumination video

photography and pixel unit measurements. *Transactions of the American Ophthalmological Society*, 95:261–270.

Wormstone, I. M., Wang, L., and Liu, C. S. C. (2009). Posterior capsule opacification. *Experimental Eye Research*, 88(2):257–269.

Wyatt, H. J. (1993). Application of a simple mechanical model of accommodation to the aging eye. *Vision Research*, 33(5-6):731–738.

Ziebarth, N. M., Borja, D., Arrieta, E., Aly, M., Manns, F., Dortonne, I., Nankivil, D., Jain, R., and Parel, J.-M. (2008). Role of the lens capsule on the mechanical accommodative response in a lens stretcher. *Investigative Ophthalmology and Visual Science*, 49(10):4490–4496.